A light-matter interface based on ion Coulomb crystals in an optical cavity

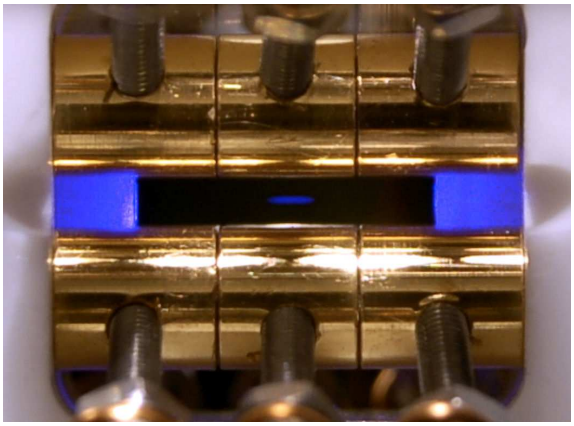

Magnus Albert

PhD Thesis

Danish National Research Foundation
Center for Quantum Optics - QUANTOP
Department of Physics and Astronomy
The University of Aarhus

November 2010

A light-matter interface based on ion Coulomb crystals in an optical cavity

Magnus Albert

PhD Thesis

Danish National Research Foundation
Center for Quantum Optics - QUANTOP
Department of Physics and Astronomy
The University of Aarhus

November 2010

This Thesis is submitted to the Faculty of Science at the University of Aarhus, Denmark, in order to fulfill the requirements for obtaining the PhD degree in Physics.
The studies have been carried out under the supervision of Prof. Michael Drewsen in the Ion Trap Group at the Department of Physics and Astronomy at the University of Aarhus from December 2007 to November 2010.

A light-matter interface based on ion Coulomb crystals in an optical cavity

Magnus Albert
The University of Aarhus, November 2010

Electronically available at `www.phys.au.dk/iontrap`.

Acknowledgements

This thesis could not have been accomplished without the assistance of many people. It is appropriate to begin it by acknowledging those whose support, encouragement, help and advice has been invaluable to me.

First and foremost I would like to thank my supervisor Prof. Michael Drewsen for giving me the great opportunity to do my PhD in the Ion Trap Group at the University of Aarhus and for guiding and motivating me in the past three years.

I am also very grateful to my post-doc Aurelién Dantan , whose enthusiasm and immense knowledge has contributed a lot to this work. I enjoyed his company a lot - both in the laboratory and on the beach volleyball court.

I would also like to thank all the other people of the cavity-trap-team for their contributions and for making the long days in the laboratory so enjoyable and productive: Joan Marler, for introducing me to the world of LabView and for all her input to the experiment and the nice atmosphere in the lab, my predecessor Peter Herskind for introducing me to the experiment and the lab equipment and for entrusting me with the project, Rasmus Bogh Linnet for taking over with great enthusiasm and skill and all the students for their work on laser systems, reference cavities, frequency doubling systems, simulations, etc... Even though it has been hard work at times it was also a lot of fun!

A big thank-you goes to the former and present members of the Ion Trap Group, not only for the fruitful discussions about physics and the daily support in the laboratory, but also for making my time here in Århus so pleasant and enjoyable.

I also acknowledge all the help and support of the staff from the electronics department, the construction group and the mechanical workshop.

While writing this thesis I benefitted a lot from discussions with Aurélien Dantan and Andreas Stute who took the big effort of proof-reading it and to whom I am very grateful. Their comments and remarks improved the thesis a lot.

Finally, I would like to thank my family and my friends for their support and encouragement in the past three years.

Magnus Albert, November 2010

List of publications

Part of the work presented in this thesis has been published in the following articles:

[I] M. Albert, A. Dantan, and M. Drewsen.
Cavity electromagnetically induced transparency and optical switching with ion Coulomb crystals.
Manuscript in preparation.

[II] M. Albert, J. Marler, P.F. Herskind, A. Dantan, and M. Drewsen.
Collective strong coupling between ion Coulomb crystals and an optical cavity field: Theory and Experiments.
Manuscript in preparation.

[III] A. Dantan, J. Marler, M. Albert, D. Guénot, and M. Drewsen.
Noninvasive vibrational mode spectroscopy of ion Coulomb crystals through resonant collective coupling to an optical cavity field.
Physical Review Letters **105**, 103001 (2009).

[IV] A. Dantan, M. Albert, J. Marler, P.F. Herskind, and M. Drewsen.
Large ion Coulomb crystals: A near-ideal medium for coupling optical cavity modes to matter.
Physical Review A **80**, 041802 (2009).

[V] P.F. Herskind, A. Dantan, M. Albert, J. Marler, and M. Drewsen.
Positioning of the rf potential minimum line of a linear Paul trap with micrometer precision.
Journal of Physics B **42**, 154008 (2009).

[VI] P.F. Herskind, A. Dantan, J. Marler, M. Albert, and M. Drewsen.
Realization of collective strong coupling with ion Coulomb crystals in an optical cavity.
Nature Physics **5**, 494 (2009).

Contents

1. Introduction

Since the early days of quantum mechanics, the coherent interaction between light and matter has been one of the major subjects of quantum physics [1]. While the coherent manipulation of the quantum properties of both light and matter merely was of theoretical interest for many decades, the advent of coherent light sources triggered a rapid development of technologies that today are used in quantum optics laboratories around the world to trap and coherently manipulate atoms and photons, even down to the single particle level.

The field of quantum information processing (QI) [2] emerged from this rapid development with the ultimate goal of exploiting the properties of quantum mechanics for communication and computation purposes and to tackle problems that are difficult, if not impossible, to solve classically. In quantum communication, the use of quantum key distribution allows to establish secure communication channels between two distant sites which, because of the no-cloning theorem [3, 4], are inherently protected against eavesdropping [5]. Quantum computing uses fundamental quantum mechanical effects like superposition and entanglement to reduce the complexity of certain classes of computational problems that are practically not solvable on a classical computer [6–8]. In both fields the quantum information itself is represented by so-called qubits, where each qubit consists of a quantum mechanical two-level system, and processing of quantum information is established by unitary quantum gates.

For the purpose of quantum communication, photons are ideally suited as qubits, where the two states of the qubit can be encoded e.g. into left- and right-handed circular polarization states of the photon [9, 10]. Photons can be quickly transmitted over large distances through free-space or optical fibers, while preserving their internal state, due to the weak interaction with the environment.

Numerous systems are studied as possible qubits for the processing and storage of quantum information, e.g. nuclear spins [11], superconducting Josephson junctions [12], quantum dots [13], neutral atoms [14], photons [15] and ions [16, 17]. In particular, trapped ions are promising candidates for the implementation of quantum information devices due to their coherence properties and the excellent control of both their position and internal degree of freedom [18, 19]. Due to their charge, ions can be easily trapped in Paul traps, where the ions are confined by a combination of radio frequency and static electric fields, or in Penning traps, where confinement is achieved by a combination of static electric and magnetic fields. Sophisticated techniques of laser cooling can be used to cool strings of few ions to their motional ground state [18, 20]. Depending on the internal structure of the ion, single qubit operations can be accomplished by transitions in the optical or microwave domain, while phonons can be used to mediate two-qubit gate operations [16, 17]. Many breakthroughs in QI have been achieved with ions, e.g. high fidelity quantum gates [21–24], highly entangled many particle states [25, 26], implementations of simple quantum algorithms [27, 28] and teleportation of quantum states [29, 30]. Furthermore, ions have also proven to be well suited for applications in metrology, preci-

sion spectroscopy and frequency standards [31–34] and for quantum simulations [35, 36]. While many of the basic requirements for a quantum computer were demonstrated in proof-of-principle experiments, scaling these systems to sizes where a quantum computer could practically surpass classical computers, remains a big challenge. For ion traps, many research groups are designing and testing miniaturized traps, to make ion-based quantum computer technology scalable to few tens or hundreds of qubits [37].

In a more general approach one can envision to attain scalability by interfacing stationary qubits, which act as a quantum processor, with photons to distribute the quantum information between distant nodes. In such quantum networks [10, 38] the efficient transfer of quantum information between the quantum nodes and flying qubits is crucial and makes efficient light-matter interfaces an important building block for these quantum information networks.

If the storage and retrieval of the quantum state of a light field can be actively controlled in a light-matter interface, such devices may, furthermore, serve as a quantum memory to temporarily store the information carried by the light. Such devices can, e.g., be used to synchronize simultaneously performed gate operations on various quantum nodes, or to produce on-demand photons from heralded single or entangled photon sources. Moreover, in the field of quantum communication, when envisioning the realization of large-scale networks, chains of light-matter interfaces acting as quantum repeaters [10] are required for the reliable transfer of qubits over long distances.

For a quantum memory used in quantum information science, one can identify three important requirements and criteria, which will determine the quality of such a light-matter interface [39]:

- The efficient storage and retrieval of the quantum state.
- Sufficiently long storage times.
- The multimode capacity, i.e. the capability of simultaneously storing multiple quantum states.

Quantum memories were successfully demonstrated in hot and cold atomic vapors via the storage and retrieval of single photons [40–44], of squeezed vacuum states [45, 46] and entangled states [47] using free-propagating laser beams. Due to the small interaction cross sections in the atom-photon interaction the storage efficiency is typically very low in these experiments. Furthermore, for non-stationary atoms, the diffusion in and out of the interaction beams, as well as atomic collisions, will generally limit the achievable storage times to the microsecond-range. While sophisticated techniques can extend the storage times to several milliseconds [43, 44], they are typically only possible at the expense of lower efficiencies.

As an alternative to neutral atomic clouds, solid-state based light-matter interfaces [48] should in principle allow for long storage times and classical light pulses containing many photons have been stored in rare-earth ion doped crystals for several seconds [49]. Furthermore, the storage of entanglement was recently demonstrated [50, 51]. In these experiments, the storage time was limited to few microseconds and the low optical density of the used ion doped crystals limited the efficiency of the storage and readout. Both properties depend on the dopants and their concentration and long storage times [49] and high efficiencies [52, 53] have been demonstrated for different systems, the combination

of both in one system remains an open challenge. Due to their long time stability, solid state quantum memories allow for the simultaneous storage of multiple photons [54].

The efficiency of a light-matter interface can be substantially enhanced, when enclosing the atomic medium in the mode volume of an optical cavity. In such a cavity the electromagnetic field has well defined spatio-temporal modes and the coherent interaction between a material system and specific modes can be substantially higher than in free space. Taking advantage of this enhancement, atomic ensembles interacting with a single mode of an optical cavity were proposed for the realization of high-efficiency optical quantum memories [55–57]. A basic requirement for such an cavity-based quantum-memory is the realization of the so-called *collective* strong coupling regime [55] of cavity quantum electrodynamics (CQED) [58, 59]. For an ensemble of N identical two-level systems simultaneously interacting with a single mode of the cavity field, this regime is reached when the collective coupling rate, g_{N}, at which single excitations are coherently exchanged between the ensemble and the light mode exceeds the dissipation rates in the system, namely the dipole decay rate of the two-level system, γ, and the decay of the cavity field, κ [58]. In this regime, one benefits from a collective enhancement of the coherent interaction between an ensemble and the cavity field, which scales with the square root of the number of interacting particles. Collective strong coupling, first explored with Rydberg atoms in microwave cavities [60], has been realized in the optical domain with atomic beams [61], atoms in magneto-optical traps [62–65] and Bose-Einstein condensates [66, 67].

In the context of quantum information processing, ions have already proven to be well suited for coherent manipulations, due to their excellent coherence properties and localization. They are for the same reasons particularly well suited for the realization of a long-lived and efficient light-matter interface. Enclosing ions in an optical cavity would naturally combine the technological achievements of quantum information science with those of cavity QED. Much progress has been made towards coupling single trapped ions to the light modes of optical cavities [68–74], and reaching a strong coupling with single ions would, in view of their importance for quantum information processing, be very attractive. As the coherent coupling strength is inversely proportional to the mode volume of the cavity, reaching this regime requires very small high-finesse cavities. However, the intersection of dielectric objects, such as cavity mirrors, in the vicinity of the trap region can modify the trapping potentials and makes experiments with ions in optical cavities technically challenging. For larger ensembles of trapped ions simultaneously interacting with a cavity field mode, one benefits from the collective enhancement and collective strong coupling can be achieved with comparatively longer cavities and lower finesses.

Large clouds of ions can be stably trapped in both Penning and Paul traps and, when cooled below a certain critical temperature, undergo a phase transition to a long-range ordered state, referred to as an ion Coulomb crystal [75–77]. In these objects, the ions are still well separated and most of the single-particle properties which make ions well-suited for QI, like long coherence times and well defined addressable optical transitions, are preserved. In addition, ion Coulomb crystals also possess many properties of more traditional solids, like a uniform density and long-term stability. Ion Coulomb crystals can contain up to hundreds of thousands of ions and can be stably trapped for hours [78].

In this thesis we will investigate the potential of large ion Coulomb crystals in optical cavities for realizing a high-efficiency and long-lived light-matter interface which could satisfy the previously mentioned criteria of ref. [39].

Our group could recently demonstrate that the collective strong coupling regime could be reached with $^{40}Ca^{+}$ ion Coulomb crystals in an optical cavity [79, 80]. In addition, we measured coherence times for collective coherences between Zeeman substates in the millisecond range, which illustrates that the good coherence properties of single trapped ions are retained in large ion Coulomb crystals. The results of these studies will be reviewed in chapter 5 in this thesis. In a subsequent experiment, we will show, how the solid-like properties of ion Coulomb crystals, such as e.g. their uniform density, can be used to strongly couple large crystals to different transverse modes of the cavity field, with identical coupling strengths [81]. This has promising applications for e.g. for spatial multimode storage of multiple photons. The results of these investigations will be presented in chapter 6. Moreover, we will in chapter 7 also demonstrate how the coherent light-matter interaction can be used to study the motional degree of freedom of the ion crystals. We will present a novel noninvasive spectroscopy technique that can be used to investigate normal mode dynamics in these crystals [82], and which opens up for coherent manipulations of ion Coulomb crystals' collective vibrational modes.

Ref. [55] proposes to realize ensemble-based quantum memories in a cavity by mapping the state of a single photon onto a collective excitation of the storage medium using the effect of electromagnetically induced transparency (EIT) [83, 84]. EIT is a quantum interference effect, where the optical response of a material system to a weak probe field (carrying the quantum information) can be tailored by a second, much stronger control field. The resonant absorption of the probe field can be completely suppressed via a destructive two-path quantum interference effect, which can also give rise to large nonlinearities. First observed in hot and cold atomic gasses [85], the use of EIT to control the atomic absorption and dispersion properties was spectacularly demonstrated in slow- and stopped light experiments [86–88], where the group velocity of a light pulse in cold and warm clouds of neutral atoms was slowed down to few meters per second and even stopped [88, 89]. In these experiments the stored light pulses contained several thousands of photons. However, the same technique can be used at the quantum limit, where the probe light pulses contains a single photon [84, 90, 91]. In this limit, the quantum state of the light can be mapped on a collective excitation of the atomic medium and EIT is at the heart of most quantum memory schemes [39].

An important step towards the realization of a cavity based light-matter interface is hence the observation of EIT in the system. Cavity EIT was successfully observed for ensembles of cold and hot neutral atoms [92, 93], and, most recently, the enhanced cavity interaction also allowed for the observation of cavity EIT with few and even single atoms [94, 95]. Moreover, ensembles of neutral atoms confined in the mode volume of an optical cavity were successfully used to store and transfer single photons with high efficiency [96, 97]. However, the achieved storage time was still limited by the thermal diffusion of the atoms in and out of the cavity mode. Combining the advantages of the cavity enhanced light-matter interaction with a physical system, for which the thermal diffusion and collisions are sufficiently suppressed, offers attractive possibilities of realizing a long-lived quantum memory with a high efficiency.

We will in chapter 8 report on the first experimental observation of cavity EIT with ions. In a novel, all-cavity geometry we demonstrate excellent control over the atomic transparency and observe narrow EIT windows (tens of kHz), which are one to two orders of magnitude lower than in experiments with neutrals in cavities [92–95]. In combination with the achievement of collective strong coupling and the measured coherence times of

milliseconds, these results demonstrate that ion Coulomb crystals in optical cavities are indeed an excellent candidate for the realization of both long-lived and high-efficiency quantum memories, with the potential to be used in multimode configurations.

Beside its importance for a quantum memory, the realization of cavity EIT with very narrow windows and good control over the atomic transparency also has promising applications for the observation of nonlinear effects [98] at low light levels or controlled photon-photon interactions [99, 100]. We will in chapter 9 present a promising first step towards a cavity mediated photon-photon interaction by the implementation of an all optical switching scheme, where the transmission of a probe photon is controlled via the nonlinear interaction with an additional weak field in the cavity.

The thesis is structured as follows:

CHAPTER 2 contains a review of the trapping and laser cooling of ions, with a focus on large ion Coulomb crystals. Furthermore, it will introduce a thermodynamical description of the crystals in terms of cold nonneutral plasmas.

CHAPTER 3 summarizes the CQED theory for the interaction of an ensemble of identical two-level systems with a single cavity field mode.

CHAPTER 4 briefly explains the experimental setup, the lasers and the detection systems.

CHAPTER 5 presents results on the realization of collective strong coupling with ion Coulomb crystals and a measurement of the coherence time of collective coherences between Zeeman substates.

CHAPTER 6 presents a detailed investigation of the coherent coupling between various ion Coulomb crystals and various cavity modes.

CHAPTER 7 contains the results of investigations of collective vibrational modes of ion Coulomb crystals using a novel non-invasive spectroscopy technique at the single photon level.

CHAPTER 8 presents results on the observation of cavity electromagnetically induced transparency with ion Coulomb crystals.

CHAPTER 9 describes experiments on the realization of an all-optical switching scheme with ion Coulomb crystals based on EIT.

CHAPTER 10 concludes the thesis and gives a brief outlook.

2. Ion Coulomb crystals in a linear Paul trap

In this chapter basic concepts of ion trapping and laser cooling will be introduced, with the focus on fundamental aspects of the physics of ion Coulomb crystals. It is structured as follows: In sec. 2.1 we will start out by introducing the principles of the linear Paul traps and their mathematical description. In sec. 2.2 we will then turn towards the laser cooling of $^{40}Ca^{+}$ ions and large ion ensembles. In sec. 2.3 thermodynamic properties of ion Coulomb crystals will be discussed.

2.1. Principle of a linear Paul trap

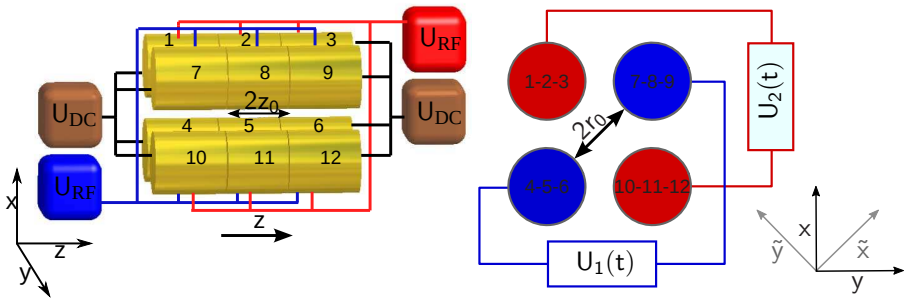

Figure 2.1.: Schematic drawing of the segmented linear Paul trap used in this thesis. The RF voltages are applied to all segments, where the same RF voltage is applied to rods 1-2-3 and 10-11-12, with relative phase of π with respect to the voltage on 4-5-6/7-8-9. The DC end cap voltages are applied to 1-4-7-10 and 3-6-9-12. To simplify the calculations, the coordinate system in this section ($\tilde{x}$, $\tilde{y}$) is tilted by 45° as compared to the rest of the thesis (x, y).

In 1955 Wolfgang Paul and his student Erhard Fischer demonstrated how ions can be trapped in an oscillating quadrupole field [101, 102]. Their "ion cage" was a further development of the quadrupole mass filter, where in addition to the radially confining radio-frequency (RF) potential, electrostatic (DC) potentials were applied to two endcaps to form a 3-dimensional trap for charged particles.
The quadrupole trap used in our experiments consists of four sets of segmented cylindrical rods, as shown in fig 2.1. In this linear Paul trap the axial confinement is obtained by applying DC voltages U_{DC} to the outermost sections of the rods. The resulting electrostatic

potential along the z-trap axis for a single particle with charge Q and mass M is given by

$$\Phi_z(z) = \eta U_{\mathrm{DC}} \frac{z^2}{z_0^2} = \frac{1}{2} M \omega_z^2 z^2, \tag{2.1}$$

where η is the axial geometric constant determined by the trap geometry (see [80]), $2z_0$ is the length of the center electrode and ω_z is the harmonic frequency of the axial potential given by

$$\omega_z = \sqrt{\frac{2\eta Q U_{\mathrm{DC}}}{M z_0^2}}. \tag{2.2}$$

Confinement in the radial plane of the linear Paul trap is ensured by applying two oscillating electric potentials with a relative phase shift of π, $U_1(t) = U_{\mathrm{RF}} \cos(\Omega_{\mathrm{RF}} t)$ and $U_2(t) = U_{\mathrm{RF}} \cos(\Omega_{\mathrm{RF}} t + \pi)$, to the two sets of diagonally opposite rods, as shown in fig. 2.1 b. The oscillating fields give rise to a radial potential of the form[1]:

$$\Phi_{\mathrm{rad}}(\tilde{x}, \tilde{y}, t) = \frac{\tilde{x}^2 - \tilde{y}^2}{2 r_0^2} U_{\mathrm{RF}} \cos(\Omega_{\mathrm{RF}} t) - \frac{\eta}{2} \frac{\tilde{x}^2 + \tilde{y}^2}{z_0^2} U_{\mathrm{DC}}, \tag{2.3}$$

where r_0 corresponds to the half distance between the diagonally opposite rods. The first term in this equation is the potential originating from the RF-voltages, while the second term comes from the application of DC voltages on the end-electrodes. The classical equation of motion for a particle with mass M and charge Q is given by $M\ddot{\mathbf{r}} = -Q\nabla\Phi(\mathbf{r})$, where $\Phi(\boldsymbol{r}) = \Phi_z(z) + \Phi_{\mathrm{rad}}(\tilde{x}, \tilde{y}, t)$ is the total potential. The radial and the axial part separate and inserting the potential of eq. (2.3) leads to the so called Mathieu differential equations, see e.g. [18]:

$$\frac{\partial \tilde{x}}{\partial \tau^2} + [a - 2q\cos(2\tau)]\,\tilde{x} = 0 \tag{2.4a}$$

$$\frac{\partial \tilde{y}}{\partial \tau^2} + [a + 2q\cos(2\tau)]\,\tilde{y} = 0. \tag{2.4b}$$

For convenience, the dimensionless parameters

$$\tau = \frac{\Omega_{\mathrm{RF}} t}{2} \tag{2.5a}$$

$$a = \frac{-4\eta Q U_{\mathrm{DC}}}{M z_0^2 \Omega_{\mathrm{RF}}^2} \tag{2.5b}$$

$$q = \frac{2 Q U_{\mathrm{RF}}}{M r_0^2 \Omega_{\mathrm{RF}}^2} \tag{2.5c}$$

were introduced. Depending on the values of these parameters, the solution of the Mathieu equations can correspond to non-diverging trajectories, i.e. the amplitude of the motion is bound and the particle is stably trapped, or to diverging trajectories, i.e. the motion is unbound and the particle is expelled from the trap. The stability of the trapping generally depends on the charge-to-mass ratio of the particle Q/M. More details on the stability of

[1] The origin of the coordinate system is chosen at the center of the trap. To simplify the calculations, the coordinate system in this section $(\tilde{x}, \tilde{y})$ is tilted by 45° as compared to the rest of the thesis (x, y).

linear Paul traps can be found in [18, 103]. In most cases traps are operated in a regime where $|q| \ll 1$ and $|a| \ll 1$ and the Mathieu equations eq. (2.4) have a simple solution in this regime:

$$\tilde{x}(t) = \tilde{x}_0 \left[1 + \frac{q}{2}\cos(\Omega_{\mathrm{RF}} t)\right] \cos(\omega_{\mathrm{r}} t) \tag{2.6a}$$

$$\tilde{y}(t) = \tilde{y}_0 \left[1 - \frac{q}{2}\cos(\Omega_{\mathrm{RF}} t)\right] \cos(\omega_{\mathrm{r}} t), \tag{2.6b}$$

where $\tilde{x}_0$ and $\tilde{y}_0$ are the amplitudes of the secular motion along the $\tilde{x}$ and $\tilde{y}$ axis, respectively. The motion of the ion is a superposition of two periodic motions, the slow, so-called secular motion, at the secular frequency

$$\begin{aligned} \omega_{\mathrm{r}} &= \frac{1}{2}\sqrt{\frac{q^2}{2} + a}\,\Omega_{\mathrm{RF}} \\ &= \left(\frac{Q^2 U_{\mathrm{RF}}}{2M^2 r_0^4 \Omega_{\mathrm{RF}}^2} - \frac{\eta Q U_{\mathrm{DC}}}{M z_0^2}\right)^{1/2}. \end{aligned} \tag{2.7}$$

and the fast, so-called micromotion, at the frequency of the RF trap[2], Ω_{RF}. The slower secular motion can be understood as an oscillation in the radial (xy)-plane in a harmonic pseudo-potential $\Phi_{\mathrm{r}}(r)$, which is found by averaging over the fast oscillation in eq. (2.6):

$$\Phi_{\mathrm{r}}(r) = \frac{1}{2} M \omega_{\mathrm{r}}^2 r^2 \tag{2.8}$$

The rapid micromotion occurs at the trap frequency Ω_{RF} with an amplitude suppressed by a factor $\frac{q}{2} \ll 1$ and appears as a small modulation on the dominant secular motion.

Averaging over the fast micromotion, the trapping potential in cylindrical coordinates is given by the sum of radial pseudo-potential (see eq. (2.8)) Φ_{r} and the axial DC-potential Φ_{z} (see eq. (2.1)):

$$\Phi_{\mathrm{trap}}(\boldsymbol{r}) = \Phi_{\mathrm{z}}(z) + \Phi_{\mathrm{r}}(r) \tag{2.9}$$

2.2. Laser cooling of $^{40}Ca^{+}$ ions

Laser cooling of atoms and ions is a widely used technique in today's atomic and molecular physics and the principles have been reviewed in many articles and textbooks, see e.g. [107, 108]. Reviews on specific aspects and cooling techniques for ions can be found in [109, 110]. In this thesis we will therefore only briefly discuss the basic idea of laser cooling and focus on the aspects relevant for the cooling of $^{40}Ca^{+}$ ions and more specifically large ion Coulomb crystals.

The principle of laser cooling relies on the velocity dependent absorption probability of photons and can qualitatively be understood in a 1-dimensional model. We imagine a free two-level atom with resonance frequency ω_{at} moving in the field of two counter-propagating laser beams with velocity v. In the reference frame of the atom, the frequencies of the two lasers are shifted due to the Doppler effect: $\omega_{\pm}(v) = \omega_{\mathrm{D}}(1 \pm \frac{v}{c})$, where ω_{D} is the frequency of the laser, c the velocity of light and the positive sign applies to the

[2] As $q, a \ll 1$, the secular frequency is much smaller than the RF frequency $\omega_{\mathrm{r}} \ll \Omega_{\mathrm{RF}}$.

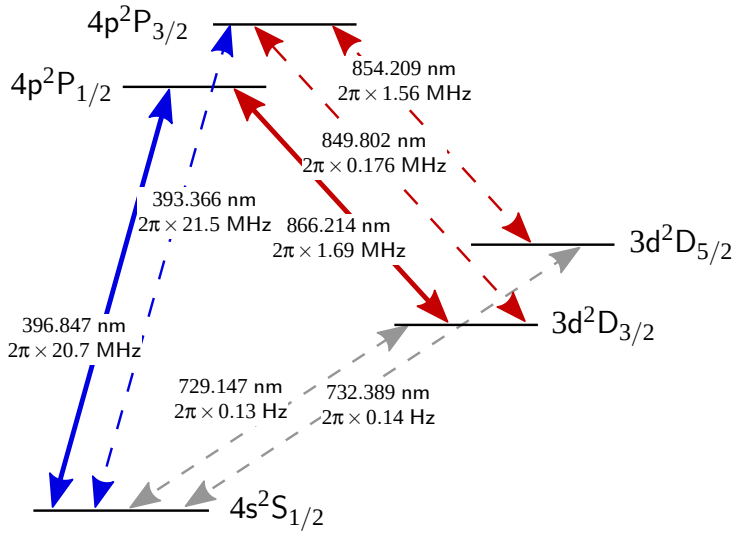

Figure 2.2.: ^{40}Ca energy level scheme, with transition wavelengths in air and transition rates $\Gamma = 2\gamma$ (taken from [104–106]). The solid lines mark the relevant transitions for Doppler cooling in this thesis, i.e. the $4s^2S_{1/2} \leftrightarrow 4p^2P_{1/2}$ Doppler cooling transition (blue) and the $3d^2D_{3/2} \leftrightarrow 4p^2P_{1/2}$ repumping transition (red).

laser towards which the atom is moving. For laser beams slightly detuned to the red of the atomic resonance the absorption probability will be higher for the photons towards which the atom is moving. In the case of moderate laser intensities, the atom will, after each absorption process, decay spontaneously and the photons will be redistributed isotropically, while the longitudinal momentum transfer in the absorption process will be directional, leading to a friction force and an effective deceleration of the atomic motion. The net force exerted on the atom, for a laser detuning $\Delta_D = \omega_{at} - \omega_D$ and a laser intensity much lower then the saturation intensity of the transition ($I \ll I_{sat}$) can be found to be[3]

$$F = \hbar k \gamma \frac{I}{I_{sat}} \left(\frac{1}{1 + ((\Delta_D + kv)/\gamma)^2} - \frac{1}{1 + ((\Delta_D - kv)/\gamma)^2} \right) \propto \alpha - \beta v. \tag{2.10}$$

Here, $k = \omega_D/c$ is the wave-vector of the laser field and $\gamma = \Gamma/2$ is the decoherence rate of the atomic dipole of the two-level system, where Γ is the spontaneous decay rate. The scheme can easily be extended to three dimensions, where the cooling of a free atom requires three sets of orthogonal counter-propagating beams. This configuration is used in three-dimensional optical molasses and magneto-optical traps [108].

Though the isotropic re-emission of spontaneous photons does not lead to a net force on the atom, it leads to diffusion and the temperature that can be reached by Doppler cooling is limited by this diffusion. In steady state, one has an equilibrium arising from the balance between friction and diffusion. In the low saturation limit and for an optimal choice of the detuning $\Delta = \gamma$, the lowest temperature that can be reached is the so-called

[3] The saturation intensity I_{sat} is defined as $I_{sat} = \frac{\hbar\omega_0\gamma}{\sigma(\omega_0)}$, where $\sigma_{abs}(\omega_0)$ is the resonant absorption cross section.

Doppler limit [107]

$$T_{\mathrm{D}} = \frac{\hbar\gamma}{k_B}. \tag{2.11}$$

The simple model of laser cooling described above assumes a free two-level atom, but the basic idea also holds for the more complex situation of a single ion confined in a linear Paul trap. The harmonic oscillation of the ion in the axial and radial trapping potentials leads to a reversion of the direction of motion after each half-period of the axial and radial oscillation. To achieve three-dimensional cooling of a single ion in this configuration it is therefore in principle sufficient to have one cooling beam with *k*-vector components along the axial and radial directions of the trap [110]. Configurations using more cooling laser beams are possible and might be beneficial in many situations. When Doppler cooling light along the radial trap direction is applied, special precaution has to be taken with the beam alignment as an off-centered beam tends to drive the quivery micromotion discussed in sec. 2.1. Furthermore, the level structure of a realistic ion is more complex than in the simple situation of a closed two-level system and efficient cooling requires additional laser fields. In all experiments presented in this thesis $^{40}Ca^{+}$ ions were used and we will now consider the specific level scheme of this ion, followed by a discussion of the particular aspects of laser cooling for large ion ensembles.

2.2.1. The $^{40}Ca^{+}$ ion

A reduced level scheme with all energy levels relevant for this thesis is shown in fig. 2.2. The $4s^2S_{1/2} \leftrightarrow 4p^2P_{1/2}$ transition of $^{40}Ca^{+}$ is used for Doppler cooling, with the laser being slightly red detuned with respect to the resonant wavelength of $\lambda = 396.847$ nm. The excited $4p^2P_{1/2}$ state spontaneously decays to both the $4s^2S_{1/2}$ ground state and the metastable $3d^2D_{3/2}$ state, with a branching ratio of $\sim 1:12$. As the lifetime of the metastable state is of the order of a second, ions decaying to this state have to be actively pumped back into the cooling cycle by an additional repumping laser, resonant with the $3d^2D_{3/2} \leftrightarrow 4p^2P_{1/2}$ transition at 866 nm. Due to the branching ratio and the lower momentum of these photons, the cooling effect is dominated by the 397 nm photons. The partial natural linewidth of the $4s^2S_{1/2} \leftrightarrow 4p^2P_{1/2}$ transition is $\Gamma = 2\gamma = 2\pi \times 20.6$ MHz and the corresponding Doppler limit (see eq. (2.11)) amounts to $T_{\mathrm{D}} \approx 0.54$ mK. The laser systems used for Doppler cooling and the optical setup will be presented in sec. 4.3.

2.2.2. Laser cooling of ion Coulomb crystals

Laser cooling of large clouds of trapped ions requires some specific considerations. As the ions interact via the Coulomb potential, the repulsion between the particles will couple their individual motional degrees of freedom. In a situation where the radial confinement is much stronger then the axial, small ensembles will arrange themselves in a string along the field-free trap axis and the axial vibrational modes of the individual ions are coupled. However, the axial and the radial motion are still uncoupled and Doppler cooling has to be performed along both the axial and the radial directions. For a less tight radial confinement, the ions will arrange themselves in a three dimensional structure, where some of the ions are located away from the RF field free trap axis. The Coulomb interaction will then lead to a coupling of the radial and the axial motions and applying Doppler cooling

light along the longitudinal axis is sufficient to achieve good three dimensional cooling. The ions positioned off the trap axis will indeed experience a non-vanishing micromotion, as was discussed in sec. 2.1. A cooling beam along the transverse direction will tend to actively drive the quivery micromotion and it is therefore preferable, especially large ensembles of ions, to only cool along the RF-field free trap axis.

In our experiments we use two counter-propagating beams along this axis to provide Doppler cooling light on the $4s^2S_{1/2} \leftrightarrow 4p^2P_{1/2}$ transition. The repumper light is in most cases sent perpendicular to the trap axis. Details will be discussed along with the description of the experimental setup in ch. 4.

2.3. The physics of ion Coulomb crystals

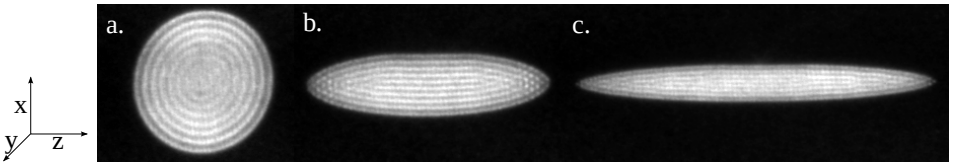

Figure 2.3.: Projection images of of an ion Coulomb crystal taken with the CCD camera during Doppler cooling. The crystal contains ~ 1600 ions, its aspect ratio and density were varied between the three images. The trapping parameters were: **a.** $U_{\mathrm{RF}} = 150$ V, $U_{\mathrm{DC}} = 9.0$ V **b.** $U_{\mathrm{RF}} = 250$ V, $U_{\mathrm{DC}} = 6.8$ V **c.** $U_{\mathrm{RF}} = 350$ V, $U_{\mathrm{DC}} = 4.7$ V

When a trapped cloud of ions is cooled below a certain critical temperature (typically some 10 mK), the ions form a spatially ordered state, referred to as an ion Coulomb crystal [76]. The properties of this crystalline structure will be discussed in more detail in this section. The size of such crystals can reach from some few ions to several hundreds of thousands [78]. In fig. 2.3 three pictures of an ion Coulomb crystal are shown. The shape of the crystal depends on the axial and radial trap frequencies and can be controlled by the RF and DC trapping voltages.

Though the regular long-range ordered structure of ion Coulomb crystals mimics the structure of more traditional solid state systems and crystals, many of their thermodynamic properties in the harmonic confinement potential of a Paul trap are very well described in the framework of a zero-temperature charged liquid plasma and we will in the following subsections introduce the basics concepts of the theory of cold nonneutral plasmas.

2.3.1. Basic theory of charged plasmas

In an ensemble of many ions simultaneously confined in a Paul trap, each individual ion experiences, beside the force exerted by the trapping potential, the Coulomb repulsion of the other ions. For a sufficiently large ensemble[4], the situation is well-described by a cold nonneutral plasma and we will briefly sketch the theoretical background for this model in

[4] What "large" means in this context will be discussed when defining the characteristic length scale in a nonneutral plasma.

this subsection. We consider an ensemble of identical ions, each with charge Q and mass M in a pseudo-potential given by eq. (2.9). At equilibrium, where the force on each ion in the plasma has to vanish, the total potential Φ_{tot} seen by the ion has to be constant [111]:

$$\boldsymbol{F} = -Q\nabla\Phi_{\text{tot}}(\boldsymbol{r}) = 0 \quad \Rightarrow \quad \Phi_{\text{tot}} = const. \tag{2.12}$$

The total potential Φ_{tot} is the sum of the trapping potential Φ_{trap} (see eq. (2.9)) and the mean electrostatic potential of the plasma Φ_{pl} caused by the charge distribution of the ions

$$\Phi_{\text{tot}}(\boldsymbol{r}) = \Phi_{\text{trap}}(\boldsymbol{r}) + \Phi_{\text{pl}}(\boldsymbol{r}). \tag{2.13}$$

In thermal equilibrium, and neglecting surface effects, it is reasonable to assume the charge distribution in the plasma and, hence, the atom density ρ_0 to be constant throughout the ensemble. We can use Poisson's law to relate the plasma potential to the density

$$\nabla^2\Phi_{\text{pl}} = -\frac{Q\rho_0}{\varepsilon_0}. \tag{2.14}$$

Inserting eqs. (2.1) and (2.8) into eq. (2.13) and applying the Laplace operator we can deduce an expression for the ion density in the plasma:

$$\rho_0 = \frac{\varepsilon_0 U_{\text{RF}}^2}{M r_0^4 \Omega_{\text{RF}}^2}. \tag{2.15}$$

It is independent of the axial potential and, for a given RF-frequency Ω_{RF}, controlled by the amplitude of the RF voltage applied to the trap electrodes (see fig. 2.3). Measuring the RF amplitude U_{RF} seen by the ions precisely, is however, not trivial in practice. We will later in this section present a method to calibrate the trap voltages on the basis of the properties of the trapped ion Coulomb crystals within this model.

The expression for the density (2.15) also sets the typical distance between neighboring ions. It can be found by assuming that each ion occupies a certain spherical volume within the plasma. The radius of the sphere is the so-called Wigner-Seitz radius a_{WS} [112], given by

$$a_{\text{WS}} = \left(\frac{3}{4\pi\rho_0}\right)^{1/3} = \left(\frac{3r_0^4 M}{4\pi\varepsilon_0}\frac{\Omega_{\text{RF}}^2}{U_{\text{RF}}^2}\right)^{1/3}. \tag{2.16}$$

Furthermore, the expression for the constant density found in eq. (2.15) can also be used to define two fundamental parameters for the physics of the plasma, namely the plasma frequency ω_p and the Debye length λ_{D}.

In thermal equilibrium, the potential in the plasma is constant as discussed in eq. (2.12). If a single ion in the plasma is displaced by a distance u from its equilibrium position, while the position of all other ions is fixed, this ion will experience a force from the electric field of the other ions. Using eq. (2.14), the force $\boldsymbol{F} = -Q\nabla^2\Phi_{\text{pl}}$ can be found by integration along the displacement u and the equation of motion reads

$$\ddot{u} = \frac{F}{M} = -\frac{Q^2\rho_0}{M\varepsilon_0}u. \tag{2.17}$$

which corresponds to a harmonic motion with a characteristic frequency

$$\omega_p = \sqrt{\frac{Q^2\rho_0}{\varepsilon_0 M}} \tag{2.18}$$

referred to as the plasma frequency. It sets the time scale for the dynamics of charge redistributions within the plasma, caused e.g. by external perturbations. The characteristic length scale in the plasma, the so-called Debye length [112], can be directly related to the plasma frequency. At thermal equilibrium, the mean kinetic energy in one dimension is $\langle E_{\text{kin}}\rangle = \frac{1}{2}k_B T$, which, using the virial theorem of the harmonic oscillator, $\langle U\rangle = \langle E_{\text{kin}}\rangle$, translates into a mean displacement of

$$\lambda_{\text{Debye}} = \sqrt{\varepsilon_0 k_B T \rho_0 Q^2}. \tag{2.19}$$

The Debye length defined in eq. (2.19) is commonly interpreted as the distance at which a perturbation by an external field is shielded by a rearrangement of the space charge in the plasma and has dropped to $1/e$. The Debye length is furthermore one of the defining criteria for a nonneutral plasma. An ensemble of charged particles is considered a plasma when the spatial extension of the whole ensemble is much larger than λ_{Debye}. With typical temperatures of the order of ~ 10 mK and densities of $\sim 10^8 - 10^9$ cm^{-3} ion ensembles as used in our experiments have a Debye length of $\lambda_{\text{Debye}} \sim 300$ nm which is much smaller then the typical ion-ion spacing of ~ 10 μm and even ensembles consisting only of very few ions will fulfill this criterion.

Finally, the Coulomb interaction of the individual particles in a nonneutral plasma is characterized by the so-called plasma coupling parameter Γ_{pl} [112]. It is given by the relative strength of the Coulomb interaction between neighboring particles and their mean thermal kinetic energy. For two charged particles at a distance $2a_{\text{WS}}$ and a temperature T this ratio is

$$\Gamma_{\text{pl}} = \frac{\Phi_{\text{Coulomb}}}{\langle E_{\text{kin}}\rangle} = \frac{1}{4\pi\varepsilon_0}\frac{Q^2}{a_{\text{WS}} k_B T}. \tag{2.20}$$

Many of the structural properties of a charged plasma will be determined by the parameter Γ_{pl} and it is e.g. used as the critical parameter to describe phase-transitions in nonneutral plasmas. For an infinite plasma, the gas to liquid transition was predicted to occur for $\Gamma_{\text{pl}} \simeq 2$ [113]. Furthermore, for even higher coupling parameters of $\Gamma_{\text{pl}} \simeq 170$, the transition to a solid phase with long-range ordered structure has been predicted [114, 115]. These crystalline structures are commonly referred to as ion Coulomb crystals and have been observed in a linear Paul trap only one year after the invention of this type of trap with aluminum dust particles (diameters ~ 20 μm) by buffer gas cooling [116]. After the advent of Doppler laser cooling, Coulomb crystals consisting of atomic ions were formed in linear Paul traps [75, 76] and Penning traps [77].

2.3.2. Zero-temperature charged liquid plasma model

In this subsection we will, based on the framework of the zero-temperature charged liquid model [111], derive an explicit expression for the plasma potential in an ion Coulomb crystals confined in a linear Paul trap, which will allow us to relate the geometrical shape

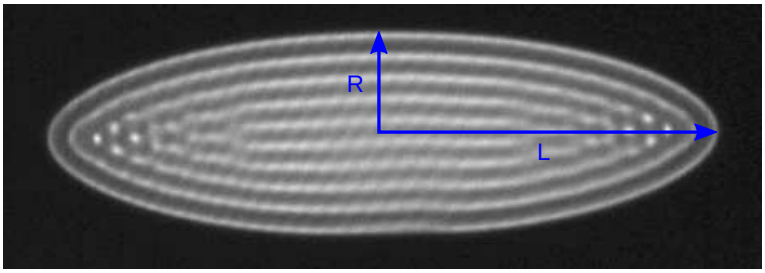

Figure 2.4.: Projection image of an ion Coulomb crystal. The aspect ratio is defined as the ratio of the crystal's half-length and its radius $\alpha = \frac{R}{L}$.

of the plasma to the trapping parameters. The trapping potential in a Paul trap is cylindrically symmetric, see eq. (2.9), and it was shown by Turner that it in this case, the equilibrium shape of a confined plasma is spheroidal [111]. The aspect ratio is defined as the ratio of axial and radial extension of the spheroid

$$\alpha = \frac{R}{L}, \tag{2.21}$$

where R and L are the crystal's radius and half-length, respectively (see fig. 2.4). The electrostatic potential arising from the charge distribution within the plasma can be written as [111]

$$\phi_{\mathrm{pl}}(r,z) = \frac{\rho_0 Q}{2\varepsilon_0} R^2 L \left[\frac{2}{\sqrt{R^2-4L^2}} \arcsin\left(1-4\frac{L^2}{R^2}\right)^{1/2} - r^2 f(R,L) - z^2 g(R,L) \right], \tag{2.22}$$

where the form of the two functions $f(R,L)$ and $g(R,L)$ depends on the aspect ratio of the crystal. Inserting the plasma potential of eq. (2.22) into (2.13) and applying Poisson's law (2.14), the axial and the radial part separate and one can relate the axial and radial trap frequencies, ω_z and ω_r, to the two functions $f(R,L)$ and $g(R,L)$:

$$\begin{aligned} \omega_r^2 &= \frac{\rho_0 Q^2}{2M\varepsilon_0} R^2 L f(R,L) \\ \omega_z^2 &= \frac{\rho_0 Q^2}{2M\varepsilon_0} R^2 L g(R,L). \end{aligned} \tag{2.23}$$

The ratio of the trap frequencies is hence directly given by the ratio of $f(R,L)$ and $g(R,L)$. Explicit expressions for $f(R,L)$ and $g(R,L)$ can be calculated on the basis of the zero-temperature charged liquid model, where one has to distinguish between the case of *prolate* spheroids with $\alpha < 1$ and *oblate* spheroids with $\alpha > 1$, for details see [111]:

$$f(R,L) = \begin{cases} -\frac{1}{(L^2-R^2)^{3/2}} \sinh^{-1}\left(\frac{L^2}{R^2}-1\right)^{1/2} + \frac{L}{(L^2-R^2)R^2} & \text{for} \quad \alpha < 1 \\ \frac{1}{(R^2-L^2)^{3/2}} \sinh^{-1}\left(1-\frac{L^2}{R^2}\right)^{1/2} - \frac{L}{(R^2-L^2)R^2} & \text{for} \quad \alpha > 1 \end{cases}$$

$$g(R,L) = \begin{cases} \frac{2}{(L^2-R^2)^{3/2}} \sinh^{-1}\left(\frac{L^2}{R^2}-1\right)^{1/2} - \frac{2}{(L^2-R^2)L} & \text{for} \quad \alpha < 1 \\ -\frac{2}{(R^2-L^2)^{3/2}} \sinh^{-1}\left(1-\frac{R^2}{L^2}\right)^{1/2} + \frac{2}{(R^2-L^2)L} & \text{for} \quad \alpha > 1 \end{cases}. \tag{2.24}$$

The ratio of the trap frequencies defined in eq. (2.23) is then given by

$$\frac{\omega_z^2}{\omega_r^2} = -2 \begin{cases} \frac{\sinh^{-1}(\alpha^{-2}-1)^{1/2} - \alpha(\alpha^{-2}-1)^{1/2}}{\sinh^{-1}(\alpha^{-2}-1)^{1/2} - \alpha^{-1}(\alpha^{-2}-1)^{1/2}} & \text{for} \quad \alpha < 1 \\ \frac{\sin^{-1}(1-\alpha^{-2})^{1/2} - \alpha(1-\alpha^{-2})^{1/2}}{\sin^{-1}(1-\alpha^{-2})^{1/2} - \alpha^{-1}(1-\alpha^{-2})^{1/2}} & \text{for} \quad \alpha > 1 \end{cases} \tag{2.24}$$

On the other hand, the ratio of the axial and radial trap frequencies is directly related to the trap voltages U_{DC} and U_{RF}. Using the expressions for the trap frequencies found in (2.2) and (2.7) one finds

$$\frac{\omega_z^2}{\omega_r^2} = \frac{QU_{RF}^2 z_0^2}{4\eta M \Omega_{RF}^2 U_{DC} r_0^4} - \frac{1}{2}. \tag{2.25}$$

The two equations for the relative trap frequencies found in eqs. (2.24) and (2.25) can be used to calibrate precisely the trap voltages as seen by the ions, and we will come back to that when presenting the experimental setup in sec. 4.7.

Furthermore, eqs. (2.24) and (2.25) provide a direct way to assess the theoretical description of the ion Coulomb crystals as a zero-temperature charged liquid by measuring the aspect ratio of these crystals for various trapping parameters, and the radio of the trap frequencies can in this context be used as a figure of merit for this description.

2.3.3. Structure and temperature

As mentioned above, a phase-transition to a long range ordered structure was predicted for an infinite plasma when $\Gamma_{pl} \gtrsim 170$ [114, 115] and, for infinitely large crystals confined in a cylindrically symmetric potential, the predicted ground state structure was found to be body-centered cubic (bcc) [114, 115]. However, for the more realistic situation of finite crystal sizes, ground state molecular dynamics simulations suggest a distortion of the long range order and finite size effects should cause the ions to arrange themselves in concentric shells, with a constant radial inter-shell spacing δ_r throughout the whole crystal [78, 117]. The inter-shell spacing can be related to the Wigner-Seitz radius defined in eq. (2.16) by

$$\delta_r = x a_{WS}, \tag{2.26}$$

where x is a numerical constant. Molecular dynamics simulations predict this proportionality factor to be $x = 1.48$ [117]. The shell structure has been experimentally confirmed in our group for ion Coulomb crystals in linear Paul traps [78, 118] and the pre-factor x was measured to agree with the theoretical expectations in our trap, see [80, 119].

The inter-shell spacing can be measured from projection images (see sec. 4.4) and eq. (2.26) provides a second possibility to calibrate the trap voltages seen by the ions and hence the ion density [80, 119, 120].

Let us point out that long range ordered structures with both bcc and face centered cubic (fcc) structures were observed in our group also in small ion Coulomb crystals containing only some thousand ions in linear Paul traps [121], even though ground state molecular dynamics simulations suggest that those structures should be suppressed by surface effects for crystals with less then ~ 5000 ions. The regular structures in such small crystals can,

however, according to molecular dynamic simulations of metastable ion configurations be attributed to the finite temperature of the ensemble [121].

In this thesis, we will present experiments using ion Coulomb crystals to investigate the coherent light-matter interaction in cavity quantum electrodynamics. For the experiments described in this thesis the structural properties of ion Coulomb crystals will have little importance. However, we would like to mention that cavity quantum electrodynamics might offer interesting perspectives to investigate these structural effects in a non-invasive way, or, conversely, that the crystal structure, if sufficiently well controlled, could be used for cavity quantum electrodynamics studies.

3. Cavity Quantum Electrodynamics

The field of Cavity Quantum Electrodynamics (CQED) studies the fundamental interaction between matter systems and electromagnetic fields confined in resonators, in situations where the quantum nature of the light field is relevant. The theory of CQED has been the subject of many books, e.g. [58, 59], and will therefore be presented only briefly in this chapter. However, as many of the general concepts of CQED will be used in the following chapters, detail derivations will be given for the important equations.

The chapter is structured as follows: In sec. 3.1 the spatial and temporal field modes of a linear optical cavity will be discussed. Sec. 3.2 will then focus on the interaction of motionless two-level atoms with a single cavity field mode and the optical Bloch equations of the system will be derived. Finally, in sec. 3.3 the results will be generalized to take into account the motion of the atoms.

3.1. Optical cavities

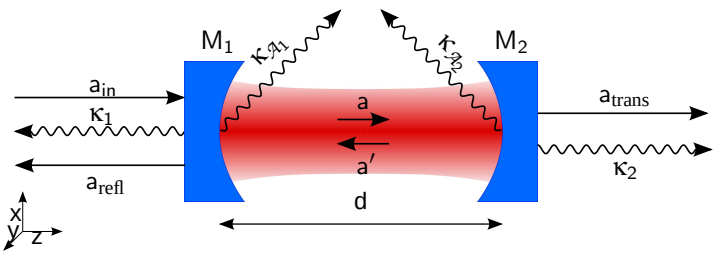

Figure 3.1.: Schematics of a Fabry-Perot cavity formed by the two mirrors M_1 and M_2 with radius of curvature r_M and separated by a distance d. The mirrors are characterized by their transmission, reflection and intensity loss coefficients T_i, R_i and $\mathcal{A}_i$ $(i = 1,2)$. An input field $\tilde{a}_{\text{in}}$ is coupled into the cavity through M1, a and a' are the intracavity fields propagating to the right and to the left, respectively. a_{refl} and a_{trans} are the reflected and transmitted fields, κ_1 and κ_2 are the decay rates of the cavity field due to the finite reflectances of M_1 and M_2, the loss rates due to absorption and scattering on the two mirrors are denoted by $\kappa_{\mathcal{A}_1}$ and $\kappa_{\mathcal{A}_2}$.

In this section, the mathematical description of a light field confined in an optical cavity will be given. The first part will introduce the concept of cavity modes, followed by a derivation of the dynamical field equation of the empty cavity and the steady state solution of this equation, together with the cavity transmission and reflection spectrum.

3.1.1. Transverse cavity modes

In many respects, an optical cavity can be understood as the optical analogous of an electrical resonance circuit. The mirrors restrict the boundary conditions for the electromagnetic field and only certain field modes with well-defined frequencies and spatial distributions can build up inside the cavity. The possible spatial field configurations are commonly decomposed into a basis of mode functions. In the paraxial approximation these modes are the so-called Hermite-Gaussian modes, which are derived and discussed in a comprehensive review by Kogelnik and Li [122] or in many textbooks, e.g. [123,124]. In this thesis only the major results of this description will be given and the reader is referred to these references for more details.

We consider a symmetric cavity formed by two mirrors, M_1 and M_2 with radius of curvature r_M and separated by a distance d, see fig. 3.1. The spatial field distributions reproducing themselves after on round trip are, in the paraxial approximation, the Hermite-Gauss modes [122]

$$E_{nm}(\boldsymbol{r}) = E_0 \Psi_{mn}(\boldsymbol{r}) = E_0 \, \Psi_n(x,z) \, \Psi_m(y,z) \, \Phi(x,y,z), \tag{3.1}$$

with the amplitude of the electric field E_0. They are decomposed into two transverse mode functions, $\Psi_n(x,z)$ and $\Psi_m(y,z)$, and one longitudinal mode function, $\Phi(x,y,z)$, where the Transverse ElectroMagnetic modes (TEM) are characterized by two non-negative indices n and m and abbreviated by TEM_{nm}. The n-th transverse mode function is given by ($u = x,y$)

$$\Psi_n(u,z) = \sqrt{\frac{w_0}{w(z)}} H_n\left(\frac{\sqrt{2}u}{w(z)}\right) \exp\left(-\frac{u^2}{w(z)^2}\right), \tag{3.2}$$

where H_n is the n-th Hermite polynomial with non-negative index n, $w(z) = w_0\sqrt{1+(\frac{z}{z_\mathrm{R}})^2}$ the position dependent beam radius, w_0 the minimum waist and $z_\mathrm{R} = \frac{\pi w_0^2}{\lambda}$ the so-called Rayleigh range. The longitudinal field mode function also depends on the transverse indices n and m and is given by

$$\Phi(x,y,z) = \sin\left(kz - (1+n+m)\arctan\frac{z}{z_\mathrm{R}} + \frac{k(x^2+y^2)}{2R(z)}\right), \tag{3.3}$$

where we have used the wavenumber $k = \frac{2\pi}{\lambda}$, and the radius of curvature of the wavefront $R(z) = z\left[1+(z_\mathrm{R}/z)^2\right]$. The phase factor $\phi_\mathrm{G}(z) = \arctan\frac{z}{z_\mathrm{R}}$ is the so called Gouy phase shift and corresponds to the relative phase difference of the fundamental TEM_{00} cavity mode and a plane wave at the same frequency. Self-consistency requires the phase shift after one round trip to be an integer multiple of 2π and we can define the corresponding resonance condition for the mode characterized by the two transverse mode indices n and m and an axial mode number $q \in \mathbb{N}$:

$$\nu_{nmq} = \nu_\mathrm{FSR} \cdot \left[q + \frac{1}{\pi}(1+n+m)\arccos\left(1-\frac{d}{r_\mathrm{M}}\right)\right], \tag{3.4}$$

where the so-called free spectral range ν_{FSR} corresponding to the frequency spacing of two subsequent axial modes is given by the inverse of the round trip time τ

$$\nu_{\mathrm{FSR}} = \frac{1}{\tau} = \frac{c}{2d}. \tag{3.5}$$

Accordingly, the resonance frequencies of neighboring transverse modes (n,m) and (n',m'), $n+m = n'+m'+1$ differ by

$$\delta\nu_{nm,n'm'} = -\frac{1}{\pi}\nu_{\mathrm{FSR}} \arccos\left(1-\frac{d}{r_{\mathrm{M}}}\right). \tag{3.6}$$

Depending on the cavity geometry, the resonance frequencies of several transverse modes can be degenerate. For confocal cavities, where the distance of the mirrors corresponds to their radius of curvature $d = r_{\mathrm{M}}$, every second transverse mode is degenerate as can be seen from eq. (3.4).

The 0-th order Hermite polynomial is given by $H_0(x) = 1$, and the fundamental TEM_{00} mode has a particularly simple form

$$\Psi_{00}(x,y,z) = \frac{w_0}{w(z)} \exp\left(-\frac{x^2+y^2}{w(z)^2}\right) \sin\left(\left[kz - \arctan\frac{z}{z_{\mathrm{R}}} + \frac{k(x^2+y^2)}{2R(z)}\right]\right). \tag{3.7}$$

The mode function is cylindrically symmetric, with a Gaussian field distribution along the transverse directions.

After having introduced the Hermite-Gauss modes as the allowed spatial field configurations of the electromagnetic field in the cavity, we will now try to find the dynamical equation and the steady state solution for the intracavity field of these modes for a certain input field amplitude.

3.1.2. Cavity field equation

We will now derive the dynamical equation for the intracavity field amplitude $a(t)$ when a input field $a_{\mathrm{in}}(t)$ is injected into the cavity[1]. A self-consistent equation for $a(t)$ can be derived by finding the field amplitude which reproduces itself after one cavity round trip. We consider a monochromatic input field a_{in} with a frequency ω_{l} and an empty Fabry-Perot resonator, formed by the two mirrors M_1 and M_2 where the input field is injected through mirror M_1, see fig 3.1.

The two cavity mirrors are characterized by the transmission, reflection and loss coefficients for the intensity T_i, R_i and $\mathcal{A}_i$ $(i = 1,2)$. The transmission and reflection coefficients for the field amplitude, t_i and r_i, are related to the corresponding intensity coefficients by $t_i = \sqrt{T_i}$ and $r_i = \sqrt{R_i}$. Likewise, the mirror losses induced by absorption and scattering, $\mathcal{A}_i$, will attenuate the field by a factor $\alpha_i = \sqrt{1-\mathcal{A}_i}$. Obviously, conservation of energy requires $T_i + R_i + \mathcal{A}_i = 1$. The amplitude of the intracavity field after one reflection on mirror M_2 reads

$$a'(t) = \alpha_2 r_2 a(t-\tau) e^{i(\Delta_{\mathrm{c}}\tau+\pi)}, \tag{3.8}$$

[1] We will use classical field amplitudes throughout the whole derivation in this section. These equations are the same for the mean value of the field operators in the semi-classical treatment which we will use later.

where τ is the cavity round trip time and $\Delta_c\tau = (\omega_c - \omega_l)\tau$ is the relative phase of the field acquired after one round trip, with $\omega_c = 2\pi\nu_{nmq}$ being the resonance frequency of the closest cavity mode, see eq. (3.4). For a certain input field $\tilde{a}_{in}(t)$, the intracavity field amplitude $a(t)$ after the first mirror has to fulfil

$$a(t) = t_1\tilde{a}_{in}(t) + \alpha_1 r_1 e^{i\pi} a'(t). \tag{3.9}$$

A self-consistent solution for the intracavity field can be found by substituting eq. (3.8) into eq. (3.9):

$$a(t) = t_1\tilde{a}_{in}(t) + \alpha_1\alpha_2 r_1 r_2 a(t-\tau)e^{i\Delta_c\tau}e^{i2\pi}. \tag{3.10}$$

Subtracting $a(t-\tau)$ on both sides and dividing by τ yields

$$\frac{a(t)-a(t-\tau)}{\tau} = t_1\sqrt{\tau}a_{in}(t) + \frac{\alpha_1\alpha_2 r_1 r_2 e^{i\Delta_c\tau} - 1}{\tau}a(t-\tau). \tag{3.11}$$

Here, the input field $\tilde{a}_{in}$ was related to the round trip time by redefining it in terms of an input photon flux per round trip via $|a_{in}|^2 \equiv {}^{|\tilde{a}_{in}|^2}/_{\tau}$.

If the losses due to absorption and scattering and due to the finite mirror transmission per round trip are small, it is convenient to express the reflectivity and loss coefficients as rates. The reflectivity coefficients can be written as the diminution of the field amplitude by the decay rate through the mirror times the round trip time:

$$r_i = 1 - \kappa_i\tau, \quad i = 1,2 \tag{3.12}$$

In the same manner we can also express the loss coefficients α_i by loss rates $\kappa_{\mathcal{A}_i}$

$$\alpha_i = 1 - \kappa_{\mathcal{A}_i}\tau, \quad i = 1,2. \tag{3.13}$$

For sufficiently short cavities the cavity decay and loss rates will be small as compared to the inverse round trip time and hence $\kappa_i\tau \ll 1$ and $\kappa_{\mathcal{A}_i}\tau \ll 1$. In this limit, the rate coefficients can be related to the intensity transmission and loss coefficients by

$$\kappa_i = \frac{1-r_i}{\tau} = \frac{1-\sqrt{1-T_i}}{\tau} \approx \frac{T_i}{2\tau} \tag{3.14a}$$

$$\kappa_{\mathcal{A}_i} = \frac{1-\alpha_i}{\tau} = \frac{1-\sqrt{1-\mathcal{A}_i}}{\tau} \approx \frac{\mathcal{A}_i}{2\tau} \tag{3.14b}$$

and we can also express the transmission rate for the field through κ_i

$$t_i = \sqrt{T_i} \approx \sqrt{2\kappa_i\tau}. \tag{3.15}$$

Furthermore, we are interested in the field amplitude for a light field close to cavity resonance and can restrict ourselves to $\omega_l \simeq \omega_c$ and assume $\Delta_c\tau \ll 1$. Substituting the rates defined in eqs. (3.12) and (3.13) into eq. (3.11) and only keeping the linear terms in κ_1, κ_2, $\kappa_{\mathcal{A}_i}$, Δ_c we find the dynamical equation for the intracavity field in the limit $\tau \to 0$

$$\dot{a}(t) = \sqrt{2\kappa_1}a_{in}(t) - (\kappa_1 + \kappa_2 + \kappa_{\mathcal{A}} + i\Delta_c)a(t). \tag{3.16}$$

Here, the mirror losses were combined into one intracavity loss rate

$$\kappa_{\mathcal{A}} = \kappa_{\mathcal{A}_1} + \kappa_{\mathcal{A}_2}. \tag{3.17}$$

In steady state, eq. (3.16) can readily be solved and one finds

$$a = \frac{\sqrt{2\kappa_1}a_{\text{in}}}{(\kappa_1+\kappa_2+\kappa_{\mathcal{A}}+i\Delta_c)}. \tag{3.18}$$

The intensity of the intracavity field is then given by

$$I = |a|^2 = \frac{2\kappa_1}{\kappa^2+\Delta_c^2}|a_{\text{in}}|^2, \tag{3.19}$$

where the total cavity field decay rate is $\kappa = \kappa_1+\kappa_2+\kappa_{\mathcal{A}}$. Using the same approximations as in the derivation of eq. (3.16) and substituting r_i, α_i and t_i by the appropriate rates, we can find the input-output relations for the transmitted and reflected field amplitudes

$$a_{\text{refl}} = t_1\alpha_1 a' - r_1 a_{\text{in}} \approx \sqrt{2\kappa_1}a - a_{\text{in}} \tag{3.20a}$$

$$a_{\text{trans}} = t_2\alpha_2 a \approx \sqrt{2\kappa_2\tau}a. \tag{3.20b}$$

The steady state cavity transmitivity $\mathcal{T}$ and reflectivity $\mathcal{R}$ spectra are defined by the transmitted and reflected intensities normalized by the input intensity

$$\mathcal{R} = \left|\frac{a_{\text{refl}}}{a_{\text{in}}}\right|^2 = \frac{(\kappa-2\kappa_1)^2+\Delta_c^2}{\kappa^2+\Delta_c^2}. \tag{3.21a}$$

$$\mathcal{T} = \left|\frac{a_{\text{trans}}}{a_{\text{in}}}\right|^2 = \frac{4\kappa_1\kappa_2}{\kappa^2+\Delta_c^2}. \tag{3.21b}$$

Both transmitivity and reflectivity are Lorentzian functions of the cavity detuning Δ_C with a FWHM

$$\delta\nu = 2\frac{\kappa}{2\pi} = 2\frac{\kappa_1+\kappa_2+\kappa_{\mathcal{A}}}{2\pi}. \tag{3.22}$$

Using eqs. (3.14) one can relate the cavity half-with directly to the mirror transmission, reflection, and loss coefficients by

$$\delta\nu \approx 2\frac{T_1+T_2+\mathcal{A}}{4\pi\tau}. \tag{3.23}$$

In Fig. 3.2 the cavity transmission and reflection as defined in eq. (3.21) are plotted as a function of cavity detuning Δ_c. The finesse $\mathcal{F}$, which is a measure of the quality factor of the cavity resonance, is given by the ratio of the free spectral range to the cavity linewidth

$$\mathcal{F} \equiv \frac{\nu_{\text{FSR}}}{\delta\nu} = \frac{\pi}{\tau(\kappa_1+\kappa_2+\kappa_{\mathcal{A}})} \approx \frac{2\pi}{T_1+T_2+\mathcal{A}}. \tag{3.24}$$

In the following section we will generalize the dynamical equation for the field in an empty cavity to the situation where a matter system interacts with a single cavity field mode and derive a full set of semi-classical equations describing the dynamics of the coupled matter-cavity system.

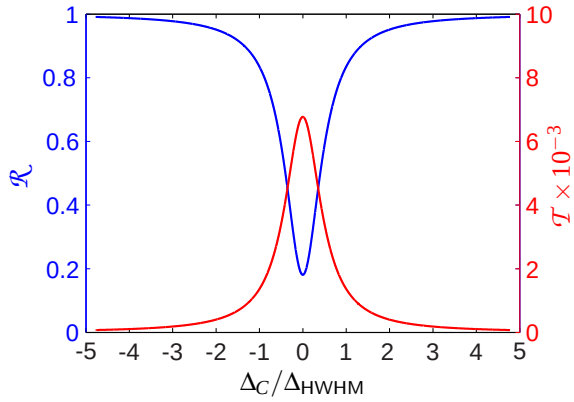

Figure 3.2.: Cavity transmission and reflection around one resonance for a cavity with similar parameters as used in our experiment. The free spectral range is $\nu_{\mathrm{FSR}} = 12.7$ GHz, the mirror transmission coefficients are $T_1 = 1500$ ppm, $T_2 = 5$ ppm and the cavity loss coefficient is $\mathcal{A} = 600$ ppm. With these parameters the finesse of the cavity amounts to $\mathcal{F} \sim 3000$.

3.2. Two-level atoms interacting with a single cavity field mode

The interaction between material systems and the electromagnetic field inside a cavity at the quantum level is the subject of Cavity Quantum Electrodynamics (CQED), see e.g. [58, 59, 125, 126]. To understand the fundamental concepts, it is instructive to first consider the simple case of a single two-level system with ground state $|g\rangle$ and excited state $|e\rangle$ interacting with a single light mode inside the cavity. The rate at which a single excitation is coherently exchanged between the field mode and the two-level system is given by

$$g = \frac{\mu_{\mathrm{ge}} E_0}{\hbar}. \tag{3.25}$$

Here, μ_{ge} is the dipole matrix element of the transition considered and E_0 the electrical field amplitude. When brought to the excited state, the atom can also couple to the quasi-continuum of the vacuum states and decay via spontaneous emission at a rate $\Gamma = 2\gamma$. As g determines the rate at which coherent evolution between the two-level system and the cavity field takes place, it should be compared to the dissipative rates. For experiments with light fields in free space the spontaneous decay rate is generally much higher than the coupling to a single field mode: $\gamma \gg g$. The situation is different, though, if the atom is positioned at an anti-node of a standing wave field inside an optical cavity. In the case of a resonant cavity, the coupling rate to the cavity field is increased and can exceed the spontaneous decay rate [127]. In a realistic situation, the cavity only covers a small solid angle and the coupling to the other vacuum modes, and, hence, the spontaneous decay rate, will be unchanged. Beside the spontaneous emission, excitations can be lost to the environment when a photon leaks out of the cavity because of the finite reflectivity or the mirrors and the decay of the cavity field at a rate κ constitutes a second source of decoherence in the system, see eq. (3.22).

It is obviously interesting to be in a regime where the coherent exchange of excitations between the two-level system and the cavity field at a rate g exceeds both the spontaneous emission and the cavity field decay rate, γ, κ. In CQED the regime where

$$g > (\kappa, \gamma) \tag{3.26}$$

is commonly referred to as the strong coupling regime [58]. It has been successfully accessed with neutral atoms [61, 128–131] and also with Cooper pairs [132] and quantum dots [133].

With the normalization of the vacuum field $\varepsilon_0 E_{\mathrm{vac}}^2 V = \frac{1}{2}\hbar\omega_{\mathrm{c}}$ the field in the cavity is given by $E_{\mathrm{vac}} = \sqrt{\frac{\hbar\omega_{\mathrm{c}}}{2\varepsilon_0 V}}$, where V is the mode volume of the cavity, and ω_{c} is the frequency of the cavity field mode. Substituting into eq. (3.25) the coherent coupling rate can be written as

$$g = \mu_{\mathrm{ge}} \sqrt{\frac{\hbar\omega_{\mathrm{c}}}{2\varepsilon_0 V}}. \tag{3.27}$$

To realize a situation where $g > \gamma$, it is according to eq. (3.27), desirable to minimize the volume of the cavity field mode. On the other hand, the finesse $\mathcal{F}$, which is inversely proportional to the length of the cavity, has to be maintained sufficiently high to also ensure $g > \kappa = \frac{\nu_{\mathrm{FSR}}}{\mathcal{F}}$, see eq. (3.24).

3.2.1. The Jaynes-Cummings model

The Jaynes-Cummings model is a widely-used quantum mechanical description of the interaction of a two-level system with a single light mode A comprehensive review of the model can be found in [134].
In this subsection we will introduce the model for the simple situation of a single two-level system interacting with a single cavity field mode at an anti-node of the standing wave field, before extending the model to the case of N atoms in the following subsection.

The Hamiltonian of the coupled system consisting of a two-level system and cavity field mode is given by

$$H = H_{\mathrm{at}} + H_{\mathrm{l}} + H_{\mathrm{int}}. \tag{3.28}$$

The first term of the Hamiltonian is the atomic part, which in the frame rotating at the laser frequency ω_{l}, is given by[2]

$$H_{\mathrm{at}} = \hbar\Delta\hat{\pi}^{(e)} \tag{3.29}$$

where $\hat{\pi}^{(e)} = |e\rangle\langle e|$ is the excited state population and $\Delta = \omega_{\mathrm{at}} - \omega_{\mathrm{l}}$ is the atomic detuning. The second term in eq. (3.28) describes a single mode of the (quantized) cavity light field and is given by[3]

$$H_{\mathrm{l}} = \hbar\Delta_{\mathrm{c}}\hat{a}^{\dagger}\hat{a}, \tag{3.30}$$

[2] Note that the time dependence of the electromagnetic field is omitted by a unitary transformation $U = \mathrm{e}^{-i\omega_{\mathrm{l}}t}$ to a frame rotating with the frequency of the light field.

[3] For convenience, the zero-point energy of the vacuum field is omitted.

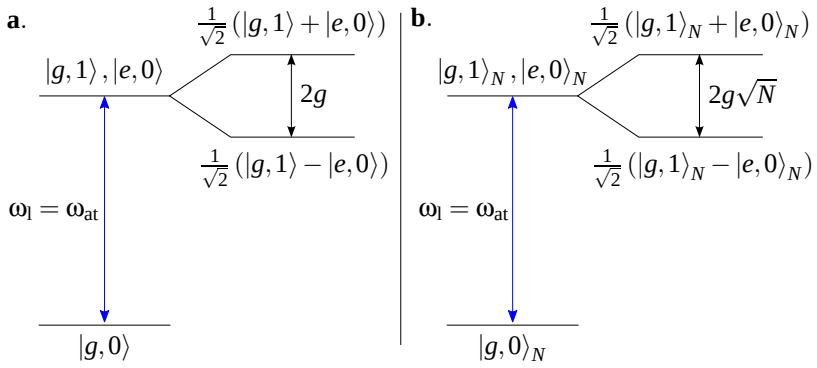

Figure 3.3.: Schematic level diagram of the vacuum Rabi splitting in the resonant case for **a.** a single two-level atom coupled to a single cavity field mode and **b.** N atoms simultaneously interacting with the field mode. For details see text.

where $\Delta_c = \omega_c - \omega_l$ is the detuning of the cavity relative to the frequency of the input field and $\hat{a}^\dagger$, $\hat{a}$ are the intracavity field creation and annihilation operators. The third term in eq. (3.28) describes the coupling between the two-level system and the light field. Using the dipole approximation and in the frame rotating with the laser frequency it is given by

$$H_{\text{int}} = -\mu_{ge}E = -\hbar g(\hat{\sigma}^\dagger + \hat{\sigma})(\hat{a}^\dagger + \hat{a}), \tag{3.31}$$

where we inserted the coherent coupling rate defined in eq. (3.27).

Applying the rotating wave approximation, i.e. neglecting the two non-energy conserving terms $\hat{\sigma}\hat{a}$ and $\hat{\sigma}^\dagger\hat{a}^\dagger$ in eq. (3.31) we find the Jaynes-Cummings Hamiltonian

$$H = \hbar\Delta\pi^{(e)} + \hbar\Delta_c(\hat{a}^\dagger\hat{a}) - \hbar g(\hat{\sigma}^\dagger\hat{a} + \hat{\sigma}\hat{a}^\dagger). \tag{3.32}$$

It can be readily diagonalized using so-called dressed states [58, 126]. In the experiments described in this thesis we focus on the investigation of the light-matter interaction at the single photon level and we can restrict the system to the three lowest states $|g,0\rangle$, $|g,1\rangle$ and $|e,0\rangle$. In this notation g,e refer to the atomic ground and excited states, and the second quantum number $0,1$ denotes the number of photons in the cavity field mode under consideration. In the case of a resonant light field, $\omega_l = \omega_{at}$, the uncoupled states $|g,1\rangle$ and the $|e,0\rangle$ are degenerate. The coupling with the cavity field will, however, mix these two states and give rise to the so called vacuum Rabi splitting of the cavity spectrum. The new eigenstates of the coupled system are $|g,0\rangle$, $|\pm\rangle \equiv \frac{1}{\sqrt{2}}(|g,1\rangle \pm |e,0\rangle)$ and the energy difference is $\Delta E = 2g$, see fig. 3.3 a. The situation is similar to the case when Rabi oscillations between ground and excited state are driven by a strong laser field. However, in the situation described here, these oscillations occur for light fields at the single photon level.

3.2.2. Interaction of N atoms with a single cavity light mode

We will now generalize the previous single-atom situation to the case where N_{tot} ions simultaneously interact with a single cavity mode. In the case of non-interacting atoms[4],

[4] For the case of an ion Coulomb crystal trapped in a linear Paul trap, this is a reasonable approximation, as the ions are well-separated, and the Coulomb interaction only couples their external degrees of freedom, as

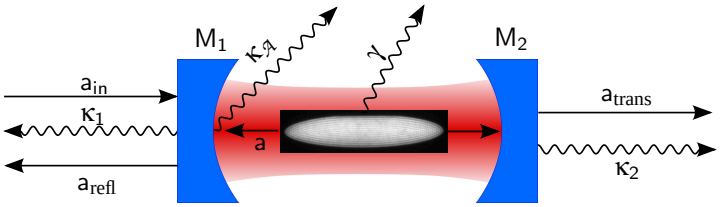

Figure 3.4.: CQED scheme considered for the description of the interaction between an ensemble of ions and the cavity field. The situation is similar to the situation depicted in fig 3.1. The resonator is formed by two mirrors M_1 and M_2, a_{in} is the input light field, a the intracavity field, a_{trans} and a_{refl} are the transmitted and reflected fields, respectively. κ_1 and κ_2 are the cavity decay rates through M_1 and M_2, all other cavity losses are merged in the rate $\kappa_{\mathcal{A}}$. The spontaneous dipole decay rate of the ions is denoted by γ.

the Hamiltonian in the rotating wave approximation defined for a single two-level system in eq. (3.32) now reads

$$H_N = \hbar\Delta \sum_{j=1}^{N_{\text{tot}}} \hat{\pi}_j^e + \hbar\Delta_c \hat{a}^\dagger \hat{a} - \hbar g \sum_{j=1}^{N_{\text{tot}}} \Psi_{nm}(\boldsymbol{r}_j)(\hat{\sigma}_j^\dagger \hat{a} + \hat{\sigma}_j \hat{a}^\dagger), \tag{3.33}$$

where $\hat{\pi}_j^{(e)}$ is the excited state population and $\hat{\sigma}_j^\dagger$ and $\hat{\sigma}_j$ are the atomic rising and lowering operators of the j-th ion (in the rotating frame) and g is the single-ion coupling rate defined in (3.27). As the ions are not necessarily located at anti-nodes of the cavity mode, we take into account the field distribution $E_0\Psi_{nm}(\boldsymbol{r}_j)$ of a single cavity Hermite-Gauss mode as introduced in eq. (3.1) and weight the contribution of each ion to the light-matter coupling with the field amplitude of the considered mode at the position of the atom.

To gain more insight into the collective behavior, it is, however, instructive to first consider the situation, where N atoms couple with equal coupling strength to a particular cavity field mode, hence $\Psi_{nm}(\boldsymbol{r}_j) = 1,\ \forall j$. For a weak excitation of the system (at most one excitation in form of a intracavity photon or a collective delocalized excitation of the atomic ensemble) we can restrict ourselves to the three lowest-lying Dicke states [58],

$$\begin{aligned} |g,n\rangle_N &= |g\rangle^{(1)}|g\rangle^{(2)}\ldots|g\rangle^{(N)}|n\rangle, \quad n=0,1 \\ |e,0\rangle_N &= \frac{1}{\sqrt{N}}\sum_{i=1}^{N}|g\rangle^{(1)}|g\rangle^{(2)}\ldots|e\rangle^{(i)}\ldots|g\rangle^{(N)}|0\rangle, \end{aligned} \tag{3.34}$$

where $|g\rangle^{(j)}$ ($|e\rangle^{(j)}$) denote the ground (excited) state of the j-th ion. The state vector $|g,n\rangle_N$ represents the coupled system of all ions in the ground state and n photons in the cavity field mode, while the state $|e,0\rangle_N$ contains no photon in the cavity field mode and one delocalized excitation which is shared by the whole atomic ensemble. The interaction Hamiltonian in eq. (3.33) couples the two states $|g,1\rangle_N$ and $|e,0\rangle_N$, the expectation value yields

$$\begin{aligned} {}_N\left\langle g,1\left|g\hbar\sum_{i=1}^{N}\left(\sigma_i^+ a+\sigma_i^- a^\dagger\right)\right|e,0\right\rangle_N &= \frac{\hbar g}{\sqrt{N}}\sum_{i=1}^{N}{}^{(i)}\left\langle g,n\left|\left(\sigma_i^+\hat{a}+\sigma_i^-\hat{a}^\dagger\right)\right|e,0\right\rangle^{(i)} \\ &= \hbar g\sqrt{N}. \end{aligned} \tag{3.35}$$

explained in chapter 2.3.

The situation is similar to the situation of a single two-level system coupled to the cavity field mode discussed in the previous section, where the excited state, $|e,0\rangle_N$, of the system now can be understood as a collective spin polarization of the ensemble and the collective coupling rate between the ensemble and the cavity field mode is enhanced by a factor $\sqrt{N}$. Again, for $\Delta = 0$ and $g = 0$, the two states $|e,0\rangle_N$ and $|g,n\rangle_N$ are degenerate. A non-zero coupling g lifts the degeneracy and the energy levels of the new collective eigenstates are separated by $2g\sqrt{N}$, as depicted in fig. 3.3 b.

An interesting regime is reached, when the collective coherent coupling rate between the N-atoms and the cavity field mode exceeds the dissipative rates in the system

$$g\sqrt{N} > (\gamma, \kappa). \tag{3.36}$$

In the literature it is referred to as as the collective strong coupling regime [58]. It was successfully accessed with atomic ensembles in the microwave regime [60] and also in the optical domain [61, 62, 135] and, more recently, with Bose-Einstein condensates [66, 67].

Collective strong coupling in our system

Based on the above discussion, we can now estimate how many ions are necessary to reach the collective strong coupling regime in our setup. In our experiments we investigate the interaction of $^{40}Ca^{+}$ ions with a cavity light field on the $3d^2D_{3/2} \leftrightarrow 4p^2P_{1/2}$ transition (see fig. 2.2) and the spontaneous decay rate of the $4p^2P_{1/2}$ level is $\gamma = 2\pi \times 11.2$ MHz. The second decoherence rate, namely the cavity field decay rate was measured to be $\kappa = 2\pi \times 2.1$ MHz [80].

The single ion coupling rate g can for the given atomic parameters and the known geometry of the cavity be calculated (see appendix A.5) and we find

$$g_{\text{theory}} = 2\pi \times (0.532 \pm 0.007)\,\text{MHz}. \tag{3.37}$$

From these values we deduce that ~ 500 ions effectively interacting with a single cavity field mode should be sufficient to reach the regime where $g\sqrt{N} > (\kappa,\ \gamma)$ in our system. We will in the next section precise this effective number of ions in our situation.

3.2.3. The optical Bloch equations

In the previous subsection, we introduced the Hamiltonian describing the coherent light-matter interaction, neglecting dissipative processes. To derive the time evolution of the system observables including the dissipative processes, i.e. spontaneous emission and decay of the cavity field, we make use of a standard Heisenberg-Langevin approach [126]. It yields the time evolution of the system observables includes the damping terms and also the noise operators describing quantum fluctuations. In the experiments presented in this thesis, we are only interested in the mean values of the operators and can restrict ourselves to the semi-classical mean values of the observables, not including the noise operators. For an arbitrary observable $\hat{o}$ the semi-classical mean value is denote by $o = \langle \hat{o} \rangle$. In the Heisenberg picture, the time evolution of an observable $\hat{o}$ is given by $\frac{\mathrm{d}\hat{o}}{\mathrm{d}t} = -\frac{i}{\hbar}[\hat{o}, H]$. Using the Hamiltonian of eq. (3.33), we can calculate the dynamical equations for the

mean values of the system observables and one finds, including the dissipative terms

$$\dot{\pi}_j^{(e)} = -ig\Psi_{nm}(\boldsymbol{r}_j)\left(\sigma_j a^\dagger - \sigma_j^\dagger a\right) - 2\gamma\pi_j^{(e)} \tag{3.38a}$$

$$\dot{\pi}_j^{(g)} = +ig\Psi_{nm}(\boldsymbol{r}_j)\left(\sigma_j a^\dagger - \sigma_j^\dagger a\right) + 2\gamma\pi_j^{(e)} \tag{3.38b}$$

$$\dot{\sigma}_j = -iag\Psi_{nm}(\boldsymbol{r}_j)\left(\pi_j^{(e)} - \pi_j^{(g)}\right) - (\gamma + i\Delta)\sigma_j \tag{3.38c}$$

$$\dot{a} = -(\kappa + i\Delta_c)a + i\sum_{j=1}^{N_{\text{tot}}} g\Psi_{nm}(\boldsymbol{r}_j)\sigma_j + \sqrt{2\kappa_1}a_{\text{in}}. \tag{3.38d}$$

The three first expressions are commonly referred to as the optical Bloch equations [136], while the last equation is the evolution equation of the cavity field including the interaction with the atoms and can be regarded as an extension of the case of the empty cavity found in eq. (3.16).

Low saturation regime

The set of differential equations in eqs. (3.38) describes the full dynamics of the coupled atom-cavity system. In the experiments presented in this thesis, the light-atom interaction is studied at the single (or few) photon level and the dynamical equations in (3.38) can be restricted to the low saturation regime. In this limit, most of the atoms remain in the ground state and we can assume $\pi_j^{(e)} \approx 0$, and $\pi_j^{(g)} \approx 1\ \forall j$. Eqs. (3.38c) and (3.38d) reduce to

$$\dot{\sigma}_j = -(\gamma + i\Delta)\sigma_j + ig\Psi_{nm}(\boldsymbol{r}_j)a, \tag{3.39a}$$

$$\dot{a} = -(\kappa + i\Delta_C)a + i\sum_{j=1}^{N_{\text{tot}}} g\Psi_{nm}(\boldsymbol{r}_j)\sigma_j + \sqrt{2\kappa_1}a_{\text{in}}. \tag{3.39b}$$

3.2.4. Steady state spectrum of the coupled atom-cavity system

In steady state the dynamical equations in (3.39) can be readily solved and one finds

$$\sigma_j = \frac{iga}{\gamma + i\Delta}\Psi_{nm}(\boldsymbol{r}_j) \tag{3.40a}$$

$$a = \frac{\sqrt{2\kappa_1}a_{\text{in}}}{\kappa + i\Delta_{\text{c}} - i\chi} \tag{3.40b}$$

where the linear susceptibility of the atomic ensemble

$$\chi = g^2 N\frac{i}{\gamma + i\Delta} \tag{3.41}$$

was introduced. In this expression the sum over the contribution of the individual ions was replaced by an effective number of interacting ions N. It will be discussed for our system in the following paragraph.

The effective number of interacting ions

The effective number of ions is defined as the sum over all ions in the crystal weighted by the field mode function Ψ_{nm} of the TEM_{nm} mode considered (see sec. 3.1.1)

$$N = \sum_{j=1}^{N_{\mathrm{tot}}} \Psi_{nm}^2(\boldsymbol{r}_j). \tag{3.42}$$

It can be understood as the situation where the interaction of the N_{tot} ions in the whole ensemble with the cavity field mode is mimicked by an ensemble of N ions all located at anti-nodes of the fundamental TEM_{00} mode.

As discussed in sec. 2.3, ion Coulomb crystals in a linear radio-frequency trap are to an excellent approximation spheroids with half-length L and radius R (see fig. 2.4) and a constant ion density, ρ_0, throughout the whole ensemble. It is then convenient to adopt a continuous medium description, in which Eq. (3.42) becomes an integral over the crystal volume V

$$N = \rho_0 \int_V \mathrm{d}\boldsymbol{r} \Psi_{nm}^2(\boldsymbol{r}) \tag{3.43}$$

In our experiment, the crystal radius and half-length, R and L, are typically much smaller than the Rayleigh range z_0, so that the axial mode function can be simplified

$$\sin^2\left[kz - \arctan(z/z_0) + kr^2/2R(z)\right] \approx \sin^2(kz). \tag{3.44}$$

Moreover, for ions randomly distributed along the cavity axis, we can average over the standing-wave longitudinal structure, which yields an effective number of ions of

$$N = \frac{\rho_0}{2} \int_{-R}^{R} \mathrm{d}x \int_{-R}^{R} \mathrm{d}y \Psi_n^2(x) \Psi_m^2(y). \tag{3.45}$$

The exact expression in eq. (3.43) can be evaluated numerically for an arbitrary TEM_{nm} knowing the crystal dimensions, its density and the cavity mode geometry. In most of experiments presented in this thesis, the cavity field mode function considered will be the fundamental TEM_{00} Gaussian mode, introduced in eq. (3.7). For typical crystals with large radial extension as compared to the cavity waist ($R \gg w_0$) and a half-length smaller than the Rayleigh range ($L \ll z_{\mathrm{R}}$) the coupling to the TEM_{00} can be further approximated and the exact expression of eq. (3.45) reduces to

$$N \simeq \rho_0 \frac{\pi w_0^2}{2} L, \tag{3.46}$$

which is simply the product of the ion density by the volume of the cavity mode in the crystal[5].

Cavity transmission and reflection spectrum

Using the input-output relations given in eq. (3.20), the cavity transmission and reflection spectrum of the coupled ion-cavity system can be calculated, taking the atomic suscepti-

[5] The volume is effectively reduced by a factor of 1/2 by the longitudinal averaging.

bility into account and one finds

$$\mathcal{R} \equiv \left|\frac{a_{\text{refl}}}{a_{\text{in}}}\right|^2 = \frac{(2\kappa_1-\kappa')^2+\Delta_c'^2}{\kappa'^2+\Delta_c'^2} \tag{3.47a}$$

$$= \frac{[\kappa_1-\kappa_2-\kappa_{\mathcal{A}}-\text{Im}(\chi)]^2+[\Delta_c-\text{Re}(\chi)]^2}{\kappa^2+\Delta^2+|\chi|^2+2[\kappa\text{Im}(\chi)+\Delta_c\text{Re}(\chi)]}$$

$$\mathcal{T} \equiv \left|\frac{a_{\text{trans}}}{a_{\text{in}}}\right|^2 = \frac{4\kappa_1\kappa_2}{\kappa'^2+\Delta_c'^2} \tag{3.47b}$$

$$= \frac{4\kappa_1\kappa_2}{\kappa^2+\Delta^2+|\chi|^2+2[\kappa\text{Im}(\chi)+\Delta_c\text{Re}(\chi)]}.$$

Here an effective cavity decay rate and an effective cavity detuning were introduced:

$$\kappa' = = \kappa+\text{Im}(\chi) = \kappa+g^2N\frac{\gamma}{\gamma^2+\Delta^2}, \tag{3.48a}$$

$$\Delta_c' = \Delta_c-\text{Re}(\chi) = \Delta_c-g^2N\frac{\Delta}{\gamma^2+\Delta^2}. \tag{3.48b}$$

Like in the case of the empty cavity in eqs. (3.21) the line shape of the reflection and transmission spectra are still Lorentzian when the cavity detuning is varied. However, the bare cavity decay rate and detuning κ and Δ_c are replaced by the effective cavity decay rate and detuning, κ' and Δ_c'. These quantities, dressed by the atoms, result in a broadening and a shift of the cavity resonance, respectively. The broadening and shift of the cavity resonance represent the change in absorption and dispersion experienced by the cavity field interacting with N ions and will be used in ch. 5 to quantify the collective coupling strength achieved in our experiments. Fig. 3.5 a. shows the cavity transmitivity as a function of cavity detuning Δ_c for an empty cavity and for 500 ions coupled to the light field for a probe laser detuning of $\Delta=\gamma$.

An interesting situation occurs when the length of the cavity, instead of being scanned, is stabilized such that the cavity resonance frequency is equal to the atomic resonance frequency $\omega_c=\omega_{at}$ (hence $\Delta_c=\Delta$). As discussed in sec. 3.2.1, varying the probe frequency amounts to probing the normal mode spectrum of the coupled atom-cavity system. In this case, the reflectivity spectrum reads

$$\mathcal{R} = \frac{[\kappa_1-\kappa_2-\kappa_{\mathcal{A}}-\text{Im}(\chi)]^2+[\Delta+\text{Re}(\chi)]^2}{\kappa^2+\Delta^2+|\chi|^2+2[\kappa\text{Im}(\chi)-\Delta\text{Re}(\chi)]} \tag{3.49a}$$

$$= \frac{(\kappa_1-\kappa_2-\kappa_{\mathcal{A}})^2+\Delta^2-g^4N^2\frac{\gamma^2-\Delta^2}{(\gamma^2+\Delta^2)^2}-2g^2N\frac{(\kappa_1-\kappa_2-\kappa_{\mathcal{A}})\gamma-\Delta^2}{\gamma^2+\Delta^2}}{\kappa^2+\Delta^2+2g^2N\frac{\gamma\kappa+\Delta^2}{\gamma^2+\Delta^2}+\frac{g^4N^2}{\gamma^2+\Delta^2}}. \tag{3.49b}$$

As a function of the common detuning Δ, it exhibits a characteristic double peak structure. The splitting of the normal modes is commonly referred to as the vacuum Rabi splitting, and was qualitatively already described by the Jaynes-Cummings model in sec. 3.2.2 (see fig. 3.3). An example for the expected cavity reflectivity spectrum when the cavity is locked on atomic resonance is shown in fig. 3.5 b. for an effective number of ions of $N=500$ and a single ion coupling rate of $g=2\pi\times 0.53$ MHz.

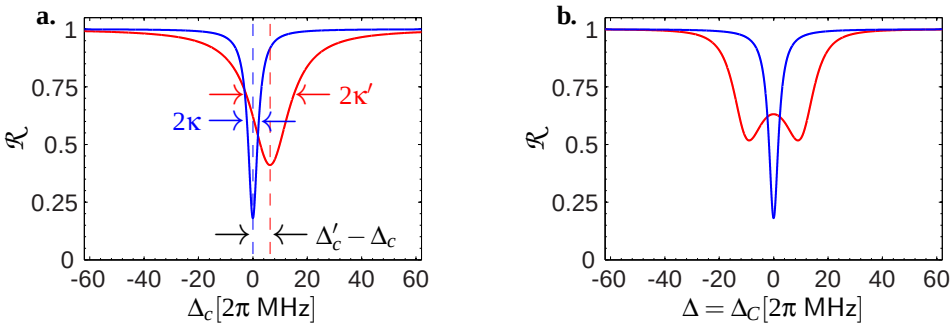

Figure 3.5.: a. Calculated reflection spectrum as a function of cavity detuning Δ_c for 500 ions coupled to the cavity mode (red line) and for the empty cavity (blue line). The probe detuning was set to $\Delta = \gamma = 2\pi \times 11.2$ MHz. **b.** Reflection spectrum for a cavity resonant with the atomic transition ($\Delta = \Delta_c$). The red line is calculated for 500 ions effectively interacting with the cavity mode and a single ion coupling rate of $g = 2\pi \times 0.53$ MHz, while the blue line corresponds to an empty cavity. The cavity parameters are identical to those defined in fig. 3.2.

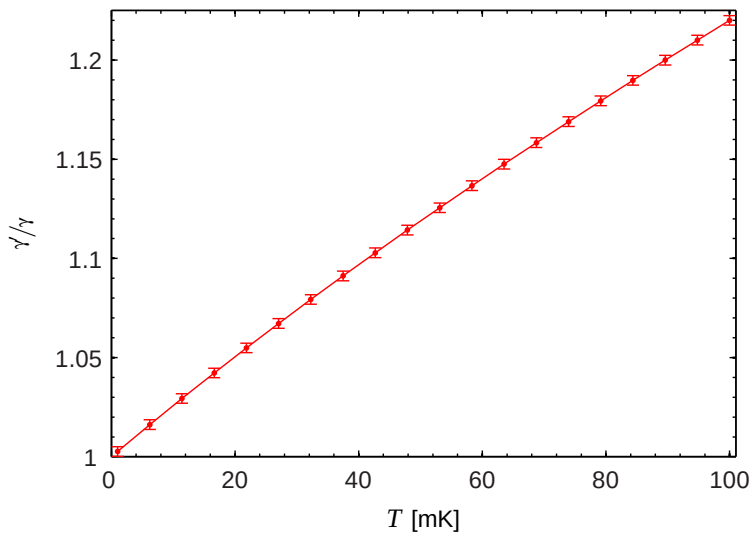

Figure 3.6.: Effective dipole decay rate γ' normalized by the natural width γ as a function of temperature T. Each data points is the result of a fit to the cavity field effective decay rate of eq. (3.51a) for a certain temperature T. As a fitting function we use the cavity effective decay rate found for the case of ions at rest (eq. (3.48a)), where the natural linewidth γ was replaced by an effective linewidth γ' to account for the finite temperature of the ensemble.

3.3. The effect of motion

The dynamical equations found in eqs. (3.38) are only valid for atoms at rest. If the velocity of the ions has a component along the axis of the cavity, the standing-wave structure of the cavity field and the Doppler shifts due to the finite velocity of the ion have to be taken into account. For an ion moving along the standing wave field with a velocity v it is convenient to define atomic dipole operators arising from the interaction with the two counter-propagating components of the standing-wave cavity field $\sigma_{j\pm} = \frac{1}{2}\sigma_j \exp(\pm ikz)$. In the low saturation limit, taking into account the opposite Doppler shifts, and for a slow motion, the evolution equations (3.40) become

$$\dot{\sigma}_{j\pm} = -[\gamma + i(\Delta \pm kv)]\,\sigma_{j\pm} + i(g/2)\Psi_{nm}(\boldsymbol{r}_j)a \tag{3.50a}$$

$$\dot{a} = -(\kappa + i\Delta_c)a + i(g/2)\sum_{j=1}^{N_{\text{tot}}} \Psi_{nm}(\boldsymbol{r}_j)\,(\sigma_{j+} + \sigma_{j-}) + \sqrt{2\kappa_1}a_{\text{in}}. \tag{3.50b}$$

For a sufficiently large ensemble and random velocities of the individual ions given by a certain probability distribution $f(v)$ the steady state mean value of the intracavity field can be calculated and is still of the same form as in the zero-velocity case (Eq. (3.40)). However, the effective cavity decay rate and the effective cavity detuning are modified. Eqs. (3.48) become

$$\kappa' = \kappa + g^2 N \int \mathrm{d}v\,\xi(\Delta, v)\, f(v)\gamma \tag{3.51a}$$

$$\Delta' = \Delta_c - g^2 N \int \mathrm{d}v\,\xi(\Delta, v)\, f(v)(\Delta - kv). \tag{3.51b}$$

where the dimensionless parameter

$$\xi(\Delta, v) = \frac{\gamma^2 + \Delta^2 + (kv)^2}{(\gamma^2 + \Delta^2)^2 + 2(\gamma^2 - \Delta^2)(kv)^2 + (kv)^4} \tag{3.52}$$

was defined. In the case of a thermal ensemble, the velocity distribution is the Maxwell-Boltzmann distribution, which for a certain temperature T is given by

$$f(v) = \sqrt{\frac{m}{2\pi k_B T}} \exp\left(-\frac{mv^2}{2k_B T}\right) \mathrm{d}v. \tag{3.53}$$

For temperatures in the few tens of mK range the variation of the cavity field effective decay rate and detuning with Δ given by Eqs. (3.51) are still well-approximated by Eqs. (3.48) replacing the natural linewidth γ by an effective dipole decay rate γ'.

Fig. 3.6 shows the effective dipole decay rate as a function of the detuning Δ deduced by fitting the numerically calculated effective cavity field decay rate for finite temperatures T in eq. (3.51a) by eq. (3.48a) calculated for ions at rest and leaving the effective dipole decay rate γ' as a free parameter. This graph will later allow us to approximate the temperature of a certain ion Coulomb crystal from the effective dipole decay rate, found by fitting the measured effective cavity field decay rate by eq. (3.48a).

4. Experimental setup

In this section the setup used for the experiments presented in this thesis will be described. The setup was to a large extent finished before the start of this PhD and we will only give a brief description of the setup. The project was started with the goal of building a quantum memory based on ion Coulomb crystals in an optical cavity and a first version of a linear Paul trap with an optical cavity incorporated was designed and built by Anders Mortensen. Details on the design considerations and first experiences with the setup can be found in his PhD thesis [137]. The project was then continued by my predecessor Peter Herskind who developed and constructed of the second trap, which is the one used for the experiments in this thesis. A very comprehensive and detailed description of both the cavity trap and also the laser systems used for our experiments is given in his PhD thesis [80].

Some of the experiments presented in this thesis required slight changes of the system, mainly of the optical setup. The relevant modifications will be described in the respective chapters. Here, we will focus on the general aspects and the main components of the experiments.

The chapter is structured as follows. In sec. 4.1 we will start out with an overview of the setup, before describing the linear Paul trap in sec. 4.2. In sec. 4.3 we will present the laser systems used for the loading, Doppler cooling and state preparation of the ions, followed by the imaging and fluorescence detection systems in sec. 4.4. In sec. 4.5 we will describe the optical cavity incorporated into the trap and in sec. 4.6 give a technical description of a general technique to geometrically displace the minimum of the radially confining RF potential in order to overlap the cavity and the trap axis. Finally, we will describe the cavity detection systems and the data acquisition system in sec. 4.8 and 4.9, respectively.

4.1. Overview

Trapping charged particles in the vicinity of dielectric objects like mirrors is very challenging, as the insertion of such dielectrics into the trapping region may significantly change the boundary conditions and perturb the field lines of the confining potential. Furthermore, charging effects on the dielectric surfaces may give rise to local patch potentials which also change the effective trapping potential. The realization of the strong coupling regime of cavity quantum electrodynamics necessitates very small cavity mode volumes (see eq. (3.27)) and is therefore difficult with ions. Only few groups have until now realized ion trap systems incorporating optical cavities to investigate the interaction of single ions with a cavity field mode [68–74] and the single-ion strong coupling regime still remains to be achieved.

The cavity trap in Århus was designed to realize an efficient quantum memory using large ion Coulomb crystals. One of the basic requirements for such a memory is the

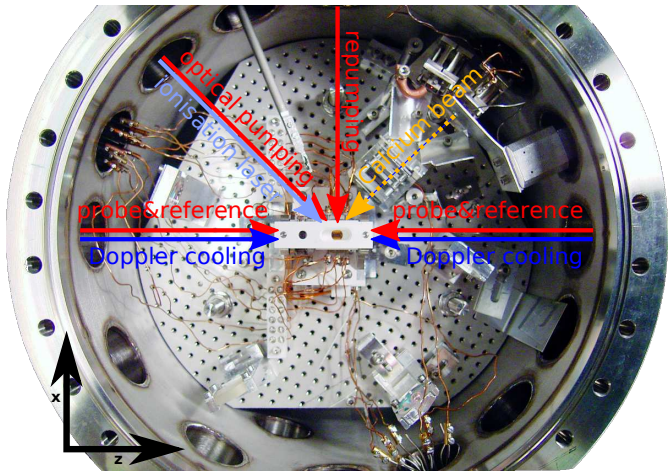

Figure 4.1.: Inside of the vacuum chamber, with the main laser beams. The chamber has a inner diameter of 40 cm. For details see text.

achievement of the collective strong coupling regime [55] (see. eq. (3.36)). For N ions effectively interacting with the cavity field mode the collective coherent coupling rate is enhanced by $\sqrt{N}$ (see eq. (3.36)). For a sufficiently large number of ions, the requirement for small cavity mode volumes therefore becomes less critical as the regime, where the collective coupling rate $g\sqrt{N}$ exceed the spontaneous dipole decay rate and the cavity field decay rate, γ and κ, can be reached although $g < (\kappa, \gamma)$.

In our setup, a segmented linear Paul trap (see sec. 4.2) is combined with a moderately high finesse cavity (see sec. 4.5). The cavity trap is mounted in a vacuum chamber under ultra-high vacuum conditions (pressure $\sim 2-5\cdot 10^{-10}$ mbar), with 8 viewports providing optical access from different sides and from the top. A picture of the inside of the vacuum chamber with the main laser beams can be seen in fig. 4.1. The vacuum chamber is positioned on an optical table, which also contains the necessary optics to distribute the different laser beams to the chamber and the detection systems. All the laser systems are located on different optical tables, and the light is brought to the trap table through optical fibers.

4.2. The linear Paul trap

The ion trap is a segmented linear Paul trap, formed by four cylindrical rods, each divided into three separate electrodes, see fig. 2.1. A mathematical description of the confinement potentials was given in sec. 2.1. The trap electrodes have a radius of $r_e = 2.60$ mm and are diagonally separated by $2r_0 = 4.70$ mm. The lengths of the central and the outer segments are $2z_0 = 5.00$ mm and $z_{\text{end}} = 5.90$ mm, respectively (see fig. 4.6). The trap is operated at a frequency of $\Omega_{\text{RF}} = 2\pi \times 4.0$ MHz. The radio-frequency field is applied to all 3 segments of each rod, with a phase difference of π between neighboring rods, see fig. 2.1.

The endcaps are formed by the four outer segments on each side and axial confinement

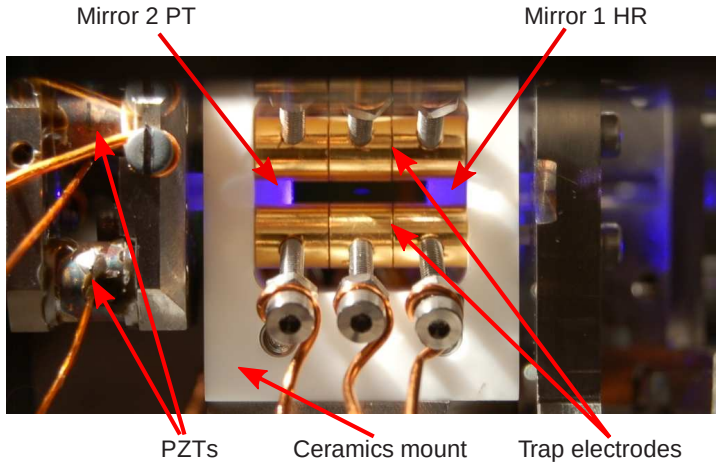

Figure 4.2.: Picture of the cavity trap setup taken through one of the view ports of the vacuum chamber. The cylindrical trap electrodes are of gold plated copper and attached to a monolithic Macor mount. The two cavity mirrors are held by titanium plates separated by two low expansion ceramics. Mirror 1 is the high reflector (HR) and directly mounted on the titanium plate. Mirror 2 is the partial transmitter (PT) and mounted on a PZT plate to allow for precise control of the cavity length.

is achieved by applying static potentials (DC) to these electrodes. In this geometry, the a- and q-parameter defined in eqs. (2.5) and (2.5) are $a = -0.84 \times 10^{-3}\, U_{\mathrm{DC}} \mathrm{V}^{-1}$ and $q = 1.38 \times 10^{-3} U_{\mathrm{RF}}/\mathrm{V}$, the axial geometrical constant is $\eta = 0.342$. The trap electrodes are manufactured from gold coated copper and mounted on cylindrical ultra low expansion rods (Zerodur), which are held in place by a monolithic ceramic frame (Macor). The RF amplitude is provided by a frequency generator[1] and amplified by an RF amplifier[2]. A home-built continuous current voltage driver is used to supply the DC end-cap voltages (electrode segments 1-4-7-10 and 2-6-9-12, respectively, see fig. 2.1) and, in addition, also allows for the selective application of DC potentials to some of the electrode segments (e.g. 1-2-3 and 4-5-6 can be controlled independently, see fig. 2.1). More details on the linear Paul trap can be found in [80] and [120].

4.3. Laser system

In this section the laser systems used for Doppler cooling, ionization and state preparation of the ions are introduced. A simplified schematic overview over all laser beams and the optical setup is shown in fig. 4.3

[1] Hewlett-Packard, HP 33120A
[2] Amplifier Research, 4W1000

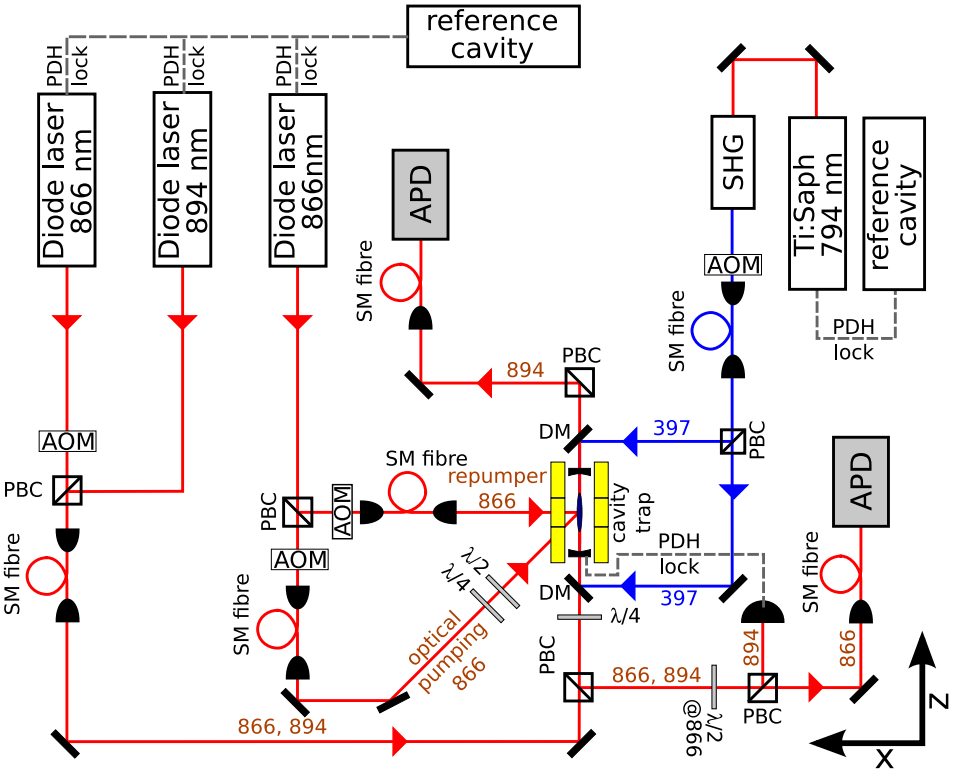

Figure 4.3.: Schematic setup of the cavity trap and the laser system. The ionization laser is not shown on the sketch. A more detailed picture of the cavity detection system is shown in fig. 4.8. The abbreviations are: Polarizing beam splitter cube (PBC), single mode (SM), acousto optical modulator (AOM), dichroic mirror (DM). Pound-Drever-Hall lock (PDH lock).

4.3.1. Doppler cooling lasers

The Doppler cooling light on the $4s^2S_{1/2} \leftrightarrow 4p^2P_{1/2}$ transition of $^{40}Ca^+$ at 397 nm (see fig. 2.2) is produced by a frequency doubled Ti:Saph laser. The frequency of this laser is stabilized using a Pound-Drever-Hall [138] locking scheme to a temperature stabilized reference cavity, formed by two mirrors on a 25 cm long quartz tube. The free spectral range of the reference cavity is $\nu_{FSR} \sim 600$ MHz. The resonator is mounted in an evacuated vacuum tube, the frequency stability was measured to be ~ 1 MHz/h, for details see [139]. The laser light sent to the reference cavity is passed through a double-pass acousto-optical modulator (AOM) allowing for the fine tuning of the frequency of the Ti:Saph laser by ± 100 MHz. When locked to the reference cavity the linewidth of the laser is of the order of ~ 100 kHz and much narrower than the natural linewidth of the $4s^2S_{1/2} \leftrightarrow 4p^2P_{1/2}$ transition in $^{40}Ca^+$ which is $\Gamma = 2\pi \times 22.4$ MHz.

The frequency doubled light is then sent through a second AOM in single-pass and the -1^{st}-diffraction order is coupled to a fiber guiding the light to the trap table (see fig. 4.3). The AOM is used to switch the Doppler cooling light on and off, with typical rise times of the order of ~ 100 ns and an on-off attenuation of > 55 dB after the fiber. On the trap table the light is split into two equally intense beams that are sent to the trap in counter propagating directions along the trap axis, with opposite circular polarizations (σ^+/σ^-).

4.3.2. Repumping and optical pumping laser

An external cavity diode laser system provides light at 866 nm, corresponding to the $3d^2D_{3/2} \leftrightarrow 4p^2P_{1/2}$ transition of $^{40}Ca^+$. It is used both to repump spontaneously decayed ions from the metastable $3d^2D_{3/2}$ level during the cooling cycle and to optically pump the population to certain Zeeman substates of the $3d^2D_{3/2}$ level. The diode laser is also frequency stabilized to a second temperature stabilized reference cavity (length 25 cm, $\nu_{FSR} \sim 600$ MHz) in a Pound-Drever-Hall scheme with a linewidth of ~ 100 kHz. Again, a double-pass AOM setup allows for the fine tuning of the laser frequency by ± 100 MHz.

The beam is split into two parts for repumping and optical pumping. Both beams are sent through single pass AOMs to allow for switching the beams on and off, the -1^{st}-diffraction order is again coupled to single-mode fibers transporting the light to the trap table (extinction after the fiber > 55 dB).

In most experiments the repumping laser is sent to the trap center along the *x*-axis, i.e. perpendicular to the cavity axis, see fig. 4.3. The polarization is chosen perpendicular to the *z*-axis, which, in the basis of the quantization axis (*z*-axis) corresponds to a superposition of σ^+ and σ^- light. With this polarization, all four magnetic substates of the $3d^2D_{3/2}$ level are addressed and repumped to the excited $4p^2P_{1/2}$ level, from which the atoms decay to the $4s^2S_{1/2}$ ground state (with a probability of 12:1). In some experiments different configurations for the injection of the repumping laser will be used, e.g. to visualize the transverse cavity modes (see fig. 5.1).

The optical pumping beam is (in most experiments) sent to the trap at an angle of 45° relative to the *z*-quantization axis, see fig. 4.3. The polarization of the optical pumping beam after the fiber is controlled by a Glan Polarizer and successively a $\lambda/4$ and a $\lambda/2$ wave plate. It has a suitable polarization, such that only the π and σ^+ transitions between the $3d^2D_{3/2}$ and $4p^2P_{1/2}$ level are addressed [140]. During optical pumping the Doppler

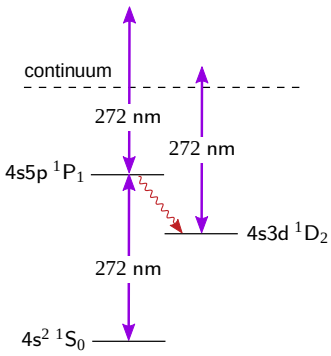

Figure 4.4.: Resonantly enhanced two-photon ionization scheme. The lifetime of the 4s5p^1 P$_1$ level is $17-60$ ns, the lifetime of the 4s3d ^{1}D$_2$ state is 18 μs

cooling beams at 397 nm are sent to the ions to transfer population of the 4s^{2}S$_{1/2}$ ground state to the metastable 3d^{2}D$_{3/2}$ state. In this configuration, the $m_j = +3/2$ state of the 3d^{2}D$_{3/2}$ level will not be addressed by any laser and the simultaneous interaction with the repumping and the Doppler cooling laser transfers the population to this quantum state.

4.3.3. Isotope selective loading

Calcium ions are loaded to the trap from a resistively heated oven containing natural abundant calcium comprising all stable Ca isotopes. With a fraction of 96.9 %, the most abundant isotope is ^{40}Ca, which is also used for all experiments presented in this thesis. However, any stable Ca isotope can be loaded [80, 120], e.g. to form bi-crystals of two simultaneously trapped isotopes [118, 141].

To load calcium into the trap, the oven is typically heated to $\sim 410^\circ$ C, and a thermal beam emerges from the oven. It is collimated by a set of skimmers and sent thought the center of the quadrupole trap at 45° relative to the trap axis, where it is perpendicularly crossed by an ionization laser beam at 272 nm allowing for the isotope selective loading of calcium. This is accomplished by a resonantly enhanced two-photon ionization process, where neutral calcium is first excited to the 4s5p^{1}P$_1$ level by a resonant photon around 272 nm and subsequently transferred to the ionization continuum, either directly from the 4s5p^{1}P$_1$ level or, after a spontaneous decay, from the metastable 4s3d^{1}D$_2$ level by a non-resonant second photon at the same wavelength (see fig. 4.4). The isotope selectivity of the process originates from the first resonant transition, which for ^{40}Ca is separated by ~ 1 GHz from the next closest isotope ^{42}Ca [142].

Light at 272 nm is produced by a fiber laser[3] at 1088 nm which is frequency quadrupled in two subsequent bow-tie cavities [143]. The fiber laser is tunable over several GHz, and any stable Ca isotope can be loaded by tuning it to the isotope specific frequency of the 4s^2 ^{1}P$_1$ $\leftrightarrow$ 4s5p ^{1}P$_1$ transition. Both the Doppler cooling and repumping lasers are on during the loading process [120]. After loading the desired number of ions into the trap the light of the ionization laser is blocked and the calcium oven is closed.

[3] Coheras Boostik

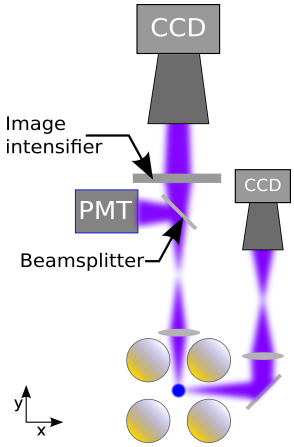

Figure 4.5.: Schematic setup of the imaging system. Two charged coupled device cameras (CCD) and one photo-multiplier tube (PMT) can be used to monitor the fluorescence of the ions. The main camera system and the PMT are mounted above the trap, while the second CCD camera is used to image the ions from the side.

4.4. Imaging and fluorescence detection systems

Two camera systems are used to visually detect the ions in the trap by collecting the reemitted fluorescence light during the Doppler cooling process. Additionally, a photo-multiplier tube can be used to monitor the fluorescence level from the trap. All three systems will be described in the following. A schematic setup of the camera systems is depicted in fig. 4.5.

4.4.1. Top camera

The main camera is mounted above the trap and images the trapped ions in the (x,z)-plane. All projection images of ion Coulomb crystals in this thesis are taken with this camera. The imaging system consists of an achromatic lens with a focal length of 75 mm mounted ~ 80 mm above the trap to collect the fluorescence light. The ions are imaged with a magnification of ~ 10 onto an image intensifier[4] consisting of two stacked multi-channel plates. The intensifier produces an amplified picture of the ions on a phosphor screen, which then is imaged with a magnification of $1/2$ by a commercial objective[5] onto a charged coupled device (CCD) camera[6] with a resolution of 640×480 pixels.

Beside the amplification, the image intensifier also provides the possibility of being gated, with gating times as short as ~ 20 ns. The gating can be used to take time resolved images of the ions and to visualize e.g. dynamics of the ion Coulomb crystals' motion.

The resolution of the camera was calibrated using an optical fiber with a known radius that was moved into the trapping zone. The fiber was illuminated by Doppler cooling light

[4] Proxitronic detector systems, MCP-Proxifier
[5] Nikon
[6] PCO sensicam

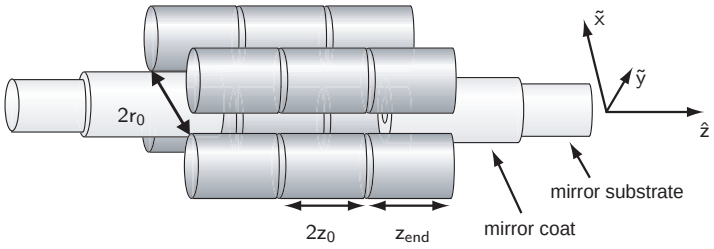

Figure 4.6.: Sketch of the linear trap with integrated cavity mirrors.

at 397 nm and the scattered light was imaged onto the CCD camera. From this measurement, the resolution was found to be 1.98 ± 0.05 $\mu m/pixel$ [80]. With this calibration, the camera can be used to determine the geometrical size of the imaged ion Coulomb crystals, as well as their transverse position in the (x,z)-plane.

4.4.2. Side camera

The resolution of 640×480 pixels limits the size of the largest ion Coulomb crystals that can be fully imaged on the top camera to a length of ~ 1.3 mm and to ~ 1.0 mm in the radial direction. In some experiments, crystals with a length of up to ~ 3 mm are used and to be able to also directly image these large crystals, a second camera system is used to monitor the ions from the side. The imaging resolution of this camera is considerably lower mainly due to the geometric restrictions imposed by the vacuum chamber geometry. The calibration is done by directly comparing images of ion Coulomb crystals taken with this camera with images of the main camera. The pixel calibration depends on the settings of the camera zoom and, for the measurements in this thesis, was 8.1 $\mu m/pixel$. Beside the measurement of the axial extension of large crystals, the side camera can also be used to determine the vertical position of the trapped ion Coulomb crystals.

4.4.3. Photo multiplier

In addition to the two cameras, a photo-multiplier tube (PMT) can be used to monitor the fluorescence level of the ions. This is especially useful in situations where the fluorescence level is used to optimize e.g. laser detunings or when the time dependence of the fluorescence level is of interest, e.g. when optimizing the optical pumping preparation. In principle, time-resolved measurements can also be performed with the gateable image intensifier, however, this requires stroboscopic measurements at particular phases of a measurement sequence, and, hence, many runs to reconstruct the fluorescence level over a longer period. With the PMT, this can be accomplished much faster and with a time-resolution of ~ 100 ns. The light sent to the PMT is split of the optical path to the top camera, just before the image intensifier on a beam splitter.

4.5. The optical cavity

In this section the optical cavity incorporated into the trap will be described. A sketch of the setup is shown in 4.6. The cavity is formed by two mirrors positioned on the axis of the quadrupole trap such that the axis of the cavity is parallel to the symmetry axis of the trap. The dielectric mirror substrates are made of fused silica. Their presence may affect the electric fields in the trap and might bend the RF-field lines and lead to an axial component of the RF-field, yielding e.g. to axial micromotion, which would result in a broadening of atomic transitions through the Doppler effect. To avoid this effect, one strategy is to make the mirror substrates as flat as possible and to extend them as close to the electrodes as possible, as was shown by simulations [137]. For this purpose, dielectric mirror coats are added around the mirror substrates to fill the space between the electrodes almost completely. They have a diameter of 4.16 mm, while the electrodes are separated by $2r_0 = 4.70$ mm (see fig. 4.6). On fig. 4.2 the mirror coats appear as blue objects to the left and the right of the trap center. Their blue appearance arises from scattering of cooling light at 397 nm. The cavity mirrors themselves have a diameter of 1.2 mm and a radius of curvature of 10 mm. They are both anti-reflection coated at a wavelength of 866 nm corresponding to the $3d^2D_{3/2} \leftrightarrow 4p^2P_{1/2}$ transition in ^{40}Ca, with mirror M_1 being partially transmitting (PT) and M_2 being a high reflector (HR). The transmission coefficients are 1500 ppm and 5 ppm, respectively. A construction of two titanium end-walls, separated by low expansion ceramics, is used to hold the mirrors in position. While the HR mirror is directly fixed to the titanium plate, a set of three piezo electric actuators (PZT) is holding a small titanium plate, on which the PT mirror is mounted, to allow for scanning or actively stabilizing the cavity length. The cavity is in a close to confocal geometry with a length of 11.8 mm, corresponding to a free spectral range of $\nu_{FSR} = 12.7$ GHz and a waist of the fundamental TEM_{00} mode of $w_0 = 37\mu$m.

The cavity field decay rate was measured to be $\kappa = 2\pi \times (2.1 \pm 0.1)$ MHz, corresponding to a finesse of $\mathcal{F} = 3000 \pm 200$ at a wavelength of 866 nm [120].

4.6. Overlapping cavity and trap axis

For the purposes of CQED a good alignment of the cavity axis and the axis of the quadrupole trap, given by the field-free nodal line of the RF potential, is necessary to achieve the best overlap between cavity field mode and the ion Coulomb crystals. In practice, it can be difficult to achieve a precise positioning of all the elements beforehand and it is therefore desirable to have a method for correcting possible misalignments once the trap is assembled.

In principle, additional DC potentials on some of the trap electrodes could be used to translate the crystals along the radial directions to optimize the overlap with the cavity mode. This would, however, move the revolution axis of the crystal away from the field-free nodal line of the RF-trapping potential. The solutions to the Mathieu equation found in eq. (2.6) would accordingly have to be changed and, for an radial offset of $(\tilde{x}_0,\ \tilde{y}_0)$, would read

$$\begin{aligned} \tilde{x}(t) &= (\tilde{x}_0 + \tilde{x}_r \cos(\omega_r t)\left[1 + \frac{q}{2}\cos(\Omega_{RF} t)\right] \\ \tilde{y}(t) &= (\tilde{y}_0 + \tilde{y}_r \cos(\omega_r t)\left[1 - \frac{q}{2}\cos(\Omega_{RF} t)\right]. \end{aligned} \tag{4.1a}$$

As a consequence, the amplitude of the quiver micromotion would be non-zero even if the secular motion was completely suppressed. This so-called excess micromotion has an amplitude of $\frac{1}{2}u_0 q,\ (u = \tilde{x}, \tilde{y})$ and can be substantial even for small displacements. It might lead to RF heating and, subsequently, to significant broadening of the linewidth of the atomic transitions and other undesirable effects.

It is therefore desirable to find a general scheme to directly control the position of the potential minimum of the radial pseudo-potential. A solution is to change the loads of the individual trapping electrodes by adding additional capacitors in parallel or in series with the electrodes. A schematic drawing is shown in fig. 4.7, the method is described in more details in [119] or [80].

In short, the method relies on the selective modification of the resonance conditions for the twelve individual electrodes, which are coupled to the RF-power supply through a 1:10 ferrite toroid transformer. Each electrode forms a LRC resonance circuit, with a capacitance C formed by the circuit and the cables and an inductance L mainly set by the transformer. The electrodes themselves have a capacitances C_t. A schematic drawing of the circuits is shown in fig. 4.7. The two opposite phases of the RF are produced by two separate circuits, both connected to the same RF source, but with the windings around the transformer coil in opposite directions. The capacitance of the circuit is measured to be $C = 2.2$ nF, each trap electrode has a capacitance of $C_t \simeq 40$ pF and the voltage on the electrode is hence given by $U_e = U_{\text{in}}/(1 + C_t/C)$. By changing the effective capacitance of the electrodes by additional serial and parallel loads, C_s and C_p, the RF-amplitude on the electrode U_e can be attenuated, as indicated on fig. 4.7.

Modifying the capacitive loads on the different chains might also lead to a change of the resonance frequency or to undesired phase shifts between the RF-fields. This effect can, however, be compensated for by an appropriate combination of parallel and serial loads and in the limit $C \gg C_t, C_p, C_s$, the resonance frequency and the relative phases can be kept nearly constant for the right ratio of C_p and C_s.

After the assembly of the trap an offset of $\simeq 90$ μm in the $x-z$-plane and of $\simeq 80$ μm in the $y-z$-plane were measured from projection images. Using the technique of moving the minimum of the RF-potential described here, the trap and cavity axis could be overlapped to within ± 1 μm [80, 119].

To show that moving the minimum of the RF potential by ~ 100 μm with our technique has no significant effect on the RF heating as compared to the unmodified circuit and that in both situations the ion Coulomb crystal are well described by the zero temperature charged liquid model introduced in sec. 2.3.2 we performed calibration measurements in both situations, as will be discussed in the following section. A precise method to measure the radial offset between cavity and trap axis will be presented in sec. 6.4.

4.7. Calibration of the trap

In sec. 2.3.2 a thermodynamical description of ion Coulomb crystals in the framework of a zero temperature charged liquid plasma model was introduced. Based on this model, an expression for the ion density in the ensemble was found in eq. (2.15), which solely depends on the RF-amplitude of the trapping potential. In practise, the amplitudes seen by the ions will depend on the actual circuit supplying the voltage to the electrodes, making it difficult to directly measure them. Furthermore, this attenuation might be modified by

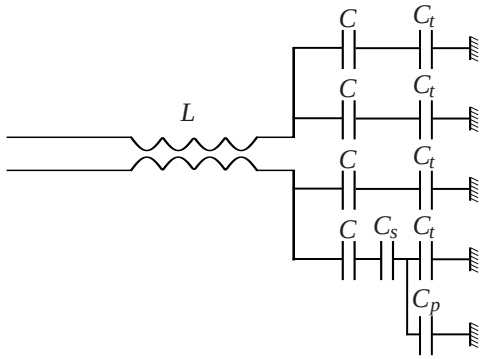

Figure 4.7.: Moving the minimum of the RF potential. The electrodes have a capacitance C_t and are connected to the RF-supply through a toroidal transformer with inductance L. The capacitive load of the remaining circuit is represented by the capacitances C. The field free nodal line of the RF potential can be moved by attenuating the RF-amplitude on selected electrodes by applying additional serial and parallel capacitance C_s and C_p, without substantially changing the resonance frequency and the relative phases.

the additional capacitances used to overlap cavity and trap axis, as was described in the previous section. A calibration of the trap voltages can however be accomplished on the basis of the plasma model and molecular dynamics calculations, as explained in sec. 2.3.2. We will in the following describe the two independent calibration methods.

The first method is based on the zero temperature charged liquid plasma model introduced in sec. 2.3.2. This model allows to relate the aspect ratio of the ion Coulomb crystals to the ratio of the trap frequencies, see eq. (2.24), which on the other hand also can be deduced from the trapping parameters, see eq. (2.25). The aspect ratios can be precisely measured from projection images, as was explained in sec. 4.4. From this we can deduce the ratio of the trap frequencies by eq. (2.24) for different trapping parameters. As the ratio of the trap frequencies also depends on the trapping parameters, we can fit them using a modified version of (2.25)

$$\frac{\omega_z}{\omega_r} = \sqrt{\frac{\alpha^2 U_{\mathrm{RF}}^2 z_0^2 Q}{4\eta M \Omega_{\mathrm{RF}}^2 (U_{\mathrm{DC}} - U_{\mathrm{off}}) r_0^4} - \frac{1}{2}} \tag{4.2}$$

to deduce an attenuation factor α for the applied RF-amplitude U_{RF} and an offset U_{off} for the axial DC-potential, which might be caused e.g. by charging effects on the cavity mirrors.

The second method uses the dependence of the inter-shell spacing for long ion Coulomb crystals on the trapping voltages, see eq. (2.26). Here, the spacing of neighboring shells has to be deduced from projection images (see sec. 4.4) and is fitted by

$$\delta_r = 1.48 \times \left(\frac{3 r_0^4 M}{4\pi\varepsilon_0} \frac{\Omega_{\mathrm{RF}}^2}{\alpha^2 U_{\mathrm{RF}}^2} \right)^{1/3} \tag{4.3}$$

where 1.48 is a constant found from molecular dynamics calculations and α again accounts for a possible attenuation of the RF amplitude.

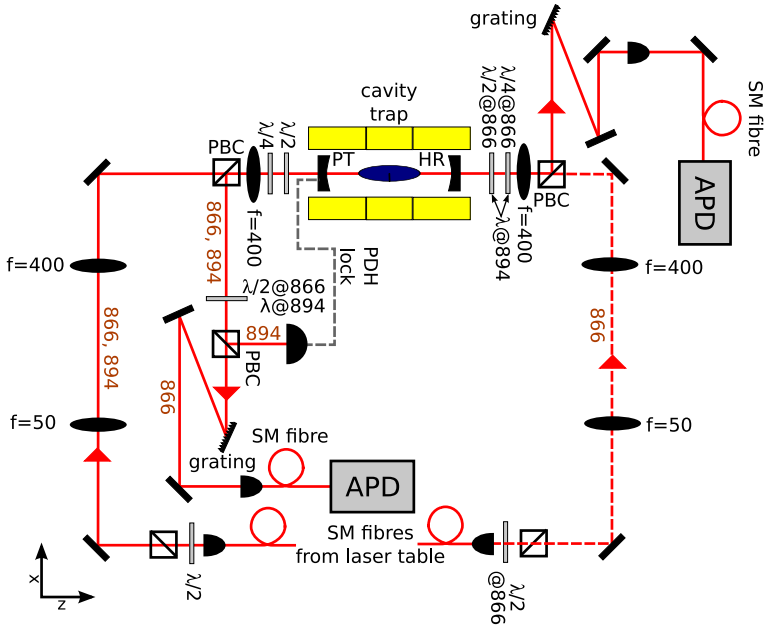

Figure 4.8.: Schematic setup of the cavity detection system. The beam path of the 866 nm probe laser when injected in transmission is indicated by the dashed line. (PBC), single mode (SM), Pound-Drever-Hall lock (PDH lock).

It is worth noticing that the first method only relies on the aspect ratio of the crystal and hence does not depend on any calibration of the length scale, whereas the measurement of the inter-shell spacing requires such a calibration. The second method might hence serve as cross-check to test the validity of the model or, assuming the correctness of the numerical pre-factor of 1.48, to check the calibration of the trap and the imaging system.

More details on the two methods can be found in [119] and [80].

4.8. Probing the cavity

In this section, the laser systems and detection setup used to probe the ion-cavity interaction will be described. A schematic drawing of the setup is shown in fig. 4.8.

4.8.1. Probe and reference lasers

Probe laser

A second external cavity diode laser at 866 nm is used to probe the interaction of the coupled ion Coulomb crystal-cavity system. We will in the following refer to this laser as the ”probe-laser”[7]. The setup of the diode laser is similar to the one used for repumping and optical pumping. It is frequency locked to the same temperature stabilized reference

[7] In ch. 8 this laser will also be used as the control laser to realize cavity electromagnetically induced transparency.

cavity in a Pound-Drever-Hall configuration, the frequency can be tuned using a double pass AOM by ± 100 MHz. As the laser is used to probe the coupled atom cavity system, the linewidth of the laser should be narrower than both the atomic dipole decay rate of $\gamma = 2\pi \times 11.2$ MHz and the decay of the cavity field at a rate of $\kappa = 2\pi \times 2.1$ MHz. It was measured in a self-heterodyne setup to be 107 ± 2 kHz when locked to the reference cavity [80].

On the trap table, two independent setups can be used to couple the probe light into the cavity either from the PT or the HR side. On the laser table, a flip mirror is used to switch the light between two separate single mode fibers guiding the light to the two setups. Before the fiber incouplers, a single pass AOM is used to shutter the beam, with the -1^{st}-diffraction order being sent to the fibers when switched on. The on-off attenuation after both fibers is > 55 dB.

The optical setup after the two fiber outcouplers will be described in sec. 4.8.2 in connection with the single photon detection scheme.

Reference laser

An additional diode laser with a wavelength of 894 nm is used during the cavity QED experiments and serves, depending on the measurements, two different purposes. Its wavelength is not resonant with any transition of $^{40}Ca^{+}$ to suppress a direct interaction of this laser with the ions. The laser is frequency locked together with the two diode lasers at 866 nm to the same reference cavity and also tunable by means of a double pass AOM before the reference cavity. The resulting linewidth was measured to be 85 ± 5 kHz [80]. Despite the narrow linewidth, the light emitted from the diode in single mode operation still contains a non-negligible contribution of photons at the wavelength of the $3d^2D_{3/2} \leftrightarrow 4p^2P_{1/2}$ at 866 nm. As this would substantially disturb the measurements, the light of the 894 nm laser is spectrally filtered with a diffraction grating (1800 lines/mm). The light is overlapped with the beam path of the probe laser to the PT-side on the laser table and sent through the same optical fiber.

When scanning the length of the cavity, the transmission level of the 894 nm laser can be monitored and the position of the transmission peak serves as a frequency reference for the cavity and gives information on cavity drifts and acoustic vibrations. The second possibility is to use the reference laser to lock the length of the cavity in a Pound-Drever-Hall scheme. Both methods will be described and discussed in more details in sec. 4.8.3

4.8.2. Cavity light detection

Due to the low light levels used for probing the ions, the detection of the reflected/transmitted photons is performed by two avalanche photo detectors (APDs). The first APD (probe-APD) is installed on the PT side of the cavity, to monitor the signal of the cavity probe. As mentioned above, the probe laser can be injected into the cavity both from the PT and the HR side, and the corresponding probe signal will, depending on the incoupling, be measured in reflection and transmission.

The first configuration, where the probe laser is injected through the PT mirror, is used in most experiments and the probe and reference beam are in this case guided to the trap table through the same polarization maintaining fiber. After the fiber a $\lambda/2$ wave-

plate and a PBC are used to ensure a well-defined linear polarization. The beam size is modematched to the cavity by a telescope and a focusing lens. Before the focusing lens, a polarizing beam splitter cube (PBC) separates the cavity reflection from the incident beam. A $\lambda/4$-waveplate transforms the polarization of the probe light to σ^--polarization and an additional $\lambda/2$-waveplate allows for small corrections of the polarization direction with respect to the quantization axis. Both waveplates can also be used to pre-compensate birefringence effects, e.g. induced by the cavity mirrors. Typical coupling efficiencies to the fundamental TEM_{00} mode are $> 95\%$.

The light reflected from the cavity is separated from the incident beam on the PBC and a higher-order waveplate (λ@894 nm, $\lambda/2$@866 nm) is used to also separate the probe and the reference laser on a second PBC, where the 894 nm light is reflected of to a photodetector or to the Pound-Driver Hall locking detector and the 866 nm light is transmitted.

Though the transmission of 894 nm light is suppressed by ~ 20 dB, the 866 nm probe light has to be spectrally filtered on a diffraction grating with 1800 lines/mm to remove any residual photons at 894 nm from the beam. It is then coupled to a single mode fiber guiding the light to the probe APD. Taking the efficiency of the APD at 866 nm ($\sim 44\%$), of the grating ($\sim 63\%$), the fiber coupling ($\sim 65\%$) and the optics ($\sim 90\%$). into account, the detection efficiency of the probe photons amounts to 16% [80].

The transmitted light on the HR side passes a combination of a $\lambda/4$ and a $\lambda/2$-waveplates at 866 nm leaving the polarization of the 894 nm unchanged. A fraction of the reference light will be reflected off the following PBC and is, after spectral filtering on a diffraction grating (1800 $^{lines}/_{mm}$), it is coupled to the second APD (reference APD). When the probe light is sent to the cavity from this side, the two waveplates are used to adjust the polarization of the incident beam.

4.8.3. Scanning and locking of the cavity

As abovementioned, the 894 nm reference laser may either serve as a frequency reference when scanning the cavity length or to lock the resonance frequency of the cavity. The two procedures will be described in more detail in this subsection.

Scanning the cavity

In several experiments described in this thesis, the length of the cavity is continuously scanned over the resonance at a rate of 30 Hz by a triangle-voltage with an amplitude corresponding to ~ 1.3 GHz. In these experiments, the cavity reflection (or transmission) spectrum is measured by repeatedly probing the reflected (or transmitted) fraction of the probe laser by the APD at typical rates of ~ 50 kHz, with integration times for the probe APD of the order of ~ 1 μs. As we want to investigate the light-matter interaction at the quantum limit, we work with mean intracavity photon numbers $\lesssim 1$. With a cavity decay rate of $2\kappa = 2\pi \times 4.2$ MHz this corresponds to at most 9 photons leaking out of the cavity during a ~ 1 μs probe interval, of which, taking the overall detection efficiency into account, only 16 % will be detected. To reconstruct the cavity spectrum, one therefore has to average over several scans, typically a few hundreds.

It turned out that the cavity mirrors are sensitive to acoustic vibrations and some mechanical resonances could be identified by deliberately exciting the vibrations. The most dominant were found around 400 Hz and 2 kHz, however, their actual frequency depends

on the voltage applied to the piezo actuators. As the frequency of this noise is faster than the rate at which the cavity length is scanned, the mechanical vibrations will slightly change the position of the cavity resonance from scan to scan, making it impossible to directly average the weak probe signal. To compensate for these vibrations and other mechanical drifts, the 894 nm laser is used as a frequency reference in these experiments. When the frequency of the reference laser is set such that the cavity is resonant for both lasers for the same cavity length, the effect of mechanical drifts on both signals will be directly correlated. For a sufficiently strong reference field, the position of the cavity resonance for the 894 nm laser can be identified on each individual scan and one can use it to shift the two signals such that the resonance peaks of the reference overlap on the different scans. As the transmission of the reference is measured with an APD, injecting the cavity with less than 1 nW is sufficient to accomplish this without influencing the state of the ions. The referencing to the 894 nm laser was tested by reconstructing the spectrum of the empty cavity, which can be independently measured with a strong probe field on a single scan, see [80].

Locking the cavity

A second measurement technique uses a cavity that is locked to the resonance frequency of the atomic transition. In these experiments, the 894 nm laser is used to actively stabilize the cavity length by appropriate feedback to the PZTs. Its frequency is set such that it overlaps on the cavity scan with a 866 nm laser resonant with the atomic transition. The reflected reference signal is then sent to a Pound-Drever-Hall lock and used to stabilize the cavity length. Though a slightly higher incident power of the reference laser is necessary as compared to the scanning of the cavity, the locking can be accomplished with input powers of the order of ~ 30 nW, corresponding to a mean intracavity photon number of $5 \cdot 10^4$.

The acoustic noise also perturbs the measurements in this scheme substantially. An active stabilization of the cavity is rendered difficult, as there are several mechanical resonances which, depending on the relative phase used in the feedback loop, can be driven easily by the stabilization. Instead of stabilizing the cavity against all mechanical vibrations, the feedback is optimized for frequencies lower than the lowest resonance at around 400 Hz and we use the transmitted signal of the reference laser to post-compensate the related fluctuations of the probe signal. Again, the acoustic noise on the two signals should be correlated and a drop of the transmitted reference signal monitored by the APD indicates that the cavity is no longer resonant with the 894 nm laser. The data is then simply filtered by setting an appropriate threshold for the reference APD signal and only keeping the data points for which the reference level exceeded the threshold. Obviously, this reduces the amount of usable data, but ensures that the cavity was resonant for the remaining data points. The method was tested for an empty cavity and the influence of different threshold values was examined, for details see [80].

4.9. Data acquisition

The whole data acquisition process is controlled by a LabView software interface using two synchronized timing and digital I/O modules[8]. The acousto-optical modulators used to shutter the different laser beams are controlled by digital TTL signals, the signals of the APDs and the PMT are directly registered by counters provided by the I/O cards. The software interface allows for the adjustment of the on/off phases of the lasers and the integration times of the APDs and the PMT. Included in the software are also the necessary routines to perform the acoustic noise compensation by referencing the probe to the reference signal when scanning the cavity and the post-data selection based on a certain threshold for the transmitted reference level for a locked cavity. Details can be found in [80].

[8] National Instruments PCI-6602

5. Realization of collective strong coupling

This chapter contains a detailed description of the experimental realization of the collective strong coupling regime with ion Coulomb crystals interacting with the fundamental TEM_{00} cavity field mode. Some of the experiments (secs. 5.3-5.6) were already described in great detail in the PhD thesis of my predecessor Peter Herskind [80]. For the sake of completeness and comprehensibility the major results will, however, be reviewed in this thesis and extended by subsequent studies and measurements.

The chapter is structured as follows: In sec. 5.1 we give a short introduction to the experiments. In sec. 5.2 we will explain in more detail how the effective number of ions is determined in the experiment. Sec. 5.3 will then introduce the experimental sequence. In sec. 5.4 and 5.5 the measurements of the collective coupling rate by different methods are presented. Sec. 5.6 shows experimental measurements of how the collective coupling rate scales with the number of interacting ions. In sec. 5.7 and sec. 5.8 measurements of the coherence time of the collective coherences between Zeeman substates and of the long time stability of the coupling are presented. Finally, sec. 5.9 gives a summary and an outlook.

5.1. Introduction

A central challenge in experimental cavity quantum electrodynamics is to reach a regime where the coherent interaction of a matter system with a cavity light field can be made faster than the dissipative processes. For a single material two-level system this so called strong coupling regime [144] is reached, when the rate, g, at which single excitations are coherently exchanged between the two-level system and the light mode exceeds the spontaneous emission rate of the two-level system, γ, and the cavity field decay rate, κ. It was first realized with atoms in microwave and optical cavities [61, 145], and has recently been realized with quantum dots [133, 146] and superconducting Josephson junctions [132, 147].

For an ensemble of N identical two-level systems simultaneously interacting with a single mode of the electromagnetic field, the coherent coupling rate is enhanced by a factor $\sqrt{N}$ and the coherent process dominates when the collective coupling rate

$$g_{\mathrm{N}} = g\sqrt{N} \tag{5.1}$$

is larger than both κ and γ. This so-called collective strong coupling regime [58] was first explored with Rydberg atoms in microwave cavities [60], and has since then been realized in the optical domain with atomic beams [61], atoms in magneto-optical traps [62–65] and Bose-Einstein condensates [66, 67].

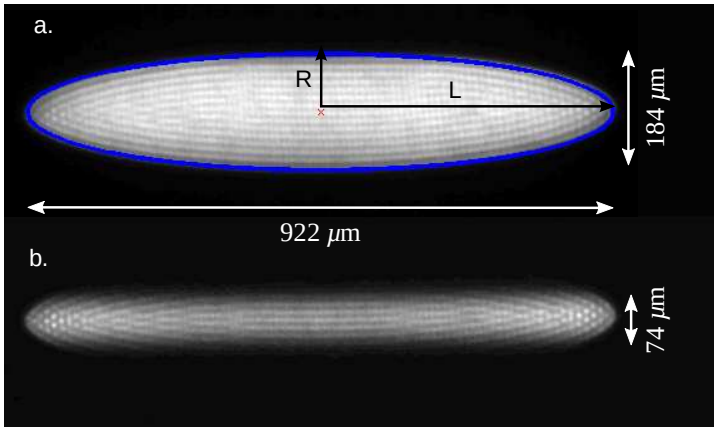

Figure 5.1.: Projection image of a crystal used in the collective strong coupling measurements. The trap was operated at a RF voltage of $U_{\mathrm{RF}} \sim 300$ V, corresponding to a density of $\rho_0 = (5.4 \pm 0.1) \cdot 10^{10}\mathrm{cm}^{-3}$. The crystal contains $N_{\mathrm{tot}} = 8780 \pm 180$ ions, of which $N = 504 \pm 10$ effectively interact with the cavity field. **a.** All ions are exposed to cooling and repumping light. **b.** Same crystal, but only the ions in the cavity mode are exposed to repumping light, now injected into the cavity. The ions outside the cavity modevolume are shelved into the metastable $3\mathrm{d}^2\mathrm{D}_{3/2}$ level and not visible.

In the optical domain, the use of ultra-high-finesse cavities with very small modevolumes allows for reaching the confinement required to achieve strong coupling with single neutral atoms [128, 131, 144]. With charged particles, however, the insertion of dielectric mirrors in the trapping region makes it extremely challenging to obtain sufficiently small cavity modevolumes, due to the associated perturbation of the trapping potentials and charging effects. Although many groups are currently making rapid progress in this direction, the strong coupling regime has not been reached with single ions yet [68–74]. Our group could recently demonstrate that the collective strong coupling regime can be realized with large ion Coulomb crystals [79, 148]. The results of these experiments will be presented in this chapter.

5.2. The effective number of ions

In sec. 3.2.4 it was mentioned that not all ions in large ion Coulomb crystals contribute equally to the collective coherent coupling and that their respective contributions have to be weighted by the intensity of the intracavity field at the position of the ions. In eq. (3.45) the effective number of interacting particles was defined as the weighted sum over all these contributions. As the ion density is constant throughout the whole ion Coulomb crystal (see eq. (2.15)) and can be calculated from the amplitude of the RF-field amplitude applied to the trapping electrodes, the effective number of ions can directly be determined from the overlap between the volume occupied by the ion Coulomb crystal and the cavity modevolume. The geometrical size of the crystal is found by taking fluorescence images of the crystal during cooling, as shown in Fig. 5.1, from which the crystal half-length L

and radius R can be extracted. The density can be extracted from the calibration of the RF voltage as explained in sec. 4.7. In all experiments presented in this chapter the coupling of ion Coulomb crystals to the fundamental TEM_{00} cavity field mode was investigated. The effective number of ions interacting with the TEM_{00} mode is then calculated using the formula

$$N = (\rho_0/2)\int_V dxdy\ \exp(-2[(x-x_0)^2+(y-y_0)^2]/w_0^2) \tag{5.2}$$

where x_0 and y_0 allow for an radial offsets between the cavity axis and the crystal revolution axis. These offsets can in principle be canceled to within a μm, as was discussed in sec. 4.6. In ch. 6.4 we will present a precise way to determining these offsets, which for the experiments presented in this chapter, were measured to be $x_0 = 3.9\ \mu$m, $y_0 = 15.7\ \mu$m. The uncertainty in the effective number of ions comes from both the uncertainty $\delta\rho_0$ in the density determination, due to the RF voltage calibration, and the uncertainty in the crystal volume δV, due to the imaging resolution δx. The relative uncertainty in the number of ions, $N = \rho_0 V$, can be expressed as

$$\frac{\delta N}{N} = \sqrt{\left(\frac{\delta\rho_0}{\rho_0}\right)^2 + \left(\frac{\delta V}{V}\right)^2} \tag{5.3}$$

where the uncertainty on the crystal volume is given by the uncertainty on the determination of the half-length and the radius from the projection images. It is given by

$$\delta V/V = \delta x\sqrt{16L^2+R^2}/2RL \tag{5.4}$$

For a typically prolate crystal as used in many of these experiments, with a half-length of $\sim 1-2$ mm and an imaging resolution $\delta x \sim \mu$m, this results in a relative uncertainty of $2-4\%$ in the effective number of ions.

Figure 5.1 a. shows a projection image of a typical crystal used for the measurements presented in this chapter. Since the crystal radial extension is larger than the cavity waist ($w_0 = 37\ \mu$m), only the ions which are positioned inside the cavity mode volume will noticeably contribute to the coupling. A visual impression of the overlap of the cavity mode with the ion crystal can be obtained by coupling the repumping laser to the TEM_{00} mode of the cavity. Only the ions inside the cavity mode interact with the repumper laser and the ions outside the cavity light field are subsequently shelved into the metastable $3d^2D_{3/2}$ level, which has a lifetime of ~ 1 s. Hence, only the ions inside the mode volume will contribute to the cooling and fluorescence, while the ions in the metastable state appear dark. This is illustrated in fig. 5.1 b. Such pictures can also be used to deduce the offset between the RF field free axis of the trap and the symmetry axis of the cavity [119] (see sec. 4.6). The same technique can in principle also be used with the side camera, albeit with a lower precision, due to the limited resolution. A more precise way of measuring the relative offset between the cavity mode and the crystal axis will be presented in sec. 6.4.

5.3. Experimental sequence

In the description of the experimental setup in the previous chapter it was mentioned in sec. 4.8.3 that the coherent coupling between the crystal and the cavity field can be

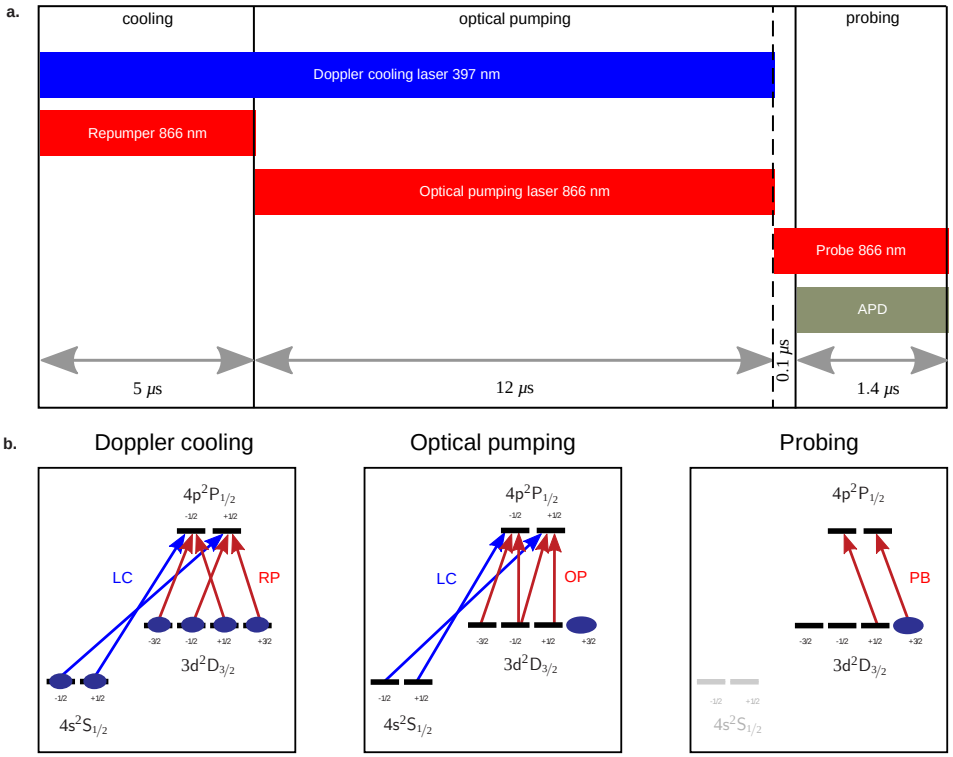

Figure 5.2.: a. Experimental sequence used to measure the collective coupling rate. **b.** Energy levels of $^{40}Ca^{+}$ including the relevant transitions addressed in the three parts of the experimental sequence. The acronyms are: LC: laser cooling beam, RP: repumping beam, OP: optical pumping beam, CB: control beam, PB: probe beam.

measured in two different ways, by either scanning or locking the cavity. In both configurations the cavity reflection spectrum is measured at a typical rate of 50 kHz using a 20 μs sequence consisting of Doppler cooling, optical pumping and probing. This sequence is shown in fig. 5.2 a. and the level schemes in fig. 5.2 b. indicate the transitions which are addressed by the several lasers during the cooling, optical pumping and probing phases.

Cooling In the first 5 μs of each sequence the ions are Doppler laser cooled on the $4s^2S_{1/2} \leftrightarrow 4p^2P_{1/2}$ transition, while a repumping laser resonant with the $3d^2D_{3/2} \leftrightarrow 4p^2P_{1/2}$ transition prevents shelving to the metastable $3d^2D_{3/2}$ state. With optimized cooling parameters typical temperatures of the crystals are in the few 10 mK range.

Optical pumping After the cooling a 12 μs period of optical pumping transfers the ions to the $m_j = +3/2$ magnetic substate of the $3d^2D_{3/2}$ level.

The optical pumping laser is resonant with the $3d^2D_{3/2} \leftrightarrow 4p^2P_{1/2}$ transition and has a polarization consisting only of σ^+- and π-polarized components. It is sent to the trap under an angle of 45° with respect to the quantization axis (see sec. 4.3.2). At the same time the Doppler cooling laser is applied to pump the population decaying to the $4s^2S_{1/2}$ ground state back to the metastable $3d^2D_{3/2}$ level.

The efficiency of the state preparation has previously been measured by selectively probing the population in the different Zeeman sublevels. This can be accomplished by injecting a strong probe pulse with either σ^- or σ^+ polarization into the cavity after the state preparation and measuring the fluorescence on the $4s^2S_{1/2} \leftrightarrow 4p^2P_{1/2}$ transition with the PMT. The probe will address the population in either the $m_J = {}^{+1}/_2,\ {}^{+3}/_2$ states (σ^--probe) or the $m_J = {}^{-1}/_2,\ {}^{-3}/_2$ states (σ^+-probe) and will pump the population in these states to the excited $4p^2P_{1/2}$ level, from where the ions with a probability of $\sim 12:1$ decay to the $4s^2S_{1/2}$ ground state. As all other lasers are turned of, each ion will emit at most one photon on this transition and the fluorescence level directly reflects the population in the addressed states. Sending the probe laser along the transverse *x*-direction and choosing the appropriate polarization furthermore also allows for the probing of the population in the $m_J = {}^{\pm 1}/_2$ state. Repeating these experiment with and without optical pumping and probing with both polarizations allows for the estimation of the optical pumping efficiency, which was found to be 97^{+3}_{-5}% [80].

Furthermore, a similar technique can be used to measure the lifetime of the collective population in the $m_j = {}^{+3}/_2$ state in the cavity mode. This is accomplished by gradually increasing the delay between the state preparation and the σ^- polarized probe pulse sent to the cavity and measuring the decrease of the fluorescence level as a function of delay. As a cross-check, one can also measure the population increase in the $m_j = {}^{-1}/_2,\ {}^{-3}/_2$ state as a function of delay using the same technique with opposite circular polarization. Both measurements agree very well and comparing them we deduced a lifetime of the population of $T_1 = (13 \pm 3)$ ms, for details see [80]. Several factors might be attributed to the finite life time. First of all, as we only measure the population in the cavity mode, ions diffusing from other parts of the crystal into the mode volume might lead to a decrease of the measured population in the addressed Zeeman substates, especially if the crystal heats up with increasing delays. Another possible cause for decay might be the presence of a non-zero transverse *B*-field which would lead to population transfer to other Zeeman substates. Finally, the finite lifetime of the $3d^2D_{3/2}$ of ~ 1 s will eventually limit the

achievable lifetime of the population, though it should play only a minor role on the measured timescales of the decay.

Probing Finally, after the state preparation, the cavity reflection signal is probed by injecting a 1.4 μs σ^--polarized probe pulse, resonant with the $3d^2D_{3/2} \leftrightarrow 4p^2P_{1/2}$ transition, into the TEM_{00} mode of the optical cavity. Its intensity is set such that the mean intracavity photon number (for an empty cavity) is less than one at any time. With a delay of 0.1 μs relative to the probe laser, the APD is turned on. The delay ensures that the field has built up inside the cavity and that the system has reached a quasi-steady state. The duration of the probing period was chosen so as to minimize the total sequence length as well as to avoid depopulation due to saturation of the transition [80].

5.4. Absorption profile and resonance shift

In sec. 3.2.4 we derived an expression for the linear susceptibility χ of the ion ensemble interacting with a single cavity field mode, see eq. (3.41). The atomic absorption and dispersion modifies the effective cavity linewidth and detuning according to (see eq. (3.48))

$$\begin{aligned} \kappa' &= \kappa + \mathrm{Im}(\chi) = \kappa + g_N^2 \frac{\gamma}{\gamma^2 + \Delta^2} \\ \Delta_C' &= \Delta_C - \mathrm{Re}(\chi) = \Delta_C - g_N^2 \frac{\Delta}{\gamma^2 + \Delta^2}. \end{aligned}$$

These two relations both depend on the square of the collective coupling rate g_N and hence provide two methods to investigate the coherent coupling of the ions with the cavity field. We first perform measurements of the atomic absorption and dispersion for a given crystal with $N \sim 500$, which according to eq. (3.36) should be sufficient to enter the collective strong coupling regime. The crystal used in these experiments is similar to the one shown in Fig. 5.1. With a density of $\rho_0 = (5.4 \pm 0.1) \times 10^8$ cm^{-3} , half-length $L = (511 \pm 1)$ μm and radius $R = (75 \pm 1)$ μm the total number of ions in the crystal is calculated to be $N_{tot} = 6500 \pm 200$ and the effective number of ions is $N = 536 \pm 18$ (see eq. (5.2)). The broadening and the shift of the cavity resonance are then measured as a function of the detuning of the probe laser, Δ. This is accomplished by scanning the cavity length over a range corresponding to ~ 1.3 GHz at a repetition rate of 30 Hz, for a fixed value of Δ. The reflection is reconstructed by sampling each cavity scan repeating the sequence shown in fig. 5.2 at a rate of 50 kHz.

The width of the reflection dip for a given detuning Δ is found by averaging over 100 cavity scans, where the reference laser is used to compensate for drifts of the cavity and acoustic noise, as was explained in sec. 4.8.3. In Fig. 5.3 various cavity reflection scans are plotted for different detunings. Each data point corresponds to the average of 100 20 μs-measurement sequences as showed in Fig. 5.2. For each detuning, several of these reflection spectra are taken, and for each the effective cavity decay rate κ' is found by fitted the data with the expected Lorentzian lineshape given in eq. (3.47a). As expected from Eq. (3.48a), the broadening of the intracavity field absorption reflects the two-level atomic medium absorption. Fig. 5.4 shows the modified cavity HWHM, κ', as a function

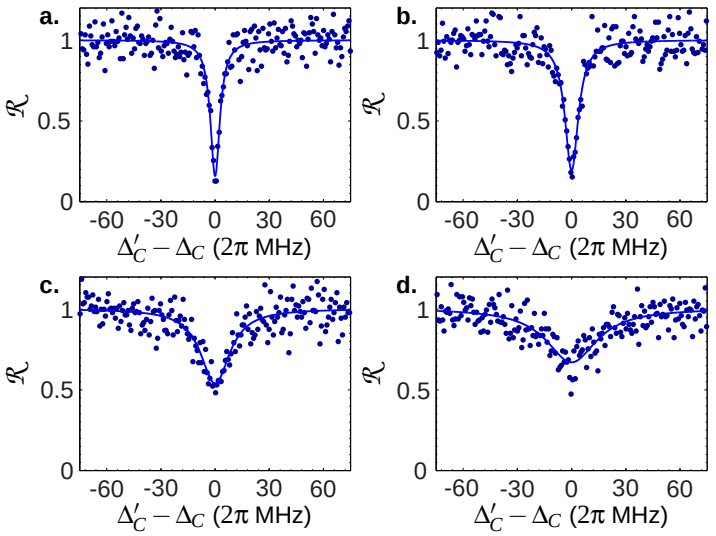

Figure 5.3.: Typical cavity reflection scans for various values of the atomic detuning Δ. The probe detunings were a. $\Delta \approx 2\pi \times 54.3$ MHz, b. $\Delta \approx 2\pi \times 24.3$ MHz, c. $\Delta \approx 2\pi \times 8.3$ MHz and d. $\Delta \approx 2\pi \times 0.3$ MHz. Solid lines are Lorentzian fits to the data, the effective cavity field decay rate κ' is deduced from the fit.

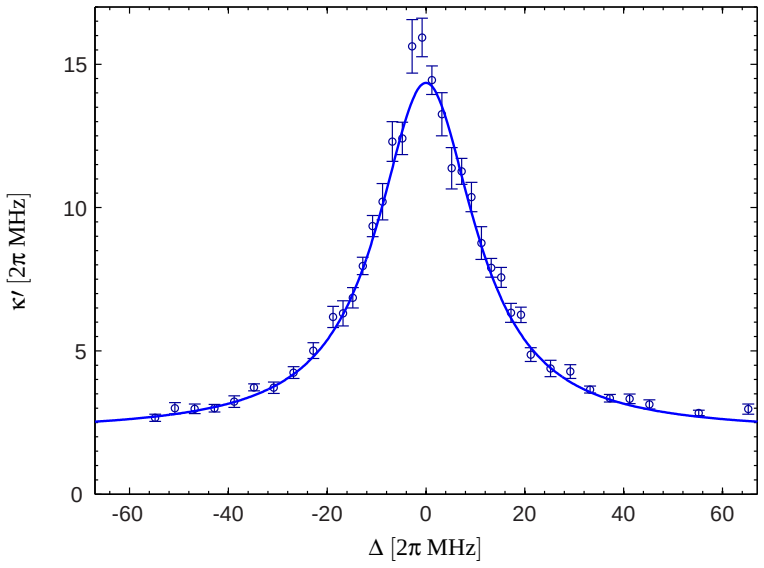

Figure 5.4.: Measured cavity field effective decay rate κ' versus probe detuning Δ for a crystal with $N = 536 \pm 18$ ions interacting with the cavity field and an optical pumping efficiency of 97%. The blue solid line is a fit to the data using eq. (3.48a).

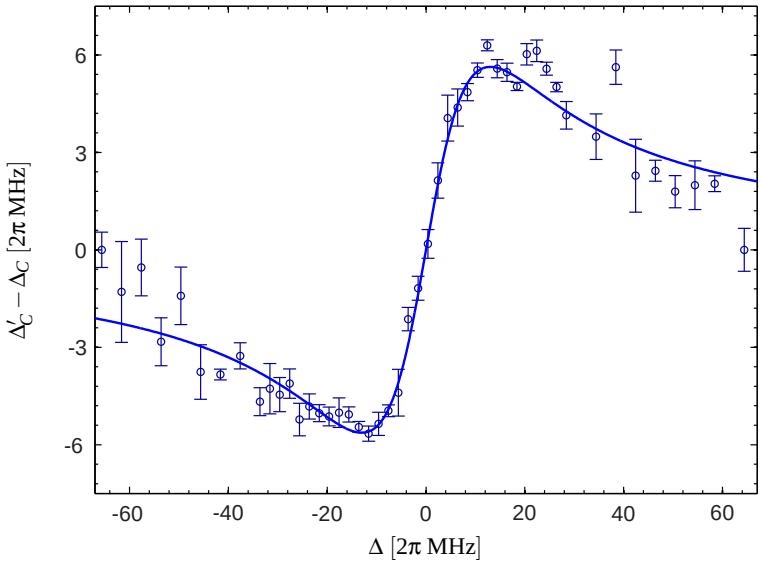

Figure 5.5.: Measured phase shift $\Delta_c' - \Delta_C$ versus atomic detuning Δ for the same crystal. The blue line is a fit to the data using eq. (3.48b).

of detuning of the probe laser, Δ. Each point is the average of 5 measurements, the solid line is a fit according to Eq. (3.48a). From the fit we deduce a collective coupling rate of $g_N = 2\pi \times (12.2 \pm 0.2)$ MHz, in good agreement with the theoretical expectation of $g_{N,\text{theory}} = 2\pi \times (12.1 \pm 0.3)$ MHz, calculated for $N = 536 \pm 18$ ions interacting with the cavity mode, an optical pumping efficiency of 97^{+3}_{-5}% [79, 80] and a single ion coupling rate of $g_{\text{theory}} = 2\pi \times (0.532 \pm 0.007)$ MHz, see eq. (3.37). Furthermore, the effective dipole decay rate γ' is left as a fit parameter to account for finite temperature effects, as discussed in sec. 3.3, eq. (3.51a). The fit yields $\gamma' = 2\pi \times (11.9 \pm 0.4)$ MHz, which, according to Fig. 3.6, would correspond to a likely temperature of $T = 24^{+20}_{-14}$ mK. The natural half-width of the cavity is also left as fitting parameter and we find $\kappa = 2\pi \times (2.2 \pm 0.1)$ MHz, in good agreement with the value deduced from an independent measurement of the FSR and the finesse of the cavity, $\kappa = 2\pi \times (2.1 \pm 0.1)$ MHz [120].

For the measurement of the effective cavity detuning, Δ_c', the frequency of the 894 nm laser is kept at a fixed position in the cavity scan, e.g. to the atomic resonance frequency. The frequency shift is then measured by comparing the position of the probe and the reference signal resonances in the cavity scan. The effective cavity detuning as a function of probe detuning is shown on Fig. 5.5. One observes the expected dispersive frequency-shift corresponding to the real part of the linear susceptibility of a two-level system probed in the low saturation regime, see eq. (3.48b). The data is fitted to the theoretical model according to Eq. (3.48b) and yields a collective coupling rate of $g_N = 2\pi \times (12.0 \pm 0.3)$ MHz and an effective dipole decay rate of $\gamma' = 2\pi \times (12.7 \pm 0.8)$ MHz. Both values are consistent with the previous measurement and the theoretical expectations. As in the previous measurement, the 894 nm resonance laser is also used to compensate systematic drifts and acoustic vibrations (see sec. 4.8.3). However, since this compensation method relies on the temporal correlations of the drifts in both signals, and thereby on their relative

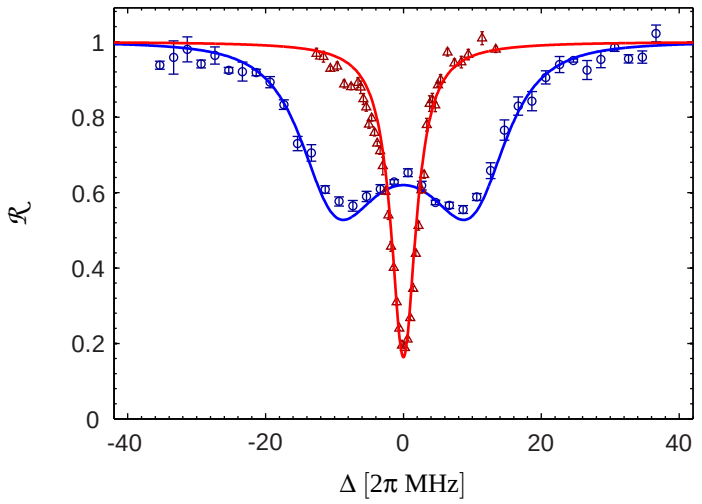

Figure 5.6.: Reflection signal of the probe as a function of $\Delta = \Delta_C$ for the empty cavity (red triangles) and with a crystal with $N = 536 \pm 18$ effectively interacting ions present in the cavity mode volume (blue circles). The solid lines are fits to the theoretical expectation of eq. (3.49).

positions in the cavity scan, the compensation becomes less effective at large detunings. This is reflected in the bigger spread and the larger error bars at larger detunings, which renders this method slightly less precise than the first absorption measurement to evaluate the collective coupling rate.

5.5. Vacuum Rabi splitting spectrum

A third complementary method to measure the collective coupling rate is based on locking the cavity on atomic resonance, $\omega_C = \omega_{at}$, as was described in sec. 4.8.3. Since the coupled atom-cavity system is probed at the single photon level one expects to observe a splitting of the normal-mode as discussed in eq. (3.49), referred to as the vacuum Rabi splitting.

The response of the coupled atom-cavity system is probed as a function of probe detuning Δ, which in this case is equal to the cavity detuning Δ_C. The cavity reflection for a particular probe detuning is found by continuously repeating the sequence shown in fig. 5.2 at a rate of 50 kHz. Here, we use the post data selection technique described in sec. 4.8.3 to keep only the data point for which the cavity was resonant. For each probe detuning, $2 \cdot 10^4$ data points are acquired and averaged. The result of this measurement is shown on Fig. 5.6. The red triangles are obtained with an empty cavity, while the blue circles were taken with the same ion Coulomb crystal as used in the previous experiments. The results are fitted using the theoretical expectations of eq. (3.49b) (solid lines in Fig. 5.6) and yield $g_N = 2\pi \times (12.2 \pm 0.2)$ MHz, a value that is in good agreement with the previous measurements. To facilitate the more complex fitting function to converge γ' and κ were set to the value deduced from the previous absorption measurement.

The collective coupling rates found for the three methods agree within their error bars and when combining the three results, we find $g_{\mathrm{N}} = 2\pi \times (12.16 \pm 0.13)$ MHz.

Conversely, using the measured value for g_{N} and the effective number of ions $N = 536 \pm 18$ extracted from the projection image of the crystal, together with the measured optical pumping efficiency of 97^{+3}_{-5}%, we can now deduce a single ion coupling rate of $g_{\mathrm{exp}} = \frac{g_N}{\sqrt{N}} = 2\pi \times (0.534 \pm 0.010)$ MHz.

This value is in excellent agreement with the expected value of $g_{\mathrm{theory}} = 2\pi \times (0.532 \pm 0.007)$ MHz, calculated according to eq. (3.27) from the knowledge of the cavity geometry and the atomic dipole moment of the considered transition.

5.6. Scaling with the number of ions

To check further the agreement between the theoretical predictions and the experimental data we investigated the dependence of the collective coupling rate on the effective number of ions. An attractive feature of ion Coulomb crystals is that the number of ions effectively interacting with a single mode of the optical cavity can be precisely controlled by the trapping potentials. While the density ρ_0 only depends on the amplitude of the RF voltage (see Eq. (2.15)), the aspect ratio of the crystal depends on the relative trap depths of the axial and radial confinement potentials which can be independently controlled by the DC voltages on the endcap electrodes. This allows for controlling the effective number of ions down to the few ion-level.

5.6.1. Cooperativity parameter

In Fig. 5.7 the dependence of the cooperativity parameter, defined as

$$C = g_{\mathrm{N}}^2 / 2\kappa\gamma', \tag{5.5}$$

is plotted as a function of the effective number of ions interacting with the TEM_{00} mode. The cooperativity was deduced by measuring the effective cavity field decay rate, $\kappa' = \kappa\,(1+2C) = \kappa + \frac{g_{\mathrm{N}}^2}{\gamma'}$, for a probe field tuned to atomic resonance ($\Delta = 0$), and for different aspect ratios and densities of several crystals. The effective number of ions in each crystals was deduced applying the method described in Sec. 5.2. The blue data points were obtained using σ^--circularly polarized probe light, hence probing the population in the $m_J = {}^{+3}/_{2}$ substate, and show the expected linear dependence on the effective number of ions. From a linear fit (solid blue line) we deduce a scaling parameter $\frac{C}{N} = (4.93 \pm 0.07) \times 10^{-3}$. The black dashed line indicates the limit where collective strong coupling is achieved which is the case for $N \gtrsim 500$ interacting ions, in agreement with the expectations.

The largest coupling observed in these experiments was measured for a crystal with a half-length of ~ 1.5 mm and a density of $\sim 6 \times 10^8$ cm^{-3}, corresponding to an effective number of ions of $N = 1570 \pm 50$. The cooperativity of this crystal was measured to be $C = 7.9 \pm 0.3$ and exceeds previously measured cooperativities with ions in optical cavities by roughly one order of magnitude [68, 69, 71].

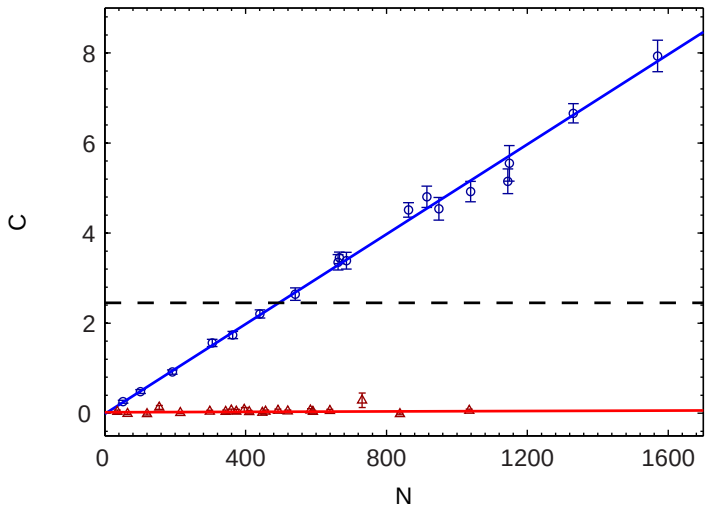

Figure 5.7.: Cooperativity as a function of the effective number of ions. The blue circles correspond to σ^- polarized probe light, while the red triangles are obtained using σ^+ light. The solid lines are linear fits, the dashed line indicates the strong collective coupling limit $g_N > (\kappa, \gamma)$.

As a check of our measurement method, the polarization of the probe light was changed to σ^+ to address the populations in the $m_J = -3/2$ and $m_J = -1/2$ substates of the $3d^2D_{3/2}$ level (red data points). Here, no effect of the coupling of the ions is observed, as expected due to the optical pumping preparation in the $m_J = +3/2$ Zeeman-substate.

5.6.2. Vacuum Rabi-Splitting spectra for different numbers of ions

A similar measurement of the collective coupling rate was performed by recording vacuum Rabi splitting spectra, such as the one presented in Fig. 5.6, for several crystals with different aspect ratios. Examples of such measurements are depicted in Fig. 5.8, showing clearly the increase in the separation between the coupled crystal+cavity normal modes as the number of ions is increased. The collective coupling rate g_N can be derived from fits to the theoretical expression (3.49). In fig. 5.9 the deduced collective coupling rate is plotted for various crystals with different effective numbers of ions. The curve is fitted with the expected square root dependency and taking the finite optical pumping efficiency of 97^{+3}_{-5}% into account. From this fit we deduce a single ion coupling rate of $g = 2\pi \times (0.525 \pm 0.002)$ MHz. This value is in agreement with the previous measurements and the theoretical expectation.

5.7. Coherence between collective Zeeman substates

The realization of the collective strong coupling is a crucial step on the way to an efficient light-matter interface [55]. However, the storage of quantum states in the system

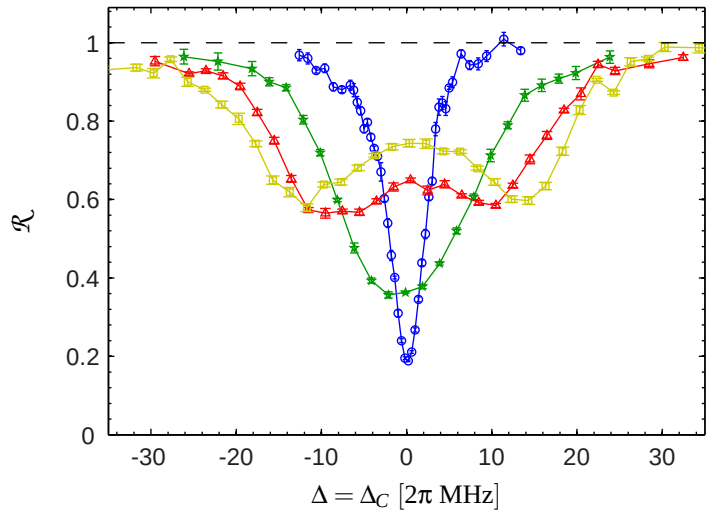

Figure 5.8.: Vacuum Rabi splitting spectra ($\Delta = \Delta_C$) obtained for increasing effective number of ions [0 (blue circles), 243 (green stars), 601 (red triangles), 914 (orange squares)].

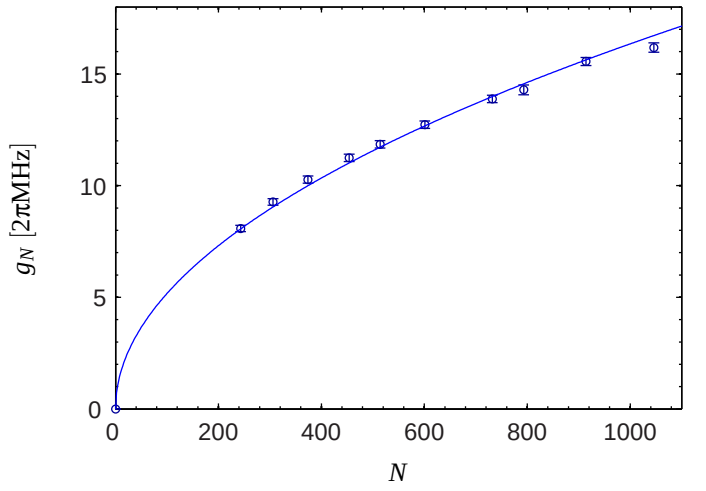

Figure 5.9.: Collective coupling rate g_N versus effective number of ions N deduced from reflectivity spectra, such as shown in Fig. 5.8, obtained with crystals of different shape and density. The solid line is a fit to the data and gives a single ion coupling rate $g = 2\pi \times (0.525 \pm 0.002)$ MHz when corrected for the optical pumping efficiency.

requires persistent coherences between the various Zeeman-substates that would be used to encode the quantum information. To evaluate the prospects for the realization of such coherent manipulations among these states, we measured the decay time of collective coherences between different Zeeman substates of the $3d^2D_{3/2}$ level. The coherences were established by Larmor precession of the magnetic spin induced by an additional *B*-field transverse to the quantization axis. In presence of this orthogonal *B*-field, the population of the different substates undergo coherent oscillations, which are measured at different times in their free-evolution by directly probing the coherent coupling between the cavity field and the ions. In order to be able to resolve the coherent population oscillations in time using the previous technique (probing time $\sim 1\ \mu$s) the amplitude of the longitudinal *B*-field was lowered to $B_z = 0.15$ G to obtain oscillation periods in the $\sim 10\ \mu$s range, and the optical pumping preparation was modified as to minimize the effect of the transverse *B*-field. The reduced *B*-field along the quantization axis could in principle make the sample more sensitive to *B*-field fluctuations. Since these fluctuations might be one of the factors eventually limiting the achievable coherence time we expect the coherence time measured by this method to be a lower bound as compared to the previous configuration with a larger longitudinal *B*-field of $B_z = 2.5$ G.

5.7.1. Experimental sequence

The coherence time measurements required the experimental configuration and the measurement sequence to be slightly modified as compared to the collective coupling rate measurements described in sec. 5.3. The Larmor precession is induced by an additional *B*-field component along the transverse *x*-direction, while the longitudinal magnetic field component B_z was lowered to optimize the contrast of the coherent population oscillations. It turned out that the optical pumping preparation used before was substantially influenced by the additional transverse *B*-field component and the state preparation scheme was therefore changed. The optical pumping light now propagates along the *x*-axis. It is π-polarized, hence transferring the atomic population symmetrically into the two outermost magnetic substates of the $3d^2D_{3/2}$ level, $m_J = \pm 3/2$.

The experimental sequence used to measure the coherence time is shown in Fig. 5.10. The ions are Doppler laser cooled during the first 5 μs, followed by a 12 μs optical pumping period. After the optical pumping, all lasers are turned off for a time τ, allowing for the free evolution of the system. Finally, a weak σ^--circularly polarized probe pulse is injected into the cavity, addressing the ions in the $m_J = +1/2$ and $m_J = +3/2$ substates. The steady state cavity reflection is measured by collecting the reflected photons with the APD for 0.5 μs. The additional delay time between optical pumping preparation and probing obviously lowers the repetition rate of the sequence significantly, especially for long delay times, and the number of data points for each sweep of the cavity will decrease. To compensate for this, the data points at longer delays had to be averaged over more cavity sweeps, which substantially increased the acquisition time and eventually limited these measurements to delays of a few hundreds of μs.

5.7.2. Theoretical description and expectations

Based on a simple four-level model the free Larmor precession-induced changes in the populations of the Zeeman substates, $|m_J = \pm 1/2,\ \pm 3/2\rangle$, of the $3d^2D_{3/2}$ level can be cal-

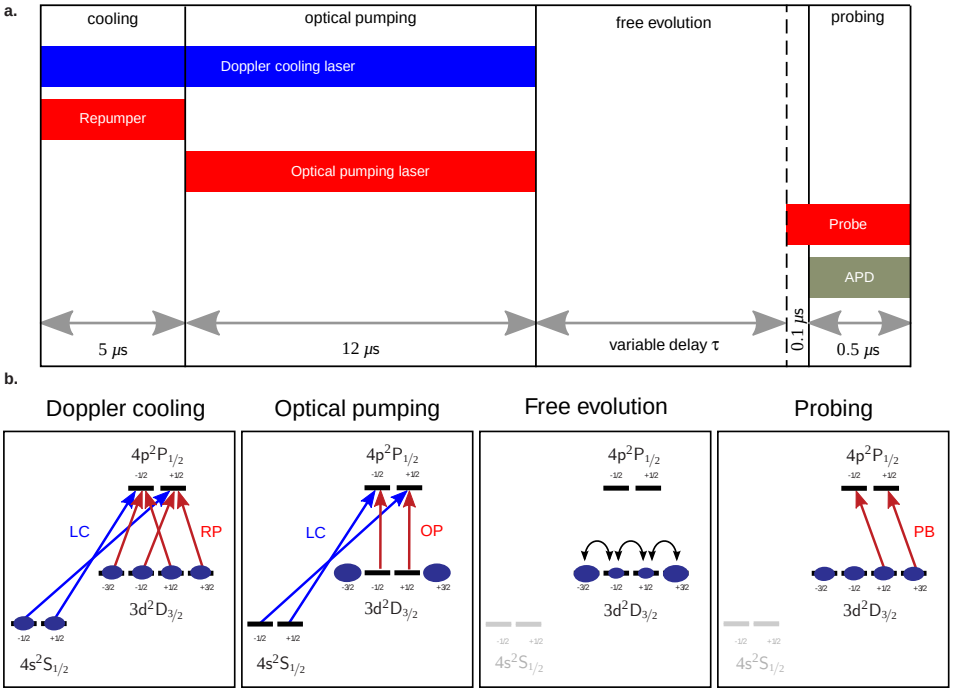

Figure 5.10.: a. Experimental sequence used to measure the coherence time of collective Zeeman substate coherences in the $3d^2D_{3/2}$ level. **b.** Energy levels of $^{40}Ca^+$ including the relevant transitions addressed. In the third phase, all lasers are turned off during a time τ and the system evolves freely in presence of a transverse magnetic field component B_x. The acronyms are: LC: laser cooling beam, RP: repumping beam, OP: optical pumping beam, CB: control beam, PB: probe beam.

culated. For an homogeneous B-field with components B_x and B_z the Hamiltonian of the four-level system can be expressed in terms of collective populations

$$\Pi_{m_J} = \sum_{j=1}^{N_{tot}} |m_J\rangle^{(j)} \langle m_J|^{(j)} \tag{5.6}$$

and spin operators

$$\sigma_{m_J,m'_J} = \sum_{j=1}^{N_{tot}} |m_J\rangle^{(j)} \langle m'_J|^{(j)}, \quad m_J \neq m'_J. \tag{5.7}$$

Here, $|m_J\rangle^{(j)}$ and $|m'_J\rangle^{(j)}$ are the state kets of the jth-ion with magnetic quantum number m_J and m'_J, respectively. The sum extends over the total number of ions. In this notation, the Hamiltonian of the free evolution reads

$$\begin{aligned} H_{\mathrm{B}} &= \hbar\omega_z \sum_{m_J} m_J \Pi_{m_J} \\ &\quad + \hbar\omega_x \sum_{m_J} \sum_{m'_J} \sqrt{m_J m'_J}\, \delta_{m_J,m'_J} \left(\sigma_{m_J,m'_J} + \sigma_{m'_J,m_J}\right), \end{aligned} \tag{5.8}$$

where the sums extend over the four Zeeman-substates. Here, δ_{m_J,m'_J} is the Kronecker delta and the Larmor frequencies ω_z and ω_x corresponding to the z and x component of the magnetic field are given by the product of the magnetic field amplitude by the gyromagnetic ratio γ_{GM}:

$$\omega_z = \gamma_{\mathrm{GM}} B_z, \quad \omega_x = \gamma_{\mathrm{GM}} B_x. \tag{5.9}$$

For a σ^--circularly polarized probe, the measured collective coupling to the cavity light mode after a certain delay time τ between optical pumping and probing will depend on the collective populations in the $m_J = {}^{+1}/_2$ and $m_J = {}^{+3}/_2$ substates. For a non-vanishing population in the $m_J = {}^{+1}/_2$ state, the effective cavity decay rate defined in Eq. (3.48a) is modified to

$$\kappa' = \kappa + g_{1/2}^2 N_{1/2} \frac{\gamma}{\gamma^2 + \Delta_{1/2}^2} + g_{3/2}^2 N_{3/2} \frac{\gamma}{\gamma^2 + \Delta_{3/2}^2}, \tag{5.10}$$

where the subscripts indicate the magnetic substate. Calculating the expectation values for the collective population in these states, one can show that the cooperativity $C(\tau)$ measured at time τ is expected to vary as

$$C(\tau) = a\cos(\omega_L \tau) + b\cos(2\omega_L \tau) + c, \tag{5.11}$$

where the combined Larmor frequency

$$\omega_L = \sqrt{\omega_z^2 + \omega_x^2} \tag{5.12}$$

was defined. The parameters a, b, c are constants depending on the efficiency of the optical pumping preparation, the Clebsch-Gordon coefficients and the magnetic field amplitudes B_z and B_x.

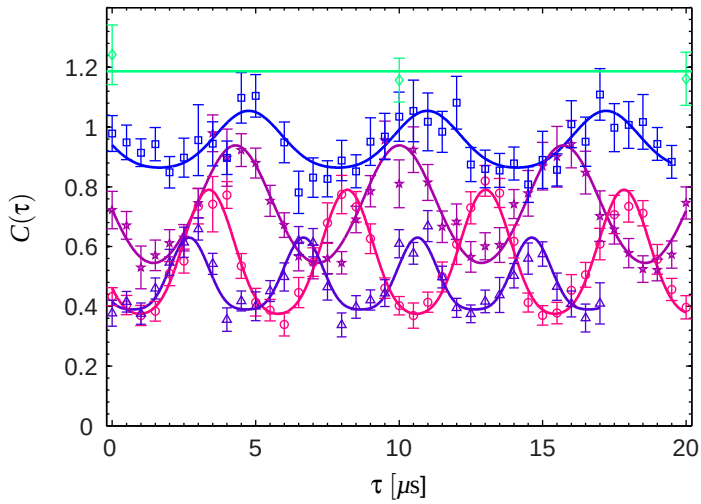

Figure 5.11.: Calibration of the Larmor frequency for different currents of the B_x coils. Shown is the cooperativity as a function of delay time τ for different transverse B-fields: $I_x = 0$ mA (open diamond), $I_x = 10$ mA (open squares), $I_x = 16$ mA (solid stars), $I_x = 26$ mA (open circles) and $I_x = 36$ mA (open triangles). The solid lines are fits according to Eq. (5.11).

5.7.3. Experimental results

The amplitudes of the magnetic fields, B_x and B_z, at the position of the ions were calibrated by measuring the dependence of the Larmor frequency ω_L with the intensity of the current used to drive the transverse magnetic field coils (see Eqs. (5.9) and (5.12)). The obtained coupling as a function of τ is shown for different currents I_x on Fig. 5.11. The curves are fitted according to Eq. (5.11) yielding the Larmor frequency. These frequencies are shown as a function of the current passing the B_x-coils in Fig. 5.12. Using the gyromagnetic ratio $\gamma_{GM} = \mu_B g_{3/2}/\hbar$ (μ_B is the Bohr magneton, $g_{3/2}$ the Landé factor of the $3d^2D_{3/2}$ level), we deduce the magnetic fields along the two axis $B_z = (0.134 \pm 0.002)$ G and $B_x = (4.91 \pm 0.09)\,\mathrm{G} \times I_x/\mathrm{A}$.

To achieve an optimal contrast of the Larmor oscillations, the measurement was carried out with moderate B-field values $B_x = B_z = 0.15$ G and the variation of the cooperativity was measured for 120 μs. To compensate for slow drifts during the measurement, each data point was normalized to the mean cooperativity, $\overline{C}$, averaged over one oscillation period. The normalized cooperativity is shown in Fig. 5.13 a., together with a fit of the form (5.11), in which decoherence processes are taken into account by multiplying the oscillating terms with an exponential decay term $\exp(-\tau/\tau_e)$, which would be expected e.g. for a homogeneous broadening of the energy levels. From this fit, we deduce a coherence time of $\tau_e = 1.7^{100}_{-0.8}$ ms. This value is comparable to previously measured coherence times for single ions in linear Paul trap in equivalent magnetic field sensitive states [149] and might be further improved by an active control of stray magnetic fields or state configurations that are less sensitive to magnetic field fluctuations. For inhomogeneous broadening, due to magnetic field gradient over the crystal, the decoherence process would be better de-

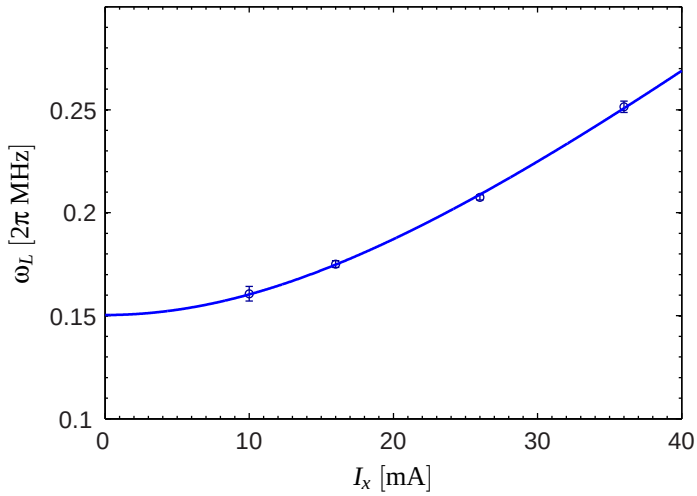

Figure 5.12.: Larmor frequency as a function of current through the B_x coils. The solid line is a fit of the form $\omega_L = \sqrt{\omega_z^2 + a^2 I_x^2}$ and we deduce $\omega_z = 2\pi \times (0.150 \pm 0.002)$ MHz and $\omega_x = 2\pi \times (5.5 \pm 0.1)\ \frac{\text{kHz}}{\text{mA}} \times I_x$.

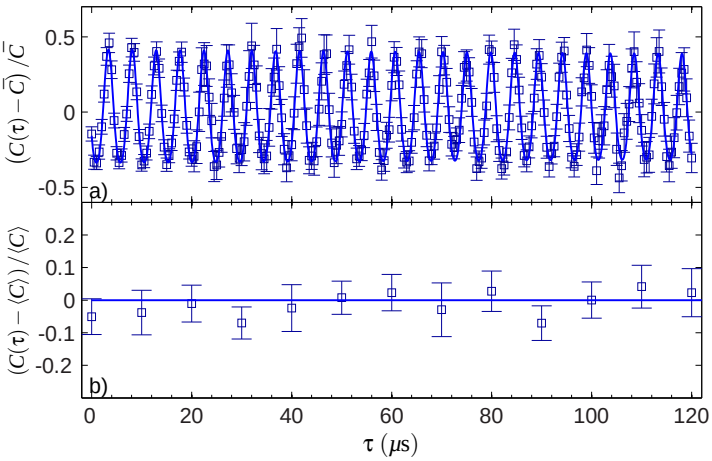

Figure 5.13.: a. Coherence as a function of delay τ. Due to the presence of a non-zero B-field component orthogonal to the quantization axis ($B_z = B_x = 0.15$ G), coherent Larmor precessions are observed. Long term drifts are compensated by normalizing to the mean of one oscillation period. The solid line corresponds to a fit, assuming an exponential decay and yields a coherence time of $\tau_e = 1.7^{100}_{-0.8}$ ms. **b.** Cooperativity as a function of delay with only the B-field along the quantization axis present ($B_x = B_y = 0,\ B_z = 0.15$ G). The data points are normalized to the mean cooperativity of $\langle C \rangle = 1.43 \pm 0.02$.

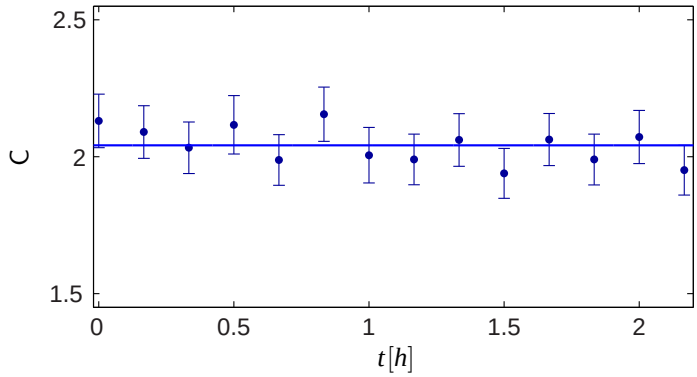

Figure 5.14.: Cooperativity for the crystal shown in fig. 5.15 measured over two hours. The coupling is constant within the error-bars. For detail see text.

scribed by a Gaussian decay [41]. Fitting the data assuming a Gaussian decay $\exp(-\tau^2/\tau_g^2)$ in Eq. (5.11) yields a coherence time of $\tau_g = 0.5^{+0.6}_{-0.2}$ ms. Due to the limitation of our measurement to time delays of $\tau \lesssim 120\mu s$, it is at present not possible to distinguish between the two decay mechanisms.

For comparison the cooperativity as a function of probe delay, $C(\tau)$, was measured with only the bias field along the quantization axis present ($B_x = 0,\ B_z = 0.15$G), as shown in Fig. 5.13 b. Here, the values are normalized to the mean cooperativity averaged over all points $\langle C \rangle$. Within the error bars the deduced cooperativities agree with a constant value of $\langle C \rangle = 1.43 \pm 0.02$.

5.8. Long term stability

To prove the capability of performing experiments using the same ion Coulomb crystal for long times, we monitored the cooperativity for a single ion Coulomb crystal over more than 2 hours. The result is shown in fig. 5.14. The cooperativity was measured on atomic resonance $\Delta = 0$ and stays constant within $\pm 1\%$, although we observe the formation of dark ions on the surface of the crystal. These dark ions are most likely formed by reactions of $^{40}Ca^+$ with residual hydrogen or oxygen atoms in the trap. As these dark ions have a higher mass, they see according to eq. (2.8) a shallower radial trapping potential and, hence, form a dark shell around the central component. However, for crystals with a radius much larger than the cavity waist, as used in this experiment, the dark ions appear in the wings of the fundamental transverse Gaussian mode profile and do not influence the coupling to the cavity.
Moreover, these dark ions can be "recycled" by irradiating the crystal with UV light from the ionization laser, most likely by photo-dissociation. The inset of fig. 5.14 shows four projection images of the same crystal taken during the long time measurement of the cooperativity. The dark shell can be clearly seen on images b. (after 1 h) and c. (after 2 h), whereas it disappeared again on image d., after the crystal was exposed to UV light. The crystal contains 12400 ± 250 ions of which 514 ± 10 interact with the cavity. From the projection images the production rate for the dark ions can be deduced and we

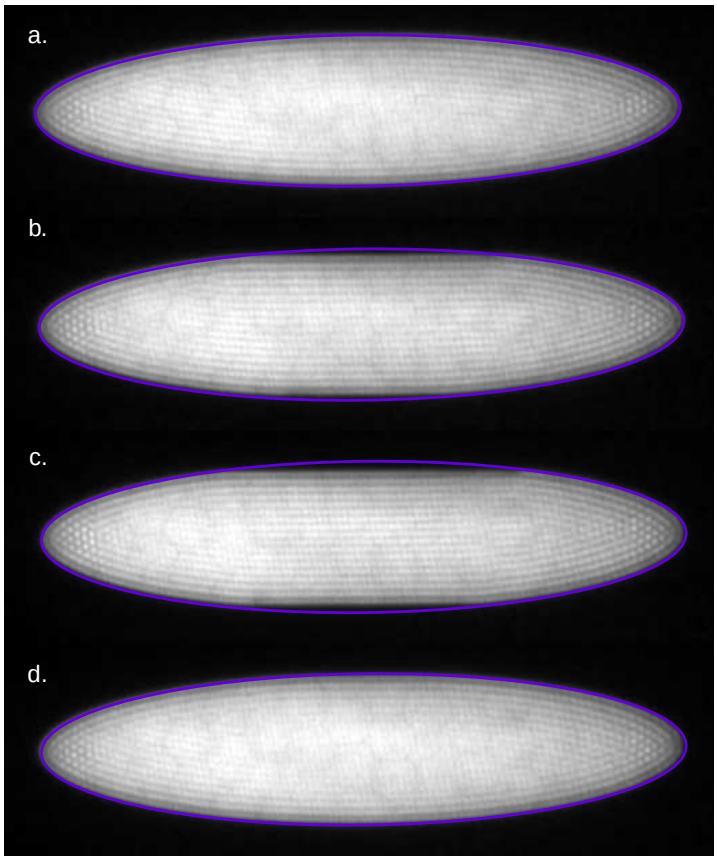

Figure 5.15.: Projection image of the crystal **a.** at the beginning of the measurement **b.** after one hour **c.** after two hours **d.** after flashing the UV laser. On image **b.** and **c.** a shell of dark ions is present emerging from chemical reactions. The crystal contains 12400 ± 250 ions of which 514 ± 10 interact with the cavity

find $R_{dark} = (10.2 \pm 0.2)\text{min}^{-1}$. This rate will, however, depend on the geometry and the density of each individual crystal, and also on the composition and pressure of the background gas in the chamber. The described recycling technique could have promising applications for reaction studies using cold single ions or ion ensembles [150].

5.9. Conclusion

To conclude, we have demonstrated the possibility to operate in the collective strong coupling regime of CQED using large ion Coulomb crystals positioned in a moderately high-finesse optical cavity. We measured cooperativities as high as $C \sim 8$, which is comparable to those used in neutral atom based quantum memories [41–47, 96, 97]. Moreover, to assess the prospect of realizing a long-lived quantum memory, we measured the decay of collective coherences between magnetic Zeeman substates and found coherence times in the millisecond range, which is of the order of what previously was measured for single ions in equivalent magnetic field sensitive states [149]. The excellent agreement of the experimental results with the theoretical predictions as well as the long-term ($\sim$ hours) temporal stability of the coupling makes ion Coulomb crystals promising candidates for the realization of quantum information processing devices such as quantum memories and repeaters [10, 38]. Using for instance cavity EIT-based protocols [55–57], the obtained coupling strengths and coherence times would make up for the realization of both high-efficiency *and* long life-time quantum memories [56, 57, 151]. Experiments showing how cavity EIT can be realized in the system will be presented in ch. 8.

The nice properties of ion Coulomb crystals also open up for the manipulation of complex multimode photonic information [81] and we will present results on the coupling to various transverse cavity modes in the following chapter.

Furthermore, the collective interaction can also be used to facilitate non-invasive spectroscopy of the collective vibrational modes of ion Coulomb crystals [152]. These experiments will be presented in ch. 7.

6. Coupling to different transverse cavity modes

In this chapter, to assess the potential of ion Coulomb crystals as a medium for multimode light-matter interfaces, we investigate the possibility to couple ion crystals to different spatial (transverse) modes of the cavity. We present a thorough characterization of the coupling of various ion Coulomb crystals to the TEM_{00} and $TEM_{10,01}$ transverse cavity modes.

The chapter is structured as follows: First, in sec. 6.2 the theoretical expectations for the coupling of ion Coulomb crystals to these modes is discussed, followed by a brief description of the experimental setup in sec. 6.3. Then, in sec. 6.4, the transverse profiles of the cavity modes are mapped out by moving small, elongated crystals along the transverse directions and monitoring the change in the collective coupling rate. In sec. 6.5 we present experiments in which the scaling of the coupling strength with the radial size of the crystals is investigated, followed by a measurement of the collective coherent coupling rate of large ion Coulomb crystals to the two modes in sec. 6.6. Finally, in sec. 6.7 we summarize the results and give a brief outlook.

6.1. Introduction

Ion Coulomb crystals combine properties of solid state systems, such as a uniform ion density (see sec. 2.3) and long time stability (see sec. 5.8) with features commonly attributed to single isolated particles, i.e. excellent coherence properties and no significant internal state perturbation due to ion-ion interactions (see sec. 5.7).

This unique combination makes ion Coulomb crystals positioned in the mode volume of an optical cavity ideal candidates for the realization of multimode quantum interfaces, where, in contrast to the traditional frequency and polarization degrees of freedom [153] the encoding of the photonic information can be performed in the spatial degree of freedom, i.e. the orthonormal transverse modes of the optical cavity. Such a system would provide an interesting basis for e.g. the realization of multimode quantum memories [55, 96], where several flying qubits could potentially be stored simultaneously in a single physical system, or for the cavity enhanced generation [69, 73, 154, 155] of nonclassical (spatially) multimode states of light [156–159].

The simultaneous coupling to multiple modes may also have applications, for e.g. quantum imaging [157–160] and cavity-mediated cooling [161–163]. For the latter, an enhancement of the dynamical cooling effect by the use of multimode geometries has been predicted [164].

In this chapter we will present results on the coherent interaction between ion Coulomb crystals of several sizes and transverse cavity modes [81]. We demonstrate how small,

needle-shaped crystals can be used to map out the transverse structure of various cavity modes and investigate the effect of the size of the crystals on the collective coupling to different transverse modes. Finally, we demonstrate that identical coupling rates for various modes can be achieved for sufficiently large ion Coulomb crystals.

6.2. Theoretical expectation

In the previous chapters, we focused our theoretical analysis of the coherent interaction between ion Coulomb crystals and the cavity fundamental TEM_{00} mode. For the experiments presented in this chapter, we will make use of different cavity modes and will in this section modify the theoretical description of sec. 3.2 to higher-order TEM_{mn} modes.

For an arbitrary transverse cavity mode the effective cavity field decay rate, introduced for the fundamental TEM_{00} mode in Eq. (3.48a), is given by

$$\kappa' = \kappa + G_{mn}^2 \frac{\gamma}{\gamma^2 + \Delta^2}, \tag{6.1}$$

where G_{mn} denotes the collective coupling rate with the TEM_{nm} mode considered, κ is the cavity field decay rate, γ is the optical dipole decay rate and Δ is the detuning of the probe laser with respect to the atomic transition frequency. In its general form, the collective coherent coupling rate, introduced for the fundamental Gaussian mode in eq. (3.45), reads

$$G_{mn}^2(x_0,y_0) = g^2 \rho_0 \int_V \mathrm{d}\mathbf{r} \Psi_m^2(x-x_0,z)\Psi_n^2(y-y_0,z)\Phi^2(x-x_0,y-y_0,z) \tag{6.2}$$

where g is the maximum single-ion coherent coupling rate (see eq. (3.27)), ρ_0 is the ion density (see eq. (2.15)) and $\Psi_n(x,z)$, $\Psi_m(y,z)$, $\Phi(x,y,z)$ are the two transverse and the longitudinal mode functions defined in eq. (3.2) and eq. (3.3), respectively. The integral extends over the volume of the spheroidal crystal $V = \frac{4}{3}\pi R^2 L$, with half-length L and radius R, and x_0 and y_0 account for possible radial offsets of the crystal revolution axis with respect to the cavity axis. As in eq. (3.45) we can average over longitudinal effects, and eq. (6.2) reduces to

$$G_{mn}^2(x_0,y_0) \simeq \frac{g^2}{2} 2L\rho_0 \int_{-R}^{R} \mathrm{d}\mathbf{x} \Psi_m^2(x-x_0,z) \int_{-R}^{R} \mathrm{d}\mathbf{y} \Psi_n^2(y-y_0,0). \tag{6.3}$$

Of particular relevance for our experiments are two approximations that can be made for ion Coulomb crystals with a radial extension that is either much smaller or much larger than the waist of the fundamental TEM_{00} mode, w_0. In the first case ($R \ll w_0$) the radial integral in eq. (6.3) is trivial and the transverse mode functions are simply evaluated at the position of the crystal (x_0,y_0)

$$G_{mn}^2(x_0,y_0) \propto \Psi_m^2(x_0,0)\Psi_n^2(y_0,0). \tag{6.4}$$

Changing the radial offsets (x_0,y_0) will accordingly modify the cavity field effective decay rate of eq. (6.1) via eq. (6.4) and one can directly map out the transverse profile of the cavity mode by measuring κ' as a function of (x_0,y_0).

In the second case, where the radius of the crystal is much larger than the cavity waist ($R \gg w_0$), the integral over the transverse mode functions yields

$$\int_{-R}^{R} \mathrm{d}u\ \Psi_n^2(u-u_0,0) \approx \int_{-\infty}^{\infty} \mathrm{d}u\ \Psi_n^2(u,0) = \sqrt{\frac{\pi}{2}} w_0, \quad \forall n, \text{ where } u = x,y. \tag{6.5}$$

The collective coupling is then independent of the transverse mode function considered and substituting this result into (6.3) and averaging over the longitudinal sinusoidal yields

$$G_{mn}^2 = g^2 \rho_0 \frac{\pi w_0^2}{2} L, \quad \forall n,m, \tag{6.6}$$

which is consistent with the result found for the TEM_{00} mode in eq. (3.46).

In the limit $R \gg w_0$, the coherent coupling rate is hence simply proportional to the volume of the cavity mode in the crystal and since the transverse mode functions are orthonormal, this volume is the same for all of them. For large ion Coulomb crystals one thus expects the collective coupling rate to be the same for all $\mathrm{TEM}_{\mathrm{nm}}$ modes. However, for large crystals there will always be ions which are located far from the RF-field free trap axis and which will experience strong micromotion, as was discussed in secs. 4.6 and 4.6. The collective coupling rate to different $\mathrm{TEM}_{\mathrm{nm}}$ mode will hence be equal only if there is no significant effect of this micromotion on the coupling with the cavity field.

As can be seen from eq. (4.1) the micromotion is in principle purely radial and one expects it not to couple into the axial motion of the ions. This prediction is also supported by molecular dynamics simulations [165].

One therefore expects the effect of micromotion on the collective coherent coupling to be negligible. However, this assumption is only valid for a perfectly symmetric trap and if the cavity and the trap axis are entirely parallel. The measurement of the collective coupling rate of large ion Coulomb crystals with different transverse modes thus allows to test the validity of these predictions and the quality of the cavity trap setup.

The issue of micromotion is also important when displacing small, elongated crystals radially into regions with large amplitudes of the micromotion and measuring their coupling with the cavity field. Such measurements will provide another sensitive test of the effect of micromotion on the collective coherent coupling.

6.3. Experimental setup

The main parts of the experimental setup were already introduced in ch. 4 and we will here only describe the necessary changes and some specific aspects for the experiments presented in this chapter.

The results of the previous chapter were all obtained by injecting the cavity through the PT and measuring the cavity reflectivity spectrum with the probe APD. When measuring the collective coupling to higher order cavity modes, the probe laser has to be mode matched to the cavity mode in question. However, this beam has a Gaussian profile, corresponding to the transverse profile of the TEM_{00} mode and coupling this beam to a higher order mode will result in a lower coupling efficiency. The fraction of the beam not overlapping with the cavity mode in question will be reflected of the cavity and would lead to a background for measurements in reflection. To avoid these problems, we inject the

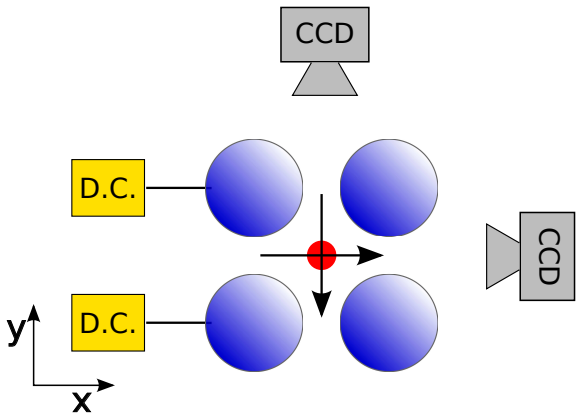

Figure 6.1.: End-view schematic: The crystals (red circle) can be displaced in the (x,y)-plane by application of appropriate DC voltages to two of the segmented electrode rods, their position and size are monitored using two CCD cameras.

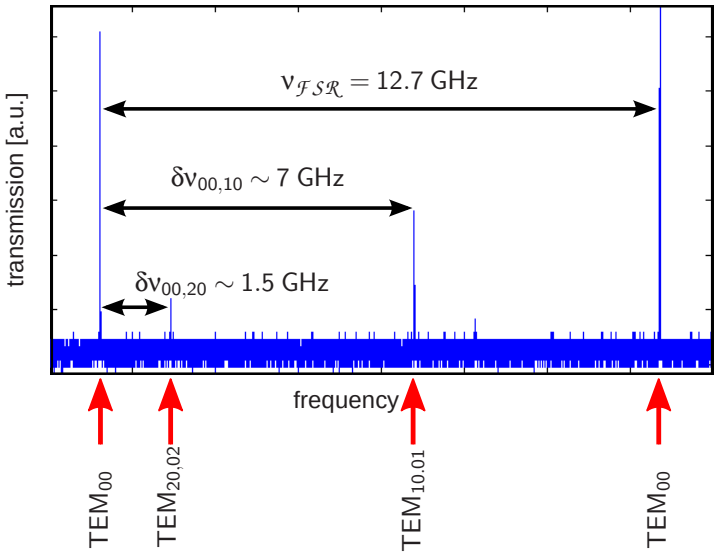

Figure 6.2.: Cavity transmission, scanned over one free spectral range and measured by a photo detector. The TEM_{00}, $TEM_{10,01}$ and $TEM_{20,02}$ transmission peaks are clearly visible and marked by the red arrows. Though not resolved on this scan, the resonance frequencies of TEM_{10} and TEM_{01} are slightly non-degenerate, most likely due to birefringence of the mirror substrates.

probe laser for the measurements in this section through the HR side into the cavity (see fig. 4.8) and measure the transmitted signal with the probe APD.

In some of the experiments, we want to deliberately translate the ion Coulomb crystal along the radial directions. As was briefly discussed in sec. 4.2, this is possible by applying additional DC voltages to two of the electrode rods. A schematic is shown in fig. 6.1. The ions are moved along the horizontal *x*-axis when applying equal voltages of the same polarity to the two rods, and along the vertical *y*-axis for voltages of opposite polarities, but equal magnitude. The position in the (x,z)- and the (y,z)-plane can be deduced from projection images obtained with the top and the side camera (see sec. 4.4), respectively.

The cavity transmission spectrum is measured by scanning the cavity over the atomic resonance at a rate of 30 Hz, see sec. 4.8.3, where the reference laser at 894 nm is used to compensate for thermal drifts and mechanical vibrations. During each sweep, the transmission is probed by repeating the experimental sequence shown in fig. 5.2 with the probe laser being mode matched to the transverse cavity mode in question. The probe intensity is as before set such that the mean photon number in the cavity is about or less than one at any time and the probe polarization is left-hand circularly-polarized.

In the description of the optical cavity in sec. 4.5 it was mentioned that the cavity mirrors (radius of curvature of 10 mm) are mounted in a close to confocal geometry with a inter-mirror distance of 11.8 mm, corresponding to a free spectral range of $\nu_{\mathcal{FSR}} = 12.7$ GHz. The frequency of the different transverse mode functions are non-degenerate, according to eq. (3.6), and the expected frequency spacing of two neighboring transverse modes $(n+m = n'+m'+1)$ amounts to $\delta\nu_{nm,n'm'} = 7.08$ GHz, In fig. 6.2 the cavity transmission spectrum when scanning the cavity length over more than one free spectral range is shown. The spectrum is obtained by measuring the transmitted intensity of a relatively strong probe field injected into the cavity with a photo-detector. The transmission peaks corresponding to the TEM_{00}, $\mathrm{TEM}_{10,01}$ and $\mathrm{TEM}_{20,02}$ modes are clearly resolved on the scan, and separated in frequency, as expected from (3.6).
Though according to eq. (3.6) the resonance frequencies for the TEM_{10} and TEM_{01} mode should be equal, we measure a slight difference of $\delta\nu_{10,01} \sim 1$ MHz, which is most likely due to birefringence effects in the substrates of the cavity mirrors.

To facilitate mode matching to a particular transverse mode and especially to distinguish the spatial orientation of e.g. the TEM_{10} and TEM_{01} mode, a CCD camera was inserted into the probe beam path before the APD to directly monitor the beam profile of the transmitted cavity signal while modematching.

6.4. Mapping out the transverse cavity mode profiles

In a first series of experiments, we explore the collective coupling of a small, elongated ion Coulomb crystal to various cavity field modes when translating it along the horizontal *x*- and the vertical *y*-directions. A projection image of the crystal is shown in fig. 6.3. It has a half-length of $L = (240 \pm 1)$ μm and a radius of $R = (21 \pm 1)$ μm. With a density of $(3.4 \pm 0.1) \cdot 10^8$ cm^{-3} the crystal contains a total of $N_{\mathrm{tot}} = 238 \pm 18$ ions. The position of the crystal's revolution axis is determined from projection images taken with the two CCD cameras. In fig. 6.4 the horizontal position for different values of the additional DC voltages applied to the two rods with equal polarity as deduced from projection images is shown. The solid line is a linear fit to the data points and yields (140 ± 2) $\frac{\mu\mathrm{m}}{\mathrm{V}}$. The

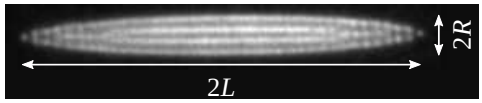

Figure 6.3.: Projection image in the (x,z)-plane of the thin needle-shaped crystal used for mapping out of the transverse cavity mode. From a projection image we deduce a half-length and a radius of $L = (240 \pm 1)$ μm, $R = (21 \pm 1)$ μm. With a density of $\rho_0 = (3.4 \pm 0.1) \cdot 10^8$ cm^{-3}, the total number of ions in the crystal is $N_{\text{tot}} = 238 \pm 18$.

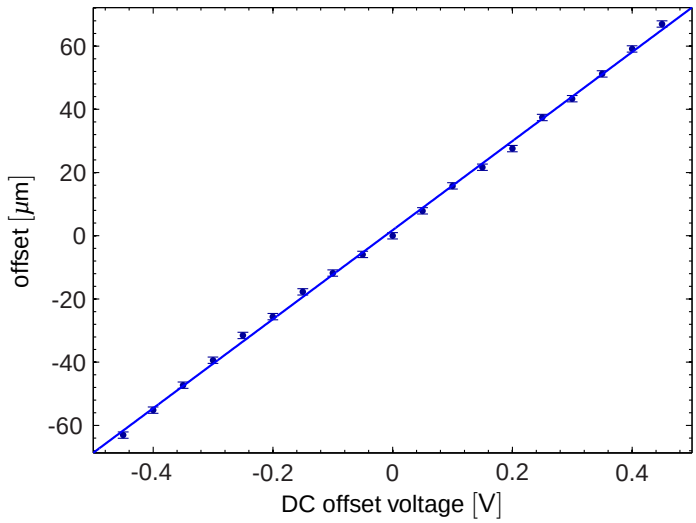

Figure 6.4.: Horizontal position of the center of a needle-shaped crystal for various DC voltages applied to two of the trap rods. The position of the crystal is deduced from projection images. The solid line is a linear fit and yields a displacement of (140 ± 2) $\frac{\mu\text{m}}{\text{V}}$.

precision in reading the position of the crystal is ± 0.8 μm [119].

In fig. 6.5 the measured coupling strengths using the Coulomb crystal of fig. 6.7 is presented in terms of G^2_{mn} normalized to $G^2_{00}(x_0 = 0,\, y_0 = 0)$ for the TEM$_{00}$ and TEM$_{10}$ modes, when translating the crystal along the horizontal x and the vertical y directions. For each position of the crystal, the coherent coupling strength is measured through the broadening of the probe pulse transmission signal (Eq. (6.1)) with the probe tuned to the atomic resonance ($\Delta = 0$). The solid lines in fig. 6.5 are theoretical predictions calculated according to eq. (6.1). For the calculation we use the geometrical size as deduced from the projection image and a density of $\rho_0 = (3.8 \pm 0.1) \times 10^8$ cm^{-1} determined from the trapping parameters (see eq. (2.15)). Though the field of the TEM$_{10}$ mode drops to zero at the center of the mode, the coherent coupling does not vanish for zero displacement of the crystal, because of its finite radial extension.

The experimental data is shown to agree very well with the theoretical predictions and since the amplitude of the radial micromotion increases with the ions' distance from the

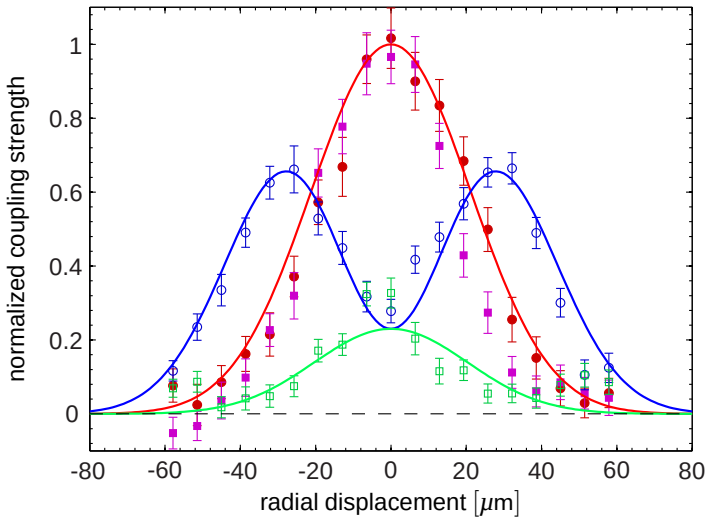

Figure 6.5.: Normalized coherent coupling strengths G^2_{00} (solid) and G^2_{10} (open) as a function of the displacement of the needle-shaped crystal along the x (circle) and y (square)-axes. The solid lines are derived from the theoretical expression given in Eq. (6.3), taking the radial extension of the crystal into account. The red line correspond to the TEM_{00} mode, the blue line to the x and the green line to the y direction of the TEM_{10} mode.

RF-field free z-axis (see eq. (4.1)), strong systematic deviations would have been expected at large displacements if excess micromotion was an issue. The excellent agreement of the measured data with the theoretical predictions indicates that the radial micromotion of ions does not couple significantly into their axial motion. While reassuring for the behavior of our trap, these findings are in agreement with predictions from molecular dynamic simulations [165].

The experiments presented in this section provide, furthermore, a very sensitive technique to measure the relative offsets between the RF-field free trap axis and the symmetry axis of the cavity. By translating small, elongated crystals along the transverse directions and measuring their coupling to the fundamental TEM_{00} mode as a function of displacement, these offsets can be measured with very high precision (better than 1 μm). In combination with the scheme to modify the position of the potential minimum of the radial pseudo-potential of the trap discussed in sec. 4.6, we could, using this measurement technique, reduce the radial offset in both transverse dimensions to less than a micrometer [119].

6.5. Effects of the size of the crystal on the cavity coupling

To check further the agreement with the theoretical predictions of eq. (6.3) we performed measurements of the collective coupling rate of crystals with fixed position, but varying radii with different transverse modes.

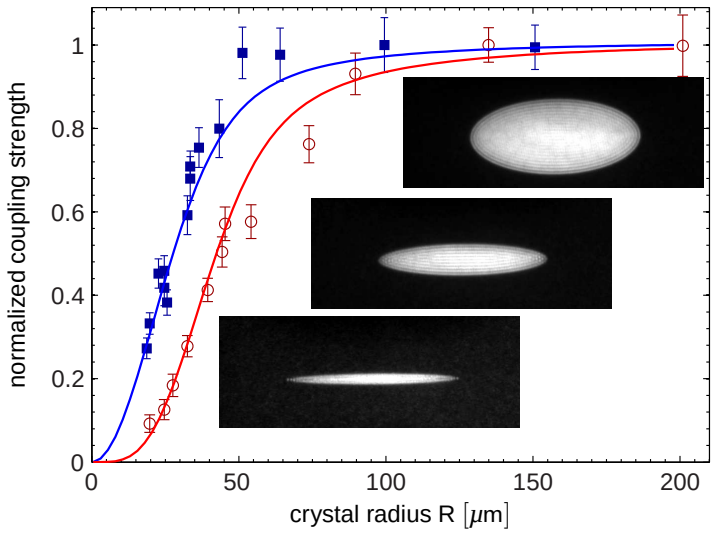

Figure 6.6.: (color online.) Normalized coherent coupling strengths G_{00}^2 (solid) and G_{10}^2 (open) as a function of the crystal radius R. The length and density of the crystals are fixed to $L = (336 \pm 1)\mu$m and $\rho_0 = (3.8 \pm 0.1) \times 10^8$ cm^{-1}, respectively. The solid lines are derived from the theoretical expression given in Eq. (6.3). The three insets show the three crystals with different radial extensions (from left to right, $R = (23 \pm 1)$ μm, $R = (63 \pm 1)$ μm and $R = (149 \pm 1)$ μm).

For narrow crystals with $R \lesssim w_0$ a significant difference in the coupling with the TEM$_{00}$ and TEM$_{10}$ mode is expected. However, these differences should vanish for increasing crystal radii and the collective coherent coupling rate is expected to converge towards the same value for big crystals with $R \gg w_0$, as discussed in eq. (6.5). This prediction was tested using crystals with a fixed half-length of $L = (336 \pm 1)$ μm and a constant density of $\rho_0 = (3.8 \pm 1) \times 10^8$ cm^{-3}. The radial extension was changed by successively loading more ions into the trap while at the same time increasing the axial confinement potential to keep the length of the crystal constant.

In Fig. 6.6 the measured coherent coupling rates for the TEM$_{00}$ and TEM$_{10}$ mode are shown for various crystal radii. The rotational symmetry axis of the various crystals was positioned to coincide with the axis of the cavity ($x_0 = y_0 = 0$). As expected, the coherent coupling rate increases with the radius, and this increase is slower for the TEM$_{10}$ mode , since most of the ions are positioned along the field free axis of this mode. As the radius of the crystals is further increased, the coupling rate with both modes converges to the same value, in good agreement with the theoretical predictions of Eq. (6.3). The solid lines are the expected coupling rates for those modes, and show good agreement with the experimental data. The inset in fig. 6.6 shows projection images of three crystals with radii $R = (23 \pm 1)$ μm, $R = (63 \pm 1)$ μm and $R = (149 \pm 1)$ μm

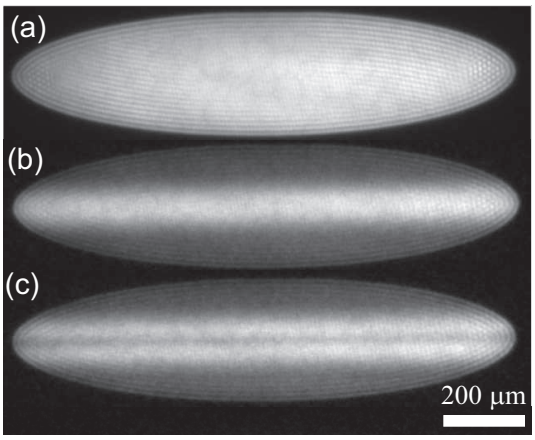

Figure 6.7.: Projection images in the $(xz)-$plane of the 1.2 mm-long Coulomb crystal used for the measurements in Fig. 6.8. **a.** The whole crystal is illuminated by 866 nm repumping light along the x-axis. **b.** and **c.** The repumping light at 866 nm is predominantly injected into the TEM_{00} (b) and TEM_{10} (c) cavity modes, for enhancing the fluorescence level within these modes.

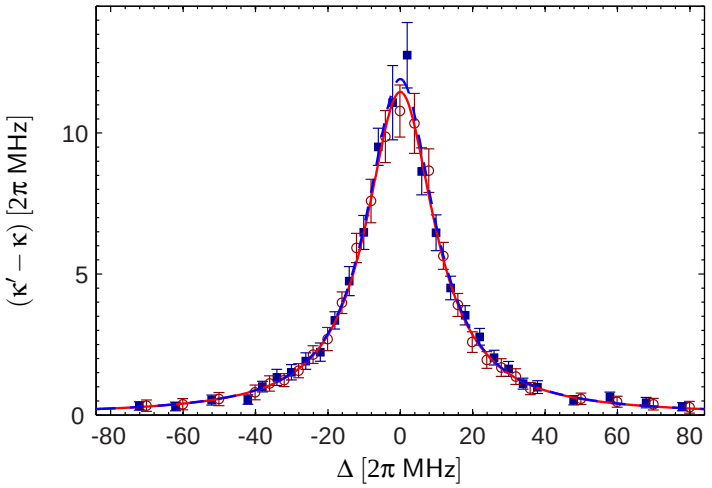

Figure 6.8.: (color online.) Broadening of the probe signal half-width $\kappa' - \kappa$ as a function of the probe detuning Δ, for the TEM_{00} (solid) and the TEM_{10} (open) modes, obtained with the crystal of Fig. 6.7. The collective coupling rates are deduced from Lorentzian fits according to Eq. 6.1 (solid lines).

6.6. Coupling with large crystals

Finally, to carefully check the prospect of using large ion Coulomb crystals as a media for multimode light-matter interfacing, we performed precise measurements of the coherent coupling rates for both the TEM_{00} and the TEM_{10} mode. To obtain a sufficiently large coupling, much larger crystals with a higher density were used. In fig. 6.7 projection images of the crystal are shown. The three images are taken with different configurations for the repumping laser. In fig. 6.7 a., all ions in the Coulomb crystal are exposed to repumping light and contribute to the fluorescence, whereas in fig. 6.7 b. the repumping laser is mode matched to the TEM_{00} mode of the cavity and only the ions inside the cavity mode will contribute to fluorescence, while the remaining ions will decay to the metastable $3d^2D_{3/2}$ state. Fig. 6.7 c. is acquired in a similar configuration, with the repumping laser now being mode matched to the TEM_{10} mode and one can clearly see the nodal line of this mode. From the projection image, we deduce a half-length of $L \sim 600\ \mu$m, a radius of $R \sim 300\ \mu$m. With an ion density of $\rho_0 = (5.4 \pm 0.1) \times 10^8\ \mathrm{cm}^{-3}$ the effective number of interacting ions is $N \sim 590$.

The coherent coupling rate was measured analogously to sec. 5.4, by measuring the broadening of the effective cavity decay rate for a series of detunings of the probe pulse from atomic resonance, Δ. The results of the measurements is shown in fig. 6.8 together with Lorentzian fits to the data based on Eq. 6.1. With G_{mn} and γ as free fitting parameters, we obtain ($G_{00} = 2\pi \times (11.6 \pm 0.1)$ MHz, $\gamma = 2\pi \times (11.3 \pm 0.3)$ MHz) for the TEM_{00} mode and ($G_{10} = 2\pi \times (11.5 \pm 0.1)$ MHz, $\gamma = 2\pi \times (11.4 \pm 0.3)$ MHz) for the TEM_{10} mode, respectively. The experimentally deduced collective coupling rates, G_{00} and G_{10}, are equal within their error bars and confirm the theoretical expectation of eq. (6.5). This also shows that the radial micromotion does not couple into the axial degree of freedom, and does hence not influence the coherent coupling, and corroborate the findings of sec. 6.4.

Moreover, the achieved coupling rates also show that the collective strong coupling regime can be reached for higher-order cavity modes. Furthermore, we also observed equal coupling strengths between large crystals and the TEM_{10} and the TEM_{01} modes, which opens up for e.g. the possibility of storing photonic qubits encoded in a spatial basis spanned by these two modes.

6.7. Conclusion

In conclusion we have performed a series of measurements to investigate the coupling of ion Coulomb crystals with various sizes with different transverse cavity field modes.

In a first experiment, we demonstrated how small, elongated crystals can be used to map out the transverse profile of the cavity modes by translating the crystals in the radial plane and measuring the coherent coupling rate to the cavity field. The results show very good agreement with the theoretical expectations, even for displacements between the revolution axis of the crystal and the field-free nodal line of the RF potential as large as $\sim 60\ \mu$m.

This experiment is to some extent reminiscent of [68], where a single $^{40}Ca^+$ ion was used as a nano-scopic probe to reconstruct the transverse field distribution of several transverse modes of an optical cavity. The main difference is that in our experiment the trans-

verse field distributions are measured not by detecting incoherent fluorescence light, but directly via the coherent coupling of the ions to the cavity field.

In a second experiment, the effect of the size of the crystal on the coupling strength to various transverse modes was investigated by measuring the collective coupling rate of crystals with varying radii to these modes. The experimental data is in good agreement with the theoretical expectations and we find the predicted scaling with the radius for both the TEM_{00} and the TEM_{10} mode.

Finally, we demonstrated how large ion Coulomb crystals ($R \gg w_0$) can be used to realize collective strong coupling to various transverse modes with equal coupling strengths. These results are very promising for e.g. the realization of complex quantum memory schemes, where one can envision the simultaneous storage and retrieval of photonic states in various cavity modes [96].

For all experiments, we find very good agreement between the measured coherent coupling and the theoretical expectations, even when displacing small, elongated crystals into regions of high micromotion or for crystals with large radial extensions, where some of the ions are positioned far from the RF-field free axis and experience strong micromotion. These results show that the coupling of the inherent radial micromotion into the axial degree of freedom is sufficiently small to have no significant effect on the coherent coupling between the ion ensemble and the cavity modes, in good agreement with molecular dynamics simulations [165].

Our results, combined with previously measured long collective Zeeman sub-state coherence times (see sec. 5.7), suggest that large ion Coulomb crystals could serve as near-ideal media for high-fidelity multimode quantum information processing and communication devices.

7. Noninvasive spectroscopy of vibrational modes

The measurements in this chapter will exploit another degree of freedom in the light-matter interaction, namely the collective motion of trapped ion Coulomb crystals. We will present a novel noninvasive spectroscopy technique which directly uses the collective coherent coupling between the ions and a cavity field at the single photon level to gain information about the collective motion of the ion crystal. This measurment technique will be used to study the normal mode dynamics of cold ion Coulomb crystals in a linear Paul trap.

The chapter is structured as follows: We start by giving a brief introduction and motivation in 7.1. Then, in sec. 7.2 a theoretical model for the collective vibrational modes of a cold nonneutral plasma will be introduced, along with a theoretical investigation of the influence of vibrational modes on the coherent light-matter interaction. In sec. 7.3 we will present the experimental technique to perform a noninvasie spectroscopy of vibrational modes using the coherent coupling with the cavity field. In sec. 7.4 some first applications of this technique will be presented along with preliminary results, before we conclude in sec. 7.5.

7.1. Introduction

In the past decades, the physics of cold confined plasmas of identical charged particles [166] has been the subject of many theoretical and experimental studies. While the availability of fast computers allowed for detailed simulations of these systems [165–170], the structural properties and equilibrium states of strongly confined plasmas in the form of ion Coulomb crystals was investigated both in Penning [171–175] and in Paul traps [75–78, 121, 141, 176].

When these strongly confined plasmas are subject to external perturbations, theoretical studies of the collective dynamics treating the plasma as a zero-temperature charged liquid predicted collective normal mode dynamics [82, 167, 168].

In Penning traps, the normal mode dynamics of magnetized spheroidal shaped charged plasmas have experimentally been observed in a series of measurements using cold laser-cooled plasmas of Be^+ ions [171–174]. In these experiments, the excitation of a particular normal mode was detected by observing changes in the fluorescence level of the ions due to the Doppler effect. The normal modes were excited by applying appropriate driving fields to the trap electrodes with a frequency matching the resonance frequency of the mode. The Doppler shifts of the atomic resonance by the driven motion lead to observable changes in the fluorescence. Using this so-called Doppler velocimetry spectroscopy technique [173], a number of normal modes could be observed and the corresponding mode frequencies could be related to specific (l,m)-modes theoretically predicted for these mag-

netized spheroidal charged plasmas [82]. A phase-coherent detection of the fluorescence at certain phases of the modulation, furthermore, allowed for an direct imaging of the axial-velocity eigenfunction of the modes [173].

While strongly confined plasmas in Penning and Paul traps are similar in many respects, the trapping environment is known to influence the properties of the trapped ensembles. The RF-trapping fields are e.g. expected to lead to much higher heating rates for the unmagnetized plasmas in Paul traps as compared to the magnetized plasmas confined in the static potential of a Penning trap [165, 177]. Furthermore, the lack of a rotational symmetry axis in Paul traps has been found to be responsible for the observation of specific crystalline structures [141].

However, the normal mode dynamics of cold unmagnetized plasmas in linear Paul traps are still expected to be governed by the zero temperature charged liquid model and collective vibrational modes were also predicted for these plasmas [82, 167]. The experimental investigation of these normal modes in an unmagnetized plasma in the form of an ion Coulomb crystal in a linear Paul trap will hence in many respects contribute to the understanding of the influence of the trapping environment on the physics of these crystals.

Moreover, since our previous studies indicate that large ion Coulomb crystals confined in a linear Paul trap are promising candidates for the realization of both high-efficient and long-lived quantum memories for light [79, 81], a study of the normal mode dynamics of these crystals might reveal important implications of the excitation of collective vibrational modes and temperature on the fidelity of such an ion based quantum memory. On the other hand, the knowledge of the normal mode dynamics in these ensembles might also open up for the prospect of storing several photonic quantum bits through coherent excitation of specific vibrational modes.

In addition, collective normal mode dynamics of large ion Coulomb crystals might also open up for using these systems for performing quantum simulations, as was recently proposed [178, 179].

Finally, ion Coulomb crystals also represent extremely interesting systems to study cavity optomechanics phenomena with a cold atomic medium [180, 181], since, in spite of their solid nature, they possess free atomic resonance properties and can hence be made very sensitive to the radiation pressure force exerted by optical fields. In this context ion Coulomb crystals could serve as model systems for more traditional solids like micromechanical oscillators [182].

In this chapter, we will present experimental studies of vibrational normal mode dynamics in cold $^{40}Ca^{+}$ ion Coulomb crystals in a linear Paul trap. We use a novel, noninvasive technique which is based on monitoring the response of the ion plasma to a single photon optical cavity field [152]. This is accomplished by measuring the effect of the collective motion on the coherent coupling between the ion ensemble and a standing wave cavity field, while deliberately exciting the normal modes. As the coherent light-matter interaction is sensitive to very small changes of frequencies, the Doppler shifts induced by the ions' motion is directly reflected on the coherent coupling rate. Since the probing does not rely on the observation of incoherently scattered photons as, e.g. in the Doppler velocimetry, the measurement can in principle be purely dispersive and does not require any excitation of the ions. This technique can therefore be used to noninvasively study thermodynamical properties of cold plasmas.

7.2. Theoretical model

In sec. 2.3 the zero-temperature charged liquid model was introduced to account for the shape and density of cold ion Coulomb crystals in a linear Paul trap. We will now extend this study to the plasma dynamics and its collective vibrational modes. For the description of the collective motional behavior we will follow the approach of ref. [82, 167, 168].

7.2.1. Normal modes of a charged liquid plasma

Despite the solid-like structure of cold ion Coulomb crystals, the thermal equilibrium state of a sufficiently large ion ensemble trapped in the cylindrical symmetric trapping potential of a linear Paul trap was in sec. 2.3 found to be governed by a zero-temperature charged liquid plasma model. The cylindrical symmetry of the confinement potential (see eq. (2.9)) imposes a spheroidal shape of the nonneutral plasma [111] with half-length L and radius R (see fig. 2.4). In the equilibrium state, where the force on each individual ions has to vanish, the total potential in the plasma has to be constant (see eq. 2.12) and the density of the ensemble, which is related to the plasma potential through Poisson's law, was also found to be constant. A perturbation of the equilibrium state, e.g. by a small time-dependent variation of the end-cap voltages, will induce small oscillations in the spheroidal plasma, which, for sufficiently small perturbations, can be treated using the linear fluid theory [168].

For a non-magnetic zero temperature charged liquid plasma[1] these perturbations are described by the (linearized) continuity, momentum and Poisson equations

$$0 = \frac{\partial}{\partial t}\delta\rho_0 + \nabla\cdot(\tilde{\rho}_0\delta\mathbf{v}) \tag{7.1a}$$

$$\frac{\partial}{\partial t}\delta\mathbf{v} = -\frac{Q}{M}\nabla\Phi \tag{7.1b}$$

$$\nabla^2\Phi = -\frac{Q}{\varepsilon_0}\delta\rho_0, \tag{7.1c}$$

where $\delta\rho_0$, $\delta\mathbf{v}$ and Φ are the perturbed density, velocity and potential, respectively. $\tilde{\rho}_0$ is the fluid density, equal to ρ_0 within the plasma and 0 outside. Standard manipulations of eqs. (7.1) yields the differential Maxwell equation

$$\varepsilon\nabla^2\Phi = 0. \tag{7.2}$$

The frequency dependent isotropic dielectric tensor ε is given by

$$\varepsilon = \begin{cases} 1 & \text{outside the plasma} \\ 1-\frac{\omega_p^2}{\omega^2} & \text{inside the plasma} \end{cases} \tag{7.3}$$

where ω_p is the plasma frequency defined in eq. (2.18). Decomposing eq. (7.2) into two parts for the potential inside and outside the plasma Φ^{in} and Φ^{out} yields

$$0 = \left(1-\frac{\omega_p^2}{\omega^2}\right)\nabla^2\Phi^{\text{in}} \tag{7.4a}$$

$$0 = \nabla^2\Phi^{\text{out}}, \tag{7.4b}$$

[1] For plasmas confined in a linear Paul trap, we can restrict the situation to non-magnetic fluids, for details on the magnetic case see [82, 167, 168]

where the potentials must match across the plasma surface S

$$\Phi^{\text{in}}(\boldsymbol{r})\Big|_S = \Phi^{\text{out}}(\boldsymbol{r})\big|_S . \tag{7.5}$$

Eq. (7.4) can either be fulfilled by $\omega = \omega_p$ or by a plasma potential fulfilling the Laplace equation $\nabla^2\Phi^{\text{in}} = 0$. The first case describes perturbations within the plasma which do not affect the external potential, and always oscillate at the plasma frequency. These are the so-called bulk plasma modes, and examples of such bulk modes are the breathing modes, where the surface of the plasma shows breathing oscillations[2]. The bulk modes will not be investigated further in this thesis. The latter case, where the Laplace equation is fulfilled both by Φ^{in} and Φ^{out}, corresponds to surface plasma oscillations. In this situation, the solution turns out to be separable in spheroidal coordinates, $\boldsymbol{r} = (\xi_1,\ \xi_2,\ \phi)$ which are related to the usual cylindrical coordinates, $\boldsymbol{r} = (\rho, \phi, z)$, by:

$$z = \xi_1\xi_2 \tag{7.6a}$$

$$\rho = \sqrt{\left[\xi_1^2 - (d^2)\right]\left[1-\xi_2^2\right]}, \tag{7.6b}$$

where $d = \sqrt{L^2 - R^2}$. ξ_1 can be understood as a generalized radial coordinate and ξ_2 as a generalized latitude, ϕ is the usual azimuthal angle. In this coordinate system, the surface of the plasma is a constant ξ_1 surface. The solution to the Laplace equation is in this frame of reference given by [168]

$$\Phi^{in} = AP_l^m(\xi_1/d)\,P_l^m(\xi_2/d)\exp(im\phi) \tag{7.7a}$$

$$\Phi^{out} = BQ_l^m(\xi_1/d)\,P_l^m(\xi_2/d)\exp(im\phi), \tag{7.7b}$$

where P_l^m and Q_l^m are the first- and second-order Legendre polynomials (see appendix B), with cylindrical indices (l,m), $l \geq |m|$ and with amplitudes A and B. The spatial variation of a certain mode is characterized by the two indices l and m, where the number of zeros encountered upon circling the equator of the spheroid is $|m|$, and $|l-m|$ upon traversing it from pole to pole along a circle. Substituting eq. (7.7) into (7.5) yields the frequencies of the (l,m) modes [82]

$$\omega_{(l,m)} = \frac{\omega_p}{\sqrt{1 - \frac{P_l^m Q_l^{m'}}{Q_l^m P_l^{m'}}}}, \tag{7.8}$$

where $P_l^m = P_l^m(1/\sqrt{1-\alpha^2})$, $Q_l^m = Q_l^m(1/\sqrt{1-\alpha^2})$ and with the prime denoting differentiation with respect to the entire argument. α denotes the aspect ratio of the crystal (see fig. 2.4).

The corresponding spatial modes generally have a non-trivial dependence on the ions' position in the crystal. For longitudinal modes $(l, m = 0)$, the displacement from the equilibrium position z_0, close to the axis of rotational symmetry ($\rho \simeq 0$), is $\delta z = z - z_0$ and can be found to be

$$\delta z \propto P_l^{0'}(z/\sqrt{L^2 - R^2}). \tag{7.9}$$

[2] In certain cases, e.g. for spherical, cylindrical and disc plasmas, the breathing mode happens to also be a crystal eigenmode.

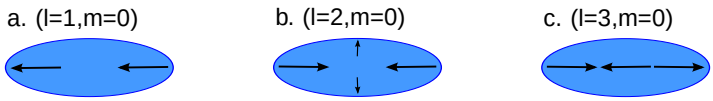

Figure 7.1.: Deformation of the ion Coulomb crystals for the three lowest-order axial modes (a. $(1,0)$. b. $(2,0)$, c. $(3,0)$) The arrows indicate the motional direction at a given time. The spatial dependence of the potential Φ^{in} can be found in tab. 7.1.

(l,m)	$\Phi_{\text{in}}(\rho,\phi,z)$
(1,0)	z
(1,1)	$\rho e^{i\phi}$
(2,0)	$[2z^2-\rho^2]/4-\frac{d^2}{2}$
(2,1)	$\rho z \exp i\phi$
(2,2)	$\rho^2 \exp 2i\phi$
(3,0)	$z[10z^2-15\rho^2-6d^2]\exp i\phi$

Table 7.1.: Spatial dependence of the potential $\Phi_{in}(\rho,\phi,z)$ for the lowest (l,m) normal modes in cylindrical coordinates.

Hence, the axial modes with $m=0$ all have a spatial variation along the z-axis and an excitation of these modes will lead to measurable Doppler shifts of the ions resonance frequency along this axis. We will later use this shift to experimentally measure these frequencies. In fig. 7.1 are depicted the spatial deformation of the spheroidal plasma for the lowest axial modes $(l=1,2,3,m=0)$.

The calculated plasma potentials in the spheroidal plasma for some of the lowest order vibrational modes are given in tab. 7.1 in cylindrical coordinates $\boldsymbol{r}=(\rho,\phi,z)$.

7.2.2. Mode excitation

Having derived expressions for the frequencies of the collective modes and for the spatial dependence of the potential in the spheroidal plasma, we can now discuss how these modes can be excited by a suitable modulation of the trapping potentials. In the experiment, this is accomplished by applying additional AC-voltages to the four pieces forming the end caps on each side of the trap (see fig. 2.1) with a frequency close to the resonance frequency of the mode. For the axial modes $(l,m=0)$ identical AC-potentials are applied to the four end pieces on each side, either in phase for the modes with even l or with a relative phase of π between the two end caps for modes with even l. For the three lowest axial modes, this is depicted schematically in fig. 7.2. More details will be given along

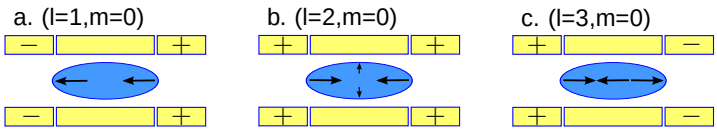

Figure 7.2.: Excitation schemes for the three lowest-order axial modes (a. $(1,0)$. b. $(2,0)$, c. $(3,0)$). The arrows indicate the direction of the motion in the plasma. The appropriate polarities of the excitation fields are indicated by the signs on the electrodes.

with the experimental setup in 7.3.1

7.2.3. Driven steady state

When a periodic external excitation force with a frequency ω close to the resonance frequency of a certain mode is applied, the collective motion and, hence, also the motion of the individual ions will after a certain transient time reach a driven steady state. For an ion located on the revolution axis of the crystal ($\rho = 0$) a simple model can be obtained by modeling the excitation with a position dependent amplitude of the driving force $F_{\text{drive}}(z)$. The equation of motion reads

$$\frac{\mathrm{d}^2 z}{\mathrm{d}t^2} + \beta \frac{\mathrm{d}z}{\mathrm{d}t} + \omega_{(l,m)}^2 (z - z_0) = \frac{F_{\text{drive}}(z_0)}{M} \cos(\omega t), \tag{7.10}$$

where z_0 is the equilibrium position of the ion, and where we assume the amplitude of the driving force to be constant within δz for each ion $F_{\text{drive}}(z) = F_{\text{drive}}(z_0)$. All damping mechanisms of the periodic motion of the ion ensemble are combined in the damping constant β. In practise, the damping will be dominated by two mechanisms namely the the off-resonant coupling to other vibrational modes [167] and the radiative damping by the Doppler cooling laser. The damping rate can hence be written as

$$\beta = \beta_{\text{cool}} + \beta_0, \tag{7.11}$$

where the first term β_{cool} corresponds to the friction induced by the laser cooling and β_0 accounts for the coupling to other modes.

Eq. (7.10) is the well-known differential equation of a driven damped harmonic oscillator. The solution in steady state is of the form $\delta z(t) = \zeta(\omega, z)\cos(\omega t - \Phi)$, where

$$\zeta(\omega, z) = \frac{F_{\text{drive}}(z_0)}{M\sqrt{(\omega - \omega_{(l,m)})^2 + 2\beta^2\omega^2}}. \tag{7.12}$$

is the frequency and position dependent amplitude and Φ is a phase. Each ion will hence oscillate with an amplitude that depends on its position, the frequency of the driving force and the amplitude of the force. Accordingly, the velocity of the individual ions is of the form

$$v(z,t) = \tilde{v}(z)\cos(\omega t - \Phi) \tag{7.13}$$

with a velocity amplitude given by

$$\tilde{v}(z) = \omega\zeta(\omega, z). \tag{7.14}$$

The driven motion of the ions will obviously, through the Doppler shift, also lead to a modulation of the atomic resonance frequencies of the individual atoms, with a shift that depends on the position in the crystal and the instantaneous velocity of the ion. We will in the next subsection discuss how this shift will influence the collective coupling of the ion Coulomb crystal with the cavity field and how this can be used to investigate the collective dynamics of the cold plasma.

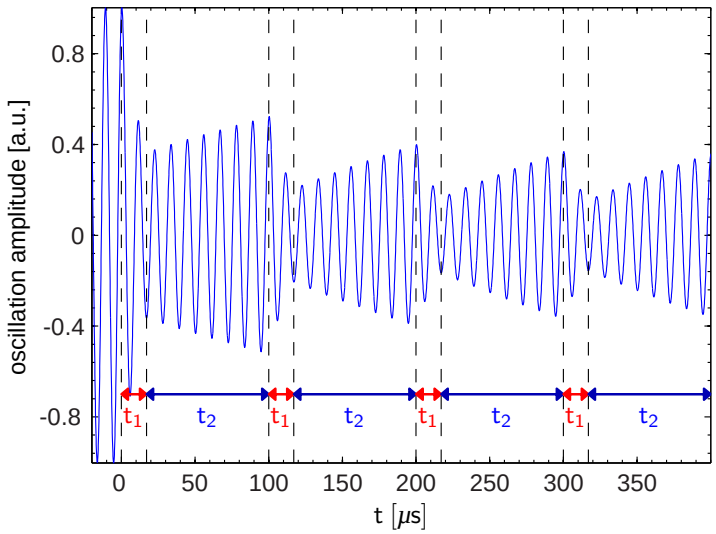

Figure 7.3.: Simulation of the amplitude of the driven motion for the $(1,0)$ mode. A sequence with cooling light with a length of $t_1 = 17$ μs alternates with a $t_2 = 83$ μs period of free evolution. The amplitude of the motion increases during the free evolution, and is damped during cooling. The remaining parameters for the simulation where $\omega = \omega_{10} = 2\pi \times 90$ kHz, $\beta_{\text{cool}} = 2\pi \times 20$ kHz and $\beta_0 = 2\pi \times 1$ kHz.

Damping in the system and modelling

As mentioned above, the friction term in eq. (7.10) is dominated by two major contributions, namely dissipation induced by laser cooling and by the coupling to additional vibrational modes. In our experiment, the Doppler cooling is only applied for a fraction of the time, as the probing of the coherent interaction between the ion Coulomb crystal and the cavity field mode requires a sequence of cooling, state preparation and probing, as depicted in 5.2. In phases where there is no cooling light present, the only friction force will be due to the off-resonant coupling to other normal modes and the equation of motion in these phases is

$$\frac{\mathrm{d}^2 z}{\mathrm{d}t^2} + \beta_0 \frac{\mathrm{d}z}{\mathrm{d}t} + \omega_{(l,m)}^2 z = \frac{F_{\text{drive}}}{M} \cos(\omega t + \varphi). \tag{7.15}$$

The experimental sequence is typically repeated at rates of ~ 50 kHz and phases with and without Doppler cooling will constantly alternate[3]. The amplitude of the driven oscillation is hence not expected to be constant, as it will decrease due to the additional friction during cooling phases and will increase again in phases where there is no Doppler cooling. The steady state solution in eq. 7.12 does not include this change of the oscillation amplitude. Nevertheless, after some iterations of the sequence, the system will obtain a quasi-steady state, where the amplitude envelope in subsequent sequences will be the same. This is illustrated in fig. 7.3 by a simulation of the evolution of the modulation amplitude for an

[3] During the optical pumping period, the effect of the Doppler cooling laser will exponentially drop, however, especially at the beginning of the optical pumping, the ions will still experience noticeable cooling.

alternating sequence shown in fig. 7.3. A cooling phase with a length of $t_{\text{cool}} = 17\ \mu$s is alternated with a $t_{\text{free}} = 83\ \mu$s long period of free evolution, where only the off-resonant coupling to other modes contributes to the damping. Initially, the simulation comprises a long phase of Doppler cooling free evolution until the system reaches a steady state with a maximum amplitude of the driven oscillation. Then, during the first cooling pulses, the amplitude of the modulation is drastically reduced. After the first cooling phase, it will increases again during the free evolution, before being damped again during the next cooling cycle. After some iterations of the sequence, a quasi steady state is reached and the evolution of the modulation amplitude is the same in subsequent sequences. The modulation frequency for the simulation was chosen to be $\omega = \omega_{10} = 2\pi \times 90$ kHz, the damping rates were set to realistic values of $\beta_{\text{cool}} = 2\pi \times 20$ kHz and $\beta_0 = 2\pi \times 1$ kHz [167]. In the measurement, the sequence time will be much shorter ($\sim 20\ \mu$s) which for typical modulation frequencies of $\sim 2\pi \times 100$ KHz corresponds only to few oscillation periods and to illustrate the effect, the simulation was conducted for a much longer sequence. However, the qualitative behavior will be the same in the experiment and we will after some iterations probe the quasi-steady state of the system.

7.2.4. Effect of the motion on the coherent coupling

In our experiment, we want to directly use the coherent coupling between ion Coulomb crystals and a single-photon cavity field to gain information on the collective motion of the ions. This will be accomplished by the same technique used to measure collective strong coupling in sec. 5.4, namely by monitoring the effective cavity decay rate κ'. For an ion ensemble at rest, this rate is, as a function of the probe detuning Δ, expected to vary as $\kappa'(\Delta) = \kappa + g_{\text{N}}^2 \frac{\gamma}{\gamma^2+\Delta^2}$ (see eq. (3.48a), where $g_{\text{N}} = g\sqrt{N}$ denotes the collective coherent coupling rate, γ is the atomic dipole decay rate and Δ is the detuning of the probe laser from atomic resonance. Already in sec. 3.3 we discussed the effect of motion on the coherent coupling rate and the effective cavity decay rate and we will start out by recapitulating some of the results we found there, before adapting them to the situation of a collective driven motion. Assuming the velocity of the ions in the ensemble to be governed by a certain velocity distribution $f(v)$ we found in eq.(3.51a) the following expression for the effective cavity decay rate

$$\kappa'(\Delta) = \kappa + g_{\text{N}}^2 \int \mathrm{d}v\, f(v)\xi(\Delta, v)\gamma = \kappa + g_{\text{N}}^2 \int \mathrm{d}z\, f(v(z))\xi(\Delta, v)\gamma,$$

where the parameter

$$\xi(\Delta, v) = \frac{\gamma^2 + \Delta^2 + (kv)^2}{(\gamma^2+\Delta^2)^2 + 2(\gamma^2 - \Delta^2)(kv)^2 + (kv)^4}$$

was defined in eq. (3.52) and $k = \frac{2\pi}{\lambda}$ is the wave vector.

When a certain collective vibrational mode is excited, the velocity distribution $f(v)$ will in general depend on the individual mode and will vary over one oscillation period of the excitation force and hence also be time dependent. The position and time dependent velocity of an ion on the crystal revolution axis[4] was found in (7.14).

[4] Obviously not all the ions contributing to the collective coherent coupling will be located on the revolution axis of the crystal. However, for crystals with a radial extension much bigger than the waist of the fundamental TEM_{00} cavity mode it is a good first approximation to treat the motion of the ions which contribute to the coherent coupling, as if they were located on axis.

For simplicity, we will in the following first discuss the excitation of the collective center of mass mode $(1,0)$, where all the ions in the ensemble at a certain time t move with equal velocity $v_z(t)$, and generalize the analysis to higher order vibrational modes afterwards.

For the center of mass mode, the velocity distribution at a certain time t will only depend on the phase of the excitation force and is simply given by a delta function $f(v(t)) = \delta(v - v_z(t))$, i.e. it does not depend on the position of the individual ions along the crystal axis. In this case, the integral in eq. (3.51a) can be simply evaluated and yields at a certain time t for the effective cavity decay rate

$$\kappa'(\Delta,t) = \kappa + g_N^2 \frac{\gamma\left[\gamma^2+\Delta^2+(kv_z(t))^2\right]}{(\gamma^2+\Delta^2)^2+2(\gamma^2-\Delta^2)(kv_z(t))^2+(kv_z(t))^4}. \tag{7.16}$$

Already from this equation it can be seen that the motion of the ions along the axis will lead to a lower effective cavity decay rate, as the coupling strength is reduced due to the Doppler-shift of the resonance. Furthermore, the instantaneous velocity and hence also the effective cavity decay rate will through the time dependence of the excitation force also depend on t. As was explained in sec. 5.3, to reconstruct the cavity reflectivity spectrum for a certain detuning of the probe laser Δ, the cavity length is scanned over the atomic resonance and we measure repeatedly the cavity reflection signal of a probe field at the single photon level, using the sequence shown in fig. 5.2 and averaging over typically 100 scans.

The measurement sequence is repeated at a rate of typically 50 kHz and has no fixed phase relation to the periodic excitation of the motion of the ions. However, if the timescale at which the velocity of the ions changes is slow as compared to the effective cavity decay time each individual scan will measure the broadening of the effective cavity decay rate at an arbitrary phase of the excitation. Averaging over many cavity reflection spectra will therefore also imply an average over the phase of the excitation field and we expect the measured mean effective cavity decay rate, κ', to be given by eq. (7.16), averaged over one oscillation period, which yields

$$\overline{\kappa'}_{(1,0)}(\Delta) = \kappa + \frac{g_N^2}{2\pi}\int_0^{2\pi} d\varphi \frac{\gamma\left[\gamma^2+\Delta^2+(k\tilde{v}_z\cos\varphi)^2\right]}{(\gamma^2+\Delta^2)^2+2(\gamma^2-\Delta^2)(k\tilde{v}_z\cos\varphi)^2+(k\tilde{v}_z\cos\varphi)^4} \tag{7.17}$$

where $\tilde{v}_z$ denotes the velocity amplitude and where the integration is performed over one oscillation period of the driven motion. For the center of mass mode, this integral can be solved analytically and yields [183]

$$\overline{\kappa'}_{1,0} = \kappa + g_N^2 \frac{\sqrt{\gamma^2+\Delta^2}\sin\left(\frac{1}{2}\arctan\left(\frac{\sqrt{4\Delta^2\gamma^2(k\tilde{v}_z)^4}}{(\gamma^2+\Delta^2)^2+(k\tilde{v}_z)^2(\gamma^2-\Delta^2)}\right)+\arctan\left(\sqrt{\frac{\gamma^2}{\Delta^2}}\right)\right)}{\left(((\gamma^2+\Delta^2)^2+(k\tilde{v}_z)^2(\gamma^2-\Delta^2))^2+4\Delta^2(k\tilde{v}_z)^4\gamma^2\right)^{\frac{1}{4}}} \tag{7.18}$$

In general, when exciting an arbitrary collective vibrational mode, the velocity distribution will be more complex and not all the ions in the crystal will at a given instance move at the same velocity. Each ion in the ensemble will still carry out a harmonic oscillations, however, the amplitude of the motion $\tilde{v}(z)$ will now depend on the ions' individual position within the plasma, see eq. (7.14). Nevertheless, we will for each measurement

of the cavity reflectivity obtain an effective cavity decay rate, corresponding to an instantaneous velocity distribution in the crystal. Moreover, as our measurement sequence is not synchronized to the periodic modulation, averaging over many scans will imply a time average. The expected mean effective cavity decay rate can hence be calculated by averaging over the known velocity amplitudes of the ions in the crystal and over one oscillation period[5]

$$\bar{\kappa}' = \kappa + \frac{g_N^2}{2\pi}\int \mathrm{d}\varphi \int \mathrm{d}\tilde{v}(z) \frac{f(\tilde{v}(z))\,\gamma[\gamma^2+\Delta^2+(k\tilde{v}(z)\cos\varphi)^2]}{(\gamma^2+\Delta^2)^2+2(\gamma^2-\Delta^2)(k\tilde{v}(z)\cos\varphi)^2+(k\tilde{v}(z)\cos\varphi)^4} \quad (7.19)$$

$$= \kappa + \frac{g_N^2}{2\pi}\int \mathrm{d}\varphi \int \mathrm{d}z \frac{\omega\zeta(z)\,\gamma[\gamma^2+\Delta^2+(k\omega\zeta(z)\cos\varphi)^2]}{(\gamma^2+\Delta^2)^2+2(\gamma^2-\Delta^2)(k\omega\zeta(z)\cos\varphi)^2+(k\omega\zeta(z)\cos\varphi)^4}.$$

where in the last step, the distribution of the velocity amplitudes $f(\tilde{v}(z))$ was replaced by the known spatial distribution of the amplitudes $\tilde{v}(z) = \omega\zeta(z)$ (see eq. (7.14), the frequency dependence is suppressed for simplicity) and where the integration is performed over the crystal's z-axis.

Beside the $(1,0)$ mode, analytic solutions of this equation can also be calculated for the $(2,0)$ mode [183]. For this mode, the integration over the velocity amplitudes, $\tilde{v}(z)$, and the phase of the excitation yields

$$\bar{\kappa}'_{2,0} = \kappa + \frac{g_N^2}{k\tilde{v}}\left[\tanh^{-1}\left(\sqrt{\frac{k\tilde{v}+\Delta+i\gamma}{k\tilde{v}-\Delta-i\gamma}}\right)+\tanh^{-1}\left(\sqrt{\frac{k\tilde{v}+\Delta-i\gamma}{k\tilde{v}-\Delta+i\gamma}}\right)\right], \quad (7.20)$$

where $\tilde{v}$ now denotes the maximum amplitude of the motion. For higher modes, the integration has to be performed numerically. It can be shown that the result of the integration in eq. (7.19) for the two lowest axial modes is also well approximated by substituting in eq. (7.19) an effective velocity averaged over one oscillation period $v^{\mathrm{eff}}_{(l,m)} = \left[\langle\tilde{v}^2\cos^2(\omega_{l,m}t+\varphi)\rangle\right]^{1/2} = \frac{\tilde{v}}{\sqrt{2}}$ [183]. This yields

$$\bar{\kappa}_{l,0} \approx \kappa + g_N^2 \frac{\gamma[\gamma^2+\Delta^2+(kv^{\mathrm{eff}}_{(l,m)})^2]}{(\gamma^2+\Delta^2)^2+2(\gamma^2-\Delta^2)(kv^{\mathrm{eff}}_{(l,m)})^2+(kv^{\mathrm{eff}}_{(l,m)})^2}. \quad (7.21)$$

7.3. Experimental results

In this section, we will present experimental results on the study of normal mode dynamics of ion Coulomb crystals in a linear Paul trap. The excitation of collective motion will, as was discussed above, be directly reflected in a lowering of the collective coherent coupling between ion Coulomb crystal and a cavity field at the single photon level.

The setup of the cavity trap, the laser systems and the detection systems were already introduced in ch. 4 and we will in this chapter only discuss the technique used to excite the collective vibrational modes of the crystal and briefly recapitulate the measurement method and its application in the context of this chapter before turning to the experimental results.

[5] One could, in principle synchronize the measurement sequence with the modulation and measure the effective cavity decay rate at certain phases of the oscillation, however, one would still have to average over the velocity amplitudes.

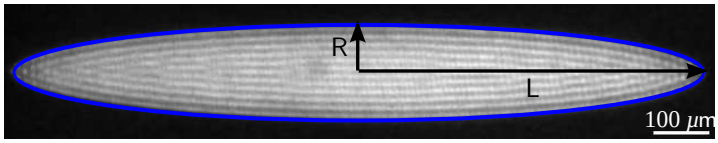

Figure 7.4.: Projection image of a crystal with a half-length $L = (602 \pm 1)$ μm, an aspect ratio $\alpha = 0.135 \pm 0.002$ and a density $\rho_0 = (2.62 \pm 0.05) \times 10^8$ cm^{-3}. It contains ~ 4000 ions of which ~ 300 effectively interact with the cavity field . The DC and RF voltage amplitudes are 2.36 V and 205 V, respectively.

7.3.1. Experimental Setup

The axial normal modes of the nonneutral plasma predicted by the zero-temperature charged liquid model can be excited by applying appropriate sinusoidal potentials to the endcaps formed by the four outer electrodes on each side of the linear Paul trap (see fig. 2.1). Depending on the symmetry of the mode, one has to either apply AC-fields in-phase (l even) or with a relative phase of π (l odd). The appropriate phases for the three lowest axial modes are indicated by the signs on the schematic electrodes in fig. 7.1. A projection image of a typical ion Coulomb crystal as used in the experiments is shown in fig. 7.4. With a half-length of $L = (602 \pm 1)$ μm, a density of $\rho_0 = (2.62 \pm 0.05) \times 10^8$ cm^{-3} the crystal contains approximately 4000 ions.

The measurement sequence used for the plasma mode diagnostics is identical to the one shown in fig. 5.2. During the first 5 μs, the ion Coulomb crystal is Doppler laser-cooled, followed by a period of 12 μs, where the ions in the crystal are prepared in the $m_J = +3/2$ magnetic sub-state of the long-lived metastable $D_{3/2}$ level by optical pumping. Finally, a weak left-handed circularly-polarized pulse (1.4 μs long) of 866 nm light is coupled into the cavity to probe the collective response of the ions. The mean intracavity photon number is, as in the previous experiments, less or about one at any time. During this probing period, the photons reflected by the cavity are measured by the probe APD. The 20 μs sequence is repeated at a rate of 50 kHz while the cavity length is scanned at a rate of 30 Hz, see sec. 4.8.3, and the cavity lineshape is reconstructed by averaging a few hundred scans. When exciting a certain normal mode of the plasma, the Doppler shift induced by the motion of the ions will effectively reduce the coherent light-matter coupling in the system, as discussed in eq. (7.16). The 20 μs measurement sequence is continuously repeated and is not synchronized with the excitation voltage modulation. On each scan the coherent coupling will hence be measured at an arbitrary phase of the sinusoidal excitation and taking the mean of many scans will effectively also average over the periodic oscillation. The averaged effective cavity decay rate is thus expected to follow eq. (7.19).

Fig. 7.5 shows the effective cavity decay for a probe laser resonant with the atomic transition ($\Delta = 0$) as a function of the frequency of the excitation voltage around the resonance of the $(2,0)$ "quadrupole" mode measured for the crystal shown in fig. 7.4. A clearly reduced effective cavity field decay rate is observed around 142 kHz. The measured resonance value of $\omega_{(2,0)}^{\text{meas}} = 2\pi \times (142.1 \pm 0.1)$ kHz is deduced from a Lorentzian-fit and in good agreement with the resonance frequency $\omega_{(2,0)}^{\text{model}} = 2\pi \times (142.2 \pm 1.1)$ kHz cal-

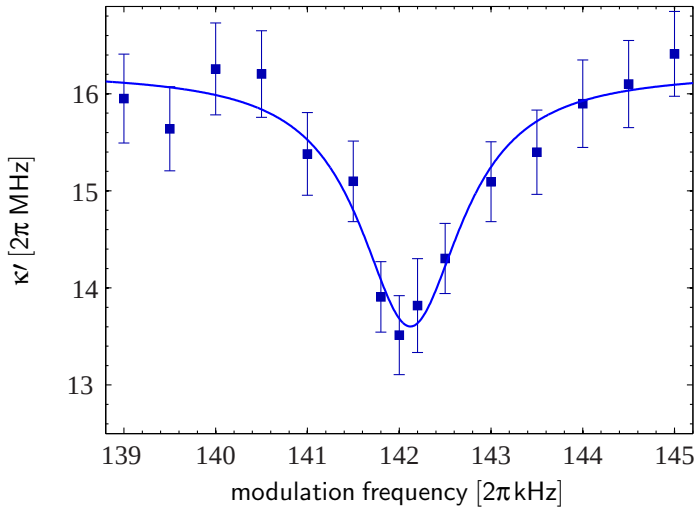

Figure 7.5.: Cavity probe linewidth as a function of the mode excitation frequency applied to drive the equivalent of the $(2,0)$ mode of the crystal shown in fig. 7.4. The probe is tuned to atomic resonance ($\Delta = 0$) and the AC modulation voltage is applied to the two endcaps in phase with a peak-to-peak amplitude of 0.75 V. The red line is a Lorentzian fit to the data and yields a resonance frequency of $\omega_{(2,0)}^{\text{model}} = 2\pi \times (142.2 \pm 1.1)$ kHz.

culated according to eq. (7.8) for the $(2,0)$ mode of a charged liquid crystal with an aspect ratio $\alpha = 0.135$ and an ion density of $\rho_0 = (2.62 \pm 0.05) \times 10^8$ cm^{-3}.

7.3.2. Vibrational mode resonance frequencies

In order to test more generally how well the uniformly charged liquid model describes unmagnetized ion plasmas confined in a linear Paul trap, the resonance frequencies of the lowest lying axial normal modes of ion crystals with various aspect ratios are determined by monitoring the effective cavity decay rate for a probe laser resonant with the atomic transition ($\Delta = 0$). The measured mode resonance frequencies are presented in Fig. 7.6 together with the predicted values from the charged liquid model (see Eq. (7.8)) for the $(1,0)$, $(2,0)$ and $(3,0)$ modes. The experimentally determined values are consistent with the theoretical prediction to better than one percent for all experimental data and clearly show that the model of a zero-temperature charged liquid plasma appropriately describes the collective dynamics of ion Coulomb crystals in linear Paul trap.

The results presented here are another test of the zero temperature charged liquid model, complementary to the measurement of the ratio of axial and radial trap frequencies for different trapping parameters, as theoretically discussed in sec. 2.3.2 and experimentally confirmed in the calibration measurements presented in sec. 4.7. Though technically more challenging, the measurements of the vibrational modes using the collective interaction of the ion ensemble with a weak cavity light field at the single photon level give the normal mode frequencies (and therefore the plasma frequency) with excellent precision.

The accurate agreement between the measured and the theoretically predicted frequen-

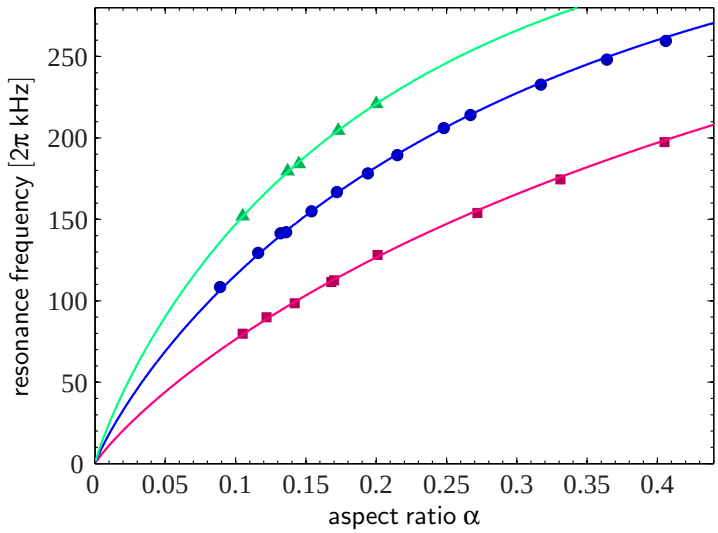

Figure 7.6.: Resonance frequencies corresponding to the $(1,0)$ (squares), the $(2,0)$ (circles) and the $(3,0)$ (triangles) modes as a function of the aspect ratio α, for a fixed plasma frequency $\omega_p = 2\pi \times 536$ kHz ($U_{rf} = 205V$). The solid lines show the theoretical predictions of eq. (7.8). The error bars are within the point size.

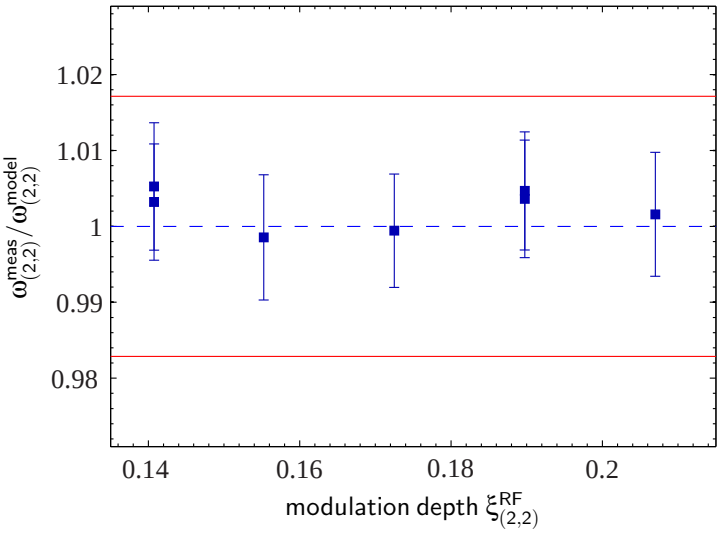

Figure 7.7.: Resonance frequency of the $(2,0)$ mode as a function of the $(2,2)$ mode off-resonant modulation depth $\xi^{rf}_{(2,2)}$ (see text) for a fixed aspect ratio $\alpha = 0.135$. The mode resonance frequency is normalized to that expected for a plasma without any excitation of the $(2,2)$ mode and the red lines show the uncertainty in the expected resonance frequency due to the density calibration. The Coulomb crystals contain between 4000 and 12000 ions (of which between 300 and 700 ions effectively interact with the cavity field), with densities of $2.6 - 5.6 \times 10^8$ cm^{-3}

cies of the normal modes of the nonmagnetic plasma may appear surprising considering that, during all measurements, the $(2,2)$ mode of the plasma is continuously off-resonantly excited by the linear RF quadrupole field confining the plasma through the micromotion. The equation of motion for an ion at the radial position (x_0, y_0) was found in eq. (2.6). The micromotion at the frequency of the RF potential modulates the slower secular motion with an amplitude given by

$$\bar{x}(t) = x_0\left[1+\frac{q}{2}\cos(\Omega_{\mathrm{RF}}t)\right] \tag{7.22a}$$

$$\bar{y}(t) = y_0\left[1-\frac{q}{2}\cos(\Omega_{\mathrm{RF}}t)\right]. \tag{7.22b}$$

These equations suggest the definition of a modulation depth for the $(2,2)$ mode

$$\xi^{rf}_{(2,2)} = \frac{q}{2} = \frac{QU_{\mathrm{RF}}}{Mr_0^2\Omega_{\mathrm{RF}}^2}. \tag{7.23}$$

Depending on the RF amplitude, this modulation depth can indeed amount to up to 20% of the secular motion amplitude of the radial extension of the crystal. The amplitude of this radial modulation is hence comparable to typical axial excitation amplitudes for the $(l,0)$ modes and one could expect deviations from the model.

To test the influence of the off-resonant excitation on the frequency of a particular (l,m) normal mode of the plasma, we performed measurements for crystals with a fixed aspect ratio of $\alpha = 0.135$ but various RF-amplitudes, and hence different modulation depths $\xi^{rf}_{(2,2)}$.

The inset of Fig. 7.6 shows the measured frequency of the $(2,0)$ mode as a function of modulation depths $\xi^{rf}_{(2,2)}$. It is is found to be constant within the current experimental accuracy and shows no systematic dependence on $\xi^{rf}_{(2,2)}$. Moreover, this result is consistent with molecular dynamics simulations from which it has been predicted that the radial RF field-driven micromotion in linear Paul traps should have an extremely weak coupling into the axial motion of the ions [165] and the measurements presented in sec. 6.4, where the coherent coupling of needle-like crystals was measured for various offsets of the crystals revolution axis from the field free nodal line of the RF potential.

7.3.3. Measurement of the mode temperature

The technique used to measure the frequency of the lowest axial frequency can also be used to measure the maximum amplitude of the driven motion of a given mode and therefore the equivalent temperature of this mode. In Fig. 7.6 a. and b., the effective cavity decay rate with and without exciting resonantly the a. $(1,0)$ and b. $(2,0)$ mode (resonance frequencies $\omega_{(1,0)} = 2\pi\times 94$ kHz and $\omega_{(2,0)} = 2\pi\times 145$ kHz) are shown as a function of the detuning of the probe with respect to the atomic resonance. The crystals used for the two experiments were similar to the one shown in fig. 7.4 with $N\sim 4000$ ions and aspect ratios of $\alpha\sim 0.13$.

Fitting the two profiles in absence of the mode excitation (red squares in fig. 7.6 a. and b.) with the expected Lorentzian shaped curve (solid red lines) of eq. (3.48a), where we beside the collective coupling rate g_{N} also left the effective cavity decay rate κ and the effective dipole decay rate γ' as free fitting parameters to account for the finite temperature

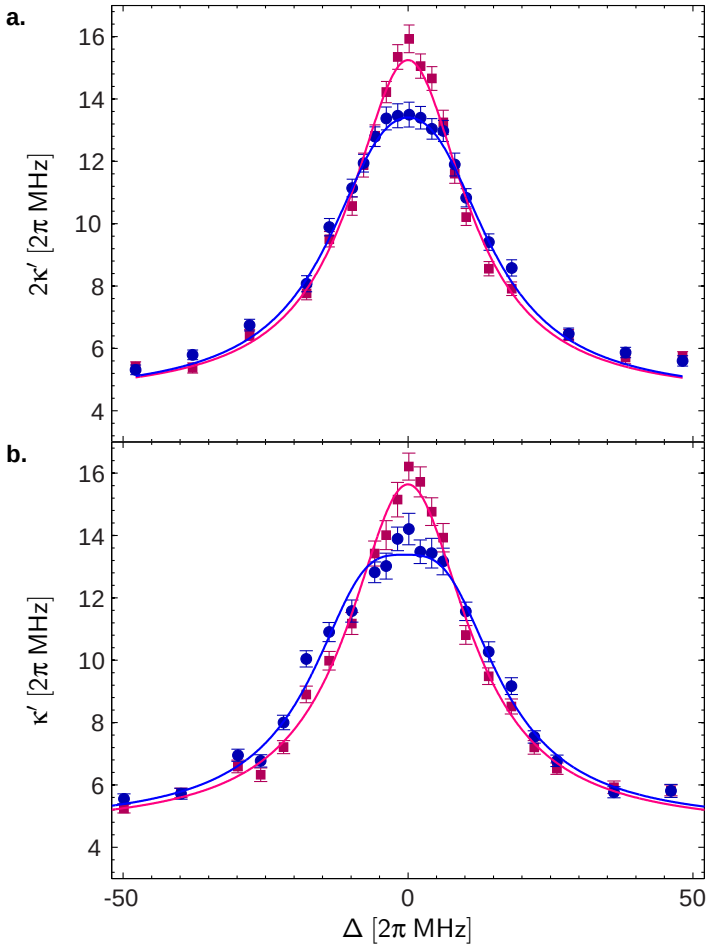

Figure 7.8.: Effective cavity decay rate as a function of the probe detuning, without (red squares) or with (blue circles) modulation for a modulation resonant with **a.** the $(1,0)$ and **b.** the $(2,0)$ mode frequency. The crystals were similar to the one presented in Fig. 7.4, with a aspect ratio of $\alpha \sim 0.13$, a density of $\rho_0 = (2.62 \pm 0.05) \cdot 10^8 \mathrm{cm}^{-1}$ and $N \sim 4000$. The solid lines are fits according to eq. (7.19).

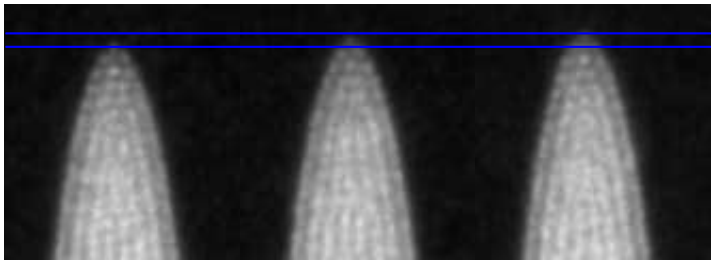

Figure 7.9.: Stroboscopic projection images of ion Coulomb crystals obtained while resonantly exciting the $(1,0)$ normal mode at three different phases of the modulation. The blue lines indicate the amplitude of the motion. The ions move by ± 9 μm around their equilibrium position.

of the sample (for a discussion see sec. 5.4). The values we deduce from the fit to the data in fig. 7.6 a. are are $(g_N, \kappa, \gamma') = 2\pi \times (8.2 \pm 0.1,\ 2.2 \pm 0.1,\ 12.3 \pm 0.5)$ MHz), while the fit in fig. 7.6 b. yields $(g_N, \kappa, \gamma') = 2\pi \times (8.4 \pm 0.2,\ 2.3 \pm 0.1,\ 12.7 \pm 0.6)$ MHz), in good agreement with the first fit.

When the $(1,0)$ or the $(2,0)$ mode are resonantly excited, the effective cavity decay rate as a function of the probe detuning is in both cases modified to a non-Lorentzian profile (blue circles in fig. 7.6 a. and b.). To determine the kinetic energy of the periodic motion, we fitted the data to eq. (7.19). From these fits, we can deduce the maximum velocities of the periodic driven motion to be $\tilde{v}^{\text{fit}}_{(1,0)} = (5.8 \pm 1.0)$ m/s for the $(1,0)$ mode and of $\tilde{v}^{\text{fit}}_{(2,0)} = (8.4 \pm 0.8)$ m/s for the $(2,0)$ mode.

To cross-check the maximum velocities deduced from the fits, a second technique can be used to directly determine the oscillation amplitude of the ions from projection images. As the typical integration times of the CCD camera is of the order of ~ 100 ms, the camera itself is not fast enough to resolve the normal mode oscillations at frequencies of ~ 100 kHz. To circumvent this limitation, we can gate the image intensifier which is incorporated into the imaging system, to acquire stroboscopic images of the ion Coulomb crystals, as was explained in sec. 4.4.1. In this configuration, the supply voltage of the image intensifier is provided by a very short pulse (~ 20 ns) and the image intensifier will only during this short period be sensitive to fluorescence light. By synchronizing these pulses to the modulation voltage on the trap electrode, the ions can be monitored at well-defined phases of the oscillation. The CCD camera will then simply obtain the averaged fluorescence of many gating cycles. The detected fluorescence level is substantially lower and the images have to be integrated over longer times. This obviously limits the achievable duty cycle and this method is not as fast to find the resonance frequency of large crystal modes. However, once the modulation frequency is determined by measuring the broadening of the effective cavity field decay rate, the stroboscopic imaging of the ions is a direct way of measuring the amplitude of the driven motion. In fig. 7.9 three stroboscopic projection images obtained at different phases of the modulation are shown. The images were taken while resonantly exciting the $(1,0)$ normal mode, at phases of the modulation of $\varphi = -\pi/2$, $\varphi = 0$ and $\varphi = +\pi/2$ and a clear displacement of the ions at the tip

of the crystal can be observed.

Using this technique, we deduce amplitudes of the periodic motion of $\tilde{z}_{1,0}^{\text{fluo}} = (9.0 \pm 1.0)\ \mu$m for the $(1,0)$ mode and $\tilde{z}_{2,0}^{\text{fluo}} = (9.5 \pm 1)\ \mu$m for the $(2,0)$ mode, corresponding to maximum velocities of $\tilde{v}_{(1,0)}^{\text{fluo}} = (5.3 \pm 0.6)\ \text{ms}^{-1}$ and $\tilde{v}_{(1,0)}^{\text{fluo}} = (8.7 \pm 0.9)\ \text{ms}^{-1}$, respectively. The results of the fluorescence based measurements are in very good agreement with the previously measured values and prove that quantitative information about the ions' motion can reliably be obtained from the ion-cavity coupling without the need for observing directly the fluorescence signal.

7.4. Outlook and Applications

In the previous sections we described how the coherent coupling between ion Coulomb crystals and a cavity field can be used to reveal information about the collective motion of the cold plasma. In this section, we will give an outlook and present some applications and preliminary results on how this measurement technique can be applied to investigate various aspects of the physics of strongly confined plasmas.

7.4.1. Measurement of temperature

Already in sec. 3.3 we discussed the effect of motion, in particular thermal motion, on the coherent interaction between ion Coulomb crystal and a cavity field mode. In this chapter we refined the simple model which was given there and could demonstrate how we can use this model to measure the kinetic energy and hence the temperature of a certain normal mode (see sec. 7.3.3).

In principle one can envision to measure more complex and possibly unknown velocity distributions in a similar fashion, and e.g. use this technique to study the thermal Maxwell-Boltzmann distribution of an unperturbed ion Coulomb crystal. This would make it possible to determine the translational temperature of large ion Coulomb crystal, which is a difficult task in practice and e.g. relies on comparison of projection images to molecular dynamics simulations [184].

The precise knowledge and possibly also control of the temperature of the sample would be valuable, e.g. for the study of possible implications for the realization of a ion Coulomb crystal-based quantum memory or for the investigation of optomechanical effects in the coherent interaction between ion Coulomb crystal and cavity light field.

Our measurement of the translational temperature of particular vibrational modes are promising first steps towards a more direct measurement of the thermal kinetic energy of large ion Coulomb crystals. However, further systematic experimental and theoretical investigations are required to approach this goal.

7.4.2. Investigation of Plasma thermodynamics

The noninvasive nature of our measurement technique, which is not based on incoherent scattering of photons and can be purely dispersive in nature, would furthermore make it possible to measure other characteristics of the cold strongly confined plasmas, which are not easily accessible with fluorescence based detection methods [171–173]. Examples are the investigation of the intrinsic coupling between the various normal modes of the

cold fluid plasma [168] and related correlation effects, or the study of the dependence of damping and coupling effects with various parameters, e.g. the density, the number of ions, the size or the temperature of the plasma. In the following, we will present preliminary results for two of the envisioned applications, namely a study of the intrinsic damping and of the influence of the density.

Off resonant-mode coupling

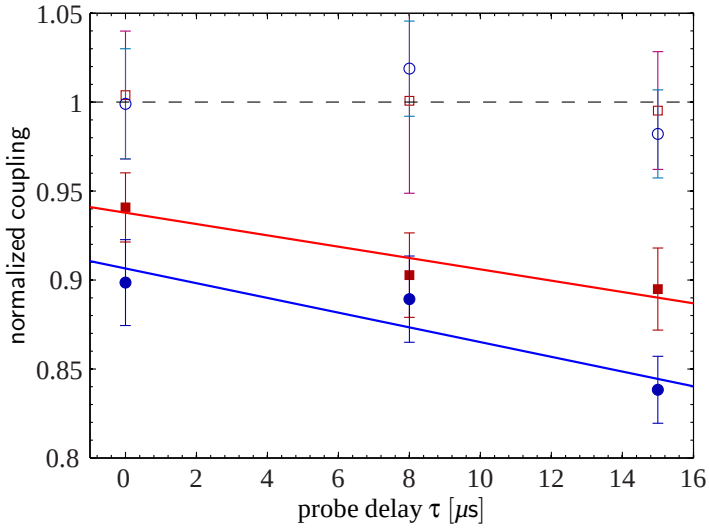

Figure 7.10.: Normalized coherent coupling rate for various delays between optical pumping and probing for the $(1,0)$ (squares) and $(2,0)$ (circles) modes, both for the case when the modes are excited by an external driving field (solid markers) and for unperturbed crystal. (open markers). The values are normalized to the mean value without modulation. The crystal parameters are: $L = (589 \pm 1)$ μm, $R = (80 \pm 1)$ μm, $\rho_0 = (2.62 \pm 0.05) \cdot 10^8$ cm$^-3$, $N = 310 \pm 10$.

As mentioned is sec. 7.2.3 the damping of the periodic motion when exciting a certain normal mode is dominated by two friction forces. On the one hand, off-resonant energy exchange with other normal modes will lead to dissipation of kinetic energy to these modes, on the other hand, the motion of the ions will be damped by Doppler laser cooling forces. The measurement of the coherent coupling between ion Coulomb crystals and the cavity field naturally takes place in a phase of the experimental sequence, where there is no cooling light applied, as the ions initially have to be prepared in suitable Zeeman substates of the metastable $3d^2D_{3/2}$ level. In most experiments, the coherent interaction is then probed directly after the optical pumping. However, it is possible to allow for of a free evolution of the system between the optical pumping and the probing. Similar measurement without a driving force were performed to study the temporal stability of coherences between collective Zeeman substates, as discussed in sec. 5.7, where the probe pulse was delayed up to ~ 100 μs after the end of the optical pumping. When driving a collective vibrational mode by applying appropriate driving fields to the endcaps, the

amplitude of the driven motion will, after cooling and optical pumping laser are switched off, increase. During this free evolution, only the intrinsic coupling to other motional normal modes of the plasma will damp the periodic motion and by delaying the probing with respect to the optical pumping it should be possible to directly measure the effect of the internal damping in the plasma. In fig. 7.10 first measurements of the coherent coupling for various delays between optical pumping and probing are depicted. The measurement is performed by measuring the effective cavity decay rate for a resonant probe beam and for a crystal with half-length and radius $L = (589 \pm 1)$ μm and $R = (80 \pm 1)$ μm, a density of $\rho_0 = (2.62 \pm 0.05) \cdot 10^8$ cm$^-3$. The effective number of ions and the aspect ratio are $N = 310 \pm 10$ and $\alpha = 0.136$. The study was carried out both for the $(1,0)$ (squares) and the $(2,0)$ (circles) mode where in both cases the effective cavity decay rate on resonance ($\omega_{(1,0)} = 2\pi \times 94$ kHz and $\omega_{(2,0)} = 2\pi \times 145$ kHz) was measured with (solid markers) and without modulation (open markers). In these measurements the measurement sequence is extended to 50 μs, where the ions are initially cooled for 20 μs and with a variable delay between the optical pumping and the probing. The coupling is normalized to the measured mean value of the unmodulated data sets. While the coupling is constant when no modulation field is present, one observes a decrease of the coherent coupling, when exciting either of the two motional modes. This illustrates that one can in principle directly observe the dynamical evolution of the plasma (without disturbing it), when no external cooling forces are present. This should allow for the investigation of various plasma characteristics in absence of external damping forces and it may, on this basis, be possible to study coupling mechanisms and correlation effects in cold nonneutral plasmas [168].

Effect of density

A second attractive application of the measurement technique described above is the perspective of a direct investigation of damping effects in the system as a function of the various parameters that will determine the physics in the ion Coulomb crystal. A first step in this direction is the measurement of the influence of the ion density on the damping, and we will here present preliminary results on this issue.

Fig. 7.11 shows the normalized coupling as a function of modulation amplitude for a. the $(1,0)$ and b the $(2,0)$ mode, measured for two different crystals with identical aspect ratios $\alpha \sim 0.14$, but different densities $\rho_0 = (2.62 \pm 0.05) \cdot 10^8$ cm^{-3} (red squares) and $\rho_0 = (5.67 \pm 0.11) \cdot 10^8$ cm^{-3} (blue circles). The coupling is measured for a resonant probe laser ($\Delta = 0$) and normalized to the coupling without modulation according to $\frac{(\kappa' - \kappa)|_{kv}}{(\kappa' - \kappa)|_{kv=0}}$. For both plasma modes, we observe a decrease of the measured coupling for both crystals when the amplitude of the AC modulation voltage is increased. However, the coupling remains substantially higher for the crystal with higher density, indicating a increased damping of the driven motion.

From the simple model of a damped harmonic oscillator one expects the modulation amplitude to scale linear with the excitation force, and the decrease of the measured normalized coupling should, according to eq. (7.19), not depend on the density, if the damping rates are assumed to be constant.

Changing the density of the crystal will, however, also influence other thermodynamic properties of the crystals, and the larger damping rate for higher density might be caused by e.g. an increased coupling to other plasma modes [167] or by effects induced by a higher temperature of the ensemble [168] and the clarification of the effect requires more

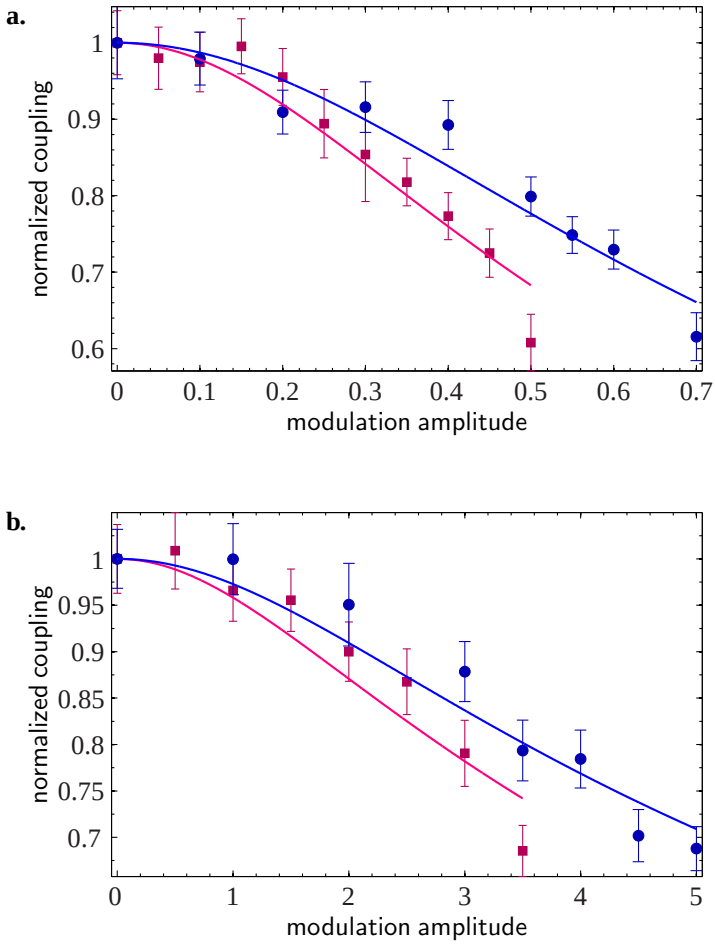

Figure 7.11.: Effect of density. Shown is the normalized coupling as a function of the modulation voltage applied to the endcaps for **a.** the (1,0) and **b.** the (2,0) mode The two sets of data correspond to two different crystals with identical aspect ratio of $\alpha \sim 0.14$ and half-length $L \sim (560)$ μm, but different densities $\rho_0 = (2.62 \pm 0.05) \cdot 10^8$ cm^{-3} (solid black squares) and $\rho_0 = (5.67 \pm 0.11) \cdot 10^8$ cm^{-3} (open red squares). The solid lines are fits to the theoretical model.

thorough studies. Our measurement shows, nevertheless, that our measurement technique could be well suited to investigate thermodynamical properties of cold plasmas.

7.5. Conclusion

In this chapter we presented a novel method to investigate normal mode dynamics in cold nonneutral plasmas in the form of ion Coulomb crystals in a linear Paul trap. The method is based on the probing of the collective coupling between the electronic state of the ions and an cavity field mode with a weak probe field at the single photon level. We found excellent agreement with the predictions of a zero-temperature charged liquid plasma model [82, 167, 168] when measuring the resonance frequencies of various plasma modes for crystals of different shape, size and density.

Furthermore, the technique was used to measure the kinetic energy and hence the temperature for two deliberately excited modes. This was accomplished by measuring the effective cavity decay rate as a function of probe detuning Δ and comparing to our model. The amplitude of the periodic motion deduced from these studies could be compared to a direct measurement of the oscillation amplitude of the periodic motion by a phase-locked imaging technique and we found good agreement between the two methods. In principle it should on this basis also be possible to measure more complex velocity distributions and, eventually, the thermal Maxwell-Boltzmann distribution of unperturbed ion crystals.

The detection technique used in our experiments uses a resonant probe field and is hence still performed in the absorptive regime. However, the fast repetition of the experimental sequence in which at most one photon is absorbed leaves the thermal state of the crystal unchanged and the technique can still be considered noninvasive provided the identical preparation of the ion ensemble at the start of each sequence. Since the probing does not rely on the observation of incoherently scattered photons as e.g. the case in Doppler velocimetry [171–173] and in Sympathetically-Cooled Single Ion Mass Spectrometry [185], the detected signal can in principle be purely dispersive in nature and does not require any excitation of the ions.

Due to the present experimental parameters, investigations are limited to crystals containing at least a few hundred ions and to vibrational amplitudes of the order of μm. It should, however, with optimal atomic transition and cavity parameters, in principle be possible to apply this measurement technique to few-ion crystals and also to situations, where the quantum nature of the vibrational excitation comes into play. In this regime, our measurement technique should also be applicable to observe e.g. radiation pressure-induced cavity optomechanical phenomena [180, 181] with cold, solid-like objects or to investigate classical and quantum phase transitions [186–190].

Finally, further investigations of higher-order $(l, 0)$ modes can be envisioned to study mode excitations using spatial- and time-modulated radiation pressure forces. For $^{40}Ca^{+}$ ions this can e.g. be achieved through the combined application of a 866 nm repumper beam with a spatially modulated intensity profile along the cavity axis and a time-varying intensity of one of the 397 nm cooling beams [185]. Eventually, for the high spatial modulation of modes with large l, the liquid model should cease to apply. Further applications could be measurements of ion Coulomb crystal temperatures and heating rates [191] and more detailed investigations of the coupling between the various normal modes at various temperatures and structural phases of the plasma [167, 168].

8. Cavity electromagnetically induced transparency

In this chapter we report on the experimental observation of electromagnetically induced transparency (EIT) with ion Coulomb crystals in an optical cavity. In connection with the results of the previous chapters, the observation of EIT with ion Coulomb crystals in optical cavities is a major step towards the realization of a quantum memory based on ions in an optical cavity [55]. We will provide a theoretical description of the system and compare the experimental results to the expectations of this model.

The chapter is structured as follows: We begin in sec. 8.1 with a brief introduction, before presenting a theoretical model of the interaction of an ensemble of three-level atoms with two light fields in sec. 8.2. In sec. 8.3.1 we describe the experimental setup. In sec. 8.4 we present the results of the observation of cavity electromagnetically induced transparency with ion Coulomb crystals and, finally, in sec. 8.5 give a conclusion and a brief outlook.

8.1. Introduction

Electromagnetically induced transparency is a widely-used quantum interference effect where the absorption and dispersion of a weak probe field propagating in an otherwise opaque medium are controlled via the coherent interaction of the medium with a more intense control field [83, 84]. Under certain circumstances, the resonant absorption of the probe field can be suppressed by the coherent interaction with the control field and the medium becomes transparent for the probe light, justifying the name of the effect "electromagnetically induced transparency". EIT has been observed in hot and cold atomic gasses [85], and particularly impressive applications are slow- and stopped light experiments [86–88], where the group velocity of a light pulse travelling through an EIT medium is drastically reduced and even stopped.

At the quantum limit, when the probe pulse only contains a single photon, the versatile control of the absorption and dispersion properties in an EIT medium has important applications in the framework of quantum information processing, as long-lived and high-efficiency quantum memories are a key ingredient for the realization of e.g. complex quantum networks [10, 38].

Quantum memories were successfully demonstrated via the storage and retrieval of single photons [40–44], squeezed vacuum states [45, 46] and entangled states [47] in atomic gases using free-propagating fields[1]. As the interaction of free-space laser beams with an atomic medium is typically very weak, the efficiency in these schemes is usually low. Furthermore, due to either particle-particle interactions or random motion of atoms in vapors, the achievable storage times are generally limited to the μs range. This limitation

[1] The storage of entanglement was recently also demonstrated in solid state systems [50, 51].

can be overcome using more complex schemes [43, 44], often at the expense of lower efficiencies.

For an atomic medium enclosed in the mode-volume of an optical cavity, the interaction with the well-defined spatio-temporal cavity modes substantially enhances the light-matter interaction. In combination with the coherent control of the atomic absorption and dispersion provided by electromagnetically induced transparency, atomic ensembles interacting with a single mode of an optical cavity in the collective strong coupling regime were proposed for the realization of high-efficiency optical quantum memories [55–57].

Cavity EIT was successfully observed for ensembles of cold and hot neutral atoms in cavities [92, 93], and, most recently, the enhanced interaction even allowed for the observation of cavity EIT with few atoms [94, 95]. Moreover, ensembles of neutral atoms confined in the mode volume of an optical cavity were successfully used to store and transfer single quanta [96, 97] with higher efficiency. The achievable coherence time in these systems is, however, still limited by the atomic motion.

Using ion Coulomb crystals confined in an optical cavity could be a possible route to circumvent both limitations in the efficiency and the achievable coherence times. Operating in the strong coupling regime (see ch. 5) and with measured coherence times of the order of $\sim$ ms our system is a promising candidate for the realization of both long-time and high-efficiency storage and retrieval of quantum information, even with the potential to explore multimode applications using various degrees of freedom, like spatio-temporal cavity modes (see ch. 6) or specific collective vibrational normal modes (see ch. 7).

In this chapter we will report on the first experimental observation of cavity electromagnetically induced transparency with ions, an important milestone on the way towards a high-efficiency quantum information tool. We use a novel "all-cavity" EIT scheme where both the control and the probe field are in the same spatial cavity mode and create EIT between Zeeman substates. We demonstrate full control over transparency of the ionic medium and observe EIT windows as narrow as a few tens of kHz for a probe field at the single photon level.

8.2. Three-level atoms in a cavity

The essential features of EIT can be described in a semi-classical theory, similar to our description of two-level atoms interacting with a single cavity field mode given in sec. 3. The goal of this section is to adapt this description to the situation where an ensemble of identical three-level atoms interacts with two light fields. However, before deriving a full set of dynamical equations for the system, we will begin by introducing EIT in a simple quantum mechanical picture using dressed-states [84, 85].

8.2.1. Dressed and dark states in a three-level system

We consider a single atom in free-space with a Λ-type energy level configuration, as depicted in fig. 8.1 a. The Λ system is formed by two long-lived ground states $|1\rangle$ and $|2\rangle$ and an excited state $|3\rangle$ which is coupled to the two ground states via a non-vanishing dipole element and can decay to the two ground states or other external levels at a rate γ.

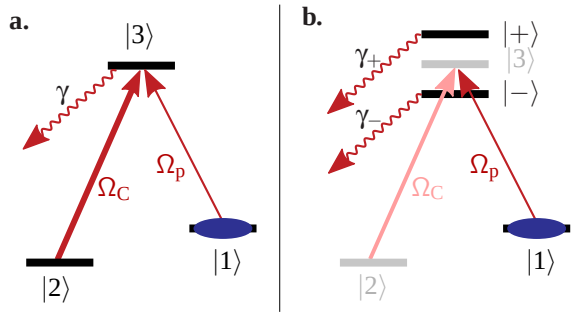

Figure 8.1.: a. Schematic Λ scheme as used for the realization of electromagnetically induced transparency. It is formed by two long-lived ground states $|1\rangle$ and $|2\rangle$ and an excited state $|3\rangle$. States $|1\rangle$ and $|3\rangle$ are coupled by a weak probe field with Rabi frequency Ω_p, while states $|2\rangle$ and $|3\rangle$ are coupled by the stronger control field with Rabi-frequency Ω_C. The excited state can decay to the two ground states or other external levels at a rate γ. **b.** Dressed state picture, where the excited state is split into an doublet of dressed states $|\pm\rangle$.

We assume the atom to be initially in state $|1\rangle$. Both ground states are coupled to the excited state by close to resonant laser fields, where the $|2\rangle \leftrightarrow |3\rangle$ transition is driven by a strong, (close to) resonant electromagnetic field with Rabi frequency Ω_C (referred to as control field), while states $|1\rangle$ and $|3\rangle$ are coupled by a weaker field with Rabi frequency Ω_P (referred to as probe field). In the dipole approximation and using the frame rotating at the frequency of the probe field the Hamiltonian of the system is given by

$$H_{int} = \hbar\Delta\sigma_{33} + \hbar\delta\sigma_{22} - \hbar\Omega_\mathrm{p}(\hat{\sigma}_{31} + \hat{\sigma}_{13}) - \hbar\Omega_C(\hat{\sigma}_{32} + \hat{\sigma}_{23}), \tag{8.1}$$

where $\Delta = \omega_{31} - \omega_\mathrm{p}$ is the detuning of the probe laser with respect to the $|1\rangle \leftrightarrow |3\rangle$ transition, $\Delta_{32} = \omega_{32} - \omega_{ctrl}$ is the detuning of the control laser with respect to the $|2\rangle \leftrightarrow |3\rangle$ transition, $\delta = \Delta - \Delta_{32}$ is the so-called two-photon detuning. Furthermore, we defined the atomic operators $\hat{\sigma}_{ab} = |a\rangle\langle b|$ $(a,b = 1,2,3)$.

The Hamiltonian can be diagonalized in the basis of the so-called "dressed" states. They are related to the "bare" states of the atom by

$$|0\rangle = \cos\theta\,|1\rangle - \sin\theta\,|2\rangle\,, \tag{8.2a}$$
$$|+\rangle = \sin\theta\sin\theta'\,|1\rangle + \cos\theta\sin\theta'\,|2\rangle + \cos\theta'\,|3\rangle\,, \tag{8.2b}$$
$$|-\rangle = \sin\theta\cos\theta'\,|1\rangle + \cos\theta\cos\theta'\,|2\rangle - \sin\theta'\,|3\rangle\,, \tag{8.2c}$$

with mixing angles θ and θ', which on two-photon resonance ($\delta = 0$) are given by

$$\tan\theta = \frac{\Omega_\mathrm{p}}{\Omega_\mathrm{C}} \tag{8.3a}$$
$$\tan 2\theta' = \frac{1}{\Delta}\sqrt{\Omega_\mathrm{p}^2 + \Omega_\mathrm{C}^2}. \tag{8.3b}$$

The new eigenket $|0\rangle$ is a superposition of state $|1\rangle$ and $|2\rangle$ and has zero eigenenergy. An atom initially prepared in this state is never excited to state $|3\rangle$, which is the only state

that can spontaneously decay. $|0\rangle$ is thus referred to as the "dark"-state of the system. The contribution of the states $|1\rangle$ and $|2\rangle$ to the dark state depends on the mixing angle θ, which is given by the ratio of the Rabi frequencies of the two fields. On the other hand, the two states $|\pm\rangle$ are a superposition of all 3 bare states and their energy will be shifted by $\hbar(\Delta \pm \sqrt{\Delta^2 + \Omega_p^2 + \Omega_C^2})$. The emergence of EIT can be understood when considering the case of a weak probe field, $\Omega_p \ll \Omega_C$, where the first mixing angle is $\theta \ll 1$. The level scheme in this case is depicted in fig. 8.1 b. In this case, the probe ground state is the dark state of the system, $|0\rangle \simeq |1\rangle$. An atom that is initially prepared in this state has no contribution of state $|3\rangle$ which is the only state that can spontaneously decay. The two states $|\pm\rangle$ can be regarded as two excited states and the absorption to these states will cancel when the frequency of the weak probe field is tuned between the two states, i.e. to $\Delta = 0$.

In the bare state picture this corresponds to the interference between two pathways. The light fields will transfer a small but finite population amplitude to state $|2\rangle$ and the absorption from state $|1\rangle$ to state $|3\rangle$ can occur either directly or via the coherent indirect path $|1\rangle \to |3\rangle \to |2\rangle \to |3\rangle$. As the Rabi frequency of the control field is much stronger than that of the probe, the probability amplitude of the indirect path will be comparable to the direct way. However, on two-photon resonance, it is of opposite sign and will hence interfere destructively with the amplitude of the direct path.

8.2.2. Dynamical equations

We will now turn to a semi-classical analysis, which will allow us to derive a full set of dynamical equations for the relevant observables of the system. We will from the beginning focus our description on the situation of a large $^{40}Ca^+$ ion Coulomb crystals confined in an optical cavity and will reuse many of the equations and approximations that were already discussed in ch. 3.

In the experiments presented here, the Λ-system in $^{40}Ca^+$ is, as depicted in fig. 8.2, formed by two Zeeman-substates of the $\left|3d^2D_{3/2}\right\rangle$ level constituting the two ground states and one Zeeman-substate of the $\left|4p^2P_{1/2}\right\rangle$ manifold corresponding to the excited state. A straight forward and logical extension of the scheme in the previous chapters is the following choice of levels:

$$|1\rangle = \left|3d^2D_{3/2},\, m_J = {}^{+3}/_{2}\right\rangle \tag{8.4a}$$

$$|2\rangle = \left|3d^2D_{3/2},\, m_J = {}^{-1}/_{2}\right\rangle \tag{8.4b}$$

$$|3\rangle = \left|4p^2P_{1/2},\, m_J = {}^{+1}/_{2}\right\rangle. \tag{8.4c}$$

The transition frequencies are for the $|1\rangle \leftrightarrow |2\rangle$ transition denoted by ω_{at} (as before) and for the $|3\rangle \leftrightarrow |2\rangle$ transition by $\omega_{32} = \omega_{at} + \omega_B$, where the degeneracy is lifted by a longitudinal B-field giving rise to a frequency shift of ω_B by the Zeeman effect (see appendix A.3). State $|1\rangle$ can spontaneously decay to the two ground and other states at a rate γ, and we model decoherence between the two (metastable) ground states $|1\rangle$ and $|2\rangle$ by adding a phenomenological decay rate γ_{12}.

We consider in analogy to sec. 3.2, the situation where the ion Coulomb crystal is confined in a linear optical cavity formed by two mirrors M_1 and M_2 and characterized by the cavity field decay rates through the two mirrors, κ_1 and κ_2 (see eq. 3.14), and the intracavity loss rate $\kappa_{\mathcal{A}}$, (see eq. 3.17).

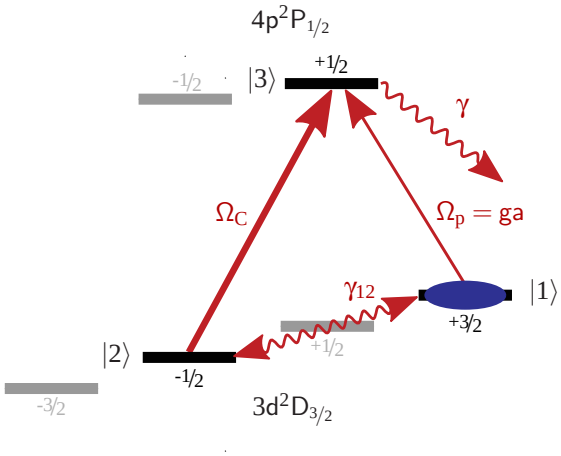

Figure 8.2.: Level scheme for the realization of electromagnetically induced transparency in $^{40}Ca^{+}$. The Λ system is formed by the metastable $m_J = +1/2$ and $m_J = -1/2$ Zeeman substates of the $\left|3d^2D_{3/2}\right\rangle$ level and the $m_J{+}1/2$ state of the $\left|4p^2P_{1/2}\right\rangle$ level.

A weak σ^--polarized probe field $\hat{a}$ with frequency ω_p close to resonance with the $|1\rangle \leftrightarrow |3\rangle$ transition is injected into the fundamental TEM_{00} mode of the cavity through mirror M_1. States $|2\rangle$ and $|3\rangle$ are coupled by the stronger, σ^+-polarized control field with a frequency ω_{ctrl} and a detuning from atomic resonance $\Delta_{32} = \omega_{32} - \omega_{ctrl}$. In a first step, we will assume the Rabi frequency of the control field to be equal for all ions. However, for the experiment presented later in this chapter, this beam will also be injected into the cavity and we will in sec. 8.2.3 take into account the effects of the transverse profile and the longitudinal standing wave structure of the control field. To facilitate the comparison between the two scenarios, we will here rescale the Rabi frequency of the uniform control field by a factor $1/\sqrt{2}$, to account for the lower mean interaction strength in the standing wave field in the latter configuration.

The interaction Hamiltonian in the frame rotating at the probe field frequency ω_p and applying the rotating wave approximation (see (3.32)) is given by

$$H_{int} = -\hbar g \sum_{j=1}^{N_{tot}} \Psi_{00}(\boldsymbol{r}_j)(\hat{\sigma}_{31,j}\hat{a} + \hat{\sigma}_{13,j}\hat{a}^\dagger) - \hbar \frac{\Omega_c}{\sqrt{2}} \sum_{j=1}^{N_{tot}} (\hat{\sigma}_{32,j} + \hat{\sigma}_{23,j}), \tag{8.5}$$

where the atomic spin operators $\sigma_{ab,j} = |a\rangle\langle b|$ $(a,b = 1,2,3)$ were defined and where Ω_c is chosen real without loss of generality[2].

Following the Heisenberg-Langevin approach introduced in sec. 3.2 we can deduce the equations of motion for the mean values of the operators in the Heisenberg picture. The dynamical equation of the mean value of the probe field operator $\hat{a}$ is of the same form as in the 2-level case in eq. (3.38d) and reads

$$\dot{a} = -(\kappa + i\Delta_c)a + i \sum_{j=1}^{N_{tot}} g\Psi_{00}(\boldsymbol{r}_j)\sigma_{13,j} + \sqrt{2\kappa_1}a_{in}. \tag{8.6}$$

[2] It is worth noticing that by writing this expression, we assume the phases of the probe and the control field to be stable with respect to each other.

For the atomic operators, we will restrict ourselves to the weak probe regime $g|a| \ll \Omega_c/\sqrt{2}$, where all the ions remain in state $|1\rangle$ ($\sigma_{11} = 1$, $\sigma_{22} = \sigma_{33} = 0$) and, to first order, only the mean values of the probe dipole σ_{13} and the ground state coherence σ_{12} are non-zero. Their equations of motion are

$$\dot{\sigma}_{13,j} = -(\gamma + i\Delta)\sigma_{13,j} + iga\Psi_{00}(\boldsymbol{r}_j) + \frac{i\Omega_C}{\sqrt{2}}\sigma_{12,j} \tag{8.7a}$$

$$\dot{\sigma}_{12,j} = -(\gamma_{12} + i\delta)\sigma_{12,j} + \frac{i\Omega_C}{\sqrt{2}}\sigma_{13,j}, \tag{8.7b}$$

where we introduced the two-photon detuning $\delta = \Delta - \Delta_{32}$ and included the phenomenological decay rate of the ground state coherence γ_{12}.

For the remaining derivation, it is convenient to define the collective operators $\hat{S}_{13} = \sum_{j=1}^{N_{tot}} \Psi_{00}(\boldsymbol{r})\hat{\sigma}_{13,j}$ and $\hat{S}_{12} = \sum_{j=1}^{N_{tot}} \Psi_{00}(\boldsymbol{r})\hat{\sigma}_{12,j}$. The dynamical equation of the mean value of the field and the two collective spin operators read

$$\dot{a} = -(\kappa + i\Delta_c)a + igS_{13} + \sqrt{2\kappa_1}a_{in}. \tag{8.8a}$$

$$\dot{S}_{13} = -(\gamma + i\Delta)S_{13} + igNa + \frac{i\Omega_C}{\sqrt{2}}S_{12} \tag{8.8b}$$

$$\dot{S}_{12} = -(\gamma_{12} + i\delta)S_{12} + i\frac{\Omega_C}{\sqrt{2}}S_{13}, \tag{8.8c}$$

where we make use of the effective number of ions, $N = \sum_{j=1}^{N_{tot}} \Psi_{00}(\boldsymbol{r})^2$, defined in eq. (3.42).

Adiabatic elimination

In the relevant situation for the experiments we will discuss later, we can assume $\gamma_{12} \ll \gamma, \kappa$ and the control field Rabi frequency is such that the slowest time constant in the dynamical equations is given by that of $S_{12}(t)$. We can therefore perform an adiabatic elimination of $a(t)$ and $S_{13}(t)$, which on the relevant timescale will follow the evolution of $S_{12}(t)$. Setting $\dot{a}(t) = \dot{\sigma}_{13}(t) = 0$ in eqs. (8.8) yields

$$a(t) = \frac{ig}{\kappa + i\Delta_C}S_{13}(t) + \frac{\sqrt{2\kappa_1}a_{in}}{\kappa + i\Delta_C} \tag{8.9a}$$

$$S_{13}(t) = \frac{1}{\gamma + i\Delta + \frac{g^2N}{\kappa + i\Delta_C}}\left[\frac{i\Omega_C}{\sqrt{2}}S_{12}(t) + \frac{igN\sqrt{2\kappa_1}a_{in}}{\kappa + i\Delta_C}\right]. \tag{8.9b}$$

Substituting these equations into eq. (8.8c) the dynamical equation of the ground state coherence becomes

$$\dot{S}_{12}(t) = -\gamma_{EIT}S_{12}(t) + \beta a_{in}, \tag{8.10}$$

where we defined

$$\gamma_{EIT} = \gamma_{12} + i\delta + \frac{\Omega_C^2/2}{\gamma + i\Delta + \frac{g^2N}{\kappa + i\Delta_C}}, \tag{8.11}$$

and

$$\beta = \frac{\Omega_C^2}{2} \frac{gN\sqrt{2\kappa_1}}{\left(\gamma + i\Delta + \frac{g^2 N}{\kappa + i\Delta_C}\right)(\kappa + i\Delta_C)}. \tag{8.12}$$

Assuming the input field to be constant and to be immediately switched on at $t = 0$ and assuming $\sigma_{12}(t = 0) = 0$ the dynamical equation is readily solved and one finds

$$S_{12}(t) = \frac{\beta a_{in}}{\gamma_{EIT}} \left[\exp(-\gamma_{EIT} t) - 1\right], \tag{8.13}$$

Accordingly, the temporal evolution of S_{12} will be set by γ_{EIT} which on one and two-photon resonance for the fields and for a resonant cavity ($\Delta = \Delta_C = \delta = 0$) reduces to

$$\gamma_{EIT} = \gamma_{12} + \frac{\Omega_C^2/2}{\gamma + \frac{g^2 N}{\kappa}} = \gamma_{12} + \frac{\Omega_C^2/2}{\gamma(1 + 2C)}. \tag{8.14}$$

In the last step, the cooperativity parameter defined in eq. (5.5) was inserted. As the time evolution of $\sigma_{13}(t)$ and also the intracavity field $a(t)$ will be dictated by $\sigma_{12}(t)$ (see eqs. (8.9)), these quantities are also expected to follow the same exponential form with the same time constant γ_{EIT}. The build up of the intracavity probe field, which for an empty cavity is given by κ, will hence in the three-level case be steered by γ_{EIT} and may becomes much slower than the cavity decay rate. It should be noted that the adiabatic elimination is only valid in a regime where $\gamma_{EIT} \ll \gamma, \kappa$, i.e. for moderate Rabi frequencies of the control field.

Steady state solution

In steady state, the mean value of the intracavity field amplitude a reduces to

$$a = \frac{\sqrt{2\kappa_1} a_{in}}{\kappa + i\Delta_c - i\tilde{\chi}_\Lambda} \tag{8.15}$$

This equation is of the same form as in the two-level situation (see eq. (3.40b)), with the linear susceptibility being replaced by its counterpart of the three-level Λ-system

$$\tilde{\chi}_\Lambda = \frac{ig^2 N}{\gamma + i\Delta} \frac{1}{1 + s}. \tag{8.16}$$

where we introduced the effective saturation parameter of the two-photon transition

$$s = \frac{\Omega_C^2/2}{(\gamma_{12} + i\delta)(\gamma + i\Delta)} \tag{8.17}$$

and used the effective number of ions $N = \rho_0 \frac{\pi w_0^2}{2} L$ (see eq. (3.46)) For a vanishing Rabi-frequency of the control field the effective saturation parameter is zero, and eq. (8.16) reduces to the two-level susceptibility of eq. (3.41).

8.2.3. Effect of the transverse mode structure

As abovementioned, the control field will in our experiment also be mode matched to the cavity and we will in this subsection include the effect of the spatial profile of this field into the model. In all the EIT experiments presented in this thesis we make use of the fundamental TEM_{00} mode for both the probe and the control field and we will for simplicity restrict the model to this case.

To distinguish the two fields we will denote the mode functions corresponding to the control and the probe field by $\Psi_{00}(\boldsymbol{r}_j, k_{\mathrm{ctrl}})$ and $\Psi_{00}(\boldsymbol{r}_j, k_{\mathrm{p}})$, where k_{ctrl} and k_{p} are the wave vectors of the control and the probe field, respectively. We will furthermore still assume the Rabi frequency of the control field to be in steady state[3]. The interaction Hamiltonian now reads

$$H_{\mathrm{int}} = -\hbar g \sum_{j=1}^{N_{\mathrm{tot}}} \Psi_{00}(\boldsymbol{r}_j, k_{\mathrm{l}} l)(\hat{\sigma}_{31,j}\hat{a} + \hat{\sigma}_{13,j}\hat{a}^{\dagger}) - \hbar\Omega_{\mathrm{C}} \sum_{j=1}^{N_{\mathrm{tot}}} \Psi_{00}(\boldsymbol{r}_j, k_{\mathrm{C}})(\hat{\sigma}_{32,j} + \hat{\sigma}_{23,j}), \quad (8.18)$$

where Ω_{C} now denotes the control field Rabi frequency at an anti-node at the center of the fundamental TEM_{00} mode.

The Zeeman splitting of the two ground states $|1\rangle$ and $|2\rangle$ is of the order of some few MHz and we can assume the frequency of the probe and the control field to be almost degenerate, hence $k \equiv k_{\mathrm{p}} \simeq k_{\mathrm{C}}$. Furthermore, for large radii and half-lengths of the crystal, we can approximate the longitudinal mode function by $\cos(kz)$, as discussed in the derivation of (3.45). With these approximations, the cavity mode functions of the probe and the control field can be written as

$$\Psi_{00}(\boldsymbol{r}_j, k_{\mathrm{l}}) \simeq \Psi_{00}(\boldsymbol{r}_j, k_{\mathrm{C}}) = \cos(kz_j)\Psi_0(x_j)\Psi_0(y_j) = \cos(kz_j)\psi_{00}(r_j). \quad (8.19)$$

In this common standing wave configuration for the control and the probe field, it is convenient to introduce dipole operators associated to the forward and backward propagating waves of both fields $\hat{\sigma}_{\alpha 3,j\pm} = \hat{\sigma}_{\alpha 3,j}\exp(\pm ikz_j)$, $\alpha = 1,2$. Substituting into the interaction Hamiltonian in eq. (8.18) yields

$$\begin{aligned} H_{\mathrm{int}} = &- \hbar\frac{g}{2}\sum_{j=1}^{N_{\mathrm{tot}}} \psi_{00}(r_j)[(\hat{a}(\hat{\sigma}_{31,j+} + \hat{\sigma}_{31,j-}) + \hat{a}^{\dagger}(\hat{\sigma}_{13,j+} + \hat{\sigma}_{13,j-})] \quad (8.20)\\ &- \hbar\frac{\Omega_{\mathrm{C}}}{2}\sum_{j=1}^{N_{\mathrm{tot}}} \psi_{00}(r_j)[(\hat{\sigma}_{32,j+} + \hat{\sigma}_{32,j-}) + (\hat{\sigma}_{23,j+} + \hat{\sigma}_{23,j-})]. \end{aligned}$$

Using the Heisenberg-Langevin formalism, we can derive the dynamical equations for the mean values of the operators in the weak probe approximation and find

$$\dot{a} = -(\kappa + i\Delta_{\mathrm{C}})a + \frac{ig}{2}\sum_{j=1}^{N_{\mathrm{tot}}} \psi_{00}(r_j)(\hat{\sigma}_{31,j+} + \hat{\sigma}_{31,j-}) + \sqrt{2\kappa_1}a_{\mathrm{in}}. \quad (8.21a)$$

$$\begin{aligned} \dot{\sigma}_{13,j\pm} = &-(\gamma + i\Delta)\sigma_{13,j\pm} + \frac{iga}{2}\psi_{00}(r_j)\,[1 + exp(\pm 2ikz_j)] \quad (8.21b)\\ &+ \frac{i\Omega_{\mathrm{C}}}{2}\sigma_{12,j}\psi_{00}(r_j)\,[1 + exp(\pm 2ikz_j)] \end{aligned}$$

$$\dot{\sigma}_{12,j} = -(\gamma_{12} + i\delta)\sigma_{12,j} + \frac{i\Omega_{\mathrm{C}}}{2}\psi_{00}(r_j)(\sigma_{13,j+} + \sigma_{13,j-}). \quad (8.21c)$$

[3] In the experiment, the time constant for the build up of the control field is set by the cavity decay rate and we will ensure the steady state condition by switching on the control field slightly before the probe field.

If the timescale at which the atoms move along the standing wave is faster than the build-up time of the fields in the cavity we can average over the longitudinal effects and all higher-spatial frequency components in $\exp(\pm 2ikz)$ average out [192–194]. This assumption is as already discussed for the two-level situation in eq. (3.45) satisfied for ion Coulomb crystals with a thermal energy of ~ 10 mK. For atoms well-localized within the standing wave pattern of the probe and the control field the calculation would lead to different results and we will discuss this case in appendix D, where we also compare our experimental findings to the predictions of the two scenarios.

When averaging over the longitudinal structure, the equations of motion will only depend on the transverse profile of the probe and control field and reduce to

$$\dot{a} = -(\kappa + i\Delta_c)a + \frac{ig}{2}\sum_{j=1}^{N_{\mathrm{tot}}} \psi_{00}(r_j)(\sigma_{31,j+} + \sigma_{31,j-}) + \sqrt{2\kappa_1}a_{\mathrm{in}}. \tag{8.22a}$$

$$\dot{\sigma}_{13,j\pm} = -(\gamma + i\Delta)\sigma_{13,j\pm} + \frac{iga}{2}\psi_{00}(r_j) + i\Omega_{\mathrm{C}}\sigma_{12,j}\psi_{00}(r_j) \tag{8.22b}$$

$$\dot{\sigma}_{12,j} = -(\gamma_{12} + i\delta)\sigma_{12,j} + \frac{i\Omega_{\mathrm{C}}}{2}(\sigma_{13,j+} + \sigma_{13,j-})\psi_{00}(r_j). \tag{8.22c}$$

Steady state solution

These equations can be solved in steady state and we find for the mean value of the intracavity field amplitude

$$a = \frac{\sqrt{2\kappa_1}a_{\mathrm{in}}}{\kappa + i\Delta_{\mathrm{C}} - i\chi_\Lambda}, \tag{8.23}$$

which is of the same form as eqs. (3.40b) and (8.15). The three-level susceptibility is now denoted by χ_Λ and is given by

$$\chi_\Lambda = \frac{ig^2}{2}\sum_{j=1}^{N_{\mathrm{tot}}} \frac{\psi_{00}^2(r_j)}{\gamma + i\Delta + \frac{\Omega_{\mathrm{C}}^2/2}{\gamma_{12}+i\delta}\psi_{00}^2(r_j)}. \tag{8.24}$$

For large ion Coulomb crystals with a uniform density, it is convenient to apply the continuous medium description introduced in eq. (3.43), and to replace the sum over the ions by the integral over the crystal volume V. We will furthermore assume to be in the regime, where the crystal radius R is much larger than the waist of the cavity mode w_o. With these assumptions, the three-level susceptibility can be written as

$$\begin{aligned}\chi_\Lambda &= \frac{ig^2}{2}\rho_0 \int_V \mathrm{d}\boldsymbol{r} \frac{\exp(-\frac{2r_j^2}{w_0^2})}{\gamma + i\Delta + \frac{\Omega_{\mathrm{C}}^2/2}{\gamma_{12}+i\delta}\exp(-\frac{2r_j^2}{w_0^2})} \\ &= \frac{ig^2 N}{\gamma + i\Delta}\frac{\ln(1+s)}{s},\end{aligned} \tag{8.25}$$

where the effective saturation parameter of the two-photon transition (see eq. (8.17)) and the effective number of ions $N = \rho_0 \frac{\pi w_0^2}{2} L$ (see eq. (3.46)) were inserted and where we used $\psi_{00}^2(r_j) = \exp(-\frac{2r_j^2}{w_0^2})$ (see eq. (3.7)).

Adiabatic elimination

Instead of directly solving eqs. (8.22) in steady state, one can gain information on the dynamic evolution of the intracavity field by performing the adiabatic elimination with respect to the slowest time evolution of σ_{12}, as was done for the homogeneous control field in eq. (8.9). Due to the transverse dependence of the control field Rabi frequency, the dynamical evolution of the EIT of the individual ions will depend on their radial position in the transverse plane. As a consequence, the dynamical field equation does not possess a simple analytic solution in the time domain. However, performing the Laplace transformation of eqs. (8.22) one can solve the set of differential equations in the Laplace space[4]. The full derivation can be found in appendix C and we will only give the main results here. The Laplace transform of the mean value of the intracavity field a reads

$$\tilde{a}[p] = \sqrt{2\kappa_1}\tilde{a}_{\text{in}}[p]\left[\kappa + i\Delta_{\text{C}} + g^2\sum_j \frac{\exp(-2r_j^2/w_0^2)}{\gamma + i\Delta + \frac{\Omega_C^2\exp(-2r_j^2/w_0^2)}{\gamma_{12}-i\delta+p}}\right]^{-1} \tag{8.26}$$

where $\tilde{a}_{\text{in}}[p]$ denotes the Laplace transformation of the input field. The corresponding dynamical evolution of the intracavity field amplitude in the time domain can be calculated from eq. (8.26) by the inverse Laplace transformation, which has to be performed numerically.

8.2.4. Reflectivity and transmittivity spectrum

In sec. 3.2.4 we calculated the probe reflection and transmission spectra in steady state for a cavity containing an ensemble of two-level system (see eq. (3.47a)) and we will briefly recapitulate the results and extend them to the three-level situation of this chapter. The interaction between the ensemble and the cavity field mode was included in eq. (3.47a) through the two-level atomic susceptibility. Substituting the three-level susceptibility of eq. (8.16) or (8.25) into the equation directly yields the probe transmission and reflectivity spectrum of the cavity, which is locked on atomic resonance ($\Delta = \Delta_C$)

$$\mathcal{R} = \frac{[\kappa_1 - \kappa_2 - \kappa_{\mathcal{A}} - \text{Im}(\chi_\Lambda)]^2 + [\Delta - \text{Re}(\chi_\Lambda)]^2}{\kappa^2 + \Delta^2 + |\chi_\Lambda|^2 + 2[\kappa\text{Im}(\chi_\Lambda) - \Delta\text{Re}(\chi_\Lambda)]} \tag{8.27}$$

$$\mathcal{T} = \frac{4\kappa_1\kappa_2}{\kappa^2 + \Delta^2 + |\chi_\Lambda|^2 + 2[\kappa\text{Im}(\chi_\Lambda) - \Delta\text{Re}(\chi_\Lambda)]}. \tag{8.28}$$

For simplicity, we denoted the three level susceptibility by χ_Λ, though it can be substituted by either of the two expressions in eqs. (8.16) and (8.25).

In fig. 8.3 a. are depicted the calculated cavity reflectivity spectra of a locked cavity ($\Delta = \Delta_{\text{C}}$) for the three-level susceptibility of a control field in the cavity (solid line, see eq. (8.25)) and a uniform control field (dashed dotted line, see eq. (8.16)), along with the expected vacuum Rabi spectrum for only the probe field being present (dashed line) and the spectrum of the empty cavity (dotted line). The calculations were performed for an effective number of ions $N = 500$ and a control field Rabi frequency of $\Omega_{\text{C}} = 2\pi \times 3$ MHz. The remaining parameters are set to the values of our experiment: $\kappa_1 = 2\pi \times 1.53$ MHz, $\kappa_{\mathcal{A}} = 2\pi \times 0.67$ MHz, $\kappa_2 = 2\pi \times 7.85$ kHz, $\Delta_{23} = 0$ MHz, $\gamma = 2\pi \times 11.2$ MHz.

[4] For a definition of the Laplace transformation see eq. (C.4) in appendix C

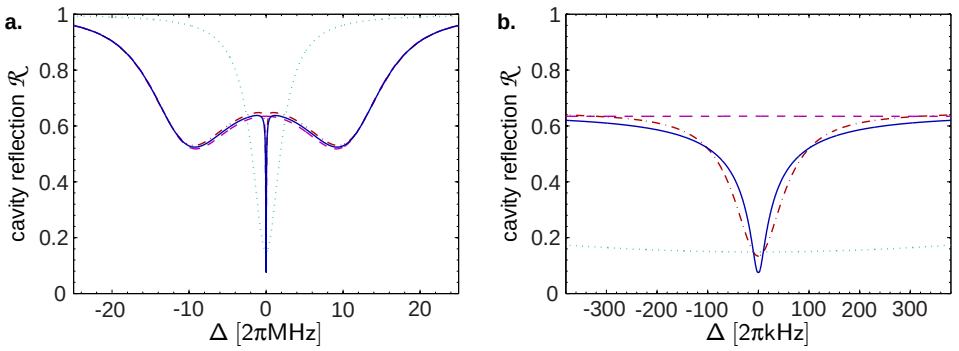

Figure 8.3.: Cavity reflection spectrum as a function of probe detuning calculated according to eq. (8.27) for **a.** a range of ± 25 MHz and **b.** a zoom around two photon resonance ± 350 kHz. The individual spectra were calculated for an empty cavity ($N = 0$, dotted line), for 500 interacting ions when the control field is off ($N = 500$, $\Omega_C = 0$ MHz, dashed line), for the same number of ions and a control Rabi frequency $\Omega_C = 2\pi \times 3$ MHz for the two cases of a uniform control field Rabi frequency (dashed dotted line) (see eq. (8.16)) and when taking the transverse profile of the control field into account (solid line) (see eq. (8.25)).

For large detunings of the probe laser, the reflectivity for the three-level case is similar to the two-level vacuum Rabi spectra. However, when approaching the atomic (and two-photon) resonance, the probe reflectivity drops drastically. This effect is present for both the uniform control field and when the transverse profile is taken into account. In this region, the absorption of the atomic medium is cancelled by EIT, as discussed in sec. 8.2.1 and the probe field is transmitted. A zoom on the spectrum for small detuning is depicted in fig. 8.3 b. and reveals the difference between the intracavity and the uniform control field. In the first case, the reflectivity dip appears pointier, and exhibits shoulders for larger detunings as opposed to the standard EIT Lorentzian profile.

For the case, where both the atomic and the two-photon detuning are zero ($\Delta = \Delta_C = 0$ and $\delta = 0$) the susceptibility becomes in both cases purely imaginary and eqs. (8.27) reduces to

$$\mathcal{R}(\Delta = 0) = \frac{[\kappa_1 - \kappa_2 - \kappa_{\mathcal{A}} - \mathrm{Im}(\chi_\Lambda)]^2}{[\kappa + \mathrm{Im}(\chi_\Lambda)]^2}. \tag{8.29a}$$

$$\mathcal{T}(\Delta = 0) = \frac{4\kappa_1\kappa_2}{[\kappa + \mathrm{Im}(\chi_\Lambda)]^2} \tag{8.29b}$$

Using these expressions, we can now also calculate the atomic transparency on resonance, defined by the ratio of the transmission of the cavity containing the medium $\mathcal{T}$ to that of the empty cavity $\mathcal{T}_0$

$$T_{\mathrm{atom}} = \frac{\mathcal{T}}{\mathcal{T}_0} = \frac{1}{(1 + \mathrm{Im}(\chi)/\kappa)^2}. \tag{8.30}$$

For a vanishing control field Rabi frequency, the transparency is hence simply given by $T_{\mathrm{atom}} = \frac{1}{(1+2C)^2}$, where C is the cooperativity defined in eq. (5.5).

Using eq. (8.29a), the transparency can be related directly to the probe reflectivity on resonance by

$$T_{\text{atom}} = \left(\frac{\kappa}{2\kappa_1}\right)^2 \left(1 \pm \sqrt{\mathcal{R}(\Delta = 0)}\right)^2, \tag{8.31}$$

where the sign of the $\sqrt{\mathcal{R}(\Delta = 0)}$ term is positive for $\mathrm{Im}(\chi) < \kappa_1 - \kappa_2 - \kappa_{\mathcal{A}}$ and negative otherwise.

8.3. Experimental setup

The experimental setup used for the EIT experiments is very similar to the setup described in ch. 4 with only few modifications which will be described here.

As abovementioned, the realization of EIT experiments requires control and probe light fields with a stable phase relation. For systems where the two transitions are addressed by two different laser sources this can be experimentally challenging. However, in our scheme for $^{40}Ca^{+}$ we use a two photon transition between Zeeman-substates, so that the atomic resonance frequencies for the probe and control field differ only by few MHz. Phase stability on the relevant time scales can hence be guarantied by using the same laser source to address both the control and the probe transition. This is accomplished by splitting the light of the probe laser (see sec. 4.8.1) on a PBC. Both the reflected and the transmitted portion of the light are first sent through AOMs, which are used for switching the beams on and off. The -1-diffraction order of each AOM is then sent through a double-pass AOM configuration, to allow for the independent control of the frequency of the two light fields. As the width of the EIT windows is expected to be as narrow as some few kHz a frequency resolution of $\lesssim 1$ kHz for these AOMs is required to resolve these narrow features. Experimentally this is ensured by the use of two direct digital synthesizers (DDS), with linewidth < 10 Hz and a frequency resolution of $\simeq 1$ Hz providing the driving frequency for the AOMs. The frequency of the DDSs is set by the experimental control computer.

In the experiments the frequency of the control beam is set to the resonance frequency of the $3d^2D_{3/2},\ m_J = {}^{-1}/_2 \leftrightarrow 4p^2P_{1/2},\ m_J = {}^{+1}/_2$ transition of $^{40}Ca^{+}$, while the frequency of the probe beam is scanned over the $3d^2D_{3/2},\ m_J = {}^{+3}/_2 \leftrightarrow 4p^2P_{1/2},\ m_J = {}^{+1}/_2$ resonance. On two photon resonance, where probe and control laser are resonant with the respective transitions, the detuning of the two fields can be calculated from the Zeeman splitting between the $m_J = {}^{-1}/_2$ and $m_J = {}^{+3}/_2$ states of the $3d^2D_{3/2}$ level. For a B-field of 2.5 G as typically used in these experiments, the splitting amounts to $\sim 2\pi \times 4.4$ MHz (for detail see appendix A.3).

As the frequency of the cavity is locked on the bare atomic resonance of the probe transition, the control laser will be injected into the cavity with a detuning corresponding to the Zeeman splitting. The intracavity Rabi frequency of the control field can accordingly be calculated by

$$\Omega_C^{\text{theory}} = g_{\text{C}}\sqrt{|a_{\text{C}}|^2} = \frac{g}{\sqrt{3}}\sqrt{\frac{2\kappa_2}{\kappa^2 + \Delta_{C,23}^2}\frac{P_{\text{in}}}{\hbar\omega_{\text{l}}}}, \tag{8.32}$$

where g_{C} denotes the single ion coupling rate of the control transition (see appendix A.5), $|a_{\text{C}}|^2$ is the intracavity photon number for the control field, $\Delta_{C,23} = \omega_C - \omega_{\text{ctrl}} \sim$

$2\pi \times 4.4$ MHz is the detuning of the control laser with respect to the cavity and set by the Zeeman splitting and P_{in} is the control power injected into the cavity. In the second step, we used eq. (3.18) to calculate the intra cavity control field amplitude for a certain input field P_{in} injected through mirror 2. The cavity decay rate through the PT was measured to be $\kappa_2 = 2\pi \times (7.85 \pm 0.08)$ kHz at a wavelength of 866.2 nm.

As the efficiency of the double-pass AOMs depend on the frequency, the probe AOM is driven by a voltage controlled RF-amplifier and calibrated over the scanning range of ± 25 MHz by finding the necessary voltage to keep the power level of the probe sent to the cavity stable for certain frequencies and extrapolating to the remaining range.

However, the intensity of the probe beam turned out to be slightly less stable in this configuration than in the previous and measuring the intensity of the cavity reflection signal for an off-resonant cavity with the APD revealed intensity fluctuations of the probe intensity level of 3.4% which we account for in the error calculations. The increased fluctuations can most likely be attributed to drifts of the voltage controlled RF-amplifier and the more complex optical setup.

8.3.1. Probing the cavity

The probe and the control beam are sent to the trap table through the two fibers to the PT and the HR side on the trap table, respectively. The reference laser at 894 nm is overlapped with the probe beam on the laser table and (as before) sent to the cavity from the PT side.

Though it is simpler, both conceptually and experimentally, to measure EIT spectra in transmission, the cavity spectra presented in this chapter will be obtained in reflection and we will briefly discuss the reasons for this. First of all, when considering the extension of the present scheme to the realization of single photon storage experiments, it is necessary to inject the single photon pulse from the PT side to achieve the highest possible efficiency. A measurement of the transmission spectrum hence would have to be carried out with the APD on the HR side. However, control and probe field possess orthogonal circular polarizations and injecting them from the two opposite sides of the cavity facilitates the independent control of the polarization of both beams. If one was to measure the transmission spectrum of the cavity on the HR side, the back reflection of the control beam would overlap with the transmitted probe signal. Even though the two beams in principle posses opposite polarizations the high input power required to achieve sufficiently high control field Rabi frequencies when injecting off-resonantly through the HR mirror would lead to a substantial background on the low signal at the single photon level which we want to measure. The second option, i.e. to inject both lasers from the PT side would require a more complex optical setup as the two beams would have to be overlapped on a non-polarizing beam splitter which would require the setup of a completely independent second beam path on this side. For these reasons, we chose to inject the probe from the PT side, and to measure the probe reflectivity signal, while injecting the control beam from the opposite side.

The setup used to probe the weak cavity reflection of the probe laser is hence similar to the one presented in 4.8. The intensity of the probe beam is again chosen so as to have a field at the single photon level in the empty cavity. It is σ^- polarized with respect to the quantization axis. The stronger control beam is injected to the cavity from the HR side and is σ^+ polarized. On the PT side, the cavity probe reflection signal has to be separated

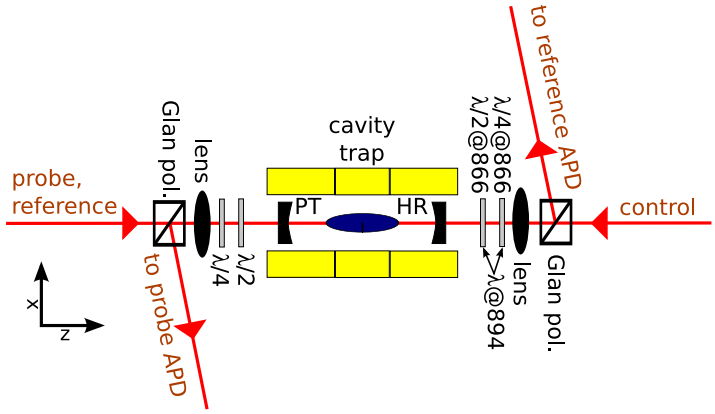

Figure 8.4.: Schematics of the modified experimental probe setup for the EIT experiments. Probe and control team are injected into the cavity from opposite sides. For details see text.

from the control light transmitted through the cavity before being sent to the probe APD. As the frequencies of the two beams are very similar, this has to be accomplished by the orthogonal circular polarizations of probe and control. It turned out that the extinction of the PBCs that were used to separate the light sent to the two APDs from the incident beams in the previous experiments was not sufficient and despite its orthogonal polarization, a fraction of the transmitted control light made it to the probe APD and caused a substantial background. The two PBCs were therefore replaced by two Glan polarizers. Their extinction was measured in a test setup consisting of two crossed Glan polarizers and the combination of $\lambda/4$ and $\lambda/2$ waveplates used in the cavity setup and was found to be better then $1:10^5$. When inserted into the experimental setup, this extinction was found to be substantially lower ($\sim 1:3\cdot10^3$), but still approximately one order of magnitude higher than in the previous configuration using the PBCs. Monitoring the control light transmitted through the cavity and reflected of the Glan polarizer with a CCD chip revealed that the intensity of this beam is inhomogeneous over the Gaussian profile. We attribute this to birefringence effects in the mirror substrates that might lead to local elliptical polarization components. These are most likely caused by tension induced by the mounting of the substrates and can explain the lower extinction on the Glan polarizers in the experimental setup.

To account for the additional background on the probe APD induced by the control field, and to check the extinction of the orthogonal polarization, we measure the background directly on the APD and adjust the waveplates on the HR side to pre-compensate the birefringence of the cavity as well as possible. The eventual remaining background is then measured and subtracted from the data.

8.3.2. Experimental sequence

In all EIT related experiments presented in this thesis, the frequency of the cavity is locked to the atomic resonance frequency for the probe, like in the measurements of the vacuum Rabi spectra in sec. 5.5. The locking scheme was described in sec. 4.8.3.

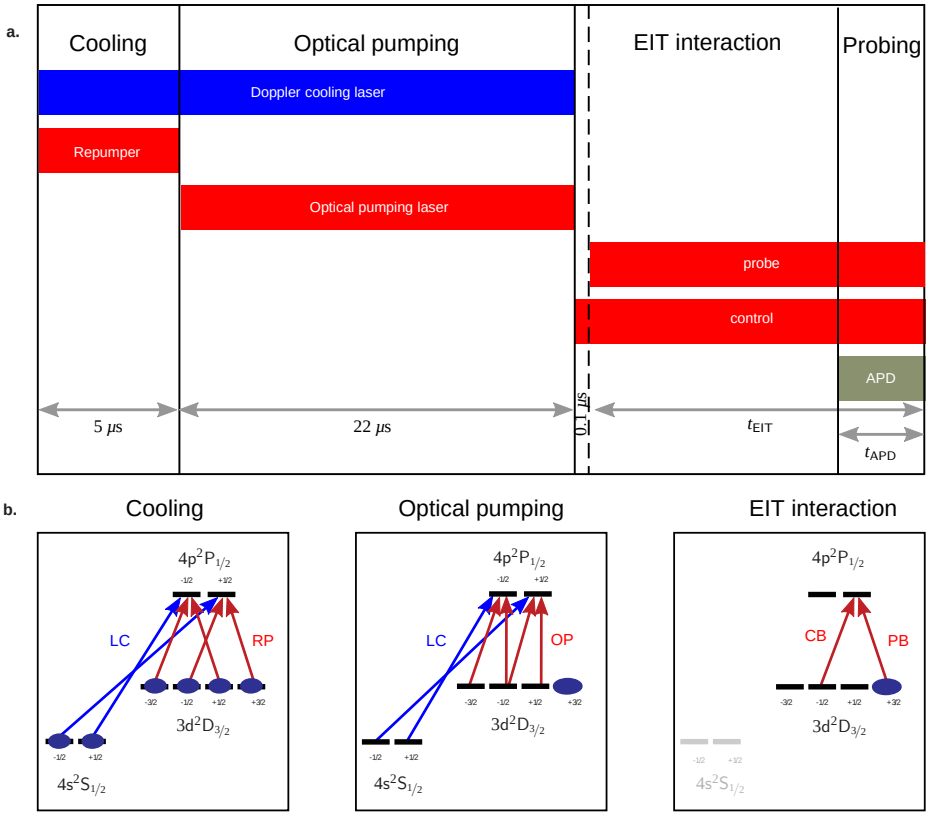

Figure 8.5.: a. Experimental sequence used in the EIT experiments. A 5 μs sequence of Doppler-cooling is followed by 22 μs optical pumping preparing the atoms in the $m_J = +3/2$ substate of the $3d^2D_{3/2}$ level. After the state preparation, the control field and after a short delay of 0.1 μs the probe are injected into the cavity for a time t_{EIT} (typically $10 - 50$ μs). At the end of the EIT interaction, the cavity reflectivity is measured by the probe APD for a time t_{APD} (typically 1.4 μs). **b.** Energy levels of $^{40}Ca^+$ including the relevant transitions and polarization for cooling, optical pumping and EIT interaction. The acronyms are: LC: laser cooling beam, RP: repumping beam, OP: optical pumping beam, CB: control beam, PB: probe beam.

The experimental sequence used in these experiments is depicted in fig. 8.5. It consists of a 5 μs sequence of Doppler-cooling, followed by 22 μs optical pumping. Then first the control field and after a short delay of 0.1 μs the probe field are injected into the cavity for an interaction time t_{EIT}. The short delay ensures that steady state is reached for the control field before injecting the probe and to avoid atom-mediated transient effects that might occur when both lasers are injected at the same time. The length of the interaction time (typically between 10 and 100 μs) will depend on the Rabi-frequency of the control field, which sets, as discussed above, the time scale for establishing the EIT. At the end of the interaction phase, the probe APD is turned on and we measure the cavity reflectivity for typically $t_{\mathrm{APD}} \sim 1.4$ μs.

The sequence is continuously repeated with a repetition frequency given by the inverse sequence time. As described in 4.8.3 the transmission signal of the reference laser is used to post-select the data points for which the cavity was resonant. The cavity reflection is measured for various detunings of the probe laser, where for each detuning of the probe, typically 10^4 data points are acquired.

8.4. Experimental results

8.4.1. Normal-mode splitting

In a first set of experiments, we measured the cavity spectrum as a function of the probe detuning Δ for the three cases of i.) an empty cavity with no ions present, ii.) a cavity containing an ion Coulomb crystal when only probe light is sent to the cavity and iii.) for the EIT case, where both the probe and the control field are injected into the cavity. The expected reflectivity spectrum for the three cases were shown in fig. 8.3 for $N = 500$.

Fig. 8.6 shows the three reflectivity spectra obtained for the different configurations. The spectrum (red squares) is taken with no ions present in the trap and shows the familiar Lorentzian reflectivity dip of the bare cavity. Fitting this data set with the expected lineshape yields a cavity field decay rate of $\kappa = 2\pi \times (2.2 \pm 0.1)$ MHz, in good agreement with previous measurements.

Then, for the second data set (green triangles), an ion Coulomb crystal is loaded into the trap and the coupled atom-cavity system is probed, and we observe the expected Vacuum Rabi splitting (see sec. 5.5). With a half-length of $L = (801 \pm 1)$ μm, a radius of $R = (141 \pm 1)$ μm and , and a ion density of $\rho_0 = (5.6 \pm 0.1) \cdot 10^8$ cm^{-3}, the crystal contains a total of $N_{\mathrm{tot}} \sim 37500$. As we will later show, this crystal is in the collective strong coupling regime with a cooperativity of $C = 3.4 \pm 0.1$. Using eq. (8.31) we determine from the reflectivity level around resonance an atomic transparency of $T_{\mathrm{atomic}} \sim (1.2 \pm 0.2)\%$ and the crystal is opaque for the probe field.

Finally, the third spectrum (blue circles) is acquired with the same crystal when both the control and the probe fields are injected into the cavity. The control field is resonant width the $3d^2D_{3/2}$, $m_J = {}^{-1}/_2 \leftrightarrow 4p^2P_{1/2}$, $m_J = {}^{+1}/_2$ transition and has an input power of 1.0 μW corresponding to an expected Rabi frequency of the control field of $\Omega_{\mathrm{C}}^{(theory)} = 2\pi \times (4.6 \pm 0.2)$ MHz (see eq. (8.32)). For large detunings of the probe laser, the spectrum is similar to the vacuum Rabi splitting. However, for small probe detunings $\Delta \simeq 0$ MHz (when the two lasers are close to two-photon resonance $\delta \simeq 0$ MHz) the cavity reflection spectrum exhibits a sharp dip and the reflection drops drastically around

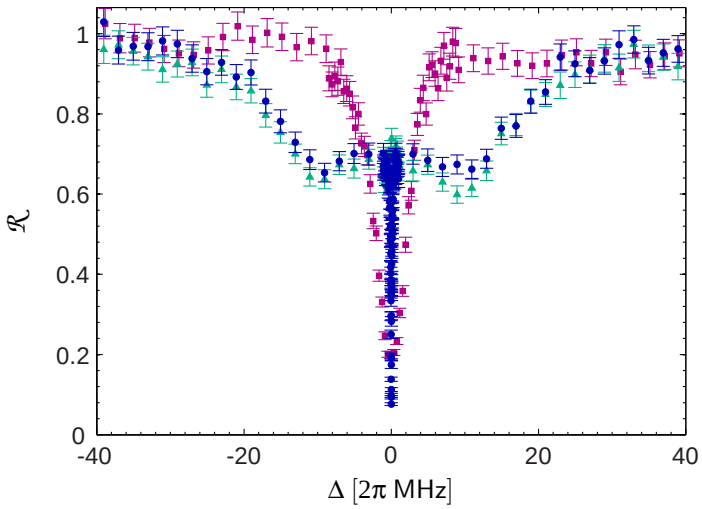

Figure 8.6.: Probe reflectivity spectrum for an empty cavity (red squares) and a cavity containing an ion Coulomb crystal without (green triangles) and with the control field present (blue circles). With a half-length of $L = (801 \pm 1)$ μm, a radius $R = (141 \pm 1)$ μm and a ion density of $\rho_0 = (5.6 \pm 0.1) \cdot 10^8$ cm^{-3}. The cooperativity was measured to be $C = 3.4 \pm 1$ (for details see text).

$\Delta = 0$ MHz. From the reflectivity level on two-photon resonance we calculate an atomic transparency on resonance of $T_{\text{atomic}} = (84 \pm 1)\%$ (see eq. (8.31)), which is two orders of magnitude higher as compared to the vacuum Rabi spectra, when there is only the probe laser present.

More quantitative information from the EIT spectrum can be obtained by fitting it to the theoretical model of eq. (8.27). Owing to the complexity of the model, we first characterize the system in order to measure the non-EIT related interaction parameters independently. For this purpose, we first measure the broadening of the cavity effective decay rate κ' (see eq. (3.48a)) as a function of probe detuning Δ by the method described in sec. 5.4. To account for the finite temperature of the crystal the spontaneous dipole decay rate γ' as well as the cavity decay rate κ are left as free fitting parameters (see secs. 3.3 and 5.4). We find $(g_{\text{N}}, \gamma', \kappa) = 2\pi \times (13.6 \pm 0.3, 12.6 \pm 0.8, \kappa = 2.5 \pm 0.2)$ MHz. The dipole decay rate found here is substantially higher than the natural dipole decay rate. This indicates that the cooling conditions might have been less optimal for these measurements as compared to those presented in e.g. sec. 5.4.

To confirm the coherent coupling rate found from the broadening of the effective cavity decay rate we furthermore obtained vacuum Rabi spectra (see sec. 5.5), which were measured both in reflection and transmission. For the measurement of the transmission spectrum, the probe laser is injected into the cavity from the HR side and the transmitted signal is measured by the probe APD on the PT side (see 4.8.2 for details). The two sets of data can be seen in fig. 8.7. Fits to the two curves yield collective coupling rates of $g_N^{(\text{refl})} = 2\pi \times (13.9 \pm 0.3)$ MHz and $g_N^{(\text{trans})} = 2\pi \times (13.8 \pm 0.1)$ MHz for the reflection and transmission spectrum, respectively. To facilitate convergence of the more complex

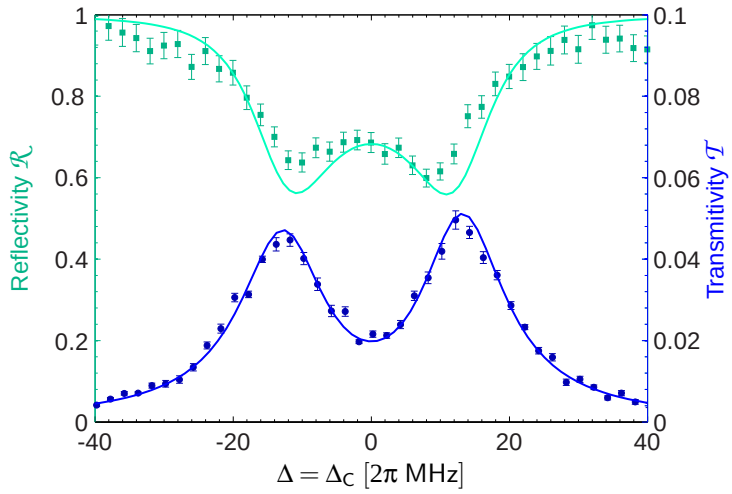

Figure 8.7.: Vacuum Rabi spectrum measured in reflection and transmission for a crystal with half-length and radius $R = (141 \pm 1)$ μm and $L = (801 \pm 1)$ μm, and a ion density of $\rho_0 = (5.6 \pm 0.1) \cdot 10^8$ cm^{-3}. The solid lines are fits to the data and yield collective coupling rates of $g_N^{(\mathrm{refl})} = 2\pi \times (13.9 \pm 0.3)$ MHz in reflection and $g_N^{(\mathrm{trans})} = 2\pi \times (13.8 \pm 0.1)$ MHz in transmission.

fitting function, the values of κ and γ are set to the previous values of $\kappa = 2\pi \times 2.2$ MHz and $\gamma = 2\pi \times 12.6$ MHz, respectively.

The collective coupling rates we find for the three different measurements all agree within their error bars and yield a cooperativity of $C = 3.4 \pm 0.1$, corresponding to an effective number of interacting ions of $N \sim 675$. For the vacuum Rabi splitting measurements we observe a better agreement of the spectra measured in transmission than in reflection, especially around the lobes of the normal modes. The reason for this discrepancy is not completely understood, but might be attributed to the more sensitive nature of the measurement in reflection. As the reflected field results from the interference between the incoming and the intracavity field leaking out of the cavity, it is more sensitive to mode matching or polarization imperfections. Nevertheless, the collective coupling rates deduced from fits to both spectra agree within their uncertainties. Furthermore, around two-photon resonance ($\Delta = \Delta_C = 0$), the reflection spectrum is still well resembled by the fit to the theoretical model and it is mainly this region which is important for the systematic studies of the EIT resonance.

Having measured the interaction parameters of the system, we can finally turn back to the cavity reflectivity spectra of fig. 8.6. A zoom around two-photon resonance is shown in fig. 8.8, for the empty cavity (red squares), the probe vacuum Rabi splitting spectrum (green triangles) and the EIT spectrum (blue circles). The solid lines in the corresponding colors represent fits to the theoretical model, using eq. (8.28). For the EIT situation, the transverse profile of the control is taken into account by using the susceptibility of (8.25). The narrow EIT window is very well resembled by the fit to the theoretical model with a clearly non-Lorentzian lineshape due to the effect of the transverse profile of the control

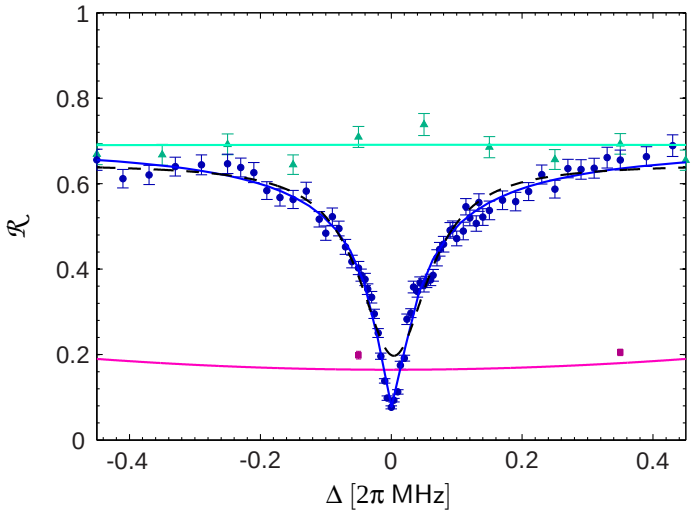

Figure 8.8.: Zoom around two-photon resonance for the probe reflectivity spectra of fig. 8.6. The curves are obtained for an empty cavity (red squares) and a cavity containing an ion Coulomb crystal with a measured cooperativity of $C = 3.4 \pm 0.1$, without (green triangles) and with control field (blue circles). The solid lines are fits to eq. (8.27), using the two-level susceptibility of eq. (3.41) for the vacuum Rabi and the three-level susceptibility of eq. (8.25) for the EIT spectrum. From the fit to the EIT spectrum, we obtain a collective coupling rate of $g_N = 2\pi \times (13.7 \pm 0.1)$ MHz, a Rabi frequency of the control field of $2\pi \times (4.1 \pm 0.1)$ MHz and a half-width of the central EIT window of (47.5 ± 2.4) kHz. The atomic transparency on resonance is increased from (1.2 ± 0.2) to (84 ± 1)%. To illustrate the non-Lorentzian lineshape of the EIT window a Lorentzian fit is also depicted (dashed black line).

field. To illustrate this effect, a Lorentzian fit to the data is also plotted (dashed black line) and deviates substantially from both the experimental data and the fit to the theoretical model. The half-width of the EIT windows is found to be $2\pi \times (47.5 \pm 2.4)$ kHz and is almost a factor 50 narrower than the bare cavity width of $\kappa = 2\pi \times 2.2$ MHz.

Moreover, on two photon resonance we deduce, according to eq. (8.31), an atomic transparency of $T_{atom} = (84 \pm 1)\%$. For this curve, the cavity reflectivity drops below the value of the empty cavity. Though this might seem surprising, this behavior is expected and can be understood from the resonant reflectivity ($\Delta = \Delta_C = 0$), given in eq. (8.29a). For a certain value of the control Rabi frequency Ω_C the atomic absorption is reduced by the EIT to the level, where it compensates the difference between the cavity decay rate through the PT, κ_1, and the sum of the decay rate through the HR, κ_2, and the intracavity loss rate, $\kappa_{\mathcal{A}}$. In this case, the atomic absorption is given by $\mathrm{Im}(\chi) \sim 2\pi \cdot 0.86$ MHz, corresponding to an atomic transparency of $T_{\mathrm{atom}} \sim 52\%$. For even higher control field Rabi frequencies, the reflection level rises again and converges to the empty cavity level when the atomic absorption goes down to zero.

Furthermore, the fit to the EIT spectrum yields a collective coupling rate of $g_N = 2\pi \times (13.7 \pm 0.1)$ MHz, a Rabi frequency of the control field of $2\pi \times (4.1 \pm 0.1)$ MHz and a ground state decoherence rate of $\gamma_{12} = 2\pi \times (1.2 \pm 0.2)$ kHz, where the effective dipole decay rate and the cavity field decay rate were fixed to the values deduced in the previous experiments ($\gamma = 2\pi \times 12.6$ MHz and $\kappa = 2\pi \times 2.2$ MHz, respectively). The collective coupling rate is in very good agreement with the value found for the Vacuum Rabi spectra and the broadening of the effective cavity decay rate. The control field Rabi frequency deduced from the fit is slightly lower than the theoretically expected value of $\Omega_{\mathrm{SW}}^{(theory)} = 2\pi \times (4.6 \pm 0.2)$ MHz. This slight discrepancy may be attributed to drifts of the laser power during the measurement, a non-ideal coupling to the cavity or polarization drifts, resulting in this specific experiment in a slightly lower intracavity field intensity. We note that the value we find for γ_{12} in this single fit is rather is an order of magnitude, due to the complexity of the fitting function[5]. As we will see in the next section this value is actually in good agreement with other systematic measurements. In principle, one could expect that the decay rate of the ground state γ_{12} could be as low as the decoherence rate we found in the measurement of the coherence time of collective Zeeman substates in sec. 5.7. The coherence time of $\tau_e = 1.7^{100}_{-0.8}$ ms we found there would correspond to a decoherence rate of $\gamma_e \sim 2\pi \times 0.1$ kHz, which is much lower as the fitted decay of the EIT ground state coherence γ_{12}, but might still be consistent with the measured spectra. The issue of the ground state decoherence rate will be further addressed in the following systematic studies and we will discuss possible differences and present limitations in sec. 8.4.4.

8.4.2. Effect of control power

An important parameter for the steady state behavior and the dynamics of the EIT interaction is the control field Rabi frequency. In this subsection we will study both steady state spectra and the dynamical build up of the transparency during the EIT interaction for various powers of the control field.

The crystal used in these experiments is slightly bigger than the previous one and we

[5] γ_{12} only appears in combination with Ω_C which leads to strong mutual dependencies of the fitting parameters.

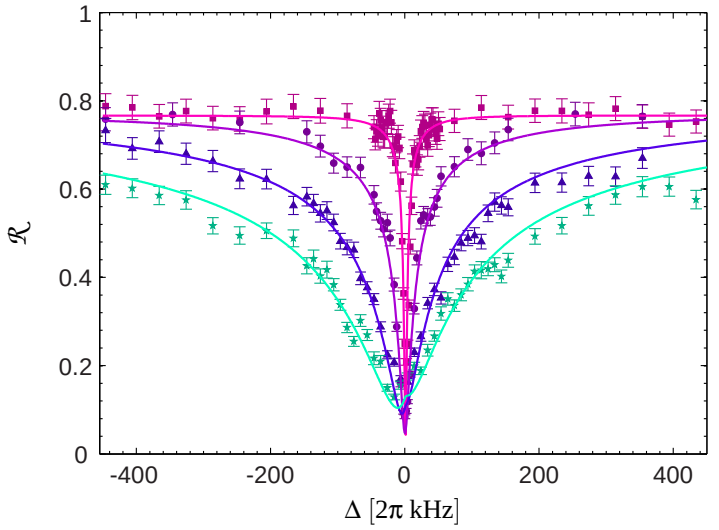

Figure 8.9.: EIT spectra for different (selected) input powers of the control field: 82 nW (squares), 414 nW (circles), 2057 nW (triangles) and 3490 nW (stars). The solid lines are fits to the model of eq. (8.27). The crystal's half-length, radius and density are $L = (863 \pm 1)\,\mu$m, $R = (125 \pm 1)\,\mu$m and $\rho_0 = (5.6 \pm 0.1) \cdot 10^8\,\mathrm{cm}^{-3}$ amounting to an effective number of ions $N = 980 \pm 20$ (taking the optical pumping efficiency of 97% into account.) From the fits we deduce control field Rabi frequencies of $2\pi \times (1.18 \pm 0.04)$ MHz, $2\pi \times (3.23 \pm 0.11)$ MHz, $2\pi \times (5.91 \pm 0.18)$ MHz and $2\pi \times (8.62 \pm 0.26)$ MHz.

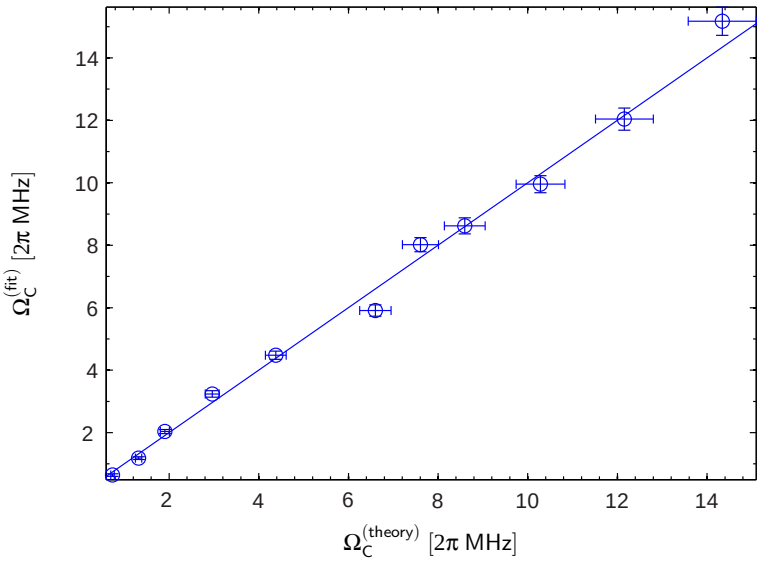

Figure 8.10.: Control Rabi frequency as deduced from fits to the EIT spectra versus the theoretical value deduced from the input power of the control laser. The solid line indicates $\Omega_C^{(fit)} = \Omega_C^{(theory)}$.

deduce from a projection image a half-length of $L = (863 \pm 1)$ μm and a radius of $R = (125 \pm 1)$ μm. With a density of $\rho_0 = (5.6 \pm 0.1) \cdot 10^8$ cm^{-3} the effective number of ions amounts to $N = 980 \pm 20$ (taking the optical pumping efficiency of 97% into account), corresponding to a expected collective coupling rate of $g_{\mathrm{N}}^{(\mathrm{theory})} = 2\pi \times (16.6 \pm 0.4)$ MHz.

In a first step, we obtain EIT spectra around two-photon resonance for various intensities of the control field. In fig. 8.9 exemplary spectra around two-photon resonance are shown for four different cavity input powers of the control laser: 82 nW (squares), 414 nW (circles), 2057 nW (triangles) and 3490 nW (stars), corresponding to expected intracavity control field Rabi frequencies $\Omega_{\mathrm{C}}^{(\mathrm{theory})}$ of $2\pi \times (1.3 \pm 0.1)$ MHz, $2\pi \times (3.0 \pm 0.2)$ MHz, $2\pi \times (6.6 \pm 0.4)$ MHz and $2\pi \times (8.6 \pm 0.5)$ MHz, respectively. The solid lines are fits to the theoretical model of eq. (8.27), and using the linear susceptibility taking the transverse profile of the control field into account, see eq. (8.25).

As expected, the width of the EIT window increases with higher control power. Furthermore, the depth of the EIT dip also increases, and for a certain range of powers of the control field drops below the reflectivity of the bare cavity and reaches a level close to zero, as mentioned in the previous subsection.

A global fit[6] of the data yields a collective coupling rate of $g_{\mathrm{N}}^{(\mathrm{fit})} = 2\pi \times (16.2 \pm 0.2)$ MHz, in good agreement with the value deduced from the effective number of ions and the single ion coupling rate g. The Rabi frequencies deduced from the fits, $\Omega_C^{(\mathrm{fit})}$, are depicted in fig. 8.10 versus the theoretically expected values calculated from the input powers of the control field according to eq. (8.32). The solid line corresponds to $\Omega_{\mathrm{C}}^{(\mathrm{fit})} = \Omega_{\mathrm{C}}^{(\mathrm{theory})}$ and we find very good agreement between the experimental values and the theoretical expectations.

For the fits, the ground state decoherence rate was based on the previous discussion set to $\gamma_{12} = 2\pi \times 1$ kHz. To check the plausibility of this choice, we repeated the fitting procedure for values of $\gamma_{12} = 2\pi \times 0.1$ kHz and $\gamma_{12} = 2\pi \times 4$ kHz. The control field Rabi frequencies deduced from these fits were then investigated as a function of the expected Rabi frequency and fitted by a linear function. The linear slopes deduced for all three values of γ_{12} are summarized in the following table

γ_{12} $[2\pi$ kHz$]$	linear slope
0.1	0.92 ± 0.02
1.0	1.00 ± 0.02
4.0	1.08 ± 0.02

Based on this comparison, a value of $\gamma_{12} \sim 1$ kHz seems reasonable and is consistent with our data. We will, therefore, for the remaining analysis in this chapter stick to this value.

Width of the EIT window

In fig. 8.11 are shown the half-widths of the EIT windows as deduced from the fits in fig. 8.6 and similar spectra (blue circles, left axis) as a function of the square of the expected control field Rabi frequency for the various input powers. The blue line is a

[6] Beside the control field Rabi frequency, all fitting parameters are assumed to be equal for the various data sets.

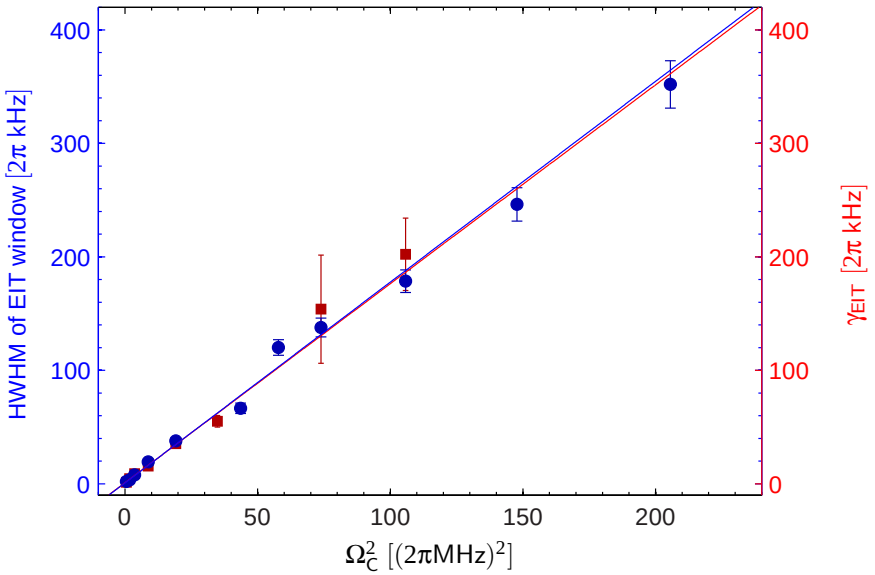

Figure 8.11.: Left Axis: Half-widths of the EIT windows depicted in fig. 8.9 as deduced form the fits to the theoretical model versus the square of the expected control field Rabi frequency (blue squares). The blue solid line is a linear fit and yields a linear slope of $a_{\mathrm{HWHM}} = (1.7 \pm 0.1)\ {}^{10^{-3}}/_{2\pi\ \mathrm{MHz}}$ and an intersection of $b_{\mathrm{HWHM}} = 2\pi \times (0.9 \pm 0.3)$ kHz. **Right Axis:** EIT build-up time constant γ_{EIT} deduced from fits to corresponding dynamical curves as shown in fig. 8.13 versus the square of the expected control field Rabi frequency (red squares). The red solid line is a linear fit and yields a slope of $a_{\gamma_{\mathrm{EIT}}} = (1.8 \pm 0.2)\ {}^{10^{-3}}/_{2\pi\ \mathrm{MHz}}$ and an intersection of $b_{\gamma_{\mathrm{EIT}}} = 2\pi \times (1.0 \pm 0.4)$ kHz. The two axis are on scale.

linear fit to the data and yields a linear slope of $a_{\mathrm{HWHM}} = (1.7 \pm 0.1)\ {}^{10^{-3}}/_{2\pi\,\mathrm{MHz}}$ and a intersection of $b_{\mathrm{HWHM}} = 2\pi \times (0.9 \pm 0.3)$ kHz. For small control field Rabi frequencies $\Omega_C \to 0$ one expects the half-width of the EIT window to be limited by the ground state decoherence rate γ_{12}, which for the analysis of the curves in fig. 8.9 was chosen to be $\gamma_{12} = 2\pi \times 1$ kHz. The intersection deduced from the linear fit in fig. 8.11 hence provides a further way to independently check the self-consistency of this assumption. For this purpose, we repeated the analysis of the half-width of the EIT for the control field Rabi frequencies for $\gamma_{12} = 2\pi \times 0.1$ kHz and $\gamma_{12} = 2\pi \times 4$ kHz. The results of linear fits to the three sets of data are summarized in the following table.

γ_{12} $[2\pi$ kHz$]$	intersection $b^{(\mathrm{HWHM})}$ $[2\pi$ kHz$]$	linear slope $a^{(\mathrm{HWHM})}$ $[{}^{10^{-3}}/_{2\pi\mathrm{MHz}}]$
0.1	0.2 ± 0.2	1.6 ± 0.1
1.0	0.9 ± 0.3	1.7 ± 0.1
4.0	6.2 ± 0.7	1.8 ± 0.1

The intersection we find for choices of $\gamma_{12} = 2\pi \times 0.1$ kHz and $\gamma_{12} = 2\pi \times 1$ kHz resemble these choices, while the value we find for $\gamma_{12} = 2\pi \times 4$ kHz clearly deviates from the assumption. In connection with the analysis of the fitted control field Rabi frequency we infer on this basis that a ground state decoherence rate of the order of ~ 1 kHz is very likely and will use this choice for the remaining analysis. We will turn back to the issue of the ground state coherence time and possible limitations in sec. 8.4.4.

Atomic transparency

An important quantity in connection with EIT is certainly the transparency of the atomic medium. Based on the Rabi-frequencies deduced from the fits, we can now, using eq. (8.30), calculate the transparency of the atomic medium T_{atom} on resonance. The result is depicted in fig. 8.12 as a function of the control field input power. For comparison, we plot the theoretical expectation, which is calculated based on (8.30) and using the Rabi frequencies found for the input power of the control field according to eq. (8.32). The remaining parameters are the experimentally deduced values, i.e. a coherent coupling rate $g_N^{\mathrm{fit}} = 2\pi \times 16.2$ MHz, a cavity decay rate of $\kappa = 2\pi \times 2.2$ MHz, an effective dipole decay rate of $\gamma' = 2\pi \times 11.7$ MHz and a decay rate for the ground state coherence of $\gamma_{12} = 2\pi \times 1$ kHz. The transparency increases from a level of $< 1\%$ for low Rabi frequencies of the control field to values above 95% for higher control field intensities and we find good agreement with the expected behavior.

Dynamical build up

To gain insight into the dynamical evolution of the EIT build up for various intensities of the control field, a series of measurements was performed, where the probe reflectivity is monitored at different delays after the control and probe fields have been turned on. This is accomplished by measuring the cavity reflection on two-photon resonance ($\delta = 0$) by the probe APD at different times in the EIT interaction phase. To obtain a sufficient time resolution, the time window for the APD was reduced to 0.5 μs in these measurements. Exemplary data sets for the same crystal as used for the measurements in fig. 8.9 are shown in fig. 8.13. The control field input powers are 82 nW (squares), 414 nW (circles),

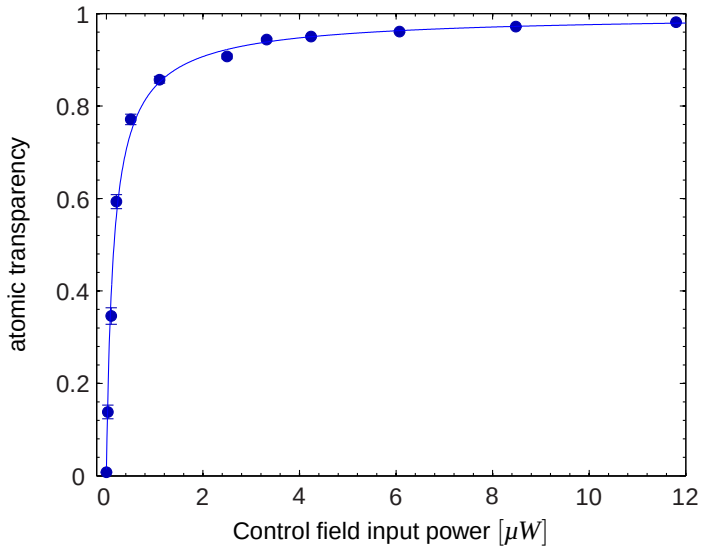

Figure 8.12.: Deduced atomic transparency for different input powers of the control field. The solid line corresponds to the theoretical expectations of eq. (8.30), where eq. (8.32) is used to deduce the Rabi frequencies for the input power of the control field. The other parameters were fixed to the values deduced in the previous measurements ($g_{\mathrm{N}}^{\mathrm{fit}} = 2\pi \times$ 16.2 MHz, $\kappa = 2\pi \times 2.2$ MHz, $\gamma' = 2\pi \times 11.7$ MHz and $\gamma_{12} = 2\pi \times 1$ kHz).

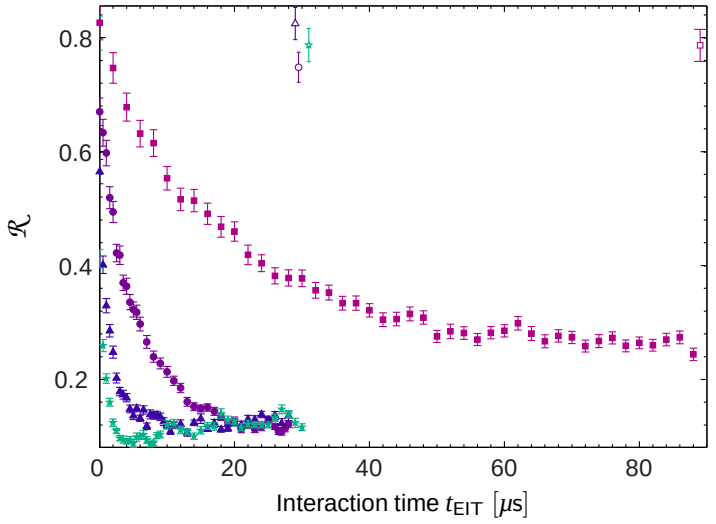

Figure 8.13.: Time evolutions of the reflectivity level for a two-photon resonant probe field for the same control field Rabi frequencies and the same crystal as in fig. 8.9. The last points (open symbols) of each curve are taken with the control field switched off to verify that no significant depopulation of the $\left|3d^2D_{3/2},\ m_J = {}^{+3}/_{2}\right\rangle$ substate has occurred during the interaction.

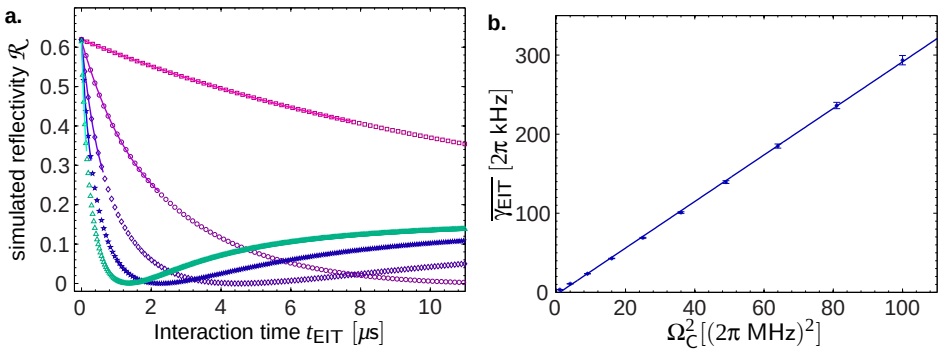

Figure 8.14.: Numerical simulation of the time evolution of the resonant cavity reflectivity. **a.** Sample curves calculated from the inverse Laplace transformation of eq. (8.26) for different intra cavity Rabi frequencies: $\Omega_C = 2\pi \times 1$ MHz (squares), $\Omega_C = 2\pi \times 3$ MHz (circles), $\Omega_C = 2\pi \times 5$ MHz (diamonds), $\Omega_C = 2\pi \times 7$ MHz (stars) and $\Omega_C = 2\pi \times 9$ MHz (triangles). The time constants of the EIT build up are extracted by fitting the beginning (to the $1/e$ level) with $a\ \exp(-2\overline{\gamma_{EIT}}t) + c$. **b.** Extracted $\overline{\gamma_{EIT}}$ as a function of the square of the control field Rabi frequency. The solid line is a fit according to $\overline{\gamma_{EIT}} = \gamma_{12} + \frac{\Omega_C^2/2a_0}{\gamma(1+2C)}$, where the scaling factor a_0 is introduced to account for the effective averaging of the Rabi frequency over the transverse profile. From the fit to the values deduced from the simulations we find $a_0^{(sim)} = (2.19 \pm 0.02)$.

2057 nW (triangles) and 3490 nW (stars) and also correspond to those of fig. 8.9. One observes a decrease of the cavity reflectivity signal with the interaction time, with a time constant depending on the control field intensity. For the highest intensities, a steady state level is reached after some few μs, while it takes several tens of μs for the lowest measured control intensities. To prove that no significant depopulation of the $\left|3d^2D_{3/2},\ m_J = {}^{+3}/_2\right\rangle$ substate occurs during the interaction time, the control field is switched off before the probe field and the last data point of each curve is measured with solely the probe field in the cavity. The corresponding data points are marked by open symbols and reach within their errors the reflectivity level at the beginning of the measurement, hence indicating that the population in the $m_J = {}^{+3}/_2$ state has not decreased during the interaction time.

As discussed in sec. 8.2.3, modelling the dynamical evolution of the mean value of the intracavity field is not trivial for an intracavity control field, where one has to take its transverse field distribution into account. For the case of a uniform control field the dynamical equations in eqs. (8.6) and (8.7) can be solved by an adiabatic elimination, see eqs. (8.9). The resulting time dependence of the intracavity field was found to be exponential, with a time constant, which, in the resonant case ($\Delta = \delta = 0$), is given by $\gamma_{EIT} = \gamma_{12} + \frac{\Omega_C^2/2}{\gamma(1+2C)}$ (see eq. (8.14)).

For the more complex situation of an intracavity control field as used in the experiment, one can solve the dynamical equations in the Laplace-domain, where for the intracavity field amplitude on finds the expression given in eq. (8.26). The inverse transformation can, however, not be performed analytically and has to be calculated numerically. This method does, hence, not provide a simple expression that could be used to fit the experimental data

in fig. 8.13.

Instead, we performed numerical simulations of the dynamical evolution of the cavity reflection signal for various Rabi frequencies of the control field Rabi frequency, some exemplary curves are depicted in fig. 8.14 a. A first useful approximation for the EIT time constant can be found by fitting the first few μs of the resulting time dependent cavity reflectivity curves with the exponential form one would expect for a homogeneous control field $\mathcal{R} = a\ \exp(-2\gamma_{\mathrm{EIT}}t) + c$.

For the case of an intracavity control field, the time evolution will depend on the radial position of the individual ions, since the time constant depends on Ω_{C}. As a result, the dynamical evolution of the cavity reflectivity will be an average of all these contributions and one will in general find a slower evolution as compared to a uniform control field with comparable Rabi frequency. In a simple heuristic picture one can account for this average by rescaling the Rabi frequency of the intracavity control field by a scaling factor a_0. In this simple model, the average time constant is hence expected to be given by $\overline{\gamma_{\mathrm{EIT}}} = \gamma_{12} + \frac{\Omega_{\mathrm{C}}^2/2a_0}{\gamma(1+2C)}$. Using the numerical simulations, we can estimate this scaling parameter a_0. The time constants $\overline{\gamma_{\mathrm{EIT}}}$ as deduced from the fits to the first part of the simulated dynamical curves are depicted in fig. 8.14 b. as a function of the square of the control field Rabi frequency Ω_{C}^2 used in the corresponding simulation and a linear fit to the simulated data points yields a scaling factor $a_0^{(\mathrm{sim})} = 2.19 \pm 0.02$.

Using the same approach for the experimental data and fitting the first few μs of the dynamical curves by $\mathcal{R} = a\ \exp(-2\overline{\gamma_{\mathrm{EIT}}}t) + c$, we can hence also deduce the corresponding time constants for build up of the electromagnetically induced transparency. On the left axis of fig. 8.9 are depicted the values deduced from these fits as a function of the control field input power (red squares). The red solid line is a linear fit to the build up time constants and yields a linear slope of $a_{\gamma_{\mathrm{EIT}}} = (1.8 \pm 0.2)\ {}^{10^{-3}}/_{2\pi\ \mathrm{MHz}}$, which for the parameters of the experiment corresponds to a scaling parameter for the Rabi frequency of of $a_0^{(\mathrm{fit})} = 2.2 \pm 0.2$ in very good agreement with the value found for the simulations.

On the left axis of the same graph are shown the half-widths of the steady state EIT windows deduced from the fits in fig. 8.11 (blue circles). The two axis are on the same scale and the two sets of data overlap within their error bars. Furthermore, the linear scaling parameter of both fits also agree within their uncertainties. Though we cannot, due to the complexity of the theoretical model, give a strict proof of the equivalence of the time constants and the corresponding half-width, it is from a physical point of view still reasonable to expect a correspondence between the time evolution of the EIT build up and the observed spectral half-width of the EIT resonance, as suggested by our experimental findings. This also provides us with simple analytical estimates for the EIT build up time constants in the range of parameters investigated here.

8.4.3. Varying the number of ions

In a subsequent experiment, we measured the dependence of the EIT on the effective number of ions and hence the collective coherent coupling rate. This is accomplished by varying the number of ions in the cavity mode by changing the RF and DC trapping voltages, as was explained in sec. 5.6, where the dependence of the collective strong coupling on the effective number of ions was investigated.

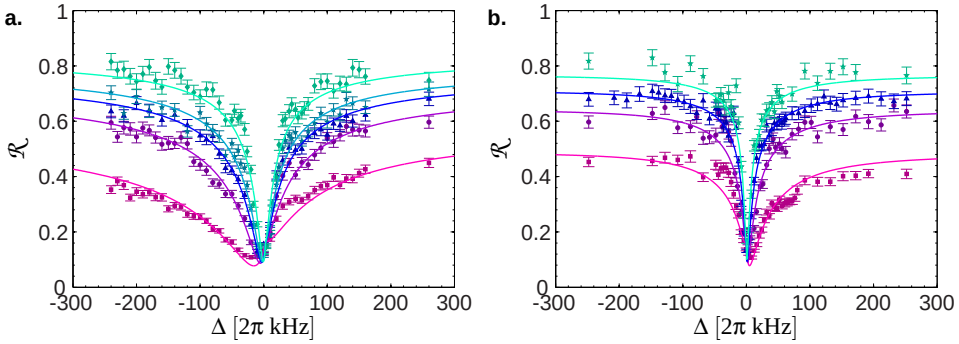

Figure 8.15.: EIT spectra for ion Coulomb crystals with different effective numbers of interacting ions for input powers of the control field of **a.** $P_{\mathrm{C,in}} = 576$ nW ($N = 393$ (squares), $N = 590$ (circles), $N = 737$ (triangles), $N = 938$ (stars), $N = 938$ (diamonds)) and **b.**. $P_{\mathrm{C,in}} = 103$ nW ($N = 362$ (squares), $N = 590$ (circles), $N = 735$ (triangles), $N = 1082$ (stars)). The solid lines are fits based on eq. (8.27) and yield control field Rabi frequencies of $\Omega_{\mathrm{C}}^{(\mathrm{fit})} = 2\pi \times (4.0 \pm 0.2)$ MHz and $\Omega_{\mathrm{C}}^{(\mathrm{fit})} = 2\pi \times (1.6 \pm 0.1)$ MHz, respectively.

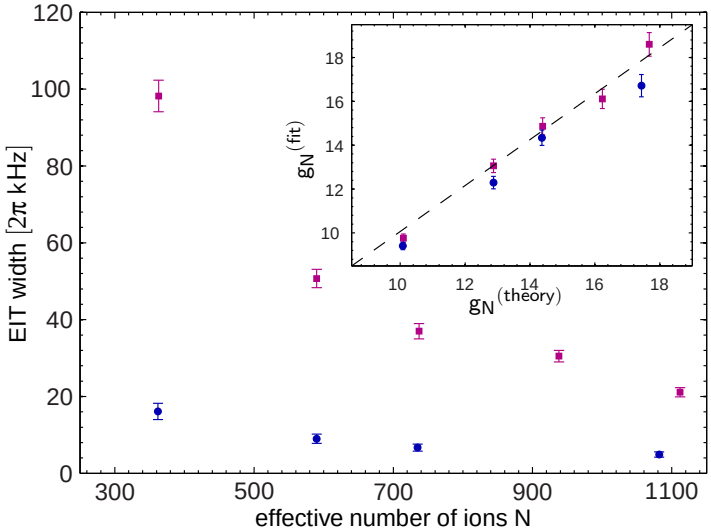

Figure 8.16.: Width of the EIT windows for different effective numbers of interacting ions for the two sets of data presented in fig. 8.15. The red squares correspond to $P_{\mathrm{C,in}} = 576$ nW, the blue circles to $P_{\mathrm{C,in}} = 103$ nW. The widths are calculated numerically based on the collective coherent coupling rates and the control field Rabi frequency deduced from the fits, and the previously measured values of κ, γ and γ_{C}.
Inset: Collective coherent coupling rate deduced from the fits versus the theoretically expected values for the two sets of data. The dashed line indicates $g_{\mathrm{N}}^{\mathrm{fit}} = g_{\mathrm{N}}^{\mathrm{theory}}$.

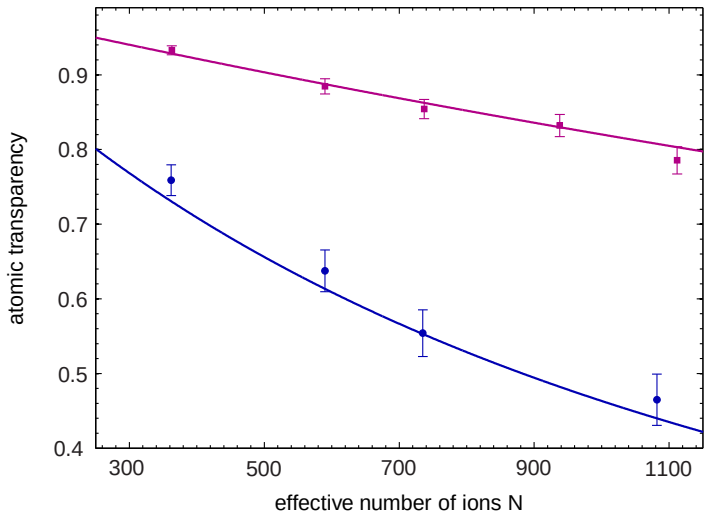

Figure 8.17.: Atomic transparency for different effective numbers of interacting ions for the two sets of data depicted in fig. 8.15 (blue circles: $P_{\mathrm{C,in}} = 576$ nW, red squares $P_{\mathrm{C,in}} = 103$ nW). The solid lines are the theoretical curves calculated according to eq. (8.30).

The measurement was performed for two fixed input powers of the control field, $P_{\mathrm{in}} = 576$ nW and $P_{\mathrm{in}} = 103$ nW. The obtained cavity reflection spectra around two photon resonance for the two sets of data are depicted in fig. 8.15 a. and b., respectively. For both sets of data, one observes a decreasing width of the EIT windows, as the number of ions and hence also the collective coherent coupling rate is increased, in accordance with the expectations from the theoretical model (see eq. (8.27)).

The solid lines are fits to the various curves based on the model in eq. (8.27) where we leave the control field Rabi frequency and the collective coupling rates as free parameters and fixing the remaining parameters to the previously measured values. The control field Rabi frequencies are found to be of $\Omega_{\mathrm{C}}^{(\mathrm{fit})} = 2\pi \times (4.0 \pm 0.2)$ MHz and $\Omega_{\mathrm{C}}^{(\mathrm{fit})} = 2\pi \times (1.6 \pm 0.1)$ MHz, respectively, in reasonable agreement with the expected values of $\Omega_{\mathrm{C}}^{(\mathrm{theory})} = 2\pi \times (3.5 \pm 0.2)$ MHz and $\Omega_{\mathrm{C}}^{(\mathrm{theory})} = 2\pi \times (1.5 \pm 0.1)$ MHz, calculated based on eq. (8.32).

In fig. 8.16 are depicted the widths of the central EIT window for the two sets of data, where the red squares correspond to the curves shown in fig. 8.15 a. and the blue circles to the ones in fig. 8.15 b. The widths are numerically calculated based on the collective coherent coupling rates and the control field Rabi frequency deduced from the fits, and the previously measured values of κ, γ and γ_{C}, as already discussed above.

The collective coherent coupling rates deduced from the fits $g_{\mathrm{N}}^{(\mathrm{fit})}$ are depicted in the inset of 8.16 versus the theoretical values $g_{\mathrm{N}}^{(\mathrm{theory})}$ calculated from the effective number of interacting ions, N, and the single ion coupling rate $g = 2\pi \times 0.53$ MHz. The dashed line indicates $g_{\mathrm{N}}^{(\mathrm{fit})} = g_{\mathrm{N}}^{(\mathrm{theory})}$ and we find good agreement of the measured values with the expectations.

Fig. 8.17 shows the corresponding transparencies for the two sets of data (blue circles: $P_{\mathrm{C,in}} = 576$ nW, red squares $P_{\mathrm{C,in}} = 103$ nW), along with the theoretical curves calculated according to eq. (8.30).

8.4.4. Discussion of the ground state coherence time

In sec. 8.4.2 we argued that the ground state decoherence rate for the experiments presented here is of the order of $\gamma_{12} \sim 2\pi \times 1$ kHz. This value was found to agree with the one found in sec. 8.4.1 and, furthermore, provides good agreement for the control field Rabi frequencies deduced from fits to EIT spectra and the theoretical expectations and is self-consistent when analyzing the half-widths of the EIT windows. A value of around $2\pi \times 1$ kHz is hence reasonable, although the complexity of the theoretical model circumvents a more precise determination of the value from the experimental data. In the future, a more precise determination of this parameter could be done through a study of very slow EIT processes, which are more sensitive to the ground state decoherence rate.

Ultimately, we expect the achievable coherence time to be of the order of what was measured in 5.7 via the decay of the collective coherences between Zeeman substates. There, we found a coherence time of $\tau_e = 1.7^{100}_{-0.8}$ ms, corresponding to a decay rate of $\gamma_e \sim 2\pi \times 0.1$ kHz. The value used in this chapter is larger by a factor of 10 and several factors might be limiting the ground state coherence at the present state of the experiment, e.g. a slight angle between probe and control field mode, non-zero transverse B-fields, electronic drifts, a higher temperature of the sample as compared to the previous measurements or an inhomogeneous light-shift that might be induced by the reference laser field in the cavity, which for the experiments presented in this chapter was injected with a substantially higher power than in the measurements of the coherence time presented in sec. 5.7. We will in the following section try to estimate the influence of the latter.

Light shift induced by the 894 nm reference laser

In all experiments presented in this chapter, the 894 nm laser is used to lock the cavity on atomic resonance, as described in sec. 4.8.3. In all experiments, the 894 nm laser is resonant with the cavity and injected into the TEM_{00} mode, and, hence, almost perfectly overlapped with the control and the probe field. As was already mentioned one possible limitation for the ground state decoherence rate might be dephasing of the various contributions throughout the transverse profile of the cavity mode induced by the inhomogeneous AC-Stark shift of the reference laser.

To clarify this influence, we will in this section present experiments where we measured cavity reflectivity spectra for various input powers of the 894 nm reference laser, using exaggeratedly high powers to amplify the effect. In fig. 8.18 are depicted spectra around two-photon resonance for various powers of the reference. The curves correspond to powers of the reference laser of 0.025 μW (squares), 0.55 μW (circles), 1.4 μW (stars), 7.9 μW (diamonds), 24.0 μW (crosses) and 40.3 μW (asterisks), where the powers are measured at the position of the locking detector. For increasing powers, one observes both a shift of the two-photon resonance and a broadening of the central EIT window. The shift is caused by a mean AC-stark shift of the two-photon resonance, while the broadening directly reflects the different light-shifts of the contributions throughout the transverse profile of the cavity mode.

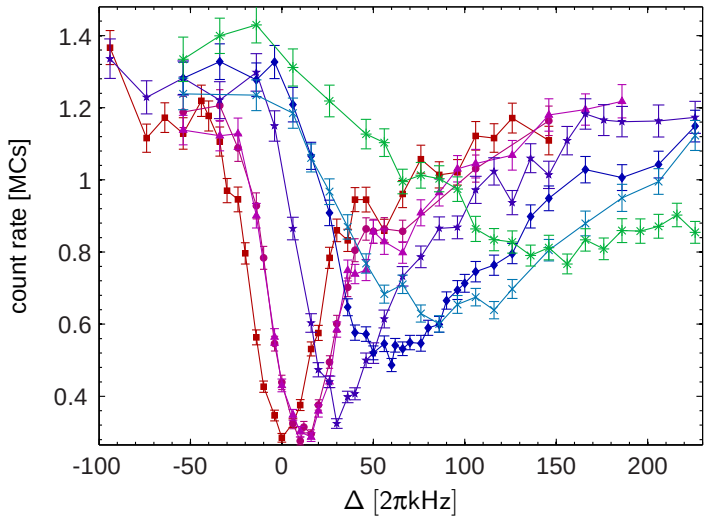

Figure 8.18.: EIT window for various powers of the 894 nm reference laser. To investigate the effect on the EIT resonance, artificially high powers of the reference laser were used. The power of the individual curves, measured at the position of the locking detector were 0.025 μW (squares), 0.55 μW (circles), 1.4 μW (stars), 7.9 μW (diamonds), 24.0 μW (crosses) and 40.3 μW (asterisks).

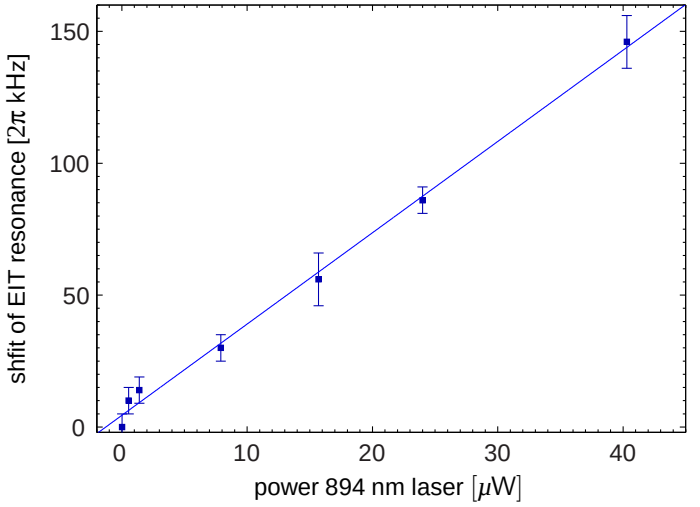

Figure 8.19.: Shift of the EIT resonance for different powers of the 894 nm reference laser. The solid line is a linear fit and yields a scaling constant of $b = 2\pi \times (3.5 \pm 0.1)\ {}^{\mathrm{kHz}}/_{\mu\mathrm{W}}$.

Fig. 8.19 shows the shift of the EIT resonance as deduced from the spectra in fig. 8.18 versus the measured power. The solid line is a linear fit to the data points and yields a scaling parameter of $b = 2\pi \times (3.5 \pm 0.1)\,{}^{\mathrm{kHz}}/_{\mu\mathrm{W}}$. As the reference laser is coupled to the cavity, this value has to be understood as a mean light shift when averaging the contributions of the individual ions over the transverse profile.

In our experiment, the locking of the cavity currently requires at least ~ 30 nW at the detector, which, with an estimated detection efficiency of $\sim 60\%$ corresponds to ~ 50 nW of reference power injected into the cavity. According to the scaling parameter, this would amount to a shift of the EIT resonance of $\sim 2\pi \times 0.1$ kHz.

This is already at the level of the decoherence rate of collective Zeeman substates measured in sec. 5.7 and the effect of the dephasing induced by the light shift might be already one of the limiting factors at the present state of the experiment.

This could also explain why the ground state decoherence rate found in this chapter differs from the measurement of the coherence time of collective Zeeman-substates presented in sec. 5.7. There, the measurement was performed by scanning the cavity over the atomic resonance (see sec. 4.8.3) while measuring the cavity reflectivity signal for a resonant probe laser. In this configuration, the 894 nm laser is used to monitor drifts of the cavity resonance which can be accomplished at powers well below 1 nW. The much lower power level could hence explains the difference of the measured ground state coherence rate in this chapter as compared to the measurement of sec. 5.7.

Though technical challenging, it should be possible to reduce this effect by an optimized locking scheme. A first step could be to use a more sensitive locking detector which would facilitate locking of the cavity resonance for even lower power levels of the reference laser. Furthermore, one could consider to inject the reference laser to a high order transverse cavity mode to minimize the spatial overlap of the reference with the probe and control fields. Finally, using a reference laser with an even larger detuning would reduce the light shift, but would require a sufficiently high reflectivity of the cavity mirrors at its wavelength to assure a finesse comparable to the finesse at the wavelength of the probe transition.

8.5. Conclusion

In this chapter we investigated both theoretically and experimentally the realization of cavity electromagnetically induced transparency with ion Coulomb crystals. In the first part, we extended the two-level model derived in sec. 3.2 to the EIT situation, where an ensemble of Λ-type three-level atoms interacts simultaneously with a strong control field and a weak probe field at the single photon level. We found analytic expressions for the atomic susceptibility for both the situation of a uniform control field Rabi frequency and the more complex case of a control field coupled to the cavity, which allowed us to calculate the expected cavity reflectivity spectra. For the case of a uniform control field, we could, furthermore, derive time dependent expressions for the mean values of the system observables in an adiabatic approximation.

The second part of the chapter was then dedicated to the experimental observation of cavity electromagnetically induced transparency. We could demonstrate how the vacuum Rabi spectra obtained with only the probe laser present is modified by the additional con-

trol laser and exhibits a very narrow transparency window when the frequency of the probe field approaches the EIT two-photon resonance. The experimental data is well reproduced by fits to the theoretical models and we find good agreement with the expectations.

We performed a systematic study of the EIT steady state spectra and dynamics by varying the control field intensity or the number of ions effectively interacting with the cavity field mode and found excellent agreement with the theoretical model.

By studying the time evolution of the resonant transparency, we could demonstrate how the build up time constant increases with higher input powers. Based on numerical simulations, we estimated the expected dependence of the EIT time constant for an intracavity control field and could based on these simulations relate our experimental data to the observed widths of the EIT windows.

In a subsequent series of measurements, we analyzed the influence of the effective number of ions on the EIT window for two different control field powers. The observed cavity reflectivity spectra are well resembled by theoretical fits and we find good agreement between the fitted control field Rabi frequencies and the expectations. We observed for both control field powers a decrease of the EIT width for an increasing number of ions and a decrease of the atomic transparency, in good agreement with the theoretical expectations.

Finally, to assess the influence of the AC-stark shift induced by the reference laser on the coherence time, we investigated the shift of the EIT resonance for increasing powers of the reference laser. For the values typically used to lock the cavity on atomic resonance the expected shift is of the order of $2\pi \times 0.1$ kHz and could already be significant for the achievable coherence time. Though the complexity of the theoretical model complicates the precise determination of the ground state decoherence rate at the present state of the experiment we could, based on several observations, estimate it to be of the order of $\sim 2\pi \times 1$ kHz.

The observation of cavity EIT is an important step on the way towards the realization of a quantum memory based on ion Coulomb crystals in an optical cavity and the first realization of the cavity STIRAP (Stimulated Raman Adiabatic Passage) scheme of ref. [55]. The storage and retrieval of single light pulses requires the dynamical control of the control field Rabi frequency [137], and detailed dynamical studies are necessary to find the optimal control parameters for our all-cavity scheme, where the transverse effects of the control field have to be taken into account. The excellent control over the transparency and the experimental interaction parameters should allow for the realization of high-efficiency and long-lived quantum memories [55, 56, 151].

Furthermore, the observed EIT windows are nearly two orders of magnitude narrower than in previous investigations with neutral atoms in cavities [92–95], which is important e.g. for the implementation of EIT based nonlinear effects [98] or to engineer interactions between single photons [99, 100]. Based on these results, we will in the following section implement an EIT-based all-cavity optical switching scheme.

9. All optical switching

In this chapter, we will present a first application of cavity EIT, namely the implementation of a low-light level all-optical switching scheme. We will demonstrate how the transmission of a probe field at the single photon level through the cavity containing the EIT medium can be controlled by an additional weak switching field. The results will be compared to an extension of the theoretical EIT model of the previous chapter to the new situation of four-level atoms.

The chapter is structured as follows: Sec. 9.1 will start with a introduction. In sec. 9.2, the three-level theory of the previous chapter will be extended to the case of four-level atoms interacting with three laser fields. Then, in sec. 9.3 we will present results on optical switching experiments in two different schemes and finally, in sec. 9.4, we will conclude and give a brief outlook.

9.1. Introduction

The control of light by itself, ultimately at the quantum level, is a long-standing challenge for quantum optics. In free space or in usual materials, the interaction cross section between single photons is typically extremely small, requiring the use of intense laser fields tightly focused on nonlinear materials. EIT offers an interesting possibility for dramatically enhancing the nonlinearity of an atomic medium [84, 90, 91, 98, 99, 195–198].

In such a medium the destructive interference of the absorption, which makes the medium transparent, is usually attended by a constructive interference of the dispersion in the media and a weak probe pulse propagating through such an EIT medium may experience huge nonlinearities, making EIT based systems well suited for the realization of nonlinear optics at the few and even single photon level. Adding to the traditional EIT Λ-system (see fig. 8.1 a.) a fourth level, different schemes have been proposed e.g. for the realization of giant Kerr-nonlinearities [98], optical switching by absorptive two-photon processes [195] or, for an EIT medium enclosed in an optical cavity, the *"photon blockade"* [99, 100, 199–201], where the transmission of a single photon is coherently controlled by a second photon. Such effects could be used to realize quantum optics devices for single photons, such as single photon transistors [202, 203] and single photon gates [204], for the generation of highly non-classical states [205] and for the observation of novel phase transitions for light [206, 207]. Photon blockade mechanisms based on the strong coupling of a single two-level system to a cavity field mode were proposed [208] and have been experimentally realized [202, 209–212]. In these experiments the statistics of the photons transmitted through the cavity is conditioned by a nonlinearity of the excitation spectrum of the coupled single atom-cavity system. However, the photon blockade scheme of ref. [99], which relies on a direct, EIT mediated nonlinear (Kerr) interaction of two photons, still remains to be demonstrated.

Nonlinear effects in such a four level system have been observed [213] and optical

switching of free propagating fields at the few photon level has been demonstrated using cold atomic gases [196–198].

In this chapter we will present a realization of an all-cavity optical switching scheme based on EIT where all laser beams are in the cavity. The narrow cavity EIT resonances observed in our system (see chap. 8) will be used to mediate the nonlinear interaction between the switching field and the probe photon and we will demonstrate how the transmission of a probe beam at the single photon level (at a wavelength of 866 nm) can be controlled by an additional (weak) switching laser (at 850 nm). In addition, we will also demonstrate a more traditional optical switching scheme, were a switching field (at 866 nm) is applied in free space. Furthermore, we will based on a semi-classical analysis derive the theoretical expressions for the atomic susceptibilities in both cases.

9.2. Four-level atoms in a cavity

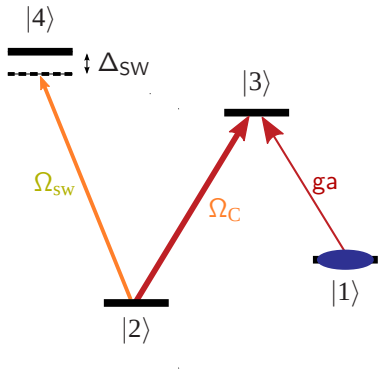

Figure 9.1.: Level scheme for all-optical switching experiments. The scheme is an extension of the standard EIT Λ-scheme depicted in fig. 8.1 a., where an additional switching field, characterized by its Rabi frequency Ω_{sw}, couples the state $|2\rangle$ to an auxiliary level, denoted by $|4\rangle$.

In this section we will discuss an extension of the three-level EIT model presented in the last chapter to the four-level situation depicted in fig. 9.1. The level scheme is based on the standard three-level EIT scheme, where the levels $|1\rangle$, $|2\rangle$, $|3\rangle$ form a Λ-system (see fig. 8.1) and where an additional so-called switching laser, characterized by its Rabi frequency Ω_{sw}, couples state $|2\rangle$ to an auxiliary excited level $|4\rangle$ with a (large) detuning Δ_{sw}.

In a qualitative picture, one expects the presence of an additional switching laser to change the energy of state $|2\rangle$ through the AC-Stark shift and, hence, to modify the two-photon resonance condition between the control and the probe field. The probe detuning at which the quantum interference occurs will accordingly be shifted to a non-zero detuning $\Delta \neq 0$. At the same time, the atomic transparency on resonance will decrease, as the AC-Stark shift increases. For appropriate values of the Rabi-frequency of the switching laser it should therefore be possible to deterministically switch the cavity in and out of resonance for the probe field.

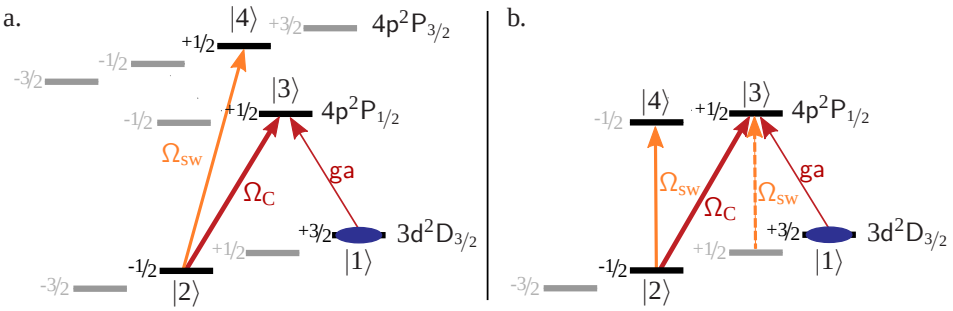

Figure 9.2.: All-cavity optical switching schemes for $^{40}Ca^{+}$. **a.** Intracavity optical switching scheme. The switching laser is coupled to the fundamental TEM_{00} mode and σ^{+}-polarized. Its frequency is close to resonance of the $3d^2D_{3/2} \leftrightarrow 4p^2P_{5/2}$ transition (detuning $\Delta_{sw} \sim 2\pi \times 4.3$ GHz). **b.** Free space configuration. The switching laser is π-polarized and close to resonance of the $3d^2D_{3/2} \leftrightarrow 4p^2P_{3/2}$ transition. For details see text.

In the following we will derive a semi-classical model of this scenario, which will be based on the analysis in sec. 3.2 and sec. 8.2. We will derive the dynamical equations of the mean values of the relevant atomic observables and the intracavity probe field, along with their steady state solutions. As in the previous chapters, we will focus on the situation of large $^{40}Ca^{+}$ ion Coulomb crystals in an optical cavity. We will investigate two distinct scenarios: First, where the switching beam is coupled to the cavity and has a well-defined spatial mode, and second, where the Rabi frequency of the switching field is uniform throughout the ensemble. Though our focus in this chapter is on the first case, implementations of both schemes are possible and will be demonstrated.

In the first case, the optical switching is accomplished by a σ^{+}-polarized field addressing the $|2\rangle = \left|3d^2D_{3/2},\ m_J = {}^{-1}/_{2}\right\rangle \leftrightarrow |4\rangle = \left|4p^2P_{3/2},\ m_J = {}^{+1}/_{2}\right\rangle$ transition in $^{40}Ca^{+}$. The switching field is in this case applied along the quantization axis and injected into the cavity. The appropriate $^{40}Ca^{+}$ level scheme with the relevant levels is depicted in fig. 9.1 a. It is a implementation of the four-level scheme proposed in ref. [99], albeit with different wavelengths for the probe and the switching fields.

In the second case, optical switching with a (close to) uniform Rabi frequency is realized by a free propagating switching beam applied along the transverse x-direction. The appropriate level scheme for $^{40}Ca^{+}$ is depicted in fig. 9.1 b. In this configuration, the polarization of the light with respect to the quantization axis is π and couples the state $|2\rangle = \left|3d^2D_{3/2},\ m_J = {}^{-1}/_{2}\right\rangle$ to the state $|4\rangle = \left|4p^2P_{3/2},\ m_J = {}^{-1}/_{2}\right\rangle$. In practise, this laser will also couple the two states $3d^2D_{3/2},\ m_J = {}^{+1}/_{2}$ and $4p^2P_{3/2},\ m_J = {}^{+1}/_{2}$. Accordingly, the excited state will also be light-shifted (and potentially power-broadened) and the scheme is not a pure four-level system. For simplicity, we will for the theoretical treatment neglect the effect on the $4p^2P_{3/2},\ m_J = {}^{+1}/_{2}$ level, and discuss them, when presenting the experimental results.

9.2.1. Free-space optical switching

The case of a free-propagating switching field with a uniform Rabi frequency is conceptionally easier and we will first derive the atomic susceptibility for this case. For simplicity, we will restrict ourselves to the situation where both the probe and the control beams are coupled to the fundamental TEM_{00} mode of the cavity, with transverse mode function $\psi_{00}(r_j) = \exp(\frac{-r_j^2}{w_0})$.

Based on the discussion in sec. 8.2.3 and in appendix D, we will furthermore assume a random distribution of the ions and a sufficiently high thermal kinetic energy of the ensemble such that one can average over the longitudinal structure of the cavity field. The Rabi-frequency of the control field, Ω_C, and the single ion coupling rate g will accordingly by scaled by a factor $1/\sqrt{2}$. To facilitate the comparison with the second configuration, where the switching field is also in the cavity, the Rabi-frequency of the switching field will also be divided by a factor of $\sqrt{2}$. Using these approximations and assumptions, the interaction Hamiltonian reads

$$\begin{aligned} H_{\mathrm{int}} = & - \hbar\frac{g}{\sqrt{2}}\sum_{j=1}^{N_{\mathrm{tot}}}\exp(\frac{-2r_j^2}{w_0^2})\left(\hat{a}\hat{\sigma}_{31,j}+\hat{a}^\dagger\hat{\sigma}_{13,j}\right) - \hbar\frac{\Omega_C}{\sqrt{2}}\sum_{j=1}^{N_{\mathrm{tot}}}\exp(\frac{-2r_j^2}{w_0^2})\left(\hat{\sigma}_{32,j}+\hat{\sigma}_{23,j}\right) \\ & - \hbar\frac{\Omega_{\mathrm{sw}}}{\sqrt{2}}\sum_{j=1}^{N_{\mathrm{tot}}}\left(\hat{\sigma}_{42,j}+\hat{\sigma}_{24,j}\right). \end{aligned} \tag{9.1}$$

As in the previous chapters, we use the Heisenberg-Langevin approach to find the dynamical equations of the mean values of the system observables. For a sufficiently large detuning of the blockade field ($|\Delta_{\mathrm{sw}}| \gg \gamma_4, \delta, \Omega_{\mathrm{sw}}$) and in the weak probe regime ($g|\hat{a}| \ll \Omega_C$) we can perform a perturbative calculation of the probe. Assuming most of the atoms in level $|1\rangle$ ($\sigma_{11} = 1,\ \sigma_{22} = \sigma_{33} = \sigma_{44} = 0$), the dynamical equations read

$$\dot{a} = -(\kappa + i\Delta_c)a + i\frac{g}{\sqrt{2}}\sum_{j=1}^{N_{\mathrm{tot}}}\exp(\frac{-2r_j^2}{w_0^2})\sigma_{31,j} + \sqrt{2\kappa_1}a_{\mathrm{in}}. \tag{9.2a}$$

$$\dot{\sigma}_{13,j\pm} = -(\gamma + i\Delta)\sigma_{13,j\pm} + i\frac{g}{\sqrt{2}}a\exp(\frac{-2r_j^2}{w_0^2}) + i\frac{\Omega_C}{\sqrt{2}}\exp(\frac{-2r_j^2}{w_0^2})\sigma_{12,j} \tag{9.2b}$$

$$\dot{\sigma}_{12,j} = -(\gamma_{12} + i\delta)\sigma_{12,j} + i\frac{\Omega_C}{\sqrt{2}}\exp(\frac{-2r_j^2}{w_0^2})\sigma_{13,j} + i\frac{\Omega_{\mathrm{sw}}}{\sqrt{2}}\sigma_{41,j}. \tag{9.2c}$$

$$\dot{\sigma}_{14,j} = -(\gamma_4 + i\Delta_{\mathrm{sw}} + i\delta)\sigma_{14,j} + i\frac{\Omega_{\mathrm{sw}}}{\sqrt{2}}\sigma_{12,j}, \tag{9.2d}$$

where Δ_{sw} is the detuning of the switching laser from the atomic resonance frequency and γ_4 is the dipole decay rate of state $|4\rangle$. Solving these equations in steady state, we retrieve for the mean value of the intracavity field operator an equation of the same form as in the three-level case (see eq. (8.23))

$$a = \frac{\sqrt{2\kappa_1}a_{\mathrm{in}}}{\kappa + i\Delta_C - i\chi_{4level}}, \tag{9.3}$$

where the four-level susceptibility is now given by

$$\chi_{4level} = \frac{ig^2}{2}\sum_{j=1}^{N_{\rm tot}} \exp(-2r_j^2/w_0^2)\left[\gamma + i\Delta + \frac{\exp(-2r_j^2/w_0^2)\Omega_C^2/2}{\gamma_{12}+i\delta+\frac{\Omega_{sw}^2/2}{\gamma_4+i\Delta_{sw}+i\delta}}\right]^{-1}. \tag{9.4}$$

We can as in the previous chapters apply the continuous medium description (see eq. (3.43)) and replace the summation over all ions by the integral over the crystal volume V:

$$\begin{aligned}\chi_{4level} &= \frac{ig^2\rho_0}{2}\int_V d\boldsymbol{r}\, \exp(-2r_j^2/w_0^2)\left[\gamma + i\Delta + \frac{\exp(-2r_j^2/w_0^2)\Omega_C^2/2}{\gamma_{12}+i\delta+\frac{\Omega_{sw}^2/2}{\gamma_4+i\Delta_{sw}+i\delta}}\right]^{-1} \\ &= \frac{ig^2N}{\gamma+i\Delta}\frac{\ln(1+\frac{s}{1+s'})}{\frac{s}{1+s'}}.\end{aligned} \tag{9.5}$$

Here, we assumed the crystal radius to be much larger than the cavity waist $R \gg w_0$ and, as in eq. (8.25), inserted the effective number of ions $N = \rho_0\frac{\pi w_0^2}{2}L$ and the effective saturation parameter of the two-photon transition s defined in eq. (8.17). In addition, we introduced the parameter

$$s' = \frac{\Omega_{sw}^2/2}{(\gamma_4+i\Delta_{sw}+i\delta)(\gamma_{12}+i\delta)}. \tag{9.6}$$

It is instructive to expand eq. (9.5) to first order in s'

$$\begin{aligned}\chi_{4level} &\simeq \frac{ig^2N}{\gamma+i\Delta}\frac{1}{1+s}\left(1+\frac{ss'}{1+s}\right) \\ &= \chi_\Lambda^{(1)} + \chi_{\rm cross}^{(3)}\frac{\Omega_{sw}^2}{2},\end{aligned} \tag{9.7}$$

where in the last step we used the (linear) three-level susceptibility of eq. (8.16) and introduced the crossed third-order nonlinear susceptibility between the probe and switching fields [98, 204]

$$\chi_{\rm cross}^{(3)} = ig^2N\frac{\Omega_C^2/2}{\left(\gamma+i\Delta+\frac{\Omega_C^2/2}{\gamma_{12}+i\delta}\right)^2}\frac{1}{\gamma_4+i\Delta_{sw}+i\delta} \tag{9.8}$$

For a vanishing Rabi-frequency of the switching field, the susceptibility found in eq. (9.5) reduces to the linear expression of the three-level situation in eq. (8.25). If the detuning of the switching field is sufficiently large ($|\Delta_{sw}| \gg \gamma_4, \delta, \Omega_{sw}$), the susceptibility becomes

$$\chi_{4level} \approx \frac{ig^2N}{\gamma+i\Delta+\frac{\Omega_C^2}{\gamma_{12}+i\delta-i\Omega_{sw}^2/2\Delta_{sw}}} \tag{9.9}$$

and the additional term in the susceptibility solely causes a shift of the effective two-photon detuning. If probe and control field are on bare two-photon resonance (without the switching field present) this switching field can be used to tune the system in and out of two photon resonance.

9.2.2. All-cavity optical switching

The second configuration, with the switching field being injected into the cavity, is slightly more complex and the transverse intensity distribution of the switching beam leads to a position dependence of the Rabi frequency of the switching field. For simplicity, we will restrict the theoretical description to the case were all three laser fields are coupled to the fundamental TEM_{00} mode of the cavity, with transverse mode function $\psi_{00}(r_j) = \exp(\frac{-r_j^2}{w_0})$. All longitudinal effects are, as before, assumed to average out and yield a scaling factor of $\sqrt{2}$ for the Rabi frequencies and g. The interaction Hamiltonian now reads

$$\begin{aligned} H_{\mathrm{int}} = & - \hbar\frac{g}{\sqrt{2}}\sum_{j=1}^{N_{\mathrm{tot}}}\exp(\frac{-2r_j^2}{w_0^2})\left(\hat{a}\hat{\sigma}_{31,j}+\hat{a}^{\dagger}\hat{\sigma}_{13,j}\right) - \hbar\frac{\Omega_{\mathrm{C}}}{\sqrt{2}}\sum_{j=1}^{N_{\mathrm{tot}}}\exp(\frac{-2r_j^2}{w_0^2})\left(\hat{\sigma}_{32,j}+\hat{\sigma}_{23,j}\right) \\ & - \hbar\frac{\Omega_{\mathrm{sw}}}{\sqrt{2}}\sum_{j=1}^{N_{\mathrm{tot}}}\exp(\frac{-2r_j^2}{w_0^2})\left(\hat{\sigma}_{42,j}+\hat{\sigma}_{24,j}\right), \end{aligned} \tag{9.10}$$

Following the same approach as previously, we can calculate the evolution equation for the mean values of the system observables. Except for $\sigma_{13,j}$ and $\sigma_{14,j}$ these are identical to those found in (9.2). In the new all-cavity configuration the dynamical equations for these two observables are given by

$$\begin{aligned} \dot{\sigma}_{12,j} &= -(\gamma_{12}+i\delta)\sigma_{12,j} + i\frac{\Omega_{\mathrm{C}}}{\sqrt{2}}\exp(-2r_j^2/w_0^2)\sigma_{13,j} \\ &\quad + i\frac{\Omega_{\mathrm{sw}}}{\sqrt{2}}\exp(-2r_j^2/w_0^2)\sigma_{41,j} \end{aligned} \tag{9.11a}$$

$$\dot{\sigma}_{14,j} = -(\gamma_4 + i\Delta_{\mathrm{sw}} + i\delta)\sigma_{14,j} + i\frac{\Omega_{\mathrm{sw}}}{\sqrt{2}}\exp(-2r_j^2/w_0^2)\sigma_{12,j}. \tag{9.11b}$$

Solving the full set of equations in steady state, we find the same equation for the mean value of the intracavity probe field as in eq. (9.3), where the four-level susceptibility is now given by

$$\chi_{4level,00} = \frac{ig^2}{2}\sum_{j=1}^{N_{\mathrm{tot}}}\exp(-2r_j^2/w_0^2)\left[\gamma + i\Delta + \frac{\exp(-2r_j^2/w_0^2)\Omega_{\mathrm{C}}^2/2}{\gamma_{12}+i\delta+\frac{\exp(-2r_j^2/w_0^2)\Omega_{\mathrm{sw}}^2/2}{\gamma_4+i\Delta_{\mathrm{sw}}+i\delta}}\right]^{-1}. \tag{9.12}$$

In the continuous medium description (see eq. (3.43)), and assuming (as before) $R \gg w_o$ we can replace the sums by integrals over the crystal volume and perform the integration. We find

$$\chi_{4level,00} = \frac{ig^2N}{2}\left[\frac{s\ln(1+s+s')}{(s+s')^2} + \frac{s'}{s+s'}\right], \tag{9.13}$$

where we used the same parameters as in eq. (9.5).

It is worth noticing that unlike in the case of the three-level susceptibilities in eqs. (8.16) and (8.25), the four level susceptibilities in eqs. (9.13) and (9.5) will for a non-zero value of the Rabi frequencies of the switching field in general not be purely imaginary and accordingly give rise to dispersion, even on atomic resonance.

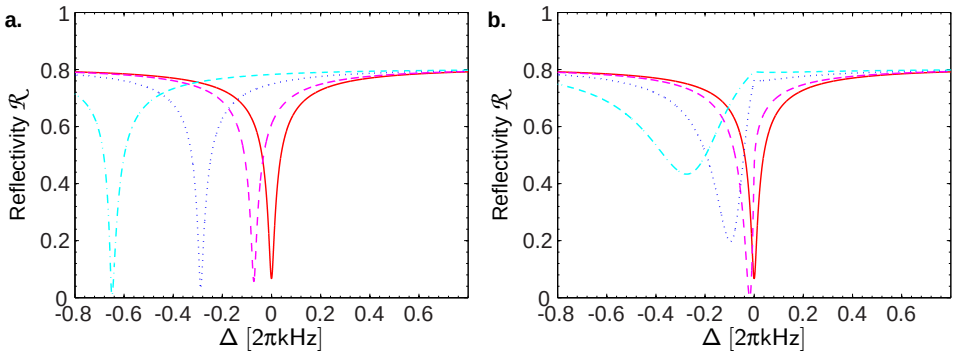

Figure 9.3.: Simulated reflectivity spectra for various Rabi frequencies of the switching field: $\Omega_{sw} = 0$ MHz (solid line), $\Omega_{sw} = 2\pi \times 25$ MHz (dashed line), $\Omega_{sw} = 2\pi \times 50$ MHz (dotted line) and $\Omega_{sw} = 2\pi \times 75$ MHz (dashed-dotted line) for **a.** a uniform switching field and **b.** for the case, when the switching field is coupled to the TEM_{00} mode of the cavity. The parameters used for the simulation were identical and are: $\Delta_{sw} = 2\pi \times 4.3$ GHz, $g_N = 2\pi \times 17$ MHz, $\Omega_C = 2\pi \times 4.35$ MHz, $\gamma_4 = 2\pi \times 11.6$ MHz, $\gamma_{12} = 2\pi \times 1$ kHz, $\gamma = 2\pi \times 11.7$ MHz, $\kappa = 2\pi \times 2.2$ MHz and $\kappa_1 = 2\pi \times 1.53$ MHz.

9.2.3. Reflectivity spectrum

Knowing the four-level susceptibilities for the two possible configurations of the switching laser, we can now also calculate the expected cavity reflectivity spectrum by substituting these susceptibilities into (8.27). In fig. 9.2 are depicted simulated reflectivity spectra for various values of the switching field Rabi frequency Ω_{sw}, where in fig. 9.3 a. we use the susceptibility found for an homogeneous switching field (see eq. (9.5)) and in fig. 9.3 b. we use the susceptibility for an intracavity switching field (see eq. (9.13)). In the first case, the switching field induces mainly a shift of the two-photon resonance, while leaving the shape of the dip nearly unaffected. For the intracavity switching field the two-photon resonance is also shifted, however less than compared to the previous case (for comparable Rabi-frequencies) and the shape of the EIT window is distorted and becomes asymmetric with a sharper rise towards low detunings of the probe.

In fig. 9.4 are depicted the shift of the EIT resonance as a function of the square of the switching field Rabi frequency for a uniform Rabi frequency (red squares) and for an intracavity switching field (blue circles). The solid lines are linear fits and yield slopes of $(116 \pm 1) \cdot 10^{-6}/2\pi\text{MHz}$ and $(52 \pm 1) \cdot 10^{-6}/2\pi\text{MHz}$, respectively. The scaling for an intracavity field is lower by approximately a factor of 2 and while in the uniform case, the dependence is fully resembled by the linear dependence, the shift deduced for the intracavity switching field deviates from a strict linear dependence. However, for low Rabi frequencies below 100 MHz, the scaling is still rather linear and facilitates a comparison of the experimental findings to the model.

In eqs. (8.29) we calculated the cavity transmittivity and reflectivity on atomic resonance for the EIT situation, where we assumed the susceptibility to be purely imaginary. As abovementioned, this is in general not the case for the four-level susceptibilities in eqs.

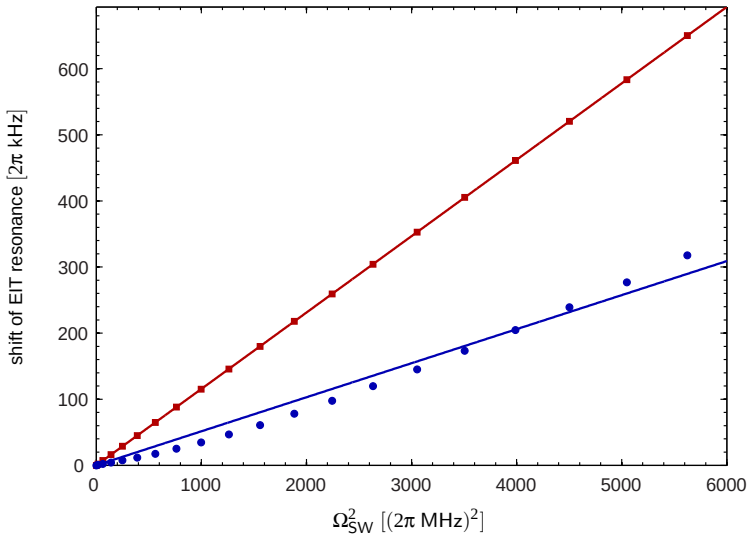

Figure 9.4.: Shift of the EIT resonance as a function of the square of the switching field Rabi frequency for a uniform Rabi frequency (red squares) and for a intracavity switching field (blue circles). Linear fits to the data yield slopes of $(116 \pm 1) \cdot 10^{-6}/2\pi\text{MHz}$ and $(52 \pm 1) \cdot 10^{-6}/2\pi\text{MHz}$, respectively.

(9.5) (9.13). On resonance, the cavity transmittivity and reflectivity now read

$$\mathcal{R} = \frac{(\kappa_1 - \kappa_2 - \kappa_{\mathcal{A}} - \text{Im}(\chi_{4\text{level}}))^2 + \text{Re}(\chi_{4\text{level}})^2}{(\kappa^2 + \text{Im}(\chi_{4\text{level}}))^2 + \text{Re}(\chi_{4\text{level}})^2} \tag{9.14a}$$

$$\mathcal{T} = \frac{4\kappa_1\kappa_2}{(\kappa^2 + \text{Im}(\chi_{4\text{level}}))^2 + \text{Re}(\chi_{4\text{level}})^2}. \tag{9.14b}$$

The resonant atomic transparency, defined by the ratio of the transmission of the cavity containing the medium $\mathcal{T}$ to that of the empty cavity $\mathcal{T}_0$, (for the three-level case see eq. (8.30)) is accordingly given by

$$T_{\text{atom}} = \frac{\mathcal{T}}{\mathcal{T}_0} = \frac{\kappa^2}{(\kappa + \text{Im}(\chi_{4\text{level}}))^2 + (\text{Re}(\chi_{4\text{level}}))^2}. \tag{9.15}$$

9.3. Experimental realization

In this section, we will present the implementation of an all-cavity optical switching scheme, where all laser fields interacting with the atoms are coupled to the fundamental TEM_{00} mode. In the second part, these results will be supplemented by a investigation of a more traditional optical switching scheme with a free-space optical switching field.

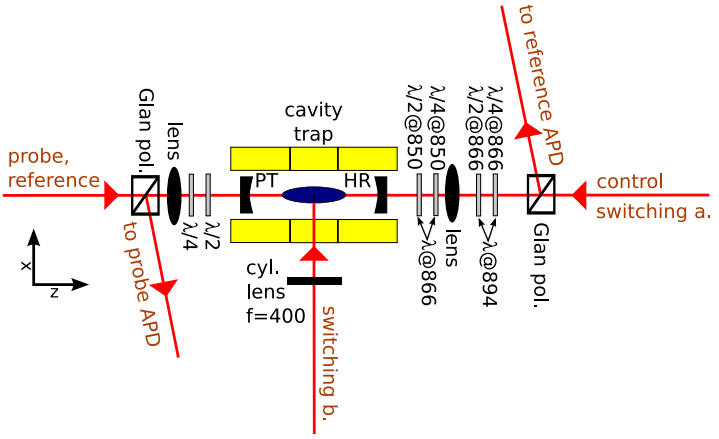

Figure 9.5.: Schematic setup for all-optical switching experiments. In the first configuration of the switching beam (labeled by switching a.) a σ^+ polarized beam at 850 nm is mode matched to the cavity from the HR side. When the cavity is locked on atomic resonance, the cavity resonance condition for the switching laser implies a detuning from the $3d^2D_{3/2} \leftrightarrow 4p^2P_{3/2}$ transition of $\Delta_{sw} = 2\pi \times 4.3$ GHz. To allow for the independent control of the polarization of control and switching beam, a set of waveplates designed as $\lambda/2$ and $\lambda/4$ waveplates at 850 nm and as λ at 866 nm are inserted after the Glan polarizer. In the second configuration (labeled by switching b.) the optical switching is accomplished by a π-polarized beam at 866 nm injected along the transverse *x*-direction. It is tuned close to the resonance frequency of the $3d^2D_{3/2} \leftrightarrow 4p^2P_{1/2}$ transition.

9.3.1. All-cavity optical switching

Experimental setup

The experimental setup used in the optical switching experiments is almost identical to the one in the previous chapter, the only difference being the additional switching laser. A schematic of the cavity trap setup and the various laser beams, including the switching beam is depicted in fig. 9.5. The sequence used in these experiments is identical to the previous chapter (see fig. 8.5), where the switching laser is applied at the same time as the control field.

The level scheme for the intracavity optical switching is shown in fig. 9.2 a. A home-built grating stabilized external cavity diode laser with a wavelength close to resonance of the $3d^2D_{3/2} \leftrightarrow 4p^2P_{1/2}$ transition at 850 nm provides the light for the optical switching field. The frequency of this laser is stabilized using a Pound-Drever-Hall locking scheme to an additional reference cavity similar to the one used for stabilizing the other diode lasers and is tunable by a double pass AOM configuration in the locking branch (similar to the setups described in sec. 4.3). As for the other lasers, we use a single pass AOM to be able to switch this beam on and off. The -1st diffraction order is coupled to a fiber and guided to the optical setup of the probe and control laser, where it is overlapped with the control beam on a PBC and sent to the HR side of the trap cavity.

Fig. 9.5 shows the beam path of this laser (labeled switching a.) to the trap cavity. The switching beam overlaps with the control field and passes the same setup as described in the previous chapter. However, as we need independent control over the polarization of the control and the switching beam, a set of waveplates is inserted before the vacuum chamber. The plates are designed as $\lambda/4$ and $\lambda/2$ waveplates at 850 nm and λ waveplates at 866 nm, and hence do not change the polarization of the control laser. The polarization of the switching laser is set to σ^+ to address the $3d^2D_{3/2}, m_J = -1/2 \leftrightarrow 4p^2P_{1/2}, m_J = +1/2$ transition.

In order to achieve the highest possible interaction strength, it is, in principle, desirable to tune the frequency of this laser close to the atomic transition frequency. However, as this laser is coupled to the cavity, the frequency of the laser also has to be resonant with the cavity. The length of the cavity is, however, set by the atomic resonance condition for the probe laser at 866 nm. It turned out that for the current cavity length, the closest TEM_{00} mode for the 850 nm laser is red detuned from atomic resonance by $\Delta_{sw} = 2\pi \times 4.3$ GHz.

The finesse of the cavity at 850 nm was measured to be $\mathcal{F}_{850} \sim 4000$ and is slightly higher than at the wavelength of the probe field. The cavity decay rate was measured to be $\kappa = 2\pi \times (1.85 \pm 0.23\,\mathrm{MHz})$.

Despite the large detuning and the σ^+ polarization of the switching beam, occasionally an off-resonant excitation of single ions to the $4p^2P_{3/2}$ state may occur, from where the ions can decay to the meta-stable $3d^2D_{5/2}$ state and are shelved. To make sure that this state is empty after each sequence, an additional repumping laser at 854 nm, close to resonance with the $3d^2D_{5/2} \leftrightarrow 4p^2P_{3/2}$ state is applied to the ions.

9.3.2. Experimental results

To demonstrate all-optical switching, we loaded a crystals with a half-length of $L = (785 \pm 14)$ μm, a radius of $R = (147 \pm 1)$ and a density of $\rho_0 = (5.6 \pm 0.1) \cdot 10^8$ cm^{-3}. With these numbers, the crystal contains $N = 930 \pm 30$ ions effectively interacting with the cavity

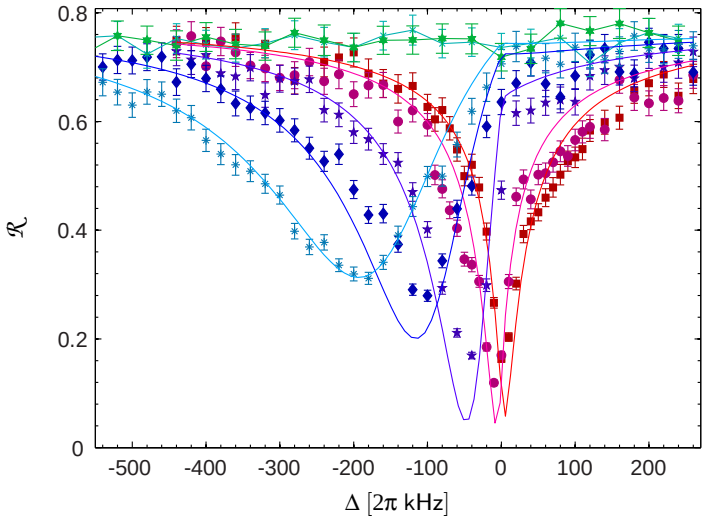

Figure 9.6.: Cavity reflectivity spectra for various input powers of the intracavity optical switching field at 850 nm. The individual curves correspond to 0 μW (red squares), 18.5 μW (lilac circles), 38.5 μW (light blue stars), 76.9 μW (blue diamonds) and 150 μW (turquoise asterisks). The solid lines are fits to the theoretical model of eq. (8.27) and using the susceptibility in eq. (9.13). To check for direct effects of the switching laser on the coherent coupling, we also obtained spectra when only the probe beam is injected (turquoise crosses) and when probe and switching beams are present (green pentagrams). The size and density of the crystal used in these experiments were $L = (785 \pm 14)$ μm, $R = (147 \pm 1)$ μm, $\rho_0 = (5.6 \pm 0.1) \cdot 10^8$ cm^{-3}, corresponding to an effective number of ions of $N = 930 \pm 30$.

mode, and the collective coupling rate is expected to be $g_N = 2\pi \times (16.2 \pm 0.3)$ MHz. The experiment is accomplished, by injecting a control laser field with an input power of $P_C = 1.1$ μW, a weak probe field at the single photon level and a switching field with variable powers into the cavity. The probe reflectivity is then measured by the probe APD at the end of the interaction period (see fig. 8.5).

Fig. 9.6 shows the probe reflection spectrum of the cavity for different input powers of the switching lasers. The input powers are: 0 μW (red squares), 18.5 μW (lilac circles), 38.5 μW (light blue stars), 76.9 μW (blue diamonds) and 150 μW (turquoise asterisks). The solid lines are fits to the theoretical model, where we reduced the parameter space by fixing the collective coupling rate to the expected value and the control field Rabi frequency to the value found from a fit to the unperturbed spectrum $\Omega_C^{(\mathrm{fit})} = 2\pi \times (4.2 \pm 0.1)$ MHz. Furthermore, the ground state decoherence rate is, as in the EIT experiments, set to $\gamma_C = 2\pi \times 1$ kHz. The control field Rabi frequency found from the fit is in good agreement with the value one expects for the input power of $P_C = 1.1$ μW of $\Omega_C^{(\mathrm{theory})} = 2\pi \times (4.4 \pm 0.2)$ MHz. For comparison we also obtained spectra when only the probe beam is injected (turquoise crosses) and when probe and switching beam are present (green pentragrams). The two curves overlap within their error bars and no direct effect of the optical switching field is observed on the coherent coupling.

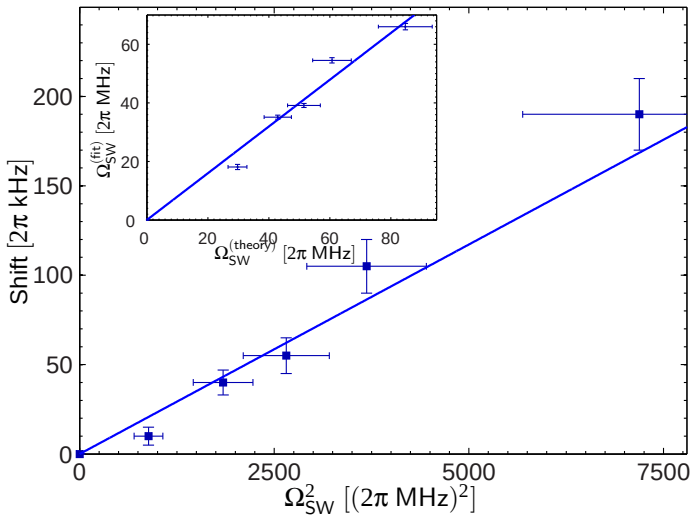

Figure 9.7.: Shift of the EIT resonance as a function of the square of the expected switching field Rabi frequency. The shift is deduced from the reflectivity spectra in fig. 9.6. The solid line is a linear fit and yields a slope of $(23 \pm 2) \cdot 10^{-6}/2\pi\text{MHz}$. **Inset:** Switching field Rabi frequency deduced from the fits as a function of the expect value, calculated from the known input power, the transition strength and the cavity parameters. The solid line is a linear fit and yields a slope of $a = (0.80 \pm 0.04)$.

The nonlinear phase-shift due to the cross-phase modulation induced by the switching field modifies the frequency of the two-photon EIT resonance. Furthermore, the transverse profile of the switching beam leads to a broadening of the EIT window as expected from the corresponding four-level susceptibility in eq. (9.13). The probe absorption level on resonance ($\Delta = 0$) gradually increases as the EIT resonance is shifted and for sufficiently high input powers reaches the absorption level of the non-EIT situation, when only the probe is injected and no control field is present.

In fig. 9.7 the observed shift of the EIT resonance is depicted as a function of the square of the expected switching field Rabi frequency calculated according to

$$\Omega_{\text{sw}}^{\text{theory}} = g_{850}\sqrt{|n_{\text{sw}}|^2} = g_{850}\sqrt{\frac{2\kappa_2}{\kappa_{850}^2}\frac{P_{\text{sw,in}}}{\hbar\omega_{\text{sw}}}}, \tag{9.16}$$

where g_{850} is the single ion coupling rate of the switching transition, see eq. (A.6), n_{sw} is the intracavity photon number, κ_{850} is the cavity decay rate at 850 nm, κ_2 is the cavity decay rate through the HR and $P_{\text{sw,in}}$ is the input power of this field. In the last step, we used (3.19) to calculated the intracavity power.

The solid line in fig. 9.7 is a linear fit and yields a scaling factor of $(23 \pm 2) \cdot 10^{-6}/2\pi\text{MHz}$. This value can be compared to the linear approximation of the scaling we found from the theoretically calculated shifts in fig. 9.4, were we found $(52 \pm 1) \cdot 10^{-6}/2\pi\text{MHz}$. To reproduce this scaling of the shift, the Rabi frequencies would have to be reduced by a factor 0.65 ± 0.05.

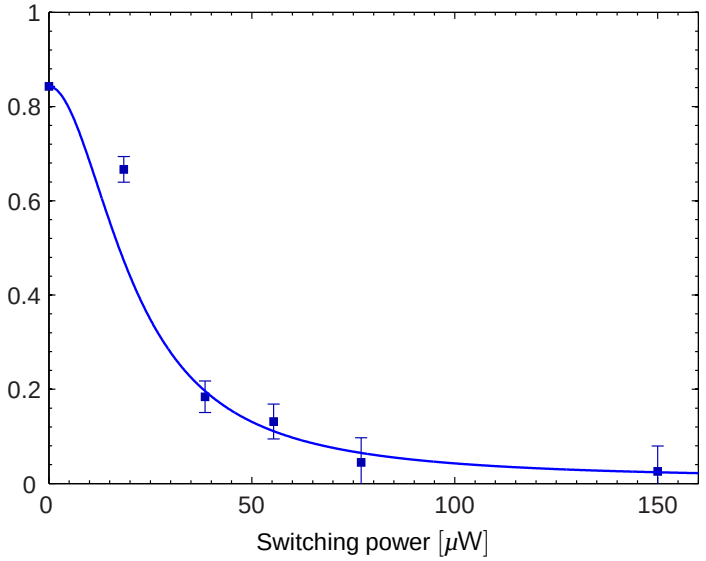

Figure 9.8.: Atomic transparency on resonance as deduced from the fits to the reflectivity spectra in fig 9.6 versus the switching power. The solid line corresponds to the theoretical expectations, calculated for the susceptibility of eq. (9.13) in eq. (9.15). The Rabi frequencies were adjusted by a factor of 0.80 as suggested by the measurements shown in the inset of fig. 9.7. The transparency drops from a level of $\sim 84\%$ without the switching field to below 2% for the highest input powers.

To cross-check this systematic deviation, we can compare the switching field Rabi frequency independently deduced from the fits to the reflectivity spectra in fig. 9.6 with the theoretical expectation according to eq. (8.32). The corresponding data is depicted in the inset of fig. 9.4, along with a linear fit yielding $\Omega_{\mathrm{sw}}^{(\mathrm{fit})} = (0.80 \pm 0.04) \cdot \Omega_{\mathrm{sw}}^{(\mathrm{theory})}$. These two independent findings strongly indicate that the calibration of the intracavity switching power and hence of the theoretical switching Rabi frequency is overestimated.
This deviation may be attributed to a slight detuning of this laser from the cavity resonance which would lead to a lower intracavity field intensity, or to an imperfect modematching, which is quite likely, as the 866 nm control field and the 850 nm switching beam are injected via the same path into the cavity, and the modematching is optimized for the 866 nm laser.

In fig. 9.8 is depicted the atomic transparency on resonance ($\Delta = \Delta_{\mathrm{C}} = 0$) as a function of the fitted switching field Rabi frequency. The transparency is calculated according to eq. (9.15)), based on the parameters found from fits to the reflectivity spectra in fig. 9.6. The solid line is calculated based on the same model, and rescaling the intracavity switching Rabi frequency by a factor 0.80, as suggested by the inset of fig. 9.7. One observes a drastic decrease of the atomic transparency as the switching power is increased, and the transparency drops from $\sim 84\%$ for zero switching field to below 2% for an input switching power of 150 μW. From the plot, we estimate a $1/e$-decrease of the transparency for a Rabi frequency of the switching field of $\Omega_{\mathrm{sw}}^{(1/e)} \sim 2\pi \times 30$ MHz, corresponding to an intracavity photon number of $n_{\mathrm{sw}} = \left(\frac{\Omega_{\mathrm{sw}}}{g_{850}}\right)^2 \sim 3 \cdot 10^4$.

This rather large number of photons could be drastically reduced by a reduction of the detuning of the switching laser, which is imposed by the length of the cavity length. However, this is a technical limitation in this particular experiment and modifying the cavity length so as to be resonant for both the probe laser at 866 nm and the switching field at 850 nm would reduce the required number of photons to accomplish the switching. A simple estimate based on the scaling of the light shift according to $\Delta = \frac{\Omega_{\mathrm{sw}}^2}{\Delta_{\mathrm{sw}}} = \frac{g_{850}^2 n_{\mathrm{sw}}}{\Delta_{\mathrm{sw}}}$, illustrates that reducing the detuning of the switching field from $\Delta_{\mathrm{sw}} = 2\pi \times 4.3$ GHz to some tens of MHz would reduce the number of photons required to achieve the same light shift by a factor of ~ 1000 and one would expect to be able to control the switching of the cavity transmission of a single probe photon with only few intracavity switching photons.

9.3.3. Free-space optical switching

In a subsequent experiment, we also implemented the optical switching scheme, of fig. 9.1 b., where a free propagating switching field at 866 nm is used. We will in this part describe the experimental setup and the results of this experiment.

Experimental setup

The optical setup at the cavity is depicted in fig. 9.5, where the free-space switching laser is denoted by "switching b.". A π-polarized laser beam at 866 nm with a frequency close to the $3d^2D_{3/2} \leftrightarrow 4p^2P_{1/2}$ transition is applied to the ion Coulomb crystals along the transverse *x*-direction. The light for this beam is provided by the same laser as is used for the repumping and optical pumping (see sec. 4.3.2.). A fraction of the light of this laser is split on a PBC on the laser table and sent through a single-pass AOM which is used to

switch the beam on and off and, at the same time, to detune it from atomic resonance. The beam is then coupled to a fiber and guided to the trap table, where we use a telescope and a cylindrical lens to shape the beam in order to optimize the overlap with the elongated form of the crystal while having a sufficiently homogeneous intensity distribution. At the center of the trap the beam waist is ~ 2300 μm along the trap axis and ~ 300 μm along the transverse y-direction. Depending on whether the $+1$st or -1st diffraction order on the switching AOM is coupled to the fiber, the frequency will be detuned to the red or to the blue of the atomic resonance. The frequency of the AOM is tunable by ± 50 MHz, with a central frequency of ± 270 MHz. Both the repumping and optical pumping light has to be resonant with the atomic transition, and as the AOMs used to switch these lasers induce a blue-shift of 110 MHz (see sec. 4.3.2) the bare frequency of the laser is red detuned from the transition frequency by this amount. The tuning range of the AOM will hence correspond to red detunings of $\Delta_{sw} = 2\pi \times (380 \pm 50)$ MHz and blue detuning of $\Delta_{sw} = -2\pi \times (160 \pm 50)$ MHz for the switching field.

Experimental results

For these experiments, we used a crystal with a half-length of $L = (613 \pm 1)$ μm, a radius of $R = (139 \pm 1)$ μm and a density of $\rho_0 = (5.6 \pm 0.1) \cdot 10^8$ cm^{-1}, corresponding to an effective number of ions of $N = 710 \pm 20$ and an collective coupling rate of $g_N = 2\pi \times (14.1 \pm 0.2)$ Mhz. The optical switching experiment was accomplished for two detunings of the switching field.

In fig. 9.9 a. reflectivity spectra are shown for a switching laser detuned by $\Delta_{sw} = 2\pi \times 380$ MHz to the red of the atomic transition. The powers of the switching laser were 0 μW (red squares), 20 μW (lilac circles), 100 μW (pink triangles), 560 μW (light blue stars) and 1120 μW (blue diamonds). From a fit to the reflectivity spectra with no switching field present, we deduce a control field Rabi frequency of $\Omega_C = (2.6 \pm 0.1)$ MHz, where the collective coherent coupling rate was fixed to the expected value of $g_N = 2\pi \times (14.1 \pm 0.2)$ Mhz. One observes a shift of the EIT window with increasing switching power and, especially for large powers, a slight broadening of the transparency dip. Induced by this shift, the atomic absorption level on resonance ($\Delta = 0$) gradually increases and almost reaches the absorption level of the non-EIT configuration, with no control field present. For comparison we also recorded spectra without control and switching field and only the probe laser present (turquoise asterisks), and to check for possible effects of the switching laser on the coherent coupling with the probe and the switching laser present (green crosses). The two curves overlap within their error bars and no significant effect of the switching laser on the coherent coupling is observed.

In fig 9.9 b. similar spectra are shown for a switching field detuned by $\Delta_{sw} = -2\pi \times 160$ MHz to the blue side of the atomic transition. The individual curves correspond to switching powers of 0 μW (red squares), 50 μW (lilac circles), 150 μW (pink triangles), 300 μW (light blue stars), 560 μW (blue diamonds), 1250 μW (blue pentagrams). A fit to the unshifted reflectivity spectrum yields a control field Rabi frequency of $\Omega_C = (2.9 \pm 0.1)$ MHz, where the collective coupling rate was fixed to the previous value. To check for direct effects of the switching laser on the coherent coupling we also obtained spectra with only the probe laser being injected (turquoise asterisks) and when the probe and the switching lasers are present (green crosses) and the two spectra overlap within

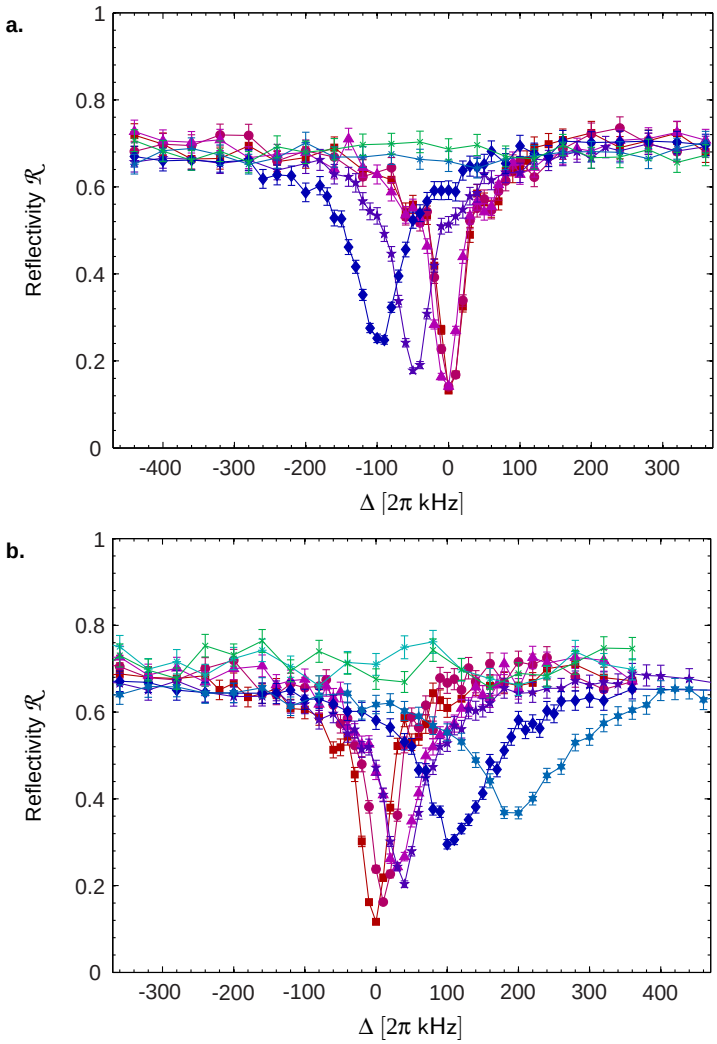

Figure 9.9.: Cavity reflectivity spectra for various input powers of the free-space optical pumping field for **a.** a switching laser detuned by $\Delta_{sw} = 2\pi \times 380$ MHz to the red of the atomic transition (The input powers are 0 μW (red squares), 20 μW (lilac circles), 100 μW (pink triangles), 560 μW (light blue stars) and 1120 μW (blue diamonds)) and for **b.** a blue-detuning of $\Delta_{sw} = -2\pi \times 160$ MHz (The input powers are 0 μW (red squares), 50 μW (lilac circles), 150 μW (pink triangles), 300 μW (light blue stars), 560 μW (blue diamonds), 1250 μW (blue pentagrams)). In both cases we observe a increasing shift of the EIT resonance with higher powers of the switching field. The crystal used in these experiments has a half-length of $L = (613 \pm 1)$ μm, a radius of $R = (139 \pm 1)$ μm and a density of $\rho_0 = (5.6 \pm 0.1) \cdot 10^8$ cm^{-1}, corresponding to an effective number of ions of $N = 710 \pm 20$. Fixing the collective coherent coupling rate to the expected value for this number of ions $g_N = 2\pi \times (14.1 \pm 0.2)$ Mhz, we deduce from a fit to the unperturbed EIT spectra of $\Omega_C = 2\pi \times (2.6 \pm 0.1)$ MHz for the red detuned and $\Omega_C = 2\pi \times (2.9 \pm 0.1)$ MHz for the blue detuned case.

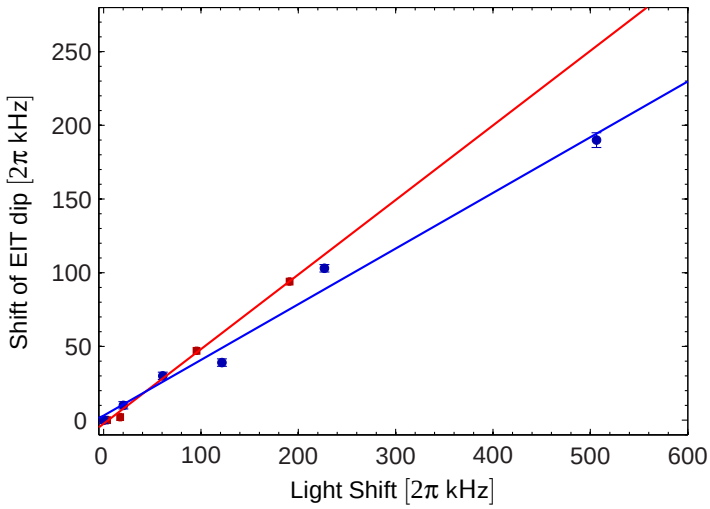

Figure 9.10.: Measured shifts of the EIT resonance versus the calculated light shift ($2\Delta_{LS} = 2\frac{\Omega_{sw}^2}{|\Delta_{sw}|}$) for the individual input powers for a red-detuning of $\Delta_{sw} = 2\pi \times 380$ MHz (red squares) and a blue-detuning of $\Delta_{sw} = -2\pi \times 160$ MHz (blue circles). The solid lines are linear fits and yield slopes of $b_{red} = (0.51 \pm 0.04)$ and $b_{blue} = (0.38 \pm 0.02)$ respectively. The different scalings are attributed to Doppler shifts induced by the radial micromotion.

their error bars, and no significant effect is observed. As in the red detuned situation, the EIT window is shifted with increasing power of the switching laser, however, to opposite detunings. The shift of the EIT resonance leads to an increasing absorption level on resonance ($\Delta = 0$) which, for high powers of the switching laser, almost reaches the non-EIT level.

According to the susceptibility calculated in eq. (9.9) and the simulated spectra in fig. 9.3 a., the free space optical switching beam should solely give rise to a shift of the EIT resonance, which can be understood in terms of the power dependent light shift of the addressed level and hence as a shift of the two-photon resonance condition, and our observation reflect this shift. However, in the measured spectra, one also observe a broadening of the EIT resonance for larger switching powers, both for the red and the blue detuned case. This effect can be attributed to power broadening of the excited state by the switching laser which also addresses the $3d^2D_{3/2}, m_J = +1/2 \leftrightarrow 4p^2P_{1/2}, m_J = +1/2$ transition and hence will lead to a shift of the EIT level $|3\rangle$ and a power related broadening of this state. This broadening is, however, not included in the model of eq. (9.9), and fitting the data with the simple model would give inadequate results, especially for high switching power. We therefore did not try to compare these results and we will limit our analysis on the investigation of the shift of the EIT window [1].

The different detunings used for the acquisition of the two sets of data circumvent a direct comparison as a function of shifting power. However, the measured shifts of the

[1] A determination of the atomic transparency (see eq. (9.15)) from reflectivity spectra relies on the precise knowledge of the various parameters in the system, which have to be determined from the model.

EIT window can be related to the bare light shift one would expect for the individual switching powers and detunings. From the input powers, and the known beam waists (see sec. 9.3.3), we can calculate the intensity of the elliptic beam at the position of the ions $I = \frac{2P_{sw}}{\pi w_z w_y}$, and the Rabi frequency of the transition Ω_π (see appendix A.4) The expected light shift of the individual levels is then simply given by $\Delta_{LS} = \frac{\Omega_\pi^2}{|\Delta_{sw}|}$. The frequency shift of the two-photon resonance, which we observe, will correspond to $2\Delta_{LS}$, as both the lower $3d^2D_{3/2}, m_J = {}^{-1}/_2$ and the upper $4p^2P_{1/2}, m_J = {}^{+1}/_2$ level are shifted in opposite direction.

In fig. 9.10 are depicted the measured shifts of the EIT resonance versus the calculated light shift ($2\Delta_{LS}$) for the individual input powers and detunings. For both sets of data, we find a linear scaling of the observed shift of the EIT resonance, however, with substantially different scalings. From the fits we find slopes of $b_{red} = (0.51 \pm 0.04)$and $b_{blue} = (0.38 \pm 0.02)$. As the switching light is applied to the ions along the transverse *x*-direction, radial motion will influence the resonance condition and the different scaling behavior is most likely a signature of the Doppler shifts induced by the radial micromotion (see sec. 2.1). To estimate the order of magnitude of this effect, one can calculate the maximum Doppler shift for an ion located at a distance corresponding to the waist of the cavity $w_0 = 37$ μm above or below the field free trap axis. According to eq. (4.1), the maximum velocity is[2] $\tilde{v} = \frac{1}{2\sqrt{2}} q w_0 \Omega_{RF}$, where $q = 0.4$ is the trap parameter defined in eq. (2.5) at the used RF voltage of 300 V, and $\Omega_{RF} = 2\pi \times 4.0$ MHz is the frequency of the RF field. With these numbers, the velocity amplitude of the radial micromotion is $\tilde{v} \sim 130$ ${}^{m}/_{s}$, which yields a Doppler shift of $k\tilde{v} \sim 2\pi \times 150$ MHz. Though this is an estimate for the maximum shift it becomes obvious that radial micromotion will play an important role at the chosen detunings of the switching laser, which makes this scheme less suited for large ion Coulomb crystals.

Furthermore, to achieve a homogeneous Rabi frequency of the switching field throughout the ensemble, this beam has to be relatively big which limits this method to relatively high switching powers, as compared to the intracavity optical switching scheme with a doubly resonant cavity.

9.4. Conclusion

In this chapter we presented a first application of the intracavity EIT system for the realization of all-optical switching schemes. We investigated theoretically two possible configurations for optical switching, where we either assumed the switching field to be uniform throughout the ensemble or to be coupled to the fundamental TEM_{00} mode of the cavity. For both scenarios we derived analytical expressions for the atomic susceptibility and could simulate the expected cavity reflectivity spectra.

We demonstrate how these scenarios can be realized in our system. For the realization of the intracavity switching scheme, we used a σ^+ polarized laser, which couples the $3d^2D_{3/2}$, $m_J = {}^{-1}/_2$ and $4p^2P_{3/2}$, $m_J = {}^{+1}/_2$ states. We observed the predicted frequency shift and broadening of the EIT window and find a frequency shift per intracavity photon of (0.9 ± 0.2) ${}^{Hz}/_{photon}$. The switching of the cavity transmission can accordingly be accomplished by 30′000 photons. However, the scheme is currently limited by the large

[2] The factor ${}^{1}/_{\sqrt{2}}$ accounts for the tilt of the coordinate system in eq. (4.1)

detuning of the switching laser of $\Delta_{sw} = 2\pi \times 4.3$ GHz which is imposed by the length of the cavity. Modifying the cavity to be doubly resonant for both the probe and the optical switching laser should allow to reduce the required number of photons to the few photon level and would offer promising applications for nonlinear optics at the few photon level. EIT-based four-level schemes were, e.g. considered for the realization of Giant-Kerr nonlinearities and cross-phase modulation schemes [98], with possible applications for quantum non-demolition measurements [214] and quantum logic operations [215].

To illustrate the possibility of free-space optical switching with a uniform switching field, we also used a π-polarized beam resonant with the $3d^2D_{3/2} \leftrightarrow 4p^2P_{1/2}$ which is shone onto the ions along the transverse *x*-direction. The experiment was conducted both for a red and a blue detuned switching field. In both cases we observe a shift of the EIT resonance for increasing powers of the switching field, however with different scalings. This is attributed to the transverse micromotion of the ions induced by the RF-trapping potential.

Ultimately, one would like to be in a regime where a single photon on the switching transition can block the transmission of a single probe photon. Such a photon-blockade scheme was proposed by Imamoglu *et al.* [99]. The suggested scheme uses intracavity EIT, where the probe and the switching fields are identical, and predicts a strong anti-bunching effect of the transmitted photons by the blockade of the cavity transmission induced by a single photon. Though Grangier *et al.* pointed out [100, 199] that this scheme puts stringent limits on the required parameters of the atomic system and the cavity, one could consider an adaption of the scheme to the four-level scheme with distinct frequencies of the probe and the switching photons.

In fact, one major limitation of the proposed scheme is the modification of the typical build up time of the probe field through the coherent interaction of control and probe field, as experimentally confirmed in sec. 8.4.2. In the frequency domain, this can be understood by a broadening of the frequency spectrum of a probe photon through the nonlinear dispersion induced by the EIT medium.

This limitation is, however, based on the assumption of identical (same wavelength) probe and switching photons, which can be overcome by considering a scheme where probe and switching photons have different wavelengths. The bandwidth of the switching photon has to be sufficiently narrow, or, equivalently the life-time in the cavity sufficiently long, so as to match the time scale of the dynamics of the probe photon. This could be accomplished by asymmetric parameters of the cavity at the two wavelengths of probe and switching field e.g. by a cavity with a much larger finesse at the wavelength of the switching laser. The realization of such a scheme would, nevertheless, require a detailed theoretical analysis, which is beyond the scope of this thesis.

10. Summary and Outlook

This thesis covers several aspects of the experimental realization of a light-matter interface based on ion Coulomb crystals in an optical cavity. The experimental studies comprise three core areas: The realization of the collective strong coupling regime of CQED with ion Coulomb crystals, the development of a novel noninvasive spectroscopy technique for studying normal mode dynamics and the observation of cavity electromagnetically induced transparency.

The work on an ion based light matter interface was started prior to this thesis and especially the construction and deployment of the cavity trap setup, the loading, the state preparation and the first observation of collective strong coupling were covered in the thesis of my predecessor Peter Herskind [80]. To characterize the collective coherent coupling between ion Coulomb crystals and specific cavity field modes, we performed a thorough investigation of this interaction. We showed that the collective strong coupling regime can be reached with ion Coulomb crystals, with cooperativities as high as $C \sim 8$, and found excellent agreement between the theoretical expectations and the experimental findings [79, 148]. Moreover, by measuring the temporal stability of collective coherences between Zeeman substates we could demonstrate coherence times in the millisecond range. To illustrate the possibility of performing repeated experiments with a well-controlled number of particles, we demonstrated the long-term stability by measuring the cooperativity of a specific crystal over more than two hours.

In a subsequent study, we investigated the coupling of ion Coulomb crystals with different sizes to various cavity modes and could show that collective strong coupling can be also reached with large ion Coulomb crystals and higher order cavity modes with equal coupling strengths [81]. In addition, the excellent agreement between theory and experiment we found in these studies importantly indicates that the inherent radial micromotion does not influence the coherent coupling of the ion Coulomb crystals and the cavity modes.

We continued the exploration of the coherent interaction between ion Coulomb crystals and the cavity field by an investigation of the normal mode dynamics of the crystals [152]. We implemented a novel noninvasive spectroscopy technique to probe the collective motion of the ions by their interaction with a cavity field at the single photon level. Using this technique, we could measure the frequency of various normal modes for crystals with different aspect ratios, as well as the kinetic energy of the driven motion.

On the way towards the realization of an ion Coulomb based quantum memory an important next step was the experimental observation of cavity electromagnetically induced transparency [148]. In a novel scheme using the magnetic Zeeman substates of $^{40}Ca^{+}$ we could demonstrate excellent control over the atomic transparency for a probe field at the single photon level, when the frequencies of the strong control field and the probe field at the single photon level are close to two-photon resonance. The observed transparency windows can be almost two orders of magnitude narrower than in previous experiments with neutral atoms in cavities [92–95]. We performed systematic studies on the influence

of various interaction parameters and find very good agreement between the results and theoretical predictions developed specifically for our system.

Finally, we could also demonstrate how the observed narrow EIT windows can be used for the implementation of a novel all-optical switching scheme. In these experiments we showed how the transmission of a probe field at the single photon level can be controlled by an additional switching laser injected into the cavity. The results could be compared to a theoretical model which we established for our system.

In summary, the studies of the coherent light-matter interaction between ion Coulomb crystals and a cavity field at the single photon level we presented in this thesis illustrate that our system can meet three important criteria for the realization of a quantum memory [39]:

- The optimal fidelity of light storage and retrieval experiments is expected to scale as $\frac{2C}{2C+1}$, as shown in refs. [56, 57]. With a measured cooperativity of $C \sim 8$ the potential storage and retrieval fidelity of our system at the present state is ~ 94 %, and should allow for the efficient transfer of the quantum state of single photons onto a collective excitation of the ensemble and vice versa. Moreover, it might be possible to confine even more ions in the cavity mode volume, e.g. by the use of bi-component crystals consisting of two stable calcium isotopes [141].

- The second important criteria is the achievable storage time. We addressed this issue by measuring the decay of collective coherences between Zeeman substates and found coherence times in the millisecond range, which is encouraging for the realization of a long-lived quantum memory. Future studies could identify possible limitations, e.g. by further investigations of heating and damping effects in the system. At the present state of the experiment establishing EIT and measuring the collective coupling requires the cooling lasers to be switched off and the ions will heat up during these periods, which eventually might limit the achievable storage time. This limitation could, as envisioned in ref. [137], be overcome by the use of bi-component crystals. In this scheme, an inner component of $^{40}Ca^{+}$ interacts with the cavity field and is used to store the probe field while the outer component, consisting of a heavier calcium isotope, is permanently laser cooled. In this way, the inner component can be sympathetically cooled without the need of incoherent scattering of photons by the $^{40}Ca^{+}$ ions.

- By demonstrating that collective strong coupling is possible between ion Coulomb crystals and various cavity field modes we could also address the multimode capability of the system. Making use of the solid-state properties of ion Coulomb crystals this spatial degree of freedom of the light field could allow for the multimode storage and retrieval of single photons and also for the realization of other multimode quantum information devices. Further investigations could comprise the observation of EIT with higher order cavity modes to e.g. investigate if EIT can be established by the control field coupled to a particular mode without influencing a probe field in a different mode.

In connection with the successful demonstration of cavity EIT these results mark an important cornerstone for the realization of a quantum memory based on ion Coulomb crystal in an optical cavity [55]. Next steps towards this goal could comprise the storage of a

classical light field using the STIRAP scheme of ref. [55] which will require the implementation of a dynamical control of the probe control field Rabi frequency. Moreover, to tailor optimized control parameters for the storage and retrieval of a light pulse, theoretical studies are currently in progress to include the effect of the transverse profile of the control field in the optimization process.

Beside their importance for the implementation of a quantum memory, our studies of a light-matter interface based on ion Coulomb crystals in an optical cavity may have a number of attractive applications in different contexts and we will at the end of this thesis sketch two possible extensions of the studies presented here.

A first promising research direction could be the further investigation of the thermodynamical properties of cold nonneutral plasmas using the noninvasive spectroscopy technique introduced in ch. 7, e.g. by a more thorough study of the influence of various crystal parameters on the intrinsic damping within the ion Coulomb crystal by the off-resonant coupling to other vibrational modes. Eventually this may also enable for a more direct measurement of the temperature of ion Coulomb crystals, which is otherwise difficult. A better understanding of the thermodynamical properties and the damping mechanisms would furthermore also have important implications for the realization of a quantum memory, e.g. to identify possible limitations for the achievable coherence times or for the storage of multiple photons by a coherent excitation of collective vibrational modes. Moreover, the combination of free particle properties like easy-to-address atomic transitions and solid state properties makes ion Coulomb crystals to a very interesting platform to investigate the coherent backaction of the cavity field on the collective motion of the ions, e.g. to investigate cavity optomechanical effects with cold, solid-like objects [180, 181] or classical and quantum phase transitions [186–190].

A second attractive direction arises from the narrowness of the observed EIT windows. The fast switching of the atomic transparency over few tens of kHz implies strong nonlinearities around two-photon resonance [84], which could be used for the exploration of nonlinear effects at low light-levels [98]. These strong nonlinearities could be exploited for e.g. implementing single-photon transistors [202, 203], or for the generation of highly nonclassical states [205]. The use of ion Coulomb crystals to achieve controlled coherent photon-photon interactions could then have applications e.g. for the realization of quantum gates at the single photon level [204] or for the observation of novel quantum phase transitions for light [206, 207].

A. The $^{40}Ca^{+}$ ion

A.1. Transition wavelengths and decay rates

Transition	Type	Wavelength λ	transition rate $\Gamma = 2\gamma$
$4s^2S_{1/2} \leftrightarrow 4p^2P_{1/2}$	dipole	396.847 nm	$2\pi \times 20.7$ MHz
$4s^2S_{1/2} \leftrightarrow 4p^2P_{3/2}$	dipole	393.366 nm	$2\pi \times 21.5$ MHz
$3d^2D_{3/2} \leftrightarrow 4p^2P_{1/2}$	dipole	866.214 nm	$2\pi \times 1.69$ MHz
$3d^2D_{3/2} \leftrightarrow 4p^2P_{3/2}$	dipole	849.802 nm	$2\pi \times 0.177$ MHz
$3d^2D_{5/2} \leftrightarrow 4p^2P_{3/2}$	dipole	854.209 nm	$2\pi \times 1.58$ MHz
$4s^2S_{1/2} \leftrightarrow 3d^2D_{3/2}$	quadrupole	732.389 nm	$2\pi \times 0.14$ Hz
$4s^2S_{1/2} \leftrightarrow 3d^2D_{5/2}$	quadrupole	729.147 nm	$2\pi \times 0.14$ Hz

Table A.1.: Relevant electric transitions in $^{40}Ca^{+}$ (see also fig. 2.2). The wavelengths of the transitions and the transition rates are taken from [104, 106].

A.2. Clebsch-Gordan coefficients

		$\mathbf{4p^2P_{1/2}}$	
		$m_J = -1/2$	$m_J = +1/2$
$\mathbf{4p^2S_{1/2}}$	$m_J = -1/2$	$-\sqrt{1/3}$	$-\sqrt{2/3}$
	$m_J = +1/2$	$\sqrt{2/3}$	$\sqrt{1/3}$
$\mathbf{3d^2D_{3/2}}$	$m_J = -3/2$	$\sqrt{1/2}$	–
	$m_J = -1/2$	$-\sqrt{1/3}$	$\sqrt{1/6}$
	$m_J = +1/2$	$\sqrt{1/6}$	$-\sqrt{1/3}$
	$m_J = +3/2$	–	$\sqrt{1/2}$

		$\mathbf{4p^2P_{3/2}}$			
		$m_J = -3/2$	$m_J = -1/2$	$m_J = +1/2$	$m_J = +3/2$
$\mathbf{3d^2D_{3/2}}$	$m_J = -3/2$	$-\sqrt{3/5}$	$-\sqrt{2/5}$	–	–
	$m_J = -1/2$	$\sqrt{2/5}$	$-\sqrt{1/15}$	$-\sqrt{8/15}$	–
	$m_J = +1/2$	–	$\sqrt{8/15}$	$\sqrt{1/15}$	$-\sqrt{2/5}$
	$m_J = +3/2$	–	–	$\sqrt{2/5}$	$\sqrt{3/5}$

Table A.2.: Clebsch-Gordan coefficients for the relevant transitions in $^{40}Ca^{+}$ [216].

A.3. Zeeman-splitting

The energy shift, ΔE_B of an arbitrary Zeeman-substates in a magnetic field B can be calculated according to

$$\Delta E_B = m_J \, g_J \, \mu_B \, B, \tag{A.1}$$

where m_J is the magnetic quantum number of the state, μ_B is the Bohr magneton and g_J is the Landé factor

$$g_J = 1 + \frac{J(J+1) + S(S+1) - L(L+1)}{2J(J+1)}, \tag{A.2}$$

where L, S and J are the quatnum numbers corresponding to the angular momentum, the electric spin and the total angular momentum, respectively. The values for g_J for the relevant states in $^{40}Ca^{+}$ are listed below.

State	L	S	J	g_J
$4s^2S_{1/2}$	0	1/2	1/2	2
$4p^2P_{1/2}$	1	1/2	1/2	2/3
$4p^2P_{3/2}$	1	1/2	3/2	4/3
$3d^2D_{3/2}$	2	1/2	3/2	4/5

A.4. Rabi frequency

The coupling strength of a particular (dipole allowed) transition for a certain intensity I of the coupling field is characterized by the Rabi-Frequency, see e.g. [1]. For the transition between two particular Zeeman-substates $|g\rangle$ and $|e\rangle$ it is, using the conventions chosen in this thesis, given by

$$\Omega_{ge} = a_{ge} \, \frac{\Gamma}{2} \sqrt{\frac{I}{2I_{sat}}} = a_{ge} \sqrt{\frac{3\pi c^2 \Gamma}{2\hbar\omega^3}} \sqrt{I}, \tag{A.3}$$

where $I_{sat} = \frac{\hbar\Gamma\omega^3}{12\pi c^2}$ is the saturation intensity of the transition, Γ and ω are the transition rate and resonance frequency of the electronic transition (see tab. A.1), and a_{ge} is the Clebsch-Gordan coefficient for the considered Zeeman-substates.

A.5. Single ion coupling strength

The coupling strength of a single photon cavity field and a single atom located at an antinode of the cavity standing wave is characterized by the coupling rate g, and corresponds to the Rabi frequency for a single photon. The intensity corresponding to a single photon field in the cavity can be calculated using the normalization condition $I_{vac} V = \hbar\omega_C$, where ω_C is the resonance frequency of the cavity, $V = \int |\Psi(\boldsymbol{r})| \mathrm{d}\boldsymbol{r} = \frac{\pi w_0^2}{4} d$ is the mode volume

of the cavity, w_0 ist the waist of the fundamental mode and d is the length of the cavity. Substituting into eq. (A.3) yields

$$g = a_{\mathrm{ge}} \sqrt{\frac{6c^3\Gamma}{\omega^2 w_0^2 d}}. \tag{A.4}$$

In our expermient, we use the $\left|\mathrm{D}_{3/2}, m_J = {}^{+3}/_{2}\right\rangle \leftrightarrow \left|\mathrm{P}_{1/2}, m_J = {}^{+1}/_{2}\right\rangle$ as the probe transition. With the partial dipole decay rate given in tab. A.1, the Clebsch-Gordan coefficient in tab. A.2 and using the length and waist of the cavity in our experiment, $d = (11.8 \pm 0.3)$ mm and $w_0 = 37$ μm [80], we can calculate the expected single ion coupling rate of the probe transition for an ion located at the anti-node of the standing wave cavity field and find

$$g_{\mathrm{theory}} = 2\pi \times (0.532 \pm 0.007)\,\mathrm{MHz}. \tag{A.5}$$

In the same way, we can also find the single ion coupling rate of the $\left|\mathrm{D}_{3/2}, m_J = {}^{+3}/_{2}\right\rangle \leftrightarrow \left|\mathrm{P}_{3/2}, m_J = {}^{+1}/_{2}\right\rangle$ transition which is used for the optical switching experiments in sec. 9.3.2. Using the partial dipole decay rate of tab. A.1 and the appropriate Clebsch-Gordan coefficient in tab. A.2 the same calculation yields

$$g_{850,\mathrm{SW}} = 2\pi \times (0.175 \pm 0.004)\,\mathrm{MHz}. \tag{A.6}$$

B. Legendre functions

The Legendre differential equation is defined as (see e.g. [217])

$$-\frac{\mathrm{d}}{\mathrm{d}x}((1-x^2)\frac{\mathrm{d}f(x)}{\mathrm{d}x})+\frac{m^2}{1-x^2}f(x)=l(l+1)f(x). \tag{B.1}$$

The first and second order Legendre functions are solutions to this equation and are in general form given by

$$P_m^l(x) = \frac{(-1)^l}{2^l.l!}(1-x^2)^{m/2}\frac{\partial d^{m+l}}{\partial dx^{m+l}}[(x^2-1)^l] \tag{B.2a}$$

$$Q_m^l = (-1)^m(z^2-1)^{\frac{m}{2}}\frac{d^m}{dz^m}Q_0^l, \tag{B.2b}$$

where

$$Q_0^n=\frac{1}{2^n n!}\frac{d^n}{dz}((z^2-1)\ln(\frac{z+1}{z-1}))-P_0^n\ln(\frac{z+1}{z-1}). \tag{B.3}$$

The lowest order functions with m=0 are given in the following table

l,m	$P_m^l(x)$	$Q_m^l(x)$
1,0	x	$\frac{1}{2}x\ln(\frac{x+1}{x-1})$
2,0	$\frac{1}{2}(3x^2-1)$	$\frac{1}{4}(3x^2-1)\ln(\frac{x+1}{x-1})-\frac{3}{2}x$
3,0	$\frac{1}{2}(5x^3-3x)$	$\frac{1}{4}(5x^3-3x)\ln(\frac{x+1}{x-1})-\frac{1}{6}-\frac{5}{6}(3x^-1)$

C. EIT: Adiabatic elimination for an intracavity control field

In 8.2.3 we found a set of dynamical equations for the mean values of the system observables for the case, when the EIT medium interacts with control and probe fields that both are coupled to a common cavity mode, see eqs. (8.22). As in the case of a uniform control field (see eq. (8.9)) one can perform an adiabatic elimination with respect to the slow time evolution of σ_{12} and finds the following set of equations for the mean values of the nonzero system observables:

$$0 = -(\kappa + i\Delta_c)a + ig\sum_{j=1}^{N_{\rm tot}} \psi_{00}(r_j)\sigma_{31,j} + \sqrt{2\kappa_1}a_{\rm in}. \tag{C.1}$$

$$0 = -(\gamma + i\Delta)\sigma_{13,j} + iga\psi_{00}(r_j) + i\frac{\Omega_{\rm C}}{2}\psi_{00}(r_j)\sigma_{12,j} \tag{C.2}$$

$$\dot{\sigma}_{12,j} = -(\gamma_{12} + i\delta)\sigma_{12,j} + i\Omega_{\rm C}\sigma_{13,j}, \tag{C.3}$$

where we set $\sigma_{31,j} = \frac{1}{2}(\sigma_{13,j+} + \sigma_{13,j-})$ and restrict ourselves to the fundamental TEM_{00} mode, hence $\psi_{00}(r_j) = exp(-2r_j^2/w_0)$ The Laplace transformation of an arbitrary funciton $f(t)$ is defined as (see e.g. [217])

$$\mathcal{L}(f(t)) = \tilde{f}[p] \equiv \int_0^\infty \exp(-pt) f(t)\mathrm{d}t, \quad p \in \mathbb{C}. \tag{C.4}$$

of these equations yields

$$0 = -(\kappa + i\Delta_c)\tilde{a} + ig\sum_{j=1}^{N_{\rm tot}} exp(-2r_j^2/w_0)\tilde{\sigma}_{31,j} + \sqrt{2\kappa_1}\tilde{a}_{\rm in}[p]. \tag{C.5a}$$

$$0 = -(\gamma + i\Delta)\tilde{\sigma}_{13,j} - ig\tilde{a}\,\exp(-2r_j^2/w_0) - i\Omega_{\rm C}\tilde{\sigma}_{12,j} \tag{C.5b}$$

$$p\tilde{\sigma}_{12,j}[p] = -(\gamma_{12} + i\delta)\tilde{\sigma}_{12,j} - i\Omega_{\rm C}\exp(-2r_j^2/w_0)\tilde{\sigma}_{13,j}. \tag{C.5c}$$

Substituting eqs. (C.5b) and (C.5c) into (C.5a) one finds the Laplace tranformation of the intracavity field which was already given in eq. (8.26)

$$\tilde{a}[p] = \sqrt{2\kappa_1}\tilde{a}_{\rm in}[p]\left[\kappa + i\Delta_{\rm C} + g^2\sum \frac{\exp(-2r_j^2/w_0^2)}{\gamma + i\Delta + \frac{\Omega_{\rm C}^2\exp(-2r_j^2/w_0^2)}{\gamma_{12} - i\delta + p}}\right]^{-1}.$$

Applying the continuous media approximation and using the effective number of ions (see eq. (3.43)) this reduces to

$$\tilde{a}[p] = \frac{\sqrt{2\kappa_1}\tilde{a}_{\rm in}[p]}{\kappa + i\Delta_{\rm C} - i\chi[p]}. \tag{C.6}$$

where

$$\chi[p] = \frac{ig^2N}{\gamma + i\Delta} \frac{\ln(1+s(p))}{s(p)} \tag{C.7}$$

and

$$s(p) = \frac{\Omega_C^2}{(\gamma_{12} - i\delta + p)(\gamma + i\Delta)} \tag{C.8}$$

On resonance eqs. (C.8) and (C.7) are purely real and the intra cavity field equation becomes

$$\tilde{a}[p] = \frac{a_{\text{in}}}{p} \frac{\sqrt{2\kappa_1}}{\kappa + \frac{g^2N}{\Omega_C^2} \ln(1 + \frac{\Omega_C^2}{(\gamma_{12}+p)\gamma})(\gamma_{12}+p)}, \tag{C.9}$$

where we assumed the probe input field to be a step function in time, given by

$$a_{\text{in}}(t) = \begin{cases} 0 & \text{for} \quad t < 0 \\ a_{\text{in}} & \text{for} \quad t > 0 \end{cases} \tag{C.10}$$

and with the Laplace transformation

$$\tilde{a}_{\text{in}}(p) = \frac{a_{\text{in}}}{p}. \tag{C.11}$$

Eq. C.9 is the analytic expression for the intracavity field and one can be used to calculate the cavity transmission or reflection, according to eqs. 3.20.

To obtain the corresponding dynamical evolution of the (resonant) intracavity field in time, one has to calculate the inverse Laplace transformation of eq. (C.9)

$$a(t) = \mathcal{L}^{-1}(\tilde{a}[p]), \tag{C.12}$$

which has no simple analytical form. However, the solution can still be found numerically.

D. Cavity EIT with well localized atoms

In sec. 8.2.3 we derivation the linear susceptibiltiy for the three-level EIT situation for an intracavity control field. There, we assumed that the timescale of the (thermal) motion of the atoms along the standing wave cavity field standing wave is fast as compared to the dynamical time of the cavity fields and that we can average over the common standing wave geometry of the control and the probe field. In this "warm" situation, the susceptibilty was found to be (see (8.25))

$$\chi_\Lambda = \frac{ig^2N}{\gamma + i\Delta}\frac{\ln(1+s)}{s},$$

where the effective saturation paramter s of the two-photon transition was defined in eq. (8.17).

Here, we will treat the "cold" situation, where the motion of the ions is slow as compared to the dynamical build up of the EIT and where the ions during the EIT interaction time are well localized within the standing wave of probe and control field. In contrast to the "warm" situation, one has to keep the higher spatial frequency components in $\exp(2ikz)$, when solving eqs. (8.21) [192, 218, 219]. In steady state, the equations can still be solved and one finds for the intracavity field the familiar expression

$$a = \frac{\sqrt{2\kappa_1}a_{\text{in}}}{\kappa + i\Delta_C - i\chi_\Lambda^{\text{cold}}},$$

where we assumed assume the probe and the control field to be coupled to the fundamental TEM_{00} mode and where the three-level susceptibility is now given by

$$\begin{aligned}
\chi_\Lambda^{\text{cold}} &= \frac{i}{2}g^2\sum_j \frac{e^{-2r_j^2/w_0^2}(1+\cos(2kz_j))}{\gamma + i\Delta + \frac{\Omega_C^2/2}{\gamma_{12}+i\delta}e^{-2r_j^2/w_0^2}(1+\cos(2kz_j))} && \text{(D.1a)}\\
&= \frac{i}{2}g^2\rho\int 2\pi r dr dz \frac{e^{-2r^2/w_0^2}(1+\cos(2kz))}{\gamma + i\Delta + \frac{\Omega_C^2/2}{\gamma_{12}+i\delta}e^{-2r^2/w_0^2}(1+\cos(2kz))} && \text{(D.1b)}\\
&= \frac{ig^2N}{\gamma+i\Delta}\frac{\ln\left(\frac{1}{2}+\sqrt{\frac{1}{4}+\frac{s}{2}}\right)}{\frac{s}{2}}, && \text{(D.1c)}
\end{aligned}$$

where the effective saturation parameter of the two-photon transition s, defined in eq. (8.17), was used. The result is similar to the "warm" situation, where we averaged over the longitudinal effects, with a similar scaling behaviour and lineshape of the EIT window. However, as compared to eq. (8.25) the effective saturation paramter s is lowered by a factor 2, resulting in an lower effective Rabi frequency.

In fig. D.1 the resulting cavity reflection spectra around two photon resonance are depicted, caclulated for the three-level susceptibilities for the standard EIT situation with a

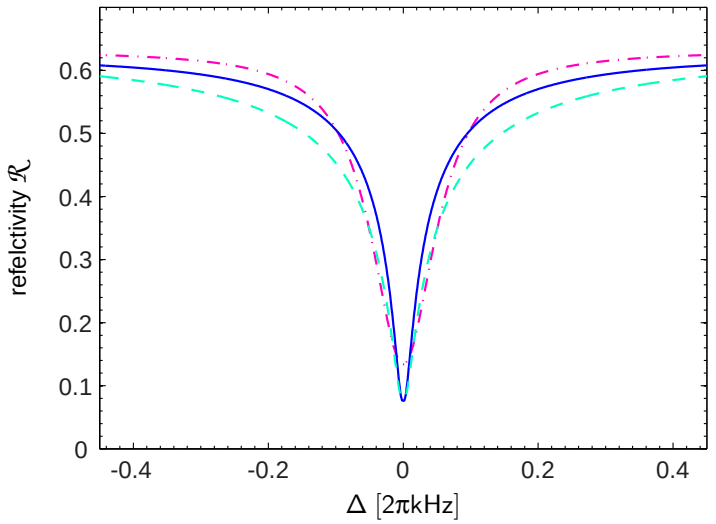

Figure D.1.: Simulated cavity reflection signal around two-photon resonance (see (8.27)), cacluated for the three-level susceptibility corresponding to the ”normal” EIT sitution, with a uniform control field Rabi frequency, see eq. (8.16) (dashed-dotted line), for the ”warm” situation with an intracavity control field, but averaging over longitudinal effects, see eq. (8.25) (solid line) and for the ”cold” situation with an intracavity control field and well-localized ions, see eq. (D.1)(dashed line). The paramters used for the simulation were: $\kappa_1 = 2\pi \times 1.53\,\text{MHz}$, $\kappa_2 = 2\pi \times 7.85\,\text{kHz}$, $\kappa_{\mathcal{A}} = 2\pi \times 0.63\,\text{MHz}$, $\gamma = 2\pi \times 11.2\,\text{kHz}$, $\gamma_{12} = 1\,\text{kHz}$, $\Omega_C = 2\pi \times 3\,\text{MHz}$, $g_N = 2\pi \times 12\,\text{MHz}$.

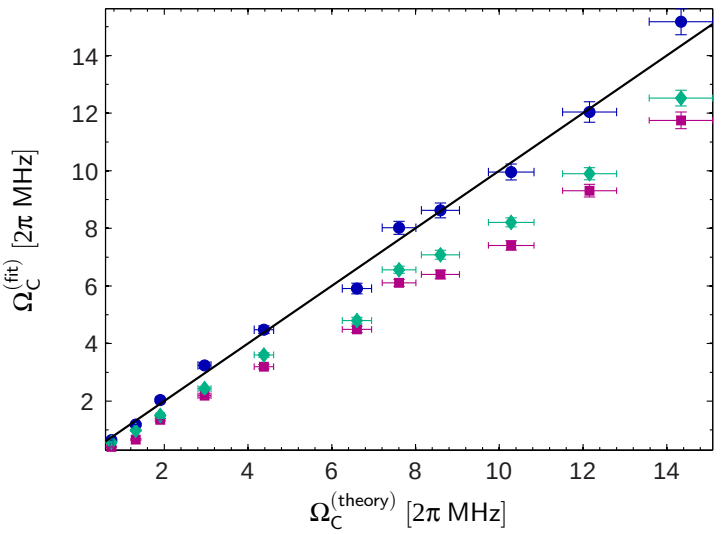

Figure D.2.: Rabi frequecies deduced from fits to the EIT spectra in sec. 8.4.2 (see fig. 8.9) for various input powers of the control field and for a crystal with $N = 980 \pm 20$ ions effectively interacting with the cavity field. The Rabi frequency are shown as a function of the expected Rabi frequency for the corresponding input powers (see eq. (8.32)), and are obtained for three different models, namely the standard EIT model with a uniform control field Rabi frequency (red squares, see eq. (8.16)), and with intracavity control fields in the "warm" situation, where longitdudinal effects average out (blue circles, see eq. (8.25)) and in the "cold" situation, where the atoms are well localized in the standing wave (green diamonds, see eq. (D.1)).

uniform control field Raby frequency, see eq. (8.16) (dashed dotted line), for the ”warm” situation with an intracavity control field, where longitudinal effects average out, see eq. (8.25) (solid line) and for the ”cold” case with ions that are well-localized within the standing wave field of probe and control, see eq. (D.1) (dashed line). The half width of the three curves are obtained for $a \simeq 1$, $a \simeq 2.51$ and $a \simeq 1.83$ respectively.

To check the validity of the ”warm” model that was used throughout ch. 8 and ch. 9 we carefully analysed the data presented in sec. 8.4.2 using the three different models and comparing the Rabi frequencies deduced from the fits, to the theoretically expected values. The results are shown in fig. D.2, and we find excellent agreement with the experimental data for the ”warm” model, whereas the Rabi frequencies found for the two other models are systematically too low.

Bibliography

[1] C. Cohen-Tannoudji, J. Dupont-Roc, G. Grynberg, *Atom-Photon Interactions: Basic Processes and Applications*, Wiley-Interscience, 1992.

[2] M. Nielsen, I. Chuang, *Quantum Computation and Quantum Information*, Cambridge Univ. Press, Cambridge, 2000.

[3] W. K. Wootters, W. H. Zurek, *A single quantum cannot be cloned*, Nature **299** (1982) 802–803.
URL http://dx.doi.org/10.1038/299802a0

[4] D. Dieks, *Communication by EPR devices*, Phys. Lett. A **92** (1982) 271–272.
URL http://dx.doi.org/10.1016/0375-9601(82)90084-6

[5] N. Gisin, G. Ribordy, W. Tittel, H. Zbinden, *Quantum cryptography*, Rev. Mod. Phys **74** (2002) 145–195.
URL http://dx.doi.org/10.1103/RevModPhys.74.145

[6] D. Deutsch, R. Jozsa, *Rapid Solution of Problems by Quantum Computation*, Proc. R. Soc. London, Ser. A **439** (1992) 553–558.
URL http://dx.doi.org/10.2307/52182

[7] L. K. Grover, *A fast quantum mechanical algorithm for database search*, in: Proceedings, 28th Annual ACM Symposium on the Theory of Computing, 1996, pp. 212–219.
URL http://arxiv.org/abs/quant-ph/9605043v3

[8] P. W. Shor, *Polynomial-Time Algorithms for Prime Factorization and Discrete Logarithms on a Quantum Computer*, SIAM Review **41** (1999) 303–332.
URL http://link.aip.org/link/?SIR/41/303

[9] J. I. Cirac, P. Zoller, H. J. Kimble, H. Mabuchi, *Quantum State Transfer and Entanglement Distribution among Distant Nodes in a Quantum Network*, Phys. Rev. Lett. **78** (1997) 3221–3224.
URL http://dx.doi.org/10.1103/PhysRevLett.78.3221

[10] L. M. Duan, M. D. Lukin, J. I. Cirac, P. Zoller, *Long-distance quantum communication with atomic ensembles and linear optics*, Nature **414** (2001) 413–418.
URL http://dx.doi.org/10.1038/35106500

[11] N. A. Gershenfeld, I. L. Chuang, *Bulk Spin-Resonance Quantum Computation*, Science **275** (1997) 350–356.
URL http://dx.doi.org/10.1126/science.275.5298.350

[12] Y. Makhlin, G. Schön, A. Shnirman, *Quantum-state engineering with Josephson-junction devices*, Rev. Mod. Phys **73** (2001) 357–400.
URL http://dx.doi.org/10.1103/RevModPhys.73.357

[13] D. Loss, D. P. DiVincenzo, *Quantum computation with quantum dots*, Phys. Rev. A **57** (1998) 120–126.
URL http://dx.doi.org/10.1103/PhysRevA.57.120

[14] Briegel, T. Calarco, D. Jaksch, J. I. Cirac, P. Zoller, *Quantum computing with neutral atoms*, J. Mod. Opt. **47** (2000) 415–451.
URL http://dx.doi.org/10.1080/09500340008244052

[15] E. Knill, R. Laflamme, G. J. Milburn, *A scheme for efficient quantum computation with linear optics*, Nature **409** (2001) 46–52.
URL http://dx.doi.org/10.1038/35051009

[16] J. I. Cirac, P. Zoller, *Quantum Computations with Cold Trapped Ions*, Phys. Rev. Lett. **74** (1995) 4091–4094.
URL http://dx.doi.org/10.1103/PhysRevLett.74.4091

[17] A. Sørensen, K. Mølmer, *Quantum Computation with Ions in Thermal Motion*, Phys. Rev. Lett. **82** (1999) 1971–1974.
URL http://dx.doi.org/10.1103/PhysRevLett.82.1971

[18] D. Leibfried, R. Blatt, C. Monroe, D. Wineland, *Quantum dynamics of single trapped ions*, Rev. Mod. Phys **75** (2003) 281–324.
URL http://dx.doi.org/10.1103/RevModPhys.75.281

[19] H. Haffner, C. Roos, R. Blatt, *Quantum computing with trapped ions*, Phys. Rep. **469** (2008) 155–203.
URL http://dx.doi.org/10.1016/j.physrep.2008.09.003

[20] F. Diedrich, J. C. Bergquist, W. M. Itano, D. J. Wineland, *Laser Cooling to the Zero-Point Energy of Motion*, Phys. Rev. Lett. **62** (1989) 403–406.
URL http://dx.doi.org/10.1103/PhysRevLett.62.403

[21] C. Monroe, D. M. Meekhof, B. E. King, W. M. Itano, D. J. Wineland, *Demonstration of a Fundamental Quantum Logic Gate*, Phys. Rev. Lett. **75** (1995) 4714–4717.
URL http://dx.doi.org/10.1103/PhysRevLett.75.4714

[22] F. Schmidt-Kaler, H. Haffner, M. Riebe, S. Gulde, G. P. Lancaster, T. Deuschle, C. Becher, C. F. Roos, J. Eschner, R. Blatt, *Realization of the Cirac-Zoller controlled-NOT quantum gate*, Nature **422** (2003) 408–411.
URL http://dx.doi.org/10.1038/nature01494

[23] D. Leibfried, B. Demarco, V. Meyer, D. Lucas, M. Barrett, J. Britton, W. M. Itano, B. Jelenkovic, C. Langer, T. Rosenband, D. J. Wineland, *Experimental demonstration of a robust, high-fidelity geometric two ion-qubit phase gate*, Nature **422** (2003) 412–415.
URL http://dx.doi.org/10.1038/nature01492

[24] J. Benhelm, G. Kirchmair, C. F. Roos, R. Blatt, *Towards fault-tolerant quantum computing with trapped ions*, Nature Phys. **4** (2008) 463–466.
URL http://dx.doi.org/10.1038/nphys961

[25] D. Leibfried, E. Knill, S. Seidelin, J. Britton, R. B. Blakestad, J. Chiaverini, D. B. Hume, W. M. Itano, J. D. Jost, C. Langer, R. Ozeri, R. Reichle, D. J. Wineland, *Creation of a six-atom 'Schrödinger cat' state*, Nature **438** (2005) 639–642.
URL http://dx.doi.org/10.1038/nature04251

[26] H. Häffner, W. Hänsel, C. F. Roos, J. Benhelm, D. Chek-Al-Kar, M. Chwalla, T. Körber, U. D. Rapol, M. Riebe, P. O. Schmidt, C. Becher, O. Gühne, W. Dür, R. Blatt, *Scalable multiparticle entanglement of trapped ions*, Nature **438** (2005) 643–646.
URL http://dx.doi.org/10.1038/nature04279

[27] S. Gulde, M. Riebe, G. P. Lancaster, C. Becher, J. Eschner, H. Haffner, F. Schmidt-Kaler, I. L. Chuang, R. Blatt, *Implementation of the Deutsch-Jozsa algorithm on an ion-trap quantum computer*, Nature **421** (2003) 48–50.
URL http://dx.doi.org/10.1038/nature01336

[28] J. Chiaverini, J. Britton, D. Leibfried, E. Knill, M. D. Barrett, R. B. Blakestad, W. M. Itano, J. D. Jost, C. Langer, R. Ozeri, T. Schaetz, D. J. Wineland, *Implementation of the Semiclassical Quantum Fourier Transform in a Scalable System*, Science **308** (2005) 997–1000.
URL http://dx.doi.org/10.1126/science.1110335

[29] M. D. Barrett, J. Chiaverini, T. Schaetz, J. Britton, W. M. Itano, J. D. Jost, E. Knill, C. Langer, D. Leibfried, R. Ozeri, D. J. Wineland, *Deterministic quantum teleportation of atomic qubits*, Nature **429** (2004) 737–739.
URL http://dx.doi.org/10.1038/nature02608

[30] M. Riebe, H. Haffner, C. F. Roos, W. Hansel, J. Benhelm, G. P. T. Lancaster, T. W. Korber, C. Becher, F. Schmidt-Kaler, D. F. V. James, R. Blatt, *Deterministic quantum teleportation with atoms*, Nature **429** (2004) 734–737.
URL http://dx.doi.org/10.1038/nature02570

[31] S. A. Diddams, T. Udem, J. C. Bergquist, E. A. Curtis, R. E. Drullinger, L. Hollberg, W. M. Itano, W. D. Lee, C. W. Oates, K. R. Vogel, D. J. Wineland, *An Optical Clock Based on a Single Trapped* $^{199}Hg^{+}$ *Ion*, Science **293** (2001) 825–828.
URL http://dx.doi.org/10.1126/science.1061171

[32] H. S. Margolis, G. P. Barwood, G. Huang, H. A. Klein, S. N. Lea, K. Szymaniec, P. Gill, *Hertz-Level Measurement of the Optical Clock Frequency in a Single* $^{88}Sr^{+}$ *Ion*, Science **306** (2004) 1355–1358.
URL http://dx.doi.org/10.1126/science.1105497

[33] T. Rosenband, P. O. Schmidt, D. B. Hume, W. M. Itano, T. M. Fortier, J. E. Stalnaker, K. Kim, S. A. Diddams, J. C. J. Koelemeij, J. C. Bergquist, D. J. Wineland, *Observation of the* $^1S_0 \rightarrow ^3P_0$ *Clock Transition in* $^{27}Al^{+}$, Phys. Rev. Lett. **98** (2007) 220801+.
URL http://dx.doi.org/10.1103/PhysRevLett.98.220801

[34] T. Rosenband, D. B. Hume, P. O. Schmidt, C. W. Chou, A. Brusch, L. Lorini, W. H. Oskay, R. E. Drullinger, T. M. Fortier, J. E. Stalnaker, S. A. Diddams, W. C. Swann, N. R. Newbury, W. M. Itano, D. J. Wineland, J. C. Bergquist, *Frequency Ratio of Al+ and Hg+ Single-Ion Optical Clocks; Metrology at the 17th Decimal Place*, Science **319** (2008) 1808–1812.
URL http://dx.doi.org/10.1126/science.1154622

[35] A. Friedenauer, H. Schmitz, J. T. Glueckert, D. Porras, T. Schaetz, *Simulating a quantum magnet with trapped ions*, Nature Phys. **4** (2008) 757–761.
URL http://dx.doi.org/10.1038/nphys1032

[36] R. Gerritsma, G. Kirchmair, F. Zahringer, E. Solano, R. Blatt, C. F. Roos, *Quantum simulation of the Dirac equation*, Nature **463** (2010) 68–71.
URL http://dx.doi.org/10.1038/nature08688

[37] D. Kielpinski, C. Monroe, D. J. Wineland, *Architecture for a large-scale ion-trap quantum computer*, Nature **417** (2002) 709–711.
URL http://dx.doi.org/10.1038/nature00784

[38] H. J. Kimble, *The quantum internet*, Nature **453** (2008) 1023–1030.
URL http://dx.doi.org/10.1038/nature07127

[39] A. I. Lvovsky, B. C. Sanders, W. Tittel, *Optical quantum memory*, Nature Photonics **3** (2009) 706–714.
URL http://dx.doi.org/10.1038/nphoton.2009.231

[40] C. W. Chou, H. de Riedmatten, D. Felinto, S. V. Polyakov, S. J. van Enk, H. J. Kimble, *Measurement-induced entanglement for excitation stored in remote atomic ensembles*, Nature **438** (2005) 828–832.
URL http://dx.doi.org/10.1038/nature04353

[41] T. Chaneliere, D. N. Matsukevich, S. D. Jenkins, S. Y. Lan, T. A. B. Kennedy, A. Kuzmich, *Storage and retrieval of single photons transmitted between remote quantum memories*, Nature **438** (2005) 833–836.
URL http://dx.doi.org/10.1038/nature04315

[42] M. D. Eisaman, A. Andre, F. Massou, M. Fleischhauer, A. S. Zibrov, M. D. Lukin, *Electromagnetically induced transparency with tunable single-photon pulses*, Nature **438** (2005) 837–841.
URL http://dx.doi.org/10.1038/nature04327

[43] B. Zhao, Y.-A. Chen, X.-H. Bao, T. Strassel, C.-S. Chuu, X.-M. Jin, J. Schmiedmayer, Z.-S. Yuan, S. Chen, J.-W. Pan, *A millisecond quantum memory for scalable quantum networks*, Nature Phys. **5** (2009) 95–99.
URL http://dx.doi.org/10.1038/nphys1153

[44] R. Zhao, Y. O. Dudin, S. D. Jenkins, C. J. Campbell, D. N. Matsukevich, T. A. B. Kennedy, A. Kuzmich, *Long-lived quantum memory*, Nature Phys. **5** (2009) 100–104.
URL http://dx.doi.org/10.1038/nphys1152

[45] K. Honda, D. Akamatsu, M. Arikawa, Y. Yokoi, K. Akiba, S. Nagatsuka, T. Tanimura, A. Furusawa, M. Kozuma, *Storage and Retrieval of a Squeezed Vacuum*, Phys. Rev. Lett. **100** (2008) 093601+.
URL http://dx.doi.org/10.1103/PhysRevLett.100.093601

[46] J. Appel, E. Figueroa, D. Korystov, M. Lobino, A. I. Lvovsky, *Quantum Memory for Squeezed Light*, Phys. Rev. Lett. **100** (2008) 093602+.
URL http://dx.doi.org/10.1103/PhysRevLett.100.093602

[47] K. S. Choi, H. Deng, J. Laurat, H. J. Kimble, *Mapping photonic entanglement into and out of a quantum memory*, Nature **452** (2008) 67–71.
URL http://dx.doi.org/10.1038/nature06670

[48] H. de Riedmatten, M. Afzelius, M. U. Staudt, C. Simon, N. Gisin, *A solid-state light-matter interface at the single-photon level*, Nature **456** (2008) 773–777.
URL http://dx.doi.org/10.1038/nature07607

[49] J. J. Longdell, E. Fraval, M. J. Sellars, N. B. Manson, *Stopped Light with Storage Times Greater than One Second Using Electromagnetically Induced Transparency in a Solid*, Phys. Rev. Lett. **95** (2005) 063601+.
URL http://dx.doi.org/10.1103/PhysRevLett.95.063601

[50] C. Clausen, I. Usmani, F. Bussieres, N. Sangouard, M. Afzelius, H. de Riedmatten, N. Gisin, *Quantum Storage of Photonic Entanglement in a Crystal*, arXiv:1009.0489 (2010).
URL http://arxiv.org/abs/1009.0489

[51] E. Saglamyurek, N. Sinclair, J. Jin, J. A. Slater, D. Oblak, F. Bussieres, M. George, R. Ricken, W. Sohler, W. Tittel, *Broadband waveguide quantum memory for entangled photons*, arXiv:1009.0490 (2010).
URL http://arxiv.org/abs/1009.0490

[52] M. P. Hedges, J. J. Longdell, Y. Li, M. J. Sellars, *Efficient quantum memory for light*, Nature **465** (2010) 1052–1056.
URL http://dx.doi.org/10.1038/nature09081

[53] T. Chanelière, J. Ruggiero, M. Bonarota, M. Afzelius, J. L. Le Gouët, *Efficient light storage in a crystal using an atomic frequency comb*, New J. Phys. **12** (2010) 023025+.
URL http://dx.doi.org/10.1088/1367-2630/12/2/023025

[54] M. Afzelius, C. Simon, H. de Riedmatten, N. Gisin, *Multimode quantum memory based on atomic frequency combs*, Phys. Rev. A **79** (2009) 052329+.
URL http://dx.doi.org/10.1103/PhysRevA.79.052329

[55] M. Fleischhauer, S. F. Yelin, M. D. Lukin, *How to trap photons? Storing single-photon quantum states in collective atomic excitations*, Opt. Commun. **179** (2000) 395–410.
URL http://dx.doi.org/10.1016/S0030-4018(99)00679-3

[56] A. Dantan, M. Pinard, *Quantum-state transfer between fields and atoms in electromagnetically induced transparency*, Phys. Rev. A **69** (2004) 043810+.
URL http://dx.doi.org/10.1103/PhysRevA.69.043810

[57] A. V. Gorshkov, A. André, M. D. Lukin, A. S. Sørensen, *Photon storage in Lambda-type optically dense atomic media. I. Cavity model*, Phys. Rev. A **76** (2007) 033804.
URL http://dx.doi.org/10.1103/PhysRevA.76.033804

[58] S. Haroche, J.-M. Raimond, *Exploring the Quantum: Atoms, Cavities, and Photons*, Oxford Graduate Texts, Oxford University Press, USA, 2006.

[59] P. R. Berman (Ed.), *Cavity Quantum Electrodynamics*, Academic Press London, 1994.

[60] Y. Kaluzny, P. Goy, M. Gross, J. M. Raimond, S. Haroche, *Observation of Self-Induced Rabi Oscillations in Two-Level Atoms Excited Inside a Resonant Cavity: The Ringing Regime of Superradiance*, Phys. Rev. Lett. **51** (1983) 1175–1178.
URL 10.1103/PhysRevLett.51.1175

[61] R. J. Thompson, G. Rempe, H. J. Kimble, *Observation of normal-mode splitting for an atom in an optical cavity*, Phys. Rev. Lett. **68** (1992) 1132–1135.
URL http://dx.doi.org/10.1103/PhysRevLett.68.1132

[62] A. Lambrecht, T. Coudreau, A. M. Steinberg, E. Giacobino, *Squeezing with cold atoms*, Europhys. Lett. **36** (1996) 93–98.
URL http://dx.doi.org/10.1209/epl/i1996-00192-1

[63] B. Nagorny, Th, A. Hemmerich, *Collective Atomic Motion in an Optical Lattice Formed Inside a High Finesse Cavity*, Phys. Rev. Lett. **91** (2003) 153003+.
URL http://dx.doi.org/10.1103/PhysRevLett.91.153003

[64] H. W. Chan, A. T. Black, V. Vuletić, *Observation of Collective-Emission-Induced Cooling of Atoms in an Optical Cavity*, Phys. Rev. Lett. **90** (2003) 063003+.
URL http://dx.doi.org/10.1103/PhysRevLett.90.063003

[65] D. Kruse, C. von Cube, C. Zimmermann, Ph, *Observation of Lasing Mediated by Collective Atomic Recoil*, Phys. Rev. Lett. **91** (2003) 183601+.
URL http://dx.doi.org/10.1103/PhysRevLett.91.183601

[66] F. Brennecke, T. Donner, S. Ritter, T. Bourdel, M. Kohl, T. Esslinger, *Cavity QED with a Bose-Einstein condensate*, Nature **450** (2007) 268–271.
URL http://dx.doi.org/10.1038/nature06120

[67] Y. Colombe, T. Steinmetz, G. Dubois, F. Linke, D. Hunger, J. Reichel, *Strong atom-field coupling for Bose-Einstein condensates in an optical cavity on a chip*, Nature **450** (2007) 272–276.
URL http://dx.doi.org/10.1038/nature06331

[68] G. R. Guthohrlein, M. Keller, K. Hayasaka, W. Lange, H. Walther, *A single ion as a nanoscopic probe of an optical field*, Nature **414** (2001) 49–51.
URL http://dx.doi.org/10.1038/35102129

[69] M. Keller, B. Lange, K. Hayasaka, W. Lange, H. Walther, *Continuous generation of single photons with controlled waveform in an ion-trap cavity system*, Nature **431** (2004) 1075–1078.
URL http://dx.doi.org/10.1038/nature02961

[70] A. B. Mundt, A. Kreuter, C. Becher, D. Leibfried, J. Eschner, S. F. Kaler, R. Blatt, *Coupling a Single Atomic Quantum Bit to a High Finesse Optical Cavity*, Phys. Rev. Lett. **89** (2002) 103001+.
URL http://dx.doi.org/10.1103/PhysRevLett.89.103001

[71] A. Kreuter, C. Becher, G. P. T. Lancaster, A. B. Mundt, C. Russo, H. Häffner, C. Roos, J. Eschner, S. F. Kaler, R. Blatt, *Spontaneous Emission Lifetime of a Single Trapped* Ca^+ *Ion in a High Finesse Cavity*, Phys. Rev. Lett. **92** (2004) 203002.
URL http://dx.doi.org/10.1103/PhysRevLett.92.203002

[72] D. R. Leibrandt, J. Labaziewicz, V. Vuletić, I. L. Chuang, *Cavity Sideband Cooling of a Single Trapped Ion*, Phys. Rev. Lett. **103** (2009) 103001+.
URL http://dx.doi.org/10.1103/PhysRevLett.103.103001

[73] H. G. Barros, A. Stute, T. E. Northup, C. Russo, P. O. Schmidt, R. Blatt, *Deterministic single-photon source from a single ion*, New J. Phys. **11** (2009) 103004+.
URL http://dx.doi.org/10.1088/1367-2630/11/10/103004

[74] F. Dubin, C. Russo, H. G. Barros, A. Stute, C. Becher, P. O. Schmidt, R. Blatt, *Quantum to classical transition in a single-ion laser*, Nature Phys. **6** (2010) 350–353.
URL http://dx.doi.org/10.1038/nphys1627

[75] F. Diedrich, E. Peik, J. M. Chen, W. Quint, H. Walther, *Observation of a Phase Transition of Stored Laser-Cooled Ions*, Phys. Rev. Lett. **59** (1987) 2931–2934.
URL http://dx.doi.org/10.1103/PhysRevLett.59.2931

[76] D. J. Wineland, J. C. Bergquist, W. M. Itano, J. J. Bollinger, C. H. Manney, *Atomic-Ion Coulomb Clusters in an Ion Trap*, Phys. Rev. Lett. **59** (1987) 2935–2938.

[77] S. L. Gilbert, J. J. Bollinger, D. J. Wineland, *Shell-Structure Phase of Magnetically Confined Strongly Coupled Plasmas*, Phys. Rev. Lett. **60** (1988) 2022–2025.
URL http://dx.doi.org/10.1103/PhysRevLett.60.2022

[78] M. Drewsen, C. Brodersen, L. Hornekær, J. S. Hangst, J. P. Schiffer, *Large Ion Crystals in a Linear Paul Trap*, Phys. Rev. Lett. **81** (1998) 2878–2881.
URL http://dx.doi.org/10.1103/PhysRevLett.81.2878

[79] P. F. Herskind, A. Dantan, J. P. Marler, M. Albert, M. Drewsen, *Realization of collective strong coupling with ion Coulomb crystals in an optical cavity*, Nature Phys. **5** (2009) 494–498.
URL http://dx.doi.org/10.1038/nphys1302

[80] P. Herskind, *Cavity Quantum Electrodynamics with Ion Coulomb Crystals*, Ph.D. thesis, Danish National Research Foundation Center for Quantum Optics - QUANTOP, Department of Physics and Astronomy, The University of Aarhus (2008).

[81] A. Dantan, M. Albert, J. P. Marler, P. F. Herskind, M. Drewsen, *Large ion Coulomb crystals: A near-ideal medium for coupling optical cavity modes to matter*, Phys. Rev. A **80** (2009) 041802+.
URL http://dx.doi.org/10.1103/PhysRevA.80.041802

[82] D. H. E. Dubin, *Theory of electrostatic fluid modes in a cold spheroidal non-neutral plasma*, Phys. Rev. Lett. **66** (1991) 2076–2079.
URL http://dx.doi.org/10.1103/PhysRevLett.66.2076

[83] S. E. Harris, *Electromagnetically Induced Transparency*, Phys. Today **50** (1997) 36–42.
URL http://dx.doi.org/10.1063/1.881806

[84] M. Fleischhauer, A. Imamoglu, J. P. Marangos, *Electromagnetically induced transparency: Optics in coherent media*, Rev. Mod. Phys **77** (2005) 633–673.
URL http://dx.doi.org/10.1103/RevModPhys.77.633

[85] K. J. Boller, A. Imamoglu, S. E. Harris, *Observation of electromagnetically induced transparency*, Phys. Rev. Lett. **66** (1991) 2593–2596.
URL http://dx.doi.org/10.1103/PhysRevLett.66.2593

[86] L. V. Hau, S. E. Harris, Z. Dutton, C. H. Behroozi, *Light speed reduction to 17 metres per second in an ultracold atomic gas*, Nature **397** (1999) 594–598.
URL http://dx.doi.org/10.1038/17561

[87] M. M. Kash, V. A. Sautenkov, A. S. Zibrov, L. Hollberg, G. R. Welch, M. D. Lukin, Y. Rostovtsev, E. S. Fry, M. O. Scully, *Ultraslow Group Velocity and Enhanced Nonlinear Optical Effects in a Coherently Driven Hot Atomic Gas*, Phys. Rev. Lett. **82** (1999) 5229–5232.
URL http://dx.doi.org/10.1103/PhysRevLett.82.5229

[88] C. Liu, Z. Dutton, C. H. Behroozi, L. V. Hau, *Observation of coherent optical information storage in an atomic medium using halted light pulses*, Nature **409** (2001) 490–493.
URL http://dx.doi.org/10.1038/35054017

[89] D. F. Phillips, A. Fleischhauer, A. Mair, R. L. Walsworth, M. D. Lukin, *Storage of Light in Atomic Vapor*, Phys. Rev. Lett. **86** (2001) 783–786.
URL http://dx.doi.org/10.1103/PhysRevLett.86.783

[90] M. D. Lukin, A. Imamoglu, *Controlling photons using electromagnetically induced transparency*, Nature **413** (2001) 273–276.
URL http://dx.doi.org/10.1038/35095000

[91] M. D. Lukin, *Colloquium: Trapping and manipulating photon states in atomic ensembles*, Rev. Mod. Phys **75** (2003) 457–472.
URL http://dx.doi.org/10.1103/RevModPhys.75.457

[92] G. Hernandez, J. Zhang, Y. Zhu, *Vacuum Rabi splitting and intracavity dark state in a cavity-atom system*, Phys. Rev. A **76** (2007) 053814+.
URL http://dx.doi.org/10.1103/PhysRevA.76.053814

[93] H. Wu, J. G. Banacloche, M. Xiao, *Observation of Intracavity Electromagnetically Induced Transparency and Polariton Resonances in a Doppler-Broadened Medium*, Phys. Rev. Lett. **100** (2008) 173602+.
URL http://dx.doi.org/10.1103/PhysRevLett.100.173602

[94] M. Mucke, E. Figueroa, J. Bochmann, C. Hahn, K. Murr, S. Ritter, C. J. Villas-Boas, G. Rempe, *Electromagnetically induced transparency with single atoms in a cavity*, Nature **465** (2010) 755–758.
URL http://dx.doi.org/10.1038/nature09093

[95] T. Kampschulte, W. Alt, S. Brakhane, M. Eckstein, R. Reimann, A. Widera, D. Meschede, *Optical Control of the Refractive Index of a Single Atom*, Phys. Rev. Lett. **105** (2010) 153603+.
URL http://dx.doi.org/10.1103/PhysRevLett.105.153603

[96] J. Simon, H. Tanji, J. K. Thompson, V. Vuletić, *Interfacing Collective Atomic Excitations and Single Photons*, Phys. Rev. Lett. **98** (2007) 183601+.
URL http://dx.doi.org/10.1103/PhysRevLett.98.183601

[97] J. Simon, H. Tanji, S. Ghosh, V. Vuletic, *Single-photon bus connecting spin-wave quantum memories*, Nature Phys. **3** (2007) 765–769.
URL http://dx.doi.org/10.1038/nphys726

[98] H. Schmidt, A. Imamoglu, *Giant Kerr nonlinearities obtained by electromagnetically induced transparency*, Opt. Lett. **21** (1996) 1936–1938.
URL http://dx.doi.org/10.1364/OL.21.001936

[99] A. Imamoglu, H. Schmidt, G. Woods, M. Deutsch, *Strongly Interacting Photons in a Nonlinear Cavity*, Phys. Rev. Lett. **79** (1997) 1467–1470.
URL http://dx.doi.org/10.1103/PhysRevLett.79.1467

[100] P. Grangier, D. F. Walls, K. M. Gheri, *Comment on "Strongly Interacting Photons in a Nonlinear Cavity"*, Phys. Rev. Lett. **81** (1998) 2833+.
URL http://dx.doi.org/10.1103/PhysRevLett.81.2833

[101] W. Paul, *Electromagnetic traps for charged and neutral particles*, Forschungsberichte des Wirtschaftsministeriums Nordrhein-Westfalen **415** (1958) x.

[102] W. Paul, *Electromagnetic traps for charged and neutral particles*, Rev. Mod. Phys. **62** (1990) 531–540.

[103] M. Drewsen, A. Brøner, *Harmonic linear Paul trap: Stability diagram and effective potentials*, Phys. Rev. A **62** (2000) 045401+.
URL http://dx.doi.org/10.1103/PhysRevA.62.045401

[104] NIST, *Atomic Spectroscopy Database*, http://www.nist.gov/pml/data/asd.cfm (November 2010).
URL http://www.nist.gov/pml/data/asd.cfm

[105] P. A. Barton, C. J. S. Donald, D. M. Lucas, D. A. Stevens, A. M. Steane, D. N. Stacey, *Measurement of the lifetime of the* $3d^2D_{5/2}$ *state in* $^{40}Ca^+$, Phys. Rev. A **62** (2000) 032503+.
URL http://dx.doi.org/10.1103/PhysRevA.62.032503

[106] D. F. V. James, *Quantum dynamics of cold trapped ions with application to quantum computation*, Appl. Phys. B **66** (1998) 181–190.

[107] W. D. Phillips, *Nobel Lecture: Laser cooling and trapping of neutral atoms*, Rev. Mod. Phys **70** (1998) 721–741.
URL http://dx.doi.org/10.1103/RevModPhys.70.721

[108] H. J. Metcalf, P. van Straten, *Laser cooling and trapping*, Springer, New York; Berlin; Heidelberg, 1999.

[109] Eschner, Jürgen and Morigi, Giovanna and Schmidt-Kaler, Ferdinand and Blatt, Rainer, *Laser cooling of trapped ions*, J. Opt. Soc. Am. B **20** (2003) 1003–1015.
URL http://dx.doi.org/10.1364/JOSAB.20.001003

[110] J. I. Cirac, L. J. Garay, R. Blatt, A. S. Parkins, P. Zoller, *Laser cooling of trapped ions: The influence of micromotion*, Phys. Rev. A **49** (1994) 421–432.
URL http://dx.doi.org/10.1103/PhysRevA.49.421

[111] L. Turner, *Collective Effects on Equilibria of Trapped Charged Plasmas*, Phys. Fluids **30** (1987) 3196–3203.
URL http://dx.doi.org/10.1063/1.866495

[112] R. C. Davidson, *Physics of nonneutral plasmas*, Imperial College Press, London, 2001.

[113] J. P. Hansen, *Statistical Mechanics of Dense Ionized Matter. I. Equilibrium Properties of the Classical One-Component Plasma*, Phys. Rev. A **8** (1973) 3096–3109.
URL http://dx.doi.org/10.1103/PhysRevA.8.3096

[114] E. L. Pollock, J. P. Hansen, *Statistical Mechanics of Dense Ionized Matter. II. Equilibrium Properties and Melting Transition of the Crystallized One-Component Plasma*, Phys. Rev. A **8** (1973) 3110–3122.
URL http://dx.doi.org/10.1103/PhysRevA.8.3110

[115] W. L. Slattery, G. D. Doolen, H. E. DeWitt, *Improved equation of state for the classical one-component plasma*, Phys. Rev. A **21** (1980) 2087–2095.
URL http://dx.doi.org/10.1103/PhysRevA.21.2087

[116] R. F. Wuerker, H. Shelton, R. V. Langmuir, *Electrodynamic Containment of Charged Particles*, J. Appl. Phys. **30** (1959) 342+.
URL http://dx.doi.org/10.1063/1.1735165

[117] R. Hasse, J. Schiffer, *The structure of the cylindrically confined Coulomb lattice*, Ann. Phys. **203** (1990) 419–448.
URL http://dx.doi.org/10.1016/0003-4916(90)90177-P

[118] L. Hornekær, N. Kjærgaard, A. M. Thommesen, M. Drewsen, *Structural Properties of Two-Component Coulomb Crystals in Linear Paul Traps*, Phys. Rev. Lett. **86** (2001) 1994–1997.
URL 10.1103/PhysRevLett.86.1994

[119] P. F. Herskind, A. Dantan, M. Albert, J. P. Marler, M. Drewsen, *Positioning of the rf potential minimum line of a linear Paul trap with micrometer precision*, J. Phys. B **42** (2009) 154008+.
URL http://dx.doi.org/10.1088/0953-4075/42/15/154008

[120] P. Herskind, A. Dantan, M. Langkilde-Lauesen, A. Mortensen, J. Sørensen, M. Drewsen, *Loading of large ion Coulomb crystals into a linear Paul trap incorporating an optical cavity*, Appl. Phys. B: Lasers Opt. **93** (2008) 373–379.
URL http://dx.doi.org/10.1007/s00340-008-3199-8

[121] A. Mortensen, E. Nielsen, T. Matthey, M. Drewsen, *Observation of Three-Dimensional Long-Range Order in Small Ion Coulomb Crystals in an rf Trap*, Phys. Rev. Lett. **96** (2006) 103001+.
URL http://dx.doi.org/10.1103/PhysRevLett.96.103001

[122] H. Kogelnik, T. Li, *Laser Beams and Resonators*, Appl. Opt. **5** (1966) 1550–1567.
URL http://dx.doi.org/10.1364/AO.5.001550

[123] B. E. A. Saleh, M. C. Teich, *Fundamentals of Photonics*, John Wiley & Sons, Inc., New York [u.a.], 1991.

[124] D. Meschede, *Optics, Light and Lasers*, WILEY-VCH Weinheim, 2004.

[125] H. Mabuchi, A. C. Doherty, *Cavity Quantum Electrodynamics: Coherence in Context*, Science **298** (2002) 1372–1377.

[126] M. Scully, M. Zubairy, *Quantum Optics*, Cambridge University Press, Cambridge, U.K.; New York, U.S.A., 1997.

[127] E. Purcell, *Spontaneous Emission Probabilities at Radio Frequencies*, Phys. Rev. **69** (1946) 681.

[128] C. J. Hood, M. S. Chapman, T. W. Lynn, H. J. Kimble, *Real-Time Cavity QED with Single Atoms*, Phys. Rev. Lett. **80** (1998) 4157–4160.
URL 10.1103/PhysRevLett.80.4157

[129] A. Boca, R. Miller, K. M. Birnbaum, A. D. Boozer, J. McKeever, H. J. Kimble, *Observation of the Vacuum Rabi Spectrum for One Trapped Atom*, Phys. Rev. Lett. **93** (2004) 233603.
URL 10.1103/PhysRevLett.93.233603

[130] J. Ye, D. W. Vernooy, H. J. Kimble, *Trapping of Single Atoms in Cavity QED*, Phys. Rev. Lett. **83** (1999) 4987–4990.
URL http://dx.doi.org/10.1103/PhysRevLett.83.4987

[131] P. Maunz, T. Puppe, I. Schuster, N. Syassen, P. W. H. Pinkse, G. Rempe, *Normal-Mode Spectroscopy of a Single-Bound-Atom Cavity System*, Phys. Rev. Lett. **94** (2005) 033002.
URL 10.1103/PhysRevLett.94.033002

[132] A. Wallraff, D. I. Schuster, A. Blais, L. Frunzio, Huang, J. Majer, S. Kumar, S. M. Girvin, R. J. Schoelkopf, *Strong coupling of a single photon to a superconducting qubit using circuit quantum electrodynamics*, Nature **431** (2004) 162–167.
URL http://dx.doi.org/10.1038/nature02851

[133] G. Khitrova, H. M. Gibbs, M. Kira, S. W. Koch, A. Scherer, *Vacuum Rabi splitting in semiconductors*, Nature Phys. **2** (2006) 81–90.
URL http://dx.doi.org/10.1038/nphys227

[134] B. W. Shore, P. L. Knight, *The Jaynes-Cummings Model*, J. Mod. Opt. **40** (1993) 1195–1238.
URL http://dx.doi.org/10.1080/09500349314551321

[135] R. J. Brecha, L. A. Orozco, M. G. Raizen, M. Xiao, H. J. Kimble, *Observation of oscillatory energy exchange in a coupled-atom-cavity system*, J. Opt. Soc. Am. B **12** (1995) 2329–2339.
URL http://dx.doi.org/10.1364/JOSAB.12.002329

[136] P. W. Milonni, J. H. Eberly, *Lasers*, John Wiley & Sons, New York, 1988.

[137] A. Mortensen, *Aspects of Ion Coulomb Crystal based Quantum Memory for Light*, Ph.D. thesis, Danish National Research Foundation Center for Quantum Optics - QUANTOP, Department of Physics and Astronomy, The University of Aarhus (2005).

[138] E. Black, *An introduction to Pound-Drever-Hall laser frequency stabilization*, Am. J. Phys. **69** (2001) 79–87.

[139] F. K. Jensen, *Laser Frequency Stabilization for use in STIRAP Experiments*, Master's thesis, Department of Physics and Astronomy, The University of Aarhus (2004).

[140] W. Happer, *Optical-Pumping*, Rev. Mod. Phys. **44** (1972) 169–249.

[141] A. Mortensen, E. Nielsen, T. Matthey, M. Drewsen, *Radio frequency field-induced persistent long-range ordered structures in two-species ion Coulomb crystals*, J. Phys. B **40** (2007) F223–F229.
URL http://dx.doi.org/10.1088/0953-4075/40/15/F01

[142] A. Mortensen, J. J. T. Lindballe, I. S. Jensen, P. Staanum, D. Voigt, M. Drewsen, *Isotope shifts of the* $4s^2\,{}^1S_0 \rightarrow 4s5p\,{}^1P_1$ *transition and hyperfine splitting of the* $4s5p\,{}^1P_1$ *state in calcium*, Phys. Rev. A **69** (2004) 042502+.
URL http://dx.doi.org/10.1103/PhysRevA.69.042502

[143] P. Herskind, J. Lindballe, C. Clausen, J. L. Sorensen, M. Drewsen, *Second-harmonic generation of light at 544 and 272 nm from an ytterbium-doped distributed-feedback fiber laser*, Opt. Lett. **32** (2007) 268–270.

[144] G. Rempe, R. J. Thompson, H. J. Kimble, *Cavity quantum electrodynamics with strong coupling in the optical domain*, Phys. Scr. **1994** (1994) 67–77.
URL http://dx.doi.org/10.1088/0031-8949/1994/T51/009

[145] M. Brune, F. Schmidt-Kaler, A. Maali, J. Dreyer, E. Hagley, J. M. Raimond, S. Haroche, *Quantum Rabi Oscillation: A Direct Test of Field Quantization in a Cavity*, Phys. Rev. Lett. **76** (1996) 1800–1803.
URL http://dx.doi.org/10.1103/PhysRevLett.76.1800

[146] A. Badolato, K. Hennessy, M. Atature, J. Dreiser, E. Hu, P. M. Petroff, A. Imamoglu, *Deterministic Coupling of Single Quantum Dots to Single Nanocavity Modes*, Science **308** (2005) 1158–1161.
URL http://dx.doi.org/10.1126/science.1109815

[147] I. Chiorescu, P. Bertet, K. Semba, Y. Nakamura, C. J. P. M. Harmans, J. E. Mooij, *Coherent dynamics of a flux qubit coupled to a harmonic oscillator*, Nature **431** (2004) 159–162.
URL http://dx.doi.org/10.1038/nature02831

[148] M. Albert, J. P. Marler, P. F. Herskind, A. Dantan, M. Drewsen, *Collective strong coupling between ion Coulomb crystals and an optical cavity field: Theory and Experiment*, manuscript in preparation (2010).

[149] S. F. Kaler, S. Gulde, M. Riebe, T. Deuschle, A. Kreuter, G. Lancaster, C. Becher, J. Eschner, H. Häffner, R. Blatt, *The coherence of qubits based on single* Ca^+ *ions*, J. Phys. B **36** (2003) 623–636.
URL http://dx.doi.org/10.1088/0953-4075/36/3/319

[150] P. F. Staanum, K. H. Højbjerre, R. Wester, M. Drewsen, *Probing Isotope Effects in Chemical Reactions Using Single Ions*, Phys. Rev. Lett. **100** (2008) 243003.
URL http://dx.doi.org/10.1103/PhysRevLett.100.243003

[151] M. D. Lukin, S. F. Yelin, M. Fleischhauer, *Entanglement of Atomic Ensembles by Trapping Correlated Photon States*, Phys. Rev. Lett. **84** (2000) 4232–4235.
URL http://dx.doi.org/10.1103/PhysRevLett.84.4232

[152] A. Dantan, J. P. Marler, M. Albert, D. Guénot, M. Drewsen, *Noninvasive Vibrational Mode Spectroscopy of Ion Coulomb Crystals through Resonant Collective Coupling to an Optical Cavity Field*, Phys. Rev. Lett. **105** (2010) 103001+.
URL http://dx.doi.org/10.1103/PhysRevLett.105.103001

[153] D. V. Vasilyev, I. V. Sokolov, E. S. Polzik, *Quantum memory for images: A quantum hologram*, Phys. Rev. A **77** (2008) 020302+.
URL http://dx.doi.org/10.1103/PhysRevA.77.020302

[154] A. T. Black, J. K. Thompson, V. Vuletić, *On-Demand Superradiant Conversion of Atomic Spin Gratings into Single Photons with High Efficiency*, Phys. Rev. Lett. **95** (2005) 133601+.
URL http://dx.doi.org/10.1103/PhysRevLett.95.133601

[155] J. K. Thompson, J. Simon, H. Loh, V. Vuletic, *A High-Brightness Source of Narrowband, Identical-Photon Pairs*, Science **313** (2006) 74–77.
URL http://dx.doi.org/10.1126/science.1127676

[156] M. F. Andersen, C. Ryu, P. Cladé, V. Natarajan, A. Vaziri, K. Helmerson, W. D. Phillips, *Quantized Rotation of Atoms from Photons with Orbital Angular Momentum*, Phys. Rev. Lett. **97** (2006) 170406+.
URL http://dx.doi.org/10.1103/PhysRevLett.97.170406

[157] K. Wagner, J. Janousek, V. Delaubert, H. Zou, C. Harb, N. Treps, J. F. Morizur, P. K. Lam, H. A. Bachor, *Entangling the Spatial Properties of Laser Beams*, Science **321** (2008) 541–543.
URL http://dx.doi.org/10.1126/science.1159663

[158] V. Boyer, A. M. Marino, P. D. Lett, *Generation of Spatially Broadband Twin Beams for Quantum Imaging*, Phys. Rev. Lett. **100** (2008) 143601+.
URL http://dx.doi.org/10.1103/PhysRevLett.100.143601

[159] V. Boyer, A. M. Marino, R. C. Pooser, P. D. Lett, *Entangled Images from Four-Wave Mixing*, Science **321** (2008) 544–547.
URL http://dx.doi.org/10.1126/science.1158275

[160] M. I. Kolobov, C. Fabre, *Quantum Limits on Optical Resolution*, Phys. Rev. Lett. **85** (2000) 3789–3792.
URL http://dx.doi.org/10.1103/PhysRevLett.85.3789

[161] V. Vuletić, H. W. Chan, A. T. Black, *Three-dimensional cavity Doppler cooling and cavity sideband cooling by coherent scattering*, Phys. Rev. A **64** (2001) 033405+.
URL http://dx.doi.org/10.1103/PhysRevA.64.033405

[162] P. Horak, H. Ritsch, *Scaling properties of cavity-enhanced atom cooling*, Phys. Rev. A **64** (2001) 033422+.
URL http://dx.doi.org/10.1103/PhysRevA.64.033422

[163] D. Kruse, M. Ruder, J. Benhelm, C. von Cube, C. Zimmermann, Ph, Th, B. Nagorny, A. Hemmerich, *Cold atoms in a high-Q ring cavity*, Phys. Rev. A **67** (2003) 051802+.
URL http://dx.doi.org/10.1103/PhysRevA.67.051802

[164] P. Domokos, H. Ritsch, *Mechanical effects of light in optical resonators*, J. Opt. Soc. Am. B **20** (2003) 1098–1130.
URL http://dx.doi.org/10.1364/JOSAB.20.001098

[165] J. P. Schiffer, M. Drewsen, J. S. Hangst, L. Hornekar, *Temperature, ordering, and equilibrium with time-dependent confining forces.*, Proc. Natl. Acad. Sci. U. S. A. **97** (2000) 10697–10700.
URL http://dx.doi.org/10.1073/pnas.190320397

[166] D. H. E. Dubin, T. M. O'Neil, *Trapped nonneutral plasmas, liquids, and crystals (the thermal equilibrium states)*, Rev. Mod. Phys. **71** (1999) 87+.
URL http://dx.doi.org/10.1103/RevModPhys.71.87

[167] D. H. E. Dubin, J. P. Schiffer, *Normal modes of cold confined one-component plasmas*, Phys. Rev. E **53** (1996) 5249–5267.
URL http://dx.doi.org/10.1103/PhysRevE.53.5249

[168] D. H. E. Dubin, *Effect of correlations on the thermal equilibrium and normal modes of a non-neutral plasma*, Phys. Rev. E **53** (1996) 5268–5290.
URL http://dx.doi.org/10.1103/PhysRevE.53.5268

[169] H. Totsuji, T. Kishimoto, C. Totsuji, K. Tsuruta, *Competition between Two Forms of Ordering in Finite Coulomb Clusters*, Phys. Rev. Lett. **88** (2002) 125002+.
URL http://dx.doi.org/10.1103/PhysRevLett.88.125002

[170] T. Matthey, J. P. Hansen, M. Drewsen, *Coulomb Bicrystals of Species with Identical Charge-to-Mass Ratios*, Phys. Rev. Lett. **91** (2003) 165001+.
URL http://dx.doi.org/10.1103/PhysRevLett.91.165001

[171] D. J. Heinzen, J. J. Bollinger, F. L. Moore, W. M. Itano, D. J. Wineland, *Rotational equilibria and low-order modes of a non-neutral ion plasma*, Phys. Rev. Lett. **66** (1991) 2080–2083.
URL http://dx.doi.org/10.1103/PhysRevLett.66.2080

[172] J. J. Bollinger, D. J. Heinzen, F. L. Moore, W. M. Itano, D. J. Wineland, D. H. E. Dubin, *Electrostatic modes of ion-trap plasmas*, Phys. Rev. A **48** (1993) 525–545.
URL http://dx.doi.org/10.1103/PhysRevA.48.525

[173] T. Mitchell, J. Bollinger, X. P. Huang, W. Itano, *Doppler imaging of plasma modes in a Penning trap*, Opt. Express **2** (1998) 314–322.
URL http://dx.doi.org/10.1364/OE.2.000314

[174] T. B. Mitchell, J. J. Bollinger, D. H. E. Dubin, X. P. Huang, W. M. Itano, R. H. Baughman, *Direct Observations of Structural Phase Transitions in Planar Crystallized Ion Plasmas*, Science **282** (1998) 1290–1293.
URL http://dx.doi.org/10.1126/science.282.5392.1290

[175] W. M. Itano, J. J. Bollinger, J. N. Tan, B. Jelenkovic, X. P. Huang, D. J. Wineland, *Bragg Diffraction from Crystallized Ion Plasmas*, Science **279** (1998) 686–689.
URL http://dx.doi.org/10.1126/science.279.5351.686

[176] G. Birkl, S. Kassner, H. Walther, *Multiple-shell structures of laser-cooled* $^{24}Mg^{+}$ *ions in a quadrupole storage ring*, Nature **357** (1992) 310–313.
URL http://dx.doi.org/10.1038/357310a0

[177] R. Blümel, C. Kappler, W. Quint, H. Walther, *Chaos and order of laser-cooled ions in a Paul trap*, Phys. Rev. A **40** (1989) 808–823.
URL http://dx.doi.org/10.1103/PhysRevA.40.808

[178] D. Porras, J. I. Cirac, *Quantum Manipulation of Trapped Ions in Two Dimensional Coulomb Crystals*, Phys. Rev. Lett. **96** (2006) 250501+.
URL http://dx.doi.org/10.1103/PhysRevLett.96.250501

[179] D. Porras, J. I. Cirac, *Effective Quantum Spin Systems with Trapped Ions*, Phys. Rev. Lett. **92** (2004) 207901+.
URL http://dx.doi.org/10.1103/PhysRevLett.92.207901

[180] K. W. Murch, K. L. Moore, S. Gupta, D. M. Stamper-Kurn, *Observation of quantum-measurement backaction with an ultracold atomic gas*, Nature Phys. **4** (2008) 561–564.
URL http://dx.doi.org/10.1038/nphys965

[181] F. Brennecke, S. Ritter, T. Donner, T. Esslinger, *Cavity Optomechanics with a Bose-Einstein Condensate*, Science **322** (2008) 235–238.
URL http://dx.doi.org/10.1126/science.1163218

[182] T. J. Kippenberg, K. J. Vahala, *Cavity Optomechanics: Back-Action at the Mesoscale*, Science **321** (2008) 1172–1176.
URL http://dx.doi.org/10.1126/science.1156032

[183] D. Guénot, *Noninvasive measurment of ion Coulomb crystals vibrational modes*, Master's thesis, The University of Aarhus (2009).

[184] C. B. Zhang, D. Offenberg, B. Roth, M. A. Wilson, S. Schiller, *Molecular-dynamics simulations of cold single-species and multispecies ion ensembles in a linear Paul trap*, Phys. Rev. A **76** (2007) 012719+.
URL http://dx.doi.org/10.1103/PhysRevA.76.012719

[185] M. Drewsen, A. Mortensen, R. Martinussen, P. Staanum, J. L. Sørensen, *Nondestructive Identification of Cold and Extremely Localized Single Molecular Ions*, Phys. Rev. Lett. **93** (2004) 243201+.
URL http://dx.doi.org/10.1103/PhysRevLett.93.243201

[186] I. García-Mata, O. V. Zhirov, D. L. Shepelyansky, *Frenkel-Kontorova model with cold trapped ions*, Eur. Phys. J. D **41** (2007) 325–330.
URL http://dx.doi.org/10.1140/epjd/e2006-00220-2

[187] A. Retzker, R. C. Thompson, D. M. Segal, M. B. Plenio, *Double Well Potentials and Quantum Phase Transitions in Ion Traps*, Phys. Rev. Lett. **101** (2008) 260504+.
URL http://dx.doi.org/10.1103/PhysRevLett.101.260504

[188] S. Fishman, G. De Chiara, T. Calarco, G. Morigi, *Structural phase transitions in low-dimensional ion crystals*, Phys. Rev. B **77** (2008) 064111+.
URL http://dx.doi.org/10.1103/PhysRevB.77.064111

[189] K. Härkönen, F. Plastina, S. Maniscalco, *Dicke model and environment-induced entanglement in ion-cavity QED*, Phys. Rev. A **80** (2009) 033841+.
URL http://dx.doi.org/10.1103/PhysRevA.80.033841

[190] K. Baumann, C. Guerlin, F. Brennecke, T. Esslinger, *Dicke quantum phase transition with a superfluid gas in an optical cavity*, Nature **464** (2010) 1301–1306.
URL http://dx.doi.org/10.1038/nature09009

[191] M. J. Jensen, T. Hasegawa, J. J. Bollinger, D. H. E. Dubin, *Rapid Heating of a Strongly Coupled Plasma near the Solid-Liquid Phase Transition*, Phys. Rev. Lett. **94** (2005) 025001+.
URL http://dx.doi.org/10.1103/PhysRevLett.94.025001

[192] F. Zimmer, A. Andre, M. Lukin, M. Fleischhauer, *Coherent control of stationary light pulses*, Opt. Commun. **264** (2006) 441–453.
URL http://dx.doi.org/10.1016/j.optcom.2006.03.075

[193] Y. W. Lin, W. T. Liao, T. Peters, H. C. Chou, J. S. Wang, H. W. Cho, P. C. Kuan, I. A. Yu, *Stationary Light Pulses in Cold Atomic Media and without Bragg Gratings*, Phys. Rev. Lett. **102** (2009) 213601+.
URL http://dx.doi.org/10.1103/PhysRevLett.102.213601

[194] J. H. Wu, M. Artoni, G. C. La Rocca, *Stationary light pulses in cold thermal atomic clouds*, Phys. Rev. A **82** (2010) 013807+.
URL http://dx.doi.org/10.1103/PhysRevA.82.013807

[195] S. E. Harris, Y. Yamamoto, *Photon Switching by Quantum Interference*, Phys. Rev. Lett. **81** (1998) 3611–3614.
URL http://dx.doi.org/10.1103/PhysRevLett.81.3611

[196] M. Yan, E. G. Rickey, Y. Zhu, *Observation of absorptive photon switching by quantum interference*, Phys. Rev. A **64** (2001) 041801+.
URL http://dx.doi.org/10.1103/PhysRevA.64.041801

[197] D. A. Braje, V. Balić, G. Y. Yin, S. E. Harris, *Low-light-level nonlinear optics with slow light*, Phys. Rev. A **68** (2003) 041801+.
URL http://dx.doi.org/10.1103/PhysRevA.68.041801

[198] A. M. C. Dawes, L. Illing, S. M. Clark, D. J. Gauthier, *All-Optical Switching in Rubidium Vapor*, Science **308** (2005) 672–674.
URL http://dx.doi.org/10.1126/science.1110151

[199] A. Imamoglu, H. Schmidt, G. Woods, M. Deutsch, *Erratum: Strongly Interacting Photons in a Nonlinear Cavity [Phys. Rev. Lett. 79, 1467 (1997)]*, Phys. Rev. Lett. **81** (1998) 2836+.
URL http://dx.doi.org/10.1103/PhysRevLett.81.2836

[200] K. M. Gheri, W. Alge, P. Grangier, *Quantum analysis of the photonic blockade mechanism*, Phys. Rev. A **60** (1999) R2673–R2676.
URL http://dx.doi.org/10.1103/PhysRevA.60.R2673

[201] M. J. Werner, A. Imamoglu, *Photon-photon interactions in cavity electromagnetically induced transparency*, Phys. Rev. A **61** (1999) 011801+.
URL http://dx.doi.org/10.1103/PhysRevA.61.011801

[202] K. M. Birnbaum, A. Boca, R. Miller, A. D. Boozer, T. E. Northup, H. J. Kimble, *Photon blockade in an optical cavity with one trapped atom*, Nature **436** (2005) 87–90.
URL http://dx.doi.org/10.1038/nature03804

[203] B. Dayan, A. S. Parkins, T. Aoki, E. P. Ostby, K. J. Vahala, H. J. Kimble, *A Photon Turnstile Dynamically Regulated by One Atom*, Science **319** (2008) 1062–1065.
URL http://dx.doi.org/10.1126/science.1152261

[204] C. Ottaviani, D. Vitali, M. Artoni, F. Cataliotti, P. Tombesi, *Polarization Qubit Phase Gate in Driven Atomic Media*, Phys. Rev. Lett. **90** (2003) 197902+.
URL http://dx.doi.org/10.1103/PhysRevLett.90.197902

[205] A. Dantan, J. Cviklinski, E. Giacobino, M. Pinard, *Spin Squeezing and Light Entanglement in Coherent Population Trapping*, Phys. Rev. Lett. **97** (2006) 023605+.
URL http://dx.doi.org/10.1103/PhysRevLett.97.023605

[206] A. D. Greentree, C. Tahan, J. H. Cole, L. C. L. Hollenberg, *Quantum phase transitions of light*, Nature Phys. **2** (2006) 856–861.
URL http://dx.doi.org/10.1038/nphys466

[207] M. J. Hartmann, F. G. S. L. Brandao, M. B. Plenio, *Strongly interacting polaritons in coupled arrays of cavities*, Nature Phys. **2** (2006) 849–855.
URL http://dx.doi.org/10.1038/nphys462

[208] L. Tian, H. J. Carmichael, *Quantum trajectory simulations of two-state behavior in an optical cavity containing one atom*, Phys. Rev. A **46** (1992) R6801–R6804.
URL http://dx.doi.org/10.1103/PhysRevA.46.R6801

[209] K. Hennessy, A. Badolato, M. Winger, D. Gerace, M. Atature, S. Gulde, S. Falt, E. L. Hu, A. Imamoglu, *Quantum nature of a strongly coupled single quantum dot-cavity system*, Nature **445** (2007) 896–899.
URL http://dx.doi.org/10.1038/nature05586

[210] D. I. Schuster, A. A. Houck, J. A. Schreier, A. Wallraff, J. M. Gambetta, A. Blais, L. Frunzio, J. Majer, B. Johnson, M. H. Devoret, S. M. Girvin, R. J. Schoelkopf, *Resolving photon number states in a superconducting circuit*, Nature **445** (2007) 515–518.
URL http://dx.doi.org/10.1038/nature05461

[211] K. Srinivasan, O. Painter, *Linear and nonlinear optical spectroscopy of a strongly coupled microdisk-quantum dot system*, Nature **450** (2007) 862–865.
URL http://dx.doi.org/10.1038/nature06274

[212] I. Schuster, A. Kubanek, A. Fuhrmanek, T. Puppe, P. W. H. Pinkse, K. Murr, G. Rempe, *Nonlinear spectroscopy of photons bound to one atom*, Nature Phys. **4** (2008) 382–385.
URL http://dx.doi.org/10.1038/nphys940

[213] H. Kang, Y. Zhu, *Observation of Large Kerr Nonlinearity at Low Light Intensities*, Phys. Rev. Lett. **91** (2003) 093601+.
URL http://dx.doi.org/10.1103/PhysRevLett.91.093601

[214] Poizat, P. Grangier, *Experimental realization of a quantum optical tap*, Phys. Rev. Lett. **70** (1993) 271–274.
URL http://dx.doi.org/10.1103/PhysRevLett.70.271

[215] Q. A. Turchette, C. J. Hood, W. Lange, H. Mabuchi, H. J. Kimble, *Measurement of Conditional Phase Shifts for Quantum Logic*, Phys. Rev. Lett. **75** (1995) 4710–4713.
URL http://dx.doi.org/10.1103/PhysRevLett.75.4710

[216] J. J. Sakurai, *Modern Quantum Mechanics*, Revised Edition, Addison-Wesley Publishing Company, Reading, Massachusetts, 1994.

[217] I. Bronstein, K. Semendjajew, *Taschenbuch der Mathematik*, 25th Edition, B.G. Teubner Verlagsgesellschaft, Stuttgart, Leipzig, 1991.

[218] K. R. Hansen, K. Mølmer, *Stationary light pulses in ultracold atomic gases*, Physical Review A **75** (2007) 065804+.
URL http://dx.doi.org/10.1103/PhysRevA.75.065804

[219] K. R. Hansen, K. Mølmer, *Trapping of light pulses in ensembles of stationary* Λ *atoms*, Physical Review A **75** (2007) 053802+.
URL http://dx.doi.org/10.1103/PhysRevA.75.053802